Aspects of Scalar Field Theory and the Dark Matter Problem

A Thesis Submitted to the
College of Graduate and Postdoctoral Studies
in Partial Fulfillment of the Requirements
for the degree of Doctor of Philosophy
in the Department of Physics and Engineering Physics
University of Saskatchewan
Saskatoon

By
Frederick S. Sage

Permission to Use

In presenting this thesis in partial fulfilment of the requirements for a Postgraduate degree from the University of Saskatchewan, I agree that the Libraries of this University may make it freely available for inspection. I further agree that permission for copying of this thesis in any manner, in whole or in part, for scholarly purposes may be granted by the professor or professors who supervised my thesis work or, in their absence, by the Head of the Department or the Dean of the College in which my thesis work was done. It is understood that any copying or publication or use of this thesis or parts thereof for financial gain shall not be allowed without my written permission. It is also understood that due recognition shall be given to me and to the University of Saskatchewan in any scholarly use which may be made of any material in my thesis.

Requests for permission to copy or to make other use of material in this thesis in whole or part should be addressed to:

Head of the Department of Physics and Engineering Physics
162 Physics Building
116 Science Place
University of Saskatchewan
Saskatoon, Saskatchewan
Canada
S7N 5E2

Dean
College of Graduate and Postdoctoral Studies
116 Thorvaldson Building
110 Science Place
University of Saskatchewan
Saskatoon, Saskatchewan
Canada
S7N 5C9

Abstract

This thesis is comprised of research on the topic of particle dark matter phenomenology, with an emphasis on models in which a scalar field plays an important role. The dark matter problem is reviewed in Chapter 1, including the evidence that it is comprised of. Also included in Chapter 1 is an overview of the standard particle physics and quantum field theory that is used in the thesis. Chapter 2 is a discussion of the constraints on models of particle dark matter from observations of the abundance, assuming thermal production mechanisms in the early universe. The thermal constraints on scalar Higgs-portal dark matter are discussed as an example. The direct detection of dark matter through nuclear recoils is covered in Chapter 3, which provides an overview of the basic theory and a discussion of the various experiments and their reported and predicted results. Some discussion of the future of direct detection is included, as is the application of the techniques to the example case of scalar Higgs-portal dark matter. Chapter 4 contains some details about the indirect detection of dark matter through observation of the products of its annihilation in the galactic halo, primarily through the gamma ray channel. Several possible gamma ray targets are considered, including the galactic core, dwarf spheroidal galaxies, and searches for signals in the isotropic background. The Chapter closes with the usual example of scalar Higgs-portal dark matter. In Chapter 5 collider signatures of dark matter are discussed. After a lengthy review of collider physics, the basic techniques for placing bounds on dark matter models using collider data are discussed, and finally the scalar Higgs-portal model is discussed in the context of collider signals. Chapter 6 explores a theoretically motivated model of vector-portal fermionic dark matter, including collider bound on the vector mediator, thermal constraints on the dark matter particle based on abundance observations, and bound from direct and indirect detection. The theoretical background renders the phenomenology of the model exceptionally predictive, and the viability of the model given current observations is discussed. Chapter 7 contains some concluding remarks.

Acknowledgements

This thesis, and the research that has gone into it, have taken some time. There are many people who have helped me along the way, without whom I would no doubt never have gotten so far.

A great deal of thanks is owed to my doctoral supervisor, Prof. Rainer Dick. Without his patient guidance and firm support over these last several years, I would never have been able to get to this point. I would also like to thank my Advisory Committee, Prof. Masoud Ghezelbash, Prof. Rob Pywell, Prof. Jacek Szmigielski, and Prof. Adam Bourassa, for their helpful advice and support throughout my degree. I must also thank my collaborators, Zhi-Wei Wang, Jason Ho, Tom Steele, and Rob Mann, for putting up with me during our work together. Finally, I must thank the late Prof. Jim Brooke, my undergraduate advisor and the instructor of several of my classes. Without his enthusiastic support, I would have stumbled many years ago.

I would like to thank Ben Zitzer and David Hanna for their assistance in sharing the data for the portion of Chapter 4 that deals with VERITAS observations of Segue I, as well as the MAGIC collaboration and Javier Rico in particular for providing the bounds on the annihilation cross sections that were used in Chapter 4.

I have been supported during these studies by a William J Rowles Fellowship, a Gerhard Herzberg Fellowship, a Teacher-Scholar Doctoral Fellowship, and several Graduate Research Fellowships. Travel during this time has been supported by several University Travel Awards and Herzberg Travel Awards.

And of course there is the inevitable list of graduate students (most of whom are no longer graduate students) who impacted (mostly positively) my academic life here. I would like to thank Tony Bathgate, Ryan Berg, Dena Burnett, Stephanie Goertzen, Adrian Hunt, Darren Hunter, Daryl Janzen, Robin Kleiv, John McLeod, Sarah Purdy, Grant Scouler, Haryanto Siahaan, Paul Smith, Greg Tomney, Niloofar Zarifi, and Dan Zawada.

And I guess I should thank my parents, for having me.

Contents

List of Tables

List of Figures

List of Abbreviations

Excluding collaborations, software packages and units

CCD	Charge-coupled device
CKM	Cabibbo-Kobayashi-Maskawa
CMB	Cosmic microwave background
CW	Coleman-Weinberg
dSph	Dwarf spheroidal
EFT	Effective field theory
FCNC	Flavor-changing neutral current
FIMP	Feebly interacting massive particle
GF	Gluon fusion
GUT	Grand unified theory
IGRB	Isotropic gamma ray background
IR	Infrared
LW	Lee-Weinberg
MACHO	Massive compact halo object
MOND	Modified Newtonian dynamics
NFW	Navarro-Frenk-White
NLO	Next-to-leading-order
PQ	Peccei-Quinn
QCD	Quantum chromodynamics
QED	Quantum electrodynamics
QFT	Quantum field theory
SD	Spin dependent
SI	Spin independent
SI units	System international units
SM	Standard model
SUSY	Supersymmetry
UV	Ultraviolet
VBF	Vector boson fusion
WIMP	Weakly interacting massive particle

Chapter 1

Background and Motivation

1.1 The dark matter problem

The nature of the dark matter that makes up much of the gravitating mass of the universe has been a mystery for half a century, and was a curiosity for the half century preceding. That the dark matter problem is real is beyond doubt, but two decades of concentrated search efforts for new physics that could resolve the problem have only been able to infer certain facts indirectly. Dark matter itself has proven frustratingly elusive, with no direct sign so far of any non-gravitational influence on the rest of the universe. The favored solution among physicists is that dark matter is some kind of exotic particle that is not a part of the Standard Model (SM) of particle physics. What properties this particle has, how it fits into the rest of particle theory, and whether or not it is even a single species of particle are all issues of ongoing research and debate.

1.1.1 Basic statement

The dark matter problem is essentially the discrepancy between theoretical predictions of the motions of certain astrophysical systems and the actual observations of said systems. The discrepancy can be resolved by including in the system gravitating mass that does not interact measurably with electromagnetic radiation; this mass is called dark matter.

Dark matter must have several properties, inferred from these observations. First, as mentioned above, it must be optically dark, interacting very weakly or not at all with the electromagnetic force. From this it follows that dark matter cannot cool by the radiation of photons as can other forms of matter. This means it is very difficult for dark matter to change temperature. Dark matter is approximately collisionless, which means that it interacts with itself (through non-gravitational means) only very weakly. As a consequence of the above properties, it is also dissipationless, avoiding the collapse into higher density gravitational structures to which baryonic matter inevitably succumbs. From the way it is bound in galactic halos, we can infer that it must be nonrelativistic. This inference allows constraints to be placed on the density and velocity distribution of particle dark matter. As no evidence of any discreteness has been observed on galactic scales, dark matter must also be a fluid on those scales.

Additionally, dark matter must be compatible with all other astrophysical observations and bounds. It must not significantly alter stellar evolution, and must be consistent with Big Bang nucleosynthesis as

currently understood. Any model of physics that hopes to explain the dark matter problem must satisfy these properties or provide compelling reasons why they do not apply. In this thesis, we study models of particle dark matter that satisfy these properties.

1.1.2 Theme of thesis

This thesis will discuss several topics that fall under the general umbrella of dark matter particle phenomenology. The basic unifying theme is the connection between scalar quantum field theories and dark matter sectors. This is somewhat vague, and so further exposition is probably warranted.

In the last several decades, there have been many models proposed that extend the SM to varying degrees. These models are usually introduced to explain one or more of the numerous phenomenological or theoretical issues in particle physics which the SM cannot address. It is not a coincidence that the majority of these models of beyond SM physics introduce one or more scalar fields. Fundamentally, the reason for this lies in the hierarchy of energy scales inherent to the SM as constructed. In 2012, the SM Higgs boson was observed [1, 2] with a mass of $m_h \simeq 125$ GeV. This validated the SM, but did not provide evidence for anything outside it.

The Lorentz scalar quantum field has played a crucial part in the development of modern particle theory. A scalar field, in the guise of the Higgs boson, was used to solve the electroweak boson mass problem that appeared in the naive electroweak gauge theory through the mechanism of spontaneous symmetry breaking. The same scalar field generates the rest masses of the SM fermions, and even the its own mass. However, the introduction of a fundamental scalar into the theory has also introduced a theoretical problem with which the community has grappled for decades. This problem is commonly known as the hierarchy problem.

In the SM Lagrangian, the only term which is dimensionful is the negative mass term of the Higgs field, which is present to explicitly break electroweak symmetry and allow the activation of the Higgs mechanism. Due to gauge invariance, a condensate (nonzero vacuum expectation value) is required to generate the necessary masses for the electroweak gauge bosons, and due to the observed Lorentz invariance of spacetime, the only condensates that can form are Lorentz scalars. The scalar Higgs field with spontaneous symmetry breaking can form this condensate, and is the final piece of the SM as it stands. However, the very existence of a fundamentally scalar field causes issues in the theory.

Scalar fields, due to the dimensionality of their couplings with particles in other representations of the Lorentz group, are highly sensitive to quantum corrections. Consider a theory in which a scalar couples through a Yukawa coupling to a fermion of mass m_ψ. The leading order correction to the scalar mass, calculated from the 1-loop correction to the scalar propagator, behaves like

$$\Delta m_\phi^2 \approx \frac{y_\psi}{(4\pi)^2} m_\psi^2. \tag{1.1}$$

This correction is clearly proportional to the fermion mass squared.

Consider such a correction to the mass of the SM Higgs boson from a fermion outside of the SM. No new fermions have been observed at energies near the electroweak scale, so for a new fermion to exist, one would expect it to have a mass $m_\psi \gg 100$ GeV. Such mass scales lead to very large quantum corrections to the SM Higgs boson mass, which is known to be about 125 GeV. If one assumes the existence of new physics, which is required at the very least by a field theory of quantum gravity, one must ask why such very large corrections do not manifest in the Higgs mass. That this Higgs mass is so close to the electroweak scale becomes highly suspicious. This unnaturalness is one aspect of the hierarchy problem, and is probably the simplest to motivate.

There are a number of ways of resolving this issue, which are the basis of a number of models for beyond SM physics. One possibility, which is the motivation behind supersymmetry (SUSY), is that the corrections are carefully cancelled term by term by other corrections of similar magnitude. Such a delicate cancellation requires some kind of custodial symmetry. Another popular resolution is to propose that the SM Higgs is not in fact a fundamental scalar, and that at some scale higher than the electroweak scale it is better described as a composite particle. This neatly avoids the issue. One could also suppose the existence of a fundamental scale much lower than the Planck scale, and alleviate the problem by reducing the need for fine-tuning, as is done in some theories of extra dimensions. All of these options and more have been extensively explored in the literature, and will continue to be explored for some time.

Given the fundamental importance of scalar fields to the SM and its extensions, it seems important to consider the role of scalar field theory in the dark matter problem. There is no requirement that scalars are involved in the dark matter problem, but it would be exceedingly odd if they were not.

This thesis explores a number of connections that can be made between scalar fields and particle dark matter, particularly those that have been explored by the author during his time at graduate school. The emphasis is on the phenomenological aspects of particle dark matter, particularly those that are related to scalar fields such as the SM Higgs. No attempt is made at exhaustiveness.

1.1.3 Outline of thesis

This thesis is organized along the following lines.

In the remainder of this Chapter, we will discuss basic aspects of particle physics relevant to subsequent Chapters. The next Section contains a summary of the pertinent aspects of the SM of particle physics and some of the details of quantum field theory that are required to study the phenomenology of particle dark matter. A review of the current evidence for the existence of dark matter is provided, including evidence from galactic scales, the scale of galaxy clusters and cosmological scales. Potential solutions to the dark matter problem, both particle in origin and otherwise, are briefly surveyed.

Chapter 2 considers particle dark matter in the early universe, with a focus on the WIMP paradigm of thermal production. The basic formalism of freeze-out is reviewed and used to constrain present day phenomenological parameters for a basic model. In Chapter 3 is a detailed discussion of the experimental

effort for the direct detection of particle dark matter. The basic theory is reviewed, and certain currently operating experiments are discussed. The status of experimental results is reported and the direct detection phenomenology of a simple model of dark matter is explored as an example.

Indirect detection of dark matter is considered in Chapter 4, primarily in the gamma ray channel. The construction of a basic photon signal from the annihilation of dark matter is reviewed. This is followed by discussion of the potential for signal observation of several different target regions and scenarios. These include signals in the IGRB, monochromatic photon line searches, targeted searches of dwarf spheroidal galaxies near the Milky Way, and an examination of dark matter explanations for the observed galactic core gamma ray excess. Other annihilation channels are briefly mentioned and an example of phenomenological calculations is once again provided with a simple model.

Chapter 5 contains a discussion of signatures of dark matter production in particle colliders. First, the basics of collider physics and calculations using the parton model are reviewed. Bounds on mediators to dark sectors are discussed next, which is followed by a discussion of collider bounds on dark matter particles, including basic dark matter production as well as the so-called 'mono-X' signatures in which a dark matter particle is produced along with a visible particle. The Chapter closes with the standard application of the material to scalar Higgs-portal dark matter. Chapter 5 closes the generic discussion of dark matter detection channels.

Chapter 6 is an exploration of a preliminary vector-portal dark matter model that has the property of partial asymptotic safety. The model is constructed in detail, including discussions of ultraviolet (UV) boundary conditions to the renormalization group equations, radiative symmetry breaking, and anomaly cancellation conditions. The phenomenology of the model is considered, first in the collider setting, and then in the context of dedicated dark matter searches.

Finally, Chapter 7 contains a summary of the results found in this thesis and presents some concluding remarks. Several Appendices have been included to provide some discussion that does not fit in the main body of the thesis.

1.2 Basic particle physics

This thesis explores the phenomenology of particle dark matter. In this context 'phenomenology' is the study of physical phenomena; for a particle physicist this is essentially the calculation of physical quantities from theoretical predictions and comparison of those predictions with experimental results. Depending on how advanced the theory and experiment are in relation with one another, the comparison step may be omitted, leaving only a prediction. For example, the SM Higgs boson was only a prediction for some forty years before it was observed.

A model of particle dark matter is a solution to the dark matter problem that posits the existence of exotic mass distributed in such a way as to explain the observed gravitational phenomena that make up said

problem. The exotic mass is assumed to admit a particle physics description, which means that the particle dark matter and its interactions are described by a quantum field theory (QFT). That it is exotic means that the QFT that describes dark matter is not part of the SM of particle physics.

To study particle dark matter then requires an understanding of the principles and techniques of QFT, both in the context of the SM and beyond. This Section provides a review of the basic elements of QFT as applied to particle physics that are required to understand the majority of the thesis. Of course, topics are treated in a very brief fashion, and several fundamental concepts that are not immediately required in the thesis are omitted. A reader looking for more detail is invited to consult their favorite QFT text (if you don't have one, maybe you should stop reading now) or one of the following references, which have been used extensively in the preparation of this thesis [3, 4, 5, 6, 7].

The SM is a QFT that describes the interactions between fundamental forms of matter, with the exception of gravitational interactions. It is a triumph of modern particle physics and is one of the most accurate physical theories that has been tested [8]. The SM is formulated as a quantum gauge field theory, where the physics is invariant under the gauge group $SU(3)_c \times SU(2)_L \times U(1)_Y$. Through Noether's Theorem, one can translate these invariance properties into the associated conserved charges. The SM consists of fermions (quarks and leptons), gauge bosons associated with the gauge symmetries, and the scalar Higgs boson. We proceed by reviewing important concepts that are part of the SM as we build it up sector by sector.

1.2.1 Conventions and notation

This section establishes the conventions and nonstandard notation that will be used in the remainder of the thesis. A list of abbreviations used also appears at the beginning of the document.

Calculations and results are generally formulated in the system of 'natural units,' in which the physical quantities c and $\hbar$ are set to the dimensionless constant 1. The exceptions are when discussing certain cross sections, when comparison to experimental results is easier in SI units of cm^2 or pb/fb (picobarns/femtobarns - see Appendix A for details), and when talking about most astrophysical phenomena. These exceptions are clearly indicated. More details on the unit systems used in this thesis and conversion factors between them and SI units are presented in Appendix A.

Spacetime indices are given by the Greek letters μ, ν, ρ, σ, λ, and κ, though we try to avoid using anything but μ and ν. Dirac indices are usually suppressed, but when made explicit, they are denoted by Greek letters starting at the beginning of the alphabet (α, β, γ, etc.). SM color indices are also usually suppressed, and denoted by capital Latin letters A, B, C when made explicit.

The Minkowski metric of flat spacetime is denoted by $\eta_{\mu\nu}$, where

$$\eta_{\mu\nu} = \eta^{\mu\nu} = \begin{pmatrix} 1 & 0 & 0 & 0 \\ 0 & -1 & 0 & 0 \\ 0 & 0 & -1 & 0 \\ 0 & 0 & 0 & -1 \end{pmatrix}. \tag{1.2}$$

Spacetime coordinates are x, y, z or subscripted versions of these letters if more are required. In four dimensional spacetime, they are four-vectors with components $x^\mu = (x^0, x^1, x^2, x^3) = (t, \bar{x})$, where the superscript μ is frequently suppressed. Four-vectors can be transformed between the covariant and contravariant bases through

$$x_\mu = \eta_{\mu\nu} x^\nu \tag{1.3}$$

$$x^\mu = \eta^{\mu\nu} x_\nu \tag{1.4}$$

Momenta are denoted by p, k, q or l, with q typically used for momentum transfer in a physical process, and l exclusively used for the loop momenta in a loop-order process. When the momenta are three-momenta, they are denoted with a bar ($\bar{p}$); when they are four-momenta, they are furnished with a frequently suppressed Greek Lorentz index ($p^\mu = (E, \bar{p})$). Our metric convention is such that $p^2 = p^\mu p_\mu = E^2 - \bar{p}^2 = m^2$.

The Mandelstam variables s, t and u are frequently used. They are, for incoming momenta p_1, p_2 and outgoing momenta p_3, p_4:

$$\begin{aligned} s &= (p_1 + p_2)^2 = (p_3 + p_4)^2 , \\ t &= (p_1 - p_3)^2 = (p_2 - p_4)^2 , \\ u &= (p_1 - p_4)^2 = (p_2 - p_3)^2 . \end{aligned} \tag{1.5}$$

The variable s is the center of mass energy of the collision squared, while the others frequently appear in cross section calculations.

The following general conventions for the labelling of classical and quantum field variables are followed, though in different Sections the same character may represent two different fields. Details of the physics of these fields is outlined in the subsequent parts of this Section. The character ϕ or φ represents a scalar field. The characters ψ and χ, or occasionally f, represent either a generic fermion field or a specific one as indicated in the text, usually with a distinguishing subscript. Vector fields are denoted by a descriptive character, or V generically. Quarks are collectively q when all six flavors are considered equivalently, or q and Q for light and heavy quarks, respectively, when that distinction needs to be made.

The Dirac gamma matrices γ^μ are used frequently throughout. Results are generally agnostic of what basis for these matrices is used; when a specific basis is used, it is indicated in the text. Likewise for the γ^5 matrix. The conjugate of a Dirac spinor ψ is given by $\bar{\psi} = \psi^\dagger \gamma^0$, where $\psi^\dagger$ is the conjugate transpose of ψ, such that the quantity $\bar{\psi}\psi$ is invariant under Lorentz transformations.

We relate the gauge coupling g for a given gauge group to the more useful scaled coupling in the usual way

$$\alpha_g = \frac{g^2}{32\pi^2}, \tag{1.6}$$

so that leading order decay rates are $\sim \alpha_g$ and leading order cross sections in the basic gauge theory are $\sim \alpha_g^2$.

1.2.2 Quantum field theory

One of the key features of modern physics is that, at certain scales, reality becomes quantum in nature. The classical point particle approximation and the classical electromagnetic wave approximation begin to break down as matter and radiation exhibit properties that cannot be described using classical physics. This is exemplified by the microscopic behaviour of the electron being better described by the Schrödinger wave equation than by the classical equations of motion. This transition can be characterized by the Planck constant $\hbar$: quantum effects are proportional to $\hbar$. Because of the scales involved, the study of particle physics is the study of inherently quantum phenomena.

Quantum field theories are the extension of the so-called first quantized theory, where the wavefunction of the latter has been interpreted as an operator. Systems with changing particle number are easily described in a QFT, which overcomes one of the main weaknesses of the first quantized theory. This is achieved by describing particle degrees of freedom as the excitations of an object called a quantum field, which is derived from the more familiar classical field through a process called second or canonical quantization.

The process can be illustrated with a simple example. Consider the classical theory of a single field $\phi(x)$, which can be described by the Lagrangian

$$\mathcal{L} = \frac{i}{2}\left(\phi^\dagger \partial_t \phi - \partial_t \phi^\dagger \phi\right) - \frac{1}{2m}\nabla\phi^\dagger \cdot \nabla\phi - \phi^\dagger V \phi. \tag{1.7}$$

This is the Schrödinger theory in the Lagrangian formalism, and describes the dynamics of a nonrelativstic free quantum particle with no spin in a classical potential V. Applying the variational procedure leads to the Schrödinger equation describing the dynamics of the field $\phi(x)$, which can be identified with the Schrödinger wavefunction of the particle. Note the Lagrangian must contain terms with products of fields that act at the same spacetime point, else there is a violation of causality (infinite propagation speed of fields).

The Lagrangian of the system contains the dynamics of the fields, but it is also important to consider the Hamiltonian representation of the theory. The Hamiltonian can be constructed by computing the canonical momentum

$$\pi(x) = \frac{\partial \mathcal{L}}{\partial\left(\partial_t \phi\right)} \tag{1.8}$$

that corresponds to the field $\phi(x)$ (and similarly for $\phi^\dagger(x)$). The Hamiltonian is then

$$\mathcal{H} = \pi(x)\partial_t\phi(x) - \mathcal{L} \tag{1.9}$$

which becomes, for the Lagrangian in Equation (1.7)

$$\mathcal{H} = \frac{1}{2m}\nabla\phi^\dagger \cdot \nabla\phi + \phi^\dagger V \phi. \tag{1.10}$$

We now have the theory undergo second quantization. The 'second' is in contrast to the so-called first quantization, where the uncertainty relation is applied to the position and momentum, and they become operators. Second quantization takes the classical field ϕ and makes it an operator that obeys a commutation algebra. It is the redefinition of the field to be an object that obeys the commutation algebra that takes the classical field theory to a quantum field theory. It is at this point, now that the fields are quantum objects, that we may claim to be working in a QFT. Similarly, the conjugate momenta $\pi(x)$ can be quantized, with the Hamiltonian and Lagrangian now describing a quantum theory. The full algebra is

$$\begin{aligned}[\phi(x), \phi^\dagger(x')] = \delta(\bar{x} - \bar{x}') = [\pi(x), \pi^\dagger(x')] = [\phi(x), \pi(x')], \\ [\phi, \phi] = [\phi^\dagger, \phi^\dagger] = [\pi, \pi] = [\pi^\dagger, \pi^\dagger] = 0.\end{aligned} \tag{1.11}$$

To proceed, we take the Fourier expansion of the field ϕ, with Fourier coefficients a and $a^\dagger$

$$\phi(x) = \int \frac{d^3k}{(2\pi)^3 2E_k}\left[a(\bar{k})e^{-i\bar{k}\cdot\bar{x}} + a^\dagger(\bar{k})e^{i\bar{k}\cdot\bar{x}}\right]. \tag{1.12}$$

The conjugate field $\phi^\dagger$ has a similar definition. This is in analogy to the plane wave representation of a free particle in the first quantized theory. It can be taken going forward as the definition of a scalar quantum field ϕ. From this expression, and a similar expression for the conjugate momenta, one can use the commutation relations for ϕ and π to get commutation relations for a and $a^\dagger$:

$$\begin{aligned}[a, a] = [a^\dagger, a^\dagger] = 0 \\ [a(k), a^\dagger(k')] = 2E_k\delta(\bar{k} - \bar{k}')\end{aligned} \tag{1.13}$$

The expression in equation (1.12) is a plane wave, so one expects to be able to write the Hamiltonian as the Hamiltonian of the simple harmonic oscillator

$$H_{SHO} = \left(n + \frac{1}{2}\right)\hbar\omega \tag{1.14}$$

This naturally encourages the interpretation of a and $a^\dagger$ as ladder operators, as in the case of the quantum harmonic oscillator. But what is the ladder here?

By taking the quantum mechanical expectation value of the field (1.12), we can see $a|\phi\rangle = 0$. Since $\phi \sim a + a^\dagger$, this supports an interpretation of a and $a^\dagger$ as creation and annihilation operators. This allows

us to rewrite the Hamiltonian in terms of the number operator $N(\bar{k}) = a^\dagger(\bar{k})a(\bar{k})$ which is the number of particles with momentum $\bar{k}$. The Hamiltonian is

$$\mathcal{H} = \int \frac{d^3k}{(2\pi)^3} E_k N(\bar{k}). \tag{1.15}$$

The ladder is thus a particle number ladder. The creation operator $a^\dagger(\bar{k})$ creates a particle with momentum $\bar{k}$ and the annihilation operator $a(\bar{k})$ annihilates a particle with momentum $\bar{k}$. This interpretation of a quantum field theory as a simple harmonic oscillator of particle creation and annihilation is fundamental to modern theoretical physics and its importance cannot be overstated.

The nonzero vacuum energy follows from the fact that the creation and annihilation operators do not commute, and can be interpreted as a consequence of the quantum nature of the system. Normal ordering is a process of successive commutations of operators to extract terms that vanish when taken as vacuum matrix elements. Explicitly, it is a process of redefining the Hamiltonian so that all the annihilation operators are to the right of all creation operators. The remaining terms can be written as functions, which allows a much simpler treatment, as we know what happens when we consider expectation values without pages of tedious calculations.

Quantization of theories with multiple fields, and of theories with fields that have different spins (see Section 1.2.4 for more discussion of these fields), proceeds in much the same manner. Further details and examples appear in any of the standard texts on QFT referenced above.

The transition to the interaction picture of a QFT allows the usefulness of the perturbative approach to become apparent. Consider a Hamiltonian that can be written in terms of a bare piece and a small interaction piece $\mathcal{H}_{int}$:

$$\mathcal{H} = \mathcal{H}_0 + \mathcal{H}_{int} \tag{1.16}$$

The interaction potential $\mathcal{H}_{int}$ is treated as a small perturbation of the free part of the theory, and a perturbative expansion similar to what is used in basic quantum mechanics can be applied. The free part is typically solvable exactly. The perturbative approach is justified by expanding in the typically small coupling constant in the potential of the theory. The perturbative expansion allows matrix elements to be written explicitly to some order in the coupling constant, allowing an approximate result to be obtained by truncation of the series. Perturbative techniques are ubiquitous in particle physics, and are discussed further in the context of relativistic QFTs in Section 1.2.4.

1.2.3 Symmetries in quantum field theory

A fundamental concept in physics is the notion of a symmetry. One says a physical theory has a symmetry if the transformations associated with that symmetry do not alter the physical predictions of the theory. Mathematically, symmetries are manifestations of abstract objects called groups, with symmetry transformations

being the elements of the group.

Mathematically, a group is a set (G) and an operation ($\cdot$) that is applied to elements of that set ($g \, \epsilon \, G$) that satisfies the following conditions:

1) Closure: For $a, b \, \epsilon \, G$, $a \cdot b \, \epsilon \, G$,

2) Associativity: For $a, b \, \epsilon \, G$, $a \cdot (b \cdot c) = (a \cdot b) \cdot c$,

3) Identity: There exists an element $e \, \epsilon \, G$ such that $e \cdot a = a \cdot e = a$ for all $a \, \epsilon \, G$,

4) Inverses: For all $a \, \epsilon \, G$ there exists an inverse element $a^{-1} \, \epsilon \, G$ such that $a \cdot a^{-1} = e$.

The mathematical formalism of groups is used in physics to study symmetries of physical theories. By this, we mean symmetry transformations of the equations of motion, which are those transformations under which solutions of the equations of motion are mapped to solutions of the equations of motion. When we say a physical theory 'has a symmetry', we mean that the transformations associated with that symmetry leave the set of solutions of the equation of motions unchanged. We say that the physics is invariant under the transformation.

In Lagrangian and Hamiltonian formulations of physical theories, the invariance of the Lagrangian of the theory under the group action is equivalent to the invariance of the theory under the symmetry. This provides a convenient way of exploring the symmetries of a theory.

As a simple example, consider a basic scalar field theory, described by the Lagrangian

$$\mathcal{L} = \frac{1}{2}\partial_\mu \phi \partial^\mu \phi - \frac{1}{2} m^2 \phi^2. \tag{1.17}$$

It can easily be shown that the Lagrangian is invariant under discrete reflections, corresponding to elements of the group Z_2, where $\phi \to \phi' = -\phi$. The theory is said to possess a Z_2 or reflection symmetry, or to be invariant under reflection.

An important consequence of the invariance of physical theories under certain symmetries follows from Noether's Theorem. The theorem states that every differentiable symmetry of the action of a physical system is associated with a quantity conserved in that system. For example, a system invariant under translation in space is a system where linear momentum is conserved, and a system in which energy is conserved is one which is invariant under translations in time. Noether's Theorem is a fundamental piece of modern theoretical physics, and provides a powerful framework for understanding conserved quantities in physics.

1.2.4 Relativistic quantum field theory

The SM is not only a QFT, but a relativistic QFT. A QFT is said to be relativistic if it is Lorentz covariant. This entails the theory having the Lorentz group (and more generally, the Poincaré group) as a symmetry. This is a requirement for any physical theory that is consistent with special relativity, which we expect for theories describing systems at relativistic energies. In general, this means that if one were to apply a Lorentz transformation to the SM Lagrangian, the resulting equations of motion that describe physical

processes would not change. A theory that changed under Lorentz transformations would give different physical results in different inertial frames, leading to inconsistent results.

The Schrödinger equation can be 'derived' from the nonrelativistic dispersion relation

$$E = \frac{\bar{p}^2}{2m} + V(\bar{x}) \tag{1.18}$$

under the replacement of variable $\bar{p}$ with the differential operator $-i\hbar\bar{\partial}$. The corresponding result when one uses the relativistic dispersion relation $E^2 = p^2 + m^2$ is the Klein-Gordon equation

$$\partial^2\phi + m^2\phi = 0 \tag{1.19}$$

where it is understood that p and ∂ are four-vectors, so $p^2 = p_\mu p^\mu$ and $\partial^2 = \partial_\mu\partial^\mu = \partial_t\partial^t - \partial_x\partial^x - \partial_y\partial^y - \partial_z\partial^z$ in the metric signature described in Section 1.2.1. We have set $c = \hbar = 1$. The Klein-Gordon equation is the relativistic equivalent of the Schrödinger equation, and is Lorentz covariant. It is the equation of motion of a relativistic scalar particle of mass m, and is derived by applying the variational procedure to the Lagrangian

$$\mathcal{L} = \frac{1}{2}\partial_\mu\phi\partial^\mu\phi - \frac{1}{2}m^2\phi^2. \tag{1.20}$$

The second quantization procedure can be applied in the same way as in the nonrelativistic case, and the interpretation of field excitations as particles naturally carries through. The Klein-Gordon field presented above is neutral, but if one makes it a complex valued scalar, the concept of charge can be introduced. In this case the Lagrangian now contains two scalar fields related by complex conjugation

$$\mathcal{L} = \frac{1}{2}\partial_\mu\phi^\dagger\partial^\mu\phi - \frac{1}{2}m^2\phi^\dagger\phi \tag{1.21}$$

and there are two Klein-Gordon equations, for the fields ϕ and $\phi^\dagger$. Because of the relationship between the two fields, they are not independent, and so a field definition similar to Equation (1.12) would contain redundancies. To remove these redundancies, we switch to a different linearly independent Fourier basis, where we can define

$$\phi(x) = \int \frac{d^3\bar{p}}{(2\pi)^3}\frac{1}{\sqrt{2E_{\bar{p}}}}\left(ae^{-ip\cdot x} + b^\dagger e^{ip\cdot x}\right) \tag{1.22}$$

and

$$\phi^\dagger(x) = \int \frac{d^3\bar{p}}{(2\pi)^3}\frac{1}{\sqrt{2E_{\bar{p}}}}\left(a^\dagger e^{ip\cdot x} + be^{-ip\cdot x}\right) \tag{1.23}$$

in terms of two sets of creation and annihilation operators a, $a^\dagger$ and b, $b^\dagger$. The different operators commute, but note that the $\phi^\dagger$ field contains operators that would annihilate the ϕ field, and vis versa. In this way, we can introduce the idea of antiparticles. The ϕ and the $\phi^\dagger$ are a particle-antiparticle pair, which can annihilate into each other. One can thus interpret the $\phi^\dagger$ as the antiparticle of the ϕ.

It is important to note that while the particles and antiparticles can be separated here, this is not always the case. This is a free theory of scalar particles, which is a trivial case of a QFT. The Klein-Gordon equation describes a theory that satisfies many of the needs of a theory of relativistic quantum particles. Because it is a QFT, it can handle changing particle number by applying the creation and annihilation operators to the field states, and it is Lorentz covariant. However, it cannot describe particles with spin, and it does not have positive definite solutions in the real case. This led to a number of issues with the interpretation of solutions before the quantum field concept had been introduced, including nonphysical results like negative energies and negative probabilities. These issues of interpretation and application were solved by the introduction of the quantum field and by the derivation of the Dirac equation, discussed shortly.

To move on, we must now discuss the interacting theory. This is essentially a quantization of the classical potential that appeared in the Schrödinger Lagrangian. Terms with two fields in them can be taken as noninteracting, but a term with three or more field operators in it describes an interaction. One of the most basic interactions that can be introduced into the scalar field theory is the ϕ^4 interaction, which is included by modifying the Klein-Gordon Lagrangian to be

$$\mathcal{L} = \frac{1}{2}\partial_\mu \phi \partial^\mu \phi - \frac{1}{2}m^2\phi^2 - \frac{\lambda}{4!}\phi^4. \tag{1.24}$$

The inclusion of this interaction makes the equation of motion unsolvable exactly, but any theory that describes reality must include interactions. Next is a demonstration of how perturbation theory can be used to perform calculations.

We now derive the standard form of the scalar propagator in perturbation theory. Observables are expectation values in quantum mechanics, and this carries over to QFT. In the interacting theory, the full propagator takes the form of the expectation value

$$G(x,y) = \frac{\langle 0 \left| T\left\{\phi(x)\,\phi(y)\,exp\left[-i\int d^4z H_I(z)\right]\right\}\right| 0\rangle}{\langle 0 \left| T\left\{exp\left[-i\int d^4z H_I(z)\right]\right\}\right| 0\rangle}$$

$$= \mathcal{Z}^{-1}\left\langle 0\left|T\left\{\phi(x)\,\phi(y)\,exp\left[-i\int d^4z H_I(z)\right]\right\}\right|0\right\rangle. \tag{1.25}$$

where T is the time ordering operator that orders events such that those with a lower t coordinate appear first and $H_I = \lambda\phi^4/4!$ is the interaction term in the basic theory. For brevity, we have denoted the denominator by $\mathcal{Z}^{-1}$. The exponential can be expanded to obtain

$$G(x,y) = \mathcal{Z}^{-1}\left\langle 0\left|T\left\{\phi(x)\,\phi(y)\left[I - i\int d^4z H_I(z) + i^2\int d^4z_1\int d^4z_2 H_I(z_1)\,H_I(z_2) + \ldots\right]\right\}\right|0\right\rangle$$

$$= \mathcal{Z}^{-1}\left\langle 0\left|T\left\{\phi(x)\,\phi(y)\left[I - i\int d^4z \frac{\lambda}{4!}\phi^4(z) + i^2\int d^4z_1\int d^4z_2 \frac{\lambda}{4!}\phi^4(z_1)\,\frac{\lambda}{4!}\phi^4(z_2) + \ldots\right]\right\}\right|0\right\rangle. \tag{1.26}$$

If the parameter λ, which regulates the strength of the interaction, is sufficiently small then we can treat terms proportional to some power of λ as negligibly small. This allows us to take a series truncated to some order in λ as an approximation to the full propagator, a standard application of perturbation theory. Here, we consider only up to the term proportional to λ. This gives

$$G_2(x,y) = \mathcal{Z}^{-1} \left\langle 0 \left| T\left\{ \phi(x)\,\phi(y) \left[I - i\int d^4z \frac{\lambda}{4!}\phi^4(z) \right] \right\} \right| 0 \right\rangle$$

$$= \mathcal{Z}^{-1} \langle 0 | T\{\phi(x)\,\phi(y)\} | 0 \rangle + \mathcal{Z}^{-1} \left\langle 0 \left| T\left\{ \phi(x)\,\phi(y)\, i\int d^4z \frac{\lambda}{4!}\phi^4(z) \right\} \right| 0 \right\rangle$$

$$= G_{free}(x,y) + G_{corr}(x,y)\,. \tag{1.27}$$

The first term is the same as the propagator in the free theory, indicating that the free theory is a reasonable approximation to the interacting theory for relatively weak interactions. The second term is a correction due to the interactions of the propagating particle with itself. Evaluation of the free propagator is a standard problem in QFT [3, 4, 7], and results in the Feynman propagator

$$G_F(x,y) = \left\langle 0 \left| \Theta\left(x^0 - y^0\right)\phi(x)\,\phi(y) + \Theta\left(y^0 - x^0\right)\phi(y)\,\phi(x) \right| 0 \right\rangle$$

$$= \langle 0 | T\{\phi(x)\,\phi(y)\} | 0 \rangle\,. \tag{1.28}$$

The Feynman propagator is identified with the 2-point correlation function. There is in fact a quicker and more understandable way of obtaining the momentum space propagator than evaluation of the integral. It is mathematically justified as well, as long as one is careful with how the functions are treated. First, we take the equation of motion for the field, in this case the Klein-Gordon equation

$$\left(\partial_\mu \partial^\mu + m^2\right)\phi = 0. \tag{1.29}$$

The propagator for the scalar particle is in fact the Green's function of this differential equation, so by definition

$$\left(\partial_\mu \partial^\mu + m^2\right) G(x,y) = -i\delta^4(x-y)\,. \tag{1.30}$$

We can then Fourier transform this equation into momentum space. The delta Fourier transforms to the identity, and the differential operators become 4-momenta. We get

$$\left(-p^2 + m^2\right) G(p) = -i. \tag{1.31}$$

This relation can be 'inverted' in a sense (the technical details involve the Cauchy principal value and the Sokhotsky-Plemelj relations) to obtain the momentum space propagator

$$G(p) = \frac{i}{p^2 - m^2 + i\epsilon}. \tag{1.32}$$

We consider the second term, the correction. We have

$$G_{corr}(x,y) = \mathcal{Z}^{-1}\frac{i\lambda}{4!}\int d^4z \left\langle 0 \left| T\left\{\phi(x)\phi(y)\phi^4(z)\right\}\right| 0\right\rangle. \tag{1.33}$$

This expectation value can be computed by inserting the expansions in terms of ladder operators for each of these fields, and then multiplying the product out and applying commutation relations until all of the expectation values had been evaluated. This would be a very time consuming process. Luckily, we may appeal to Wick's theorem, which allows us to reduce an arbitrary product of operators into a sum of 2-point correlation functions. Wick's Theorem is actually quite general, so to save space we avoid discussing it in any further depth here, referring instead to any introductory text on QFT [3, 4, 5, 6, 7].

After application of Wick's Theorem, with all tedious details of the contractions omitted, we obtain the result in terms of the free propagator

$$\begin{aligned}
&\mathcal{Z}^{-1}\frac{i\lambda}{4!}\int d^4z \left\langle 0 \left| T\left\{\phi(x)\phi(y)\phi^4(z)\right\}\right| 0\right\rangle \\
&= 3\left(-\frac{i\lambda}{4!}\right)G(x-y)\int d^4z G(z-z)G(z-z) \\
&+ 12\left(-\frac{i\lambda}{4!}\right)\int d^4z G(x-z)G(y-z)G(z-z).
\end{aligned} \tag{1.34}$$

This expression can be written as a sum of diagrams, as in Figure 1.1. This is a demonstration of the Feynman diagram representation of the perturbative expansion. The first product of diagrams corresponds to the first term, and the second diagram to the second term in the sum. The first term consists of a product of free propagators where the arguments are assigned such that one of the propagators can be separated from the others. If we look at the diagrammatic representation, we see that this expression corresponds to a pair of disconnected diagrams.

Though we have carefully avoided mentioning it in any real detail so far, it is at this point that the denominator $\mathcal{Z}$ comes into play. We lack the space to give it a full discussion, but it turns out that the disconnected diagrams are cancelled out by the denominator. For further details, any of the QFT texts in the references will suffice [3, 4, 5, 6, 7].

This expansion can reduce intractable problems to ones that are calculable. The accuracy of the result depends on which order in the expansion the result is truncated. Including higher order terms generates a more accurate result, but as can be seen in Equation 1.34, they require the evaluation of increasingly complicated integrals. For all but the simplest of theories, and very special cases of realistic theories, the third or fourth order term is around the limit of what is computable, although this is changing with modern computer-assisted techniques.

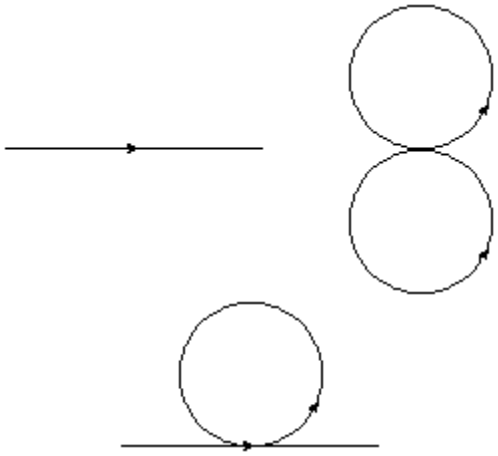

Figure 1.1: Representation in Feynman diagrams of Equation (1.34), with the first line corresponding to the disconnected components in the first term in the propagator. The second line corresponds to the second term in Equation (1.34).

1.2.5 Representations of the Lorentz group

Of special importance when studying relativistic quantum field theories is understanding how the various fields of the theory transform under the Lorentz group, or more precisely, what representation of the group they transform under. The constraint that the Lagrangian of a relativistic QFT be invariant under Lorentz transformations means that only certain combinations of fields in these representations are permissable as terms in the Lagrangian. The Lorentz group has many different representations, but only a handful appear regularly in particle physics. These include the scalar, vector and spinor representations. There are also the tensor representations, which gravitons belong to, but they are not used in this thesis.

A scalar field ϕ is the solution of a Klein-Gordon equation as above, and transforms in the trivial representation of the Lorentz group, which is to say it does not change under Lorentz transformations ($\phi \to \phi' = \phi$).

A quantity that exists in a vector representation of the Lorentz group transforms like $x^\mu \to x^{\mu\prime} = \Lambda^\mu_\nu x^\nu$, analogously to how three dimensional vectors are rotated through multiplication by a rotation matrix. Vector fields are naturally introduced when considering gauge theories, as will be discussed in Section 1.2.7.

The matter fields of the SM are fermionic at the fundamental level. This means that they have half integer spin, but a relativistic fermion cannot be described by the bosonic wave equations described above. A new kind of quantum field is required to properly describe fermionic fields, and it should exist in some finite dimensional representation of the Lorentz group if it is to be part of a consistent covariant relativistic theory. The path to the correct representation is somewhat meandering, and is often poorly explained.

We start with the rotational spinor in three dimensions, and consider extensions of the three dimensional rotation group $SO(3)$ to the full Lorentz group in 3+1 dimensions. By examining the resulting algebra, we can obtain a relationship between Lorentz spinors and the group $SU(2)$. Again by analogy with a nonrelativistc spinor, one can apply a Lorentz transformation to tease out the invariant equation of motion for the spinor under the transformation, which turns out to be the Dirac equation.

To begin, we know from studies of the nonrelativistic hydrogen atom that electron spin is intimately connected to the group $SU(2)$. This may seem inexplicable, but makes more sense when one recalls that $SU(2)$ is the double cover of the 3-dimensional rotation group $SO(3)$ [9]. Nonrelativistic electron bound states in the hydrogen atom exist in representations of $SU(2)$, which are formally related to the spinor representations of $SO(3)$, and this is tied to the fact that they have half-integer spin in 3-dimensional space. This connection between spin and $SU(2)$ representations admits an extrapolation to the Lorentz group, which can be thought of as containing rotations in 4-dimensional Minkowski space. The naive approach, which is to try to apply the relativistic dispersion relation to a nonrelativistic spinor rotationally invariant wave equation fails, as it leads to an equation that is not Lorentz invariant. This indicates that proceeding through an analysis of the representations of the Lorentz group might provide more value than attempting straightforward generalizations from the nonrelativistic case.

We consider the generators of the Lorentz group. There are six, corresponding to the three rotations (S_1, S_2, S_3) and the three boosts (K_1, K_2, K_3). They form an algebra with the following commutation relations:

$$[S_i, S_j] = i\epsilon_{ijk}S_k, \quad [S_i, K_j] = i\epsilon_{ijk}K_k, \quad [K_i, K_j] = -i\epsilon_{ijk}S_k. \tag{1.35}$$

This algebra can be complexified with the transformation

$$A_i = \frac{1}{2}\left(S_i + iK_i\right), \quad B_i = \frac{1}{2}\left(S_i - iK_i\right). \tag{1.36}$$

where generators in the A and B basis form the algebra

$$[A_i, A_j] = i\epsilon_{ijk}A_k, \quad [B_i, B_j] = i\epsilon_{ijk}B_k, \quad [A_i, B_j] = 0. \tag{1.37}$$

The A and B form two separate algebras that are each isomorphic to the $SU(2)$ algebra. Hence, is is reasonable to consider that there might be some correspondence between the Lorentz group $SO(3,1)$ and $SU(2) \times SU(2)$. It turns out that there is no isomorphism, but a different relationship. There is a 2-to-1 homomorphism of $SL(2,C)$ into $SO(3,1)$, which means that each element of $SO(3,1)$ can be mapped onto two elements of $SL(2,C)$. $SL(2,C)$ is called the universal covering group of $SO(3,1)^+$ (the proper orthochronus Lorentz group, which we mean when we refer to the full Lorentz group), and its representations can be mapped to the representations of $SU(2)$. The key point is that we can construct representations of the Lorentz group in terms of $SU(2)$ representations, which we understand well from their applications to particle spin. The dimensions of the $SU(2)$ representation determine whether or not the field has integer spin or half-integer spin, and hence whether is behaves like a fermion or a boson.

A Lorentz spinor is an object that exists in a space acted on by one of the spinor representations of the Lorentz group. Consider a pair of spinors in the two different reps of Lorentz ζ and η. These spinors transform the same under unitary trasformations, but differently under boosts (because they are in different $SU(2)$ representations:

$$\zeta \to \zeta' = H\zeta, \quad \eta \to \eta' = \bar{H}\eta \tag{1.38}$$

for a boost H.

But what kind of an equation of motion should relativistic spinors obey (which is tied to the form of the Lagrangian that describes their physics)? Consider the nonrelativistic spinor $J^i = \sigma^i/2$, written in terms of the Pauli matrices σ^i. We can boost this spinor with the transformation

$$H(\bar{p}) = \exp\left(\frac{\bar{\phi}\cdot\bar{\theta}}{2}\right) = \frac{m + E + \bar{\sigma}\cdot\bar{p}}{\sqrt{2m(E+m)}} \tag{1.39}$$

where $\bar{\phi} = \phi\hat{n}$ is the unit vector in the direction of the Lorentz boost. This form of the transformation is just the infinitesimal form of the Lorentz transformation. It can be rewritten so that

$$\bar{H} = H^{-1} = \frac{m + E - \bar{\sigma}\cdot\bar{p}}{\sqrt{2m(E+m)}}. \tag{1.40}$$

The transformation operator can be squared to give

$$H^2(\bar{p}) = \frac{\tilde{\sigma}^\mu p_\mu}{m} = \frac{E + \bar{\sigma}\cdot\bar{p}}{m} \tag{1.41}$$

where p_μ is the momentum four-vector and $\sigma^\mu = (I_{2\times 2}, \bar{\sigma})$ and $\tilde{\sigma}^\mu = (I_{2\times 2}, -\bar{\sigma})$ are the natural extension of the Pauli matrix 3-vector into Minkowski space.

A four-spinor is made of two two-spinors from different representations, and transforms under Lorentz transformations as

$$u = \begin{pmatrix} \zeta \\ \eta \end{pmatrix} \to \begin{pmatrix} M(\Lambda) & 0 \\ 0 & \bar{M}(\lambda) \end{pmatrix} \begin{pmatrix} \zeta \\ \eta \end{pmatrix} \tag{1.42}$$

Taking the transformation $M(\lambda)$ to be the boost H, we obtain for the left and right handed components of u, where we have fixed the initial rest frame and set $\zeta(\bar{0}, m) = \eta(\bar{0}, m) = \chi_m$, the two-component spinor for a spin $1/2$ particle.

$$u(\bar{p}, m) = \begin{pmatrix} u_L \\ u_R \end{pmatrix} = \begin{pmatrix} H(\bar{p}) & 0 \\ 0 & \bar{H}(\bar{p}) \end{pmatrix} \begin{pmatrix} \chi_m \\ \chi_m \end{pmatrix} \tag{1.43}$$

Elimination of χ_m gives the transformation

$$\begin{pmatrix} 0 & H^2 \\ H^{-2} & 0 \end{pmatrix} \begin{pmatrix} u_R \\ u_L \end{pmatrix} = \begin{pmatrix} u_R \\ u_L \end{pmatrix} \tag{1.44}$$

or explicitly in the Weyl representation

$$\begin{pmatrix} -m & E + \bar{\sigma}\cdot\bar{p} \\ E - \bar{\sigma}\cdot\bar{p} & -m \end{pmatrix} \begin{pmatrix} u_R \\ u_L \end{pmatrix} = 0. \tag{1.45}$$

In terms of four-vectors and four-spinors, the above equation can be written as

$$(p_\mu \gamma^\mu - m)\, u(p) = 0, \tag{1.46}$$

or, after using the relation $p_\mu = i\partial_\mu$,

$$(i\gamma^\mu \partial_\mu - m)\, u(p) = 0. \tag{1.47}$$

This is the Dirac equation that describes the behaviour of free relativistic electrons. So a Lorentz spinor with four components must satisfy the Dirac equation. The Dirac matrices γ^μ are constructed from the Pauli matrices as discussed in Section 1.2.1, and obey the Clifford algebra

$$\{\gamma^\mu, \gamma^\nu\} = 2g^{\mu\nu}. \tag{1.48}$$

The smallest irreducible representation of the algebra generated by (1.48) is four dimensional (see reference [10] for details) and so QFT works with 4×4 gamma matrices.

There are also several discrete Z_2 symmetries that are important in particle physics. Two of them (parity P and time reversal T) are the reflection symmetries that allow one to jump between the disconnected components of the complete Lorentz group. Parity reflects spatial components of a four-vector: $Px^\mu = P\,(t, \bar{r}) = (t, -\bar{r})$. Invariance of a theory under parity transformations means that applying those transformations to every four-vector in the Lagrangian will not change the resulting physics as encoded in the equations of motion. This concept of invariance is the same for the following two symmetries as well.

Time reversal reflects the time component of a four-vector: $Tx^\mu = T\,(t, \bar{r}) = (-t, \bar{r})$. The third symmetry is charge conjugation C, which operates on particles and transforms them into antiparticles (and vis versa). These discrete symmetries appear in the interactions of the SM and beyond, where they may be respected or violated, with phenomenological consequences.

These discrete symmetries are preserved in some sectors of the SM, but are violated in others. The weak sector of the SM violates parity P conservation in its interactions, and certain weak processes are known to violate the CP symmetry [8], a symmetry whose operator is composed of the product of the C and P operators. To the best of our knowledge, no SM process violates the CPT symmetry [8].

It is useful at this point to include for future reference Table 1.1, a table of the behaviour of various structures of Dirac matrices and fermion fields under the discrete symmetries. Because the discrete symmetries are all essentially reflections, a value of ± 1 is all that is required to describe the behaviour.

1.2.6 Renormalization and the renormalization group equations

This Section reviews some of the basic concepts of renormalization and the renormalization group, which are required to understand the asymptotic features of nontrivial QFTs. Renormalization is perhaps one of the most difficult aspects of QFT to understand and appreciate on a conceptual level. It came about as a

Table 1.1: Behaviour of Dirac bilinears under C, P, T symmetries (where $(-1)^\mu = (1, -1, -1, -1)$)

	$\bar{\psi}\psi$	$i\bar{\psi}\gamma^5\psi$	$\bar{\psi}\gamma^\mu\psi$	$\bar{\psi}\gamma^\mu\gamma^5\psi$
P	$+1$	-1	$(-1)^\mu$	$-(-1)^\mu$
C	$+1$	-1	$(-1)^\mu$	$(-1)^\mu$
T	$+1$	$+1$	-1	$+1$

technical trick to get around unpleasant divergences in certain calculations, and was revealed over decades to be in fact an unanticipated feature of the theory that had both explanatory and predictive power. It must be emphasized that renormalization is a feature of QFT, not a bug. It is a manifestation of the scale dependence inherent in our physical QFTs, and it provides hints of how the forces of the SM might be unified at some higher energy scale. Much of this is beyond the scope of this thesis, however, so we limit our discussion to the basics that are required as background in later Chapters. More details are, as always, available in the standard QFT references [3, 4, 5, 6], and the reader interested in even more depth is encouraged to consult the monograph of Collins [11].

Calculation of contributions from higher orders in perturbation theory requires going beyond the tree level in the Feynman diagram representation of the perturbation series. This leads to divergences in the theory. Consider the NLO contribution to the 2-point function, the propagator, in ϕ^3 scalar field theory, pictured in Figure 1.2.

This diagram corresponds to an expression containing the integral

$$\Gamma^{(2)}_{1-\text{loop}} \sim \int \frac{d^4 l}{l^2 (p-l)^2} \sim \lim_{p\to\infty} \log p^2 \tag{1.49}$$

which clearly formally diverges. Such divergences appear in nearly all higher order contributions. Dealing with these divergences mathematically in our calculations and interpreting them physically in our results is the purpose of the renormalization program.

Loops make potentially divergent integrals while propagators aid convergence by introducing further powers of momentum in the denominator, reducing the superficial degree of divergence D, which is a useful, if naive, quantity. It can be expressed for a generic theory by the following expression:

$$D = 4L - P_f - 2P_r, \tag{1.50}$$

where the number of loops is L, the number of fermion propagators is P_f and the number of massless radiation propagators is P_r.

First, the integral (1.49) above must be formalized in some way. As presented, it does not exist. The process of attaching a mathematical meaning to the integral is called regularization, which essentially involves quantifying the divergence of the integral using some parameterization. There are many different regularization schemes, each of which has uses in different theories and scenarios.

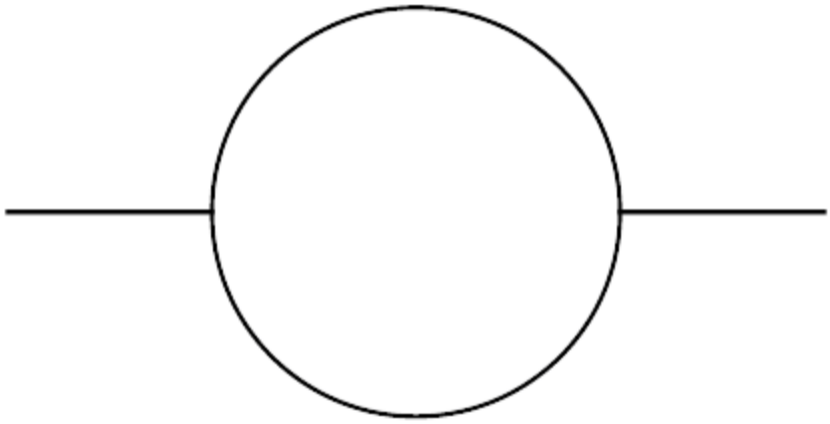

Figure 1.2: Diagrammatic representation of the 1-loop correction to the propagator in the scalar ϕ^3 theory. The expression corresponding to this diagram is divergent, and contributes to the renormalization of the scalar mass in the standard prescription.

Consider the 1-loop contribution to the 2-point function (propagator) in the ϕ^3 scalar field theory, which is given by the expression

$$i\Gamma^{(2)} = \frac{\lambda^2}{2} \int \frac{d^4 l}{(2\pi)^4} \frac{1}{l^2 (p-l)^2} \tag{1.51}$$

where p is the external momentum. From the superficial degree of divergence, we expect the integral to diverge like $\int dl/l$, which goes to infinity logarithmically with p^2.

The integral can be made finite if we impose a hard UV cutoff at Λ, so momentum contributions larger than Λ are ignored. The integral in this form goes like $\int^{\Lambda} dl/l \sim \ln(p^2/\Lambda^2)$. This quantity still diverges logarithmically as $\Lambda \to \infty$, but we have in a sense captured the divergence in terms of the cutoff Λ.

Full evaluation of the indefinite version of the integral (1.51) using the technique of differentiation under the integral gives

$$\Gamma^{(2)} = -\frac{\lambda^2}{16\pi^2} \ln(p^2) + C \tag{1.52}$$

for some integration constant C. But the integral in Equation (1.51) is divergent, so if Equation (1.52) is to be valid, C must be infinite.

If we evaluate (1.51) as a definite integral with the cutoff Λ in place, we obtain

$$\Gamma^{(2)} = -\frac{\lambda^2}{16\pi^2} \ln\left(\frac{p^2}{\Lambda^2}\right) = -\frac{\lambda^2}{16\pi^2} \ln p^2 + \frac{\lambda^2}{16\pi^2} \ln \Lambda^2. \tag{1.53}$$

It is clear that by equating Equations (1.53) and (1.52) we have found the value of the infinite constant

$$C = \frac{\lambda^2}{16\pi^2} \ln \Lambda^2 \tag{1.54}$$

which we might expect to obtain if we take $\Lambda \to \infty$.

The cutoff regulator is not particularly rigorous in this form. A more formal regularization procedure is dimensional regularization, which involves extending the divergent four dimensional integral to be over d spacetime dimensions, where d is a real number, evaluating the integral, and then taking the limit as $d \to 4$ (or setting $d = 4 \pm \epsilon$ for a small ϵ). Then one performs a Wick rotation from Minkowski space to Euclidean space and performs the integration in $d-$ dimensional spherical coordinates. A term containing $1/\epsilon$ should appear in the series expansions of the resulting functions, which quantifies the divergence of the integral.

After the regularization procedure has been completed, we are able to move on to renormalization, which is a systematic cancellation of the now-quantified divergent terms that were extracted in the regularization procedure order-by-order in perturbation theory. The divergent quantities are absorbed into so-called renormalized parameters of the theory which are subsequently set equal to the physical values. This leaves formally finite results at any given order in the expansion. Renormalization is a rescaling of terms (both fields and parameters like masses and coupling constants) in the Lagrangian without changing its basic structure. The renormalized perturbation theory is physically equivalent to the bare perturbation theory when used to compute results.

The renormalization procedure for a theory to a given order is as follows. First, compute the divergent contributions to the amplitude using some regularization technique to obtain an expression in terms of the bare couplings and masses and the regulator (ϵ for dimensional regularization, Λ for cutoff regularization, etc.). Using the relations between the bare and renormalized quantities, compute the renormalized mass and coupling to a given order, as well as the S-matrix elements and the field strength renormalization. With these expressions, eliminate the bare quantities in terms of the renormalized quantities, which amounts to rescaling the parameters of the theory to take the divergences into account. The resulting expression should be finite in the divergent limit of the regulator, and one can define the values of the S-matrix elements, and hence the renormalized parameters, in terms of experimental results.

In a renormalizable theory, divergent quantities can be fixed by a finite number of experimentally determined observables. A theory that is nonrenormalizable would have more divergences than can be absorbed into parameters and fields, leaving divergent terms lingering at every order in the expansion. Any theory that claims to be complete should be renormalizable, but nonrenormalizable theories can have their uses, when treated as effective theories.

The renormalization procedure requires the introduction of a scale μ at which the n-point functions are evaluated. This parameter cannot be avoided, but observables such as cross sections do not depend on the renormalization scale. The presence of an invariance implies the existence of a symmetry of the theory. This is known as invariance under renormalization group transformations, or transformations of the form

$$\Gamma_r^{(n)} = Z(\lambda, \mu)\Gamma^{(n)} \tag{1.55}$$

By observing that unrenormalized n-point functions are independent of the renormalization scale and that renormalized n-point functions are not, one can use the relation between the two to obtain a mathematical statement:

$$\mu\frac{\partial}{\partial\mu}\Gamma_r^{(n)} = \mu\frac{d}{d\mu}\left[Z(\lambda, \mu)\Gamma^{(n)}\right] = 0. \tag{1.56}$$

This is a mathematical statement of the fact that physics does not depend on the renormalization point μ. Equation (1.56) is equivalent to

$$\mu\frac{\partial}{\partial\mu}\Gamma_r^{(n)} = \mu\frac{n}{2}\frac{d}{d\mu}\log Z(\lambda, \mu)\Gamma_r^{(n)} \tag{1.57}$$

which can be written

$$\left[\mu\frac{\partial}{\partial\mu} + \beta(\lambda)\frac{\partial}{\partial\lambda} - n\gamma(\lambda)\right]\Gamma_r^{(n)} = 0 \tag{1.58}$$

This is known as the Callan-Symanzik equation [12, 13, 14]. The beta function is $\beta(\lambda) = \mu d\lambda/d\mu$ and the anomalous dimension is $\gamma(\lambda) = (\mu/2) \times (d\log Z/d\mu)$. The beta function $\beta(\lambda)$ can be thought of as the rate of change of the renormalized coupling λ_r with respect to scale μ where there is a fixed bare coupling λ_0 at μ. The Callan-Symanzik equation is an example of a renormalization group equation, which describes the behaviour of the renormalized amplitude $\Gamma_r^{(n)}$ as the renormalization scale μ is varied. It is actually of great physical importance for gauge theories.

The behaviour of the theory in the asymptotic limits is determined by the sign of the beta function. For $\beta > 0$, the coupling is 0 in the IR regime and constant in the UV. If $\beta = 0$, the theory is finite, and the renormalized coupling is always equal to the bare coupling. The theory itself will be scale invariant as well. The case $\beta < 0$ describes asymptotic freedom, where the coupling λ_r goes to zero in the UV limit. This final case is very important for interactions of quarks and gluons in the SM.

One can use β and γ in the renormalization group equation to compute running couplings to some order in perturbation theory by solving the differential equation

$$\frac{\partial}{\partial\log(p/\mu)}\lambda = \beta(\lambda) \tag{1.59}$$

with $\beta(\lambda)$ computed to the necessary order in perturbation theory. This is especially useful in understanding QCD, which will be discussed in Section 1.2.8, and in describing the high energy behaviour of the SM. It is also crucial in studying high energy extensions of the SM that need to be reconciled with observed physics at low energies. This application is required to understand the model discussed in Chapter 6.

1.2.7 The gauge principle and quantum electrodynamics

An application of symmetry principles to quantum field theories that underlies much of modern particle physics is the gauge principle. Fundamentally, the gauge principle is the bridge connecting force fields and particles in a QFT.

Consider a theory of free fermions. The basic Dirac Lagrangian takes the form

$$\mathcal{L} = \bar{\psi}\left(i\gamma^{\mu}\partial_{\mu} - m\right)\psi. \tag{1.60}$$

This Lagrangian is clearly invariant under a global $U(1)$ transformation. However, the situation changes when the global symmetry is changed to a local or gauge symmetry, where the symmetry parameter is position dependent ($\alpha \to \alpha(x)$). In that case, the fermion fields transform as

$$\psi(x) \to \psi'(x) = e^{-i\alpha(x)}\psi(x), \tag{1.61}$$

$$\bar{\psi}(x) \to \bar{\psi}'(x) = e^{i\alpha(x)}\bar{\psi}(x). \tag{1.62}$$

The kinetic term is no longer invariant under local $U(1)$ tranformations, due to the action of the derivative on the local gauge parameter $\alpha(x)$:

$$\begin{aligned}\bar{\psi}(x)\partial_{\mu}\psi(x) &\to \bar{\psi}'(x)\partial_{\mu}\psi'(x)\\ &= \bar{\psi}(x)e^{i\alpha(x)}\partial_{\mu}\left(e^{-i\alpha(x)}\psi(x)\right)\\ &= \bar{\psi}(x)\partial_{\mu}\psi(x) - i\bar{\psi}(x)\left(\partial_{\mu}\alpha(x)\right)\psi(x).\end{aligned}$$

To make the Lagrangian invariant under the $U(1)$ gauge tranformation we modify the kinetic term, replacing the spacetime derivative ∂_{μ} with a gauge covariant derivative D_{μ}, defined such that the expression $\bar{\psi}(x)D_{\mu}\psi(x)$ is invariant under gauge transformations. Explicit construction of the covariant derivative requires an additional field, transforming as a Lorentz vector, that compensates for the transformation of the gauge parameter $\alpha(x)$. This field, traditionally denoted $A_{\mu}(x)$, is called the gauge field. The gauge field transforms as

$$A_{\mu}(x) \to A'_{\mu}(x) = A_{\mu}(x) + \frac{1}{e}\partial_{\mu}\alpha(x). \tag{1.63}$$

The covariant derivative is then written

$$D_{\mu}\psi(x) = \left(\partial_{\mu} + ieA_{\mu}(x)\right)\psi(x). \tag{1.64}$$

It can be seen that the mass term is trivially gauge invariant. The gauge invariant Lagrangian is then

$$\mathcal{L} = \bar{\psi}\left(i\gamma^{\mu}D_{\mu} - m\right)\psi. \tag{1.65}$$

As the Lagrangian is, the gauge field $A_\mu(x)$ is nondynamical, having no kinetic term. Following the variational procedure generates a trivial equation of motion for the gauge field, that has a constant A_μ as the only solution. This theory is uninteresting, and will fail to reproduce any interesting physical theories. To make the gauge field dynamical, we include a term involving derivatives of $A_\mu(x)$. The simplest gauge invariant term involving such derivatives is

$$\mathcal{L}_{A_{kin}} = -\frac{1}{4}F^{\mu\nu}F_{\mu\nu} \tag{1.66}$$

where the tensor $F_{\mu\nu} = \partial_\mu A_\nu - \partial_\nu A_\mu$ is called the field strength tensor. This field strength tensor is a full Lorentz tensor, and can be identified with the electromagnetic field strength tensor of classical electrodynamics.

The full $U(1)$ gauge invariant Lagrangian of a theory of massive fermions with a dynamical gauge field, which happens to be the Lagrangian of quantum electrodynamics, is

$$\mathcal{L} = \bar{\psi}i\gamma^\mu\left(\partial_\mu + ieA_\mu\right)\psi - m\bar{\psi}\psi - \frac{1}{4}F^{\mu\nu}F_{\mu\nu}. \tag{1.67}$$

Note that there is no way to add a term proportional to $A_\mu A^\mu$ that can act as a mass term for the gauge field, as such a term would not be gauge invariant (however, see Section 1.2.11). The gauge field thus remains massless as a consequence of the gauge symmetry. This theory is called an Abelian gauge field theory, because it has the $U(1)$ gauge symmetry, which is an Abelian (commutative) group.

Abelian gauge theory is the prototypical example of a theory with force field interactions, and is exemplified by QED, the theory of photons and electrons. Massless Abelian gauge theory provides a theory with a massless mediator, implying the existence of a long range force. Aside from QED, $U(1)$ theories appear in other parts of the SM and beyond, as they are the simplest of the possible gauge groups, and have the tendency of appearing in the low energy manifestations of larger symmetry groups.

1.2.8 Nonabelian gauge theory and quantum chromodynamics

It is possible to formulate a gauge theory with a group other than $U(1)$. If the group is not Abelian, the resulting gauge theory is called nonabelian. Nonabelian gauge theories have some subtleties compared to the somewhat straightforward Abelian theories, but it also turns out that they are very useful in particle physics.

The prototypical nonabelian gauge theory is invariant under $SU(N)$ transformations, where N is some positive integer, and is known as the Yang-Mills theory. Following the reasoning used in the previous section, and proceeding from Equation (1.60), we note that the Lagrangian is not invariant unless there is a set of fermions that transform into one another under $SU(N)$.

The number of fermions required is a function of which representation of $SU(N)$ they transform under. For the trivial (1D) representation, there would only need to be a single fermion (that transforms trivially, as a $SU(N)$ scalar), while higher dimensional representations require more fermions. For example the fundamental representation of $SU(N)$ is N-dimensional, and so requires N fermions.

Fermion fields transform as

$$\psi(x) \to \psi'(x) = e^{-ig_3(x)t^a}\psi(x), \tag{1.68}$$

$$\bar{\psi}(x) \to \bar{\psi}'(x) = e^{ig_3(x)t^a}\bar{\psi}(x). \tag{1.69}$$

A convenient representation of the generators of $SU(N)$ is given by $t^C_{ab} = \frac{\lambda^C_{ab}}{2}$ (in terms of the Gell-Mann matrices λ^C for $N = 3$); they obey the algebra

$$\left[t^A, t^B\right] = if_{ABC}t^C, \tag{1.70}$$

where the f_{ABC} are structure constants of the algebra. Explicit values may easily be obtained from any standard reference.

Quantum chromodynamics (QCD) is the theory of the strong interactions of quarks and gluons. It is a quantum Yang-Mills gauge field theory, with gauge group $SU(3)_c$, where the conserved charge c is called the color charge. That there are three colors ($N = 3$) is deduced from experiment. The QCD Lagrangian is

$$\mathcal{L}_{QCD} = \sum_q \bar{\psi}_{q,a}\left(i\delta_{ab}\gamma^\mu\partial_\mu - g_b\gamma^\mu t^C_{ab}A^C_\mu - m_q\delta_{ab}\right)\psi_{q,b} - \frac{1}{4}F^C_{\mu\nu}F^{C\mu\nu} \tag{1.71}$$

where $\psi_{q,a}$ is a fermionic quark of flavour q, color a and mass m_q, which exists in the fundamental representation of $SU(3)_c$. There are six different flavors of quark, each with a different mass value, and they are divided into three generations based on their electroweak properties. The difference between QCD and a generic $SU(N_c)$ quantum Yang-Mills theory is in the number of colors and the number of flavors. QCD as implemented in the SM has $N_c = 3$ and $N_f = 6$, which has important consequences for the high energy behaviour of the theory. The gluon gauge field A^C_μ exists in the adjoint representation of $SU(3)_c$ and has a field strength tensor

$$F^C_{\mu\nu} = \partial_\mu A^C_\nu - \partial_\nu A^C_\mu - g_s f_{CAB}A^A_\mu A^B_\nu. \tag{1.72}$$

Gluons are Lorentz vectors, and are massless. A key difference between QCD and QED is that while photons do not carry electric charge, gluons do carry color charge. This significantly changes the dynamics of the theory, as can be seen by the gluon interaction terms in the Lagrangian (1.71) above.

As was discussed briefly in Section 1.2.6, the β function of a theory describes how the coupling parameter of the theory changes as the energy scale changes. The application of this construction to QCD leads to descriptions of phenomena which would otherwise be very difficult to explain, namely asymptotic freedom and confinement.

The β function in terms of the strong coupling α_s rather than the gauge parameter g_s is

$$\mu^2_R\frac{d\alpha_s}{d\mu^2_R} = \beta(\alpha_s) = -\left(b_0\alpha_s^2 + b_1\alpha_s^3 + b_2\alpha_s^4 + ...\right) \tag{1.73}$$

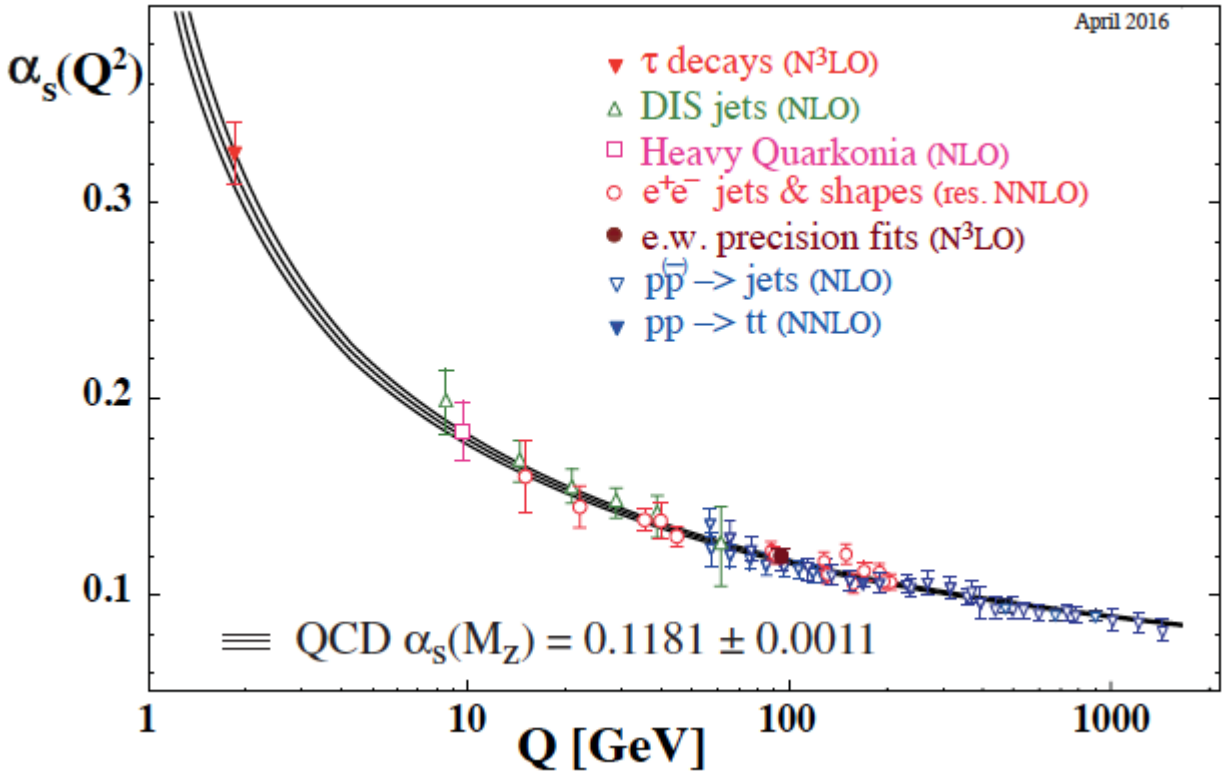

Figure 1.3: Experimental verification of the running coupling α_s and asymptotic freedom in perturbative QCD, with data from a variety of sources. Figure originally published in [8].

and, in perturbation theory, the first few coefficients for an $SU(N)$ gauge theory are

$$b_0 = \frac{11C_A - 4N_f T_R}{12\pi} = \frac{33 - 2N_f}{12\pi} \tag{1.74}$$

with the $N = 3$ color gauge theory parameters inserted after the final equality. By inserting $N_f = 6$, one can obtain the QCD β function. As discussed previously, the asymptotic behaviour of the theory can be determined from this function. Extracting the running coupling of QCD, we have to (LO/NLO)

$$\alpha_s(Q) = \frac{4\pi}{\beta_0} \frac{1}{\log\left(\frac{Q^2}{\Lambda^2_{QCD}}\right)} \tag{1.75}$$

which is plotted through experimental data in Figure 1.3. One can see that the coupling gets smaller as $Q \to \infty$, and larger as $Q \to 0$, until perturbation theory inevitably breaks down. The parameter $\Lambda_{QCD} = 213$ MeV is the energy scale of QCD. Because the running coupling, and hence the interaction strength, goes to 0 as $Q \to \infty$, QCD is said to be an asymptotically free theory. Fot reference $\alpha_s \simeq 0.1$ from around 100 GeV to the TeV scale, which changes so little that it can be useful to approximate $d\alpha_s/dQ = 0$ in that region.

A consequence of the extremely strong QCD coupling in the IR is the phenomenon of confinement. Confinement is essentially a statement that there can be no free color charged particles, or at least that free

color charged particles form bound states on a time scale that is smaller than can be measured. The strong coupling is powerful enough at low energies that a free quark or gluon will pull colored particles out of the vacuum to form bound states, at the cost of some of its energy. The other side of this is that QCD is an extremely short range force, in constrast to QED. The force mediators themselves carry charge, and so are subject to confinement, just as the quark fields are. The color force is not seen at low energies, except in the form of residual interactions such as nuclear binding energies.

A key feature of confining gauge theories such as QCD is the formation of bound states at low energies. For QCD, these bound states are called hadrons, and they are of paramount phenomenological importance, as they are the only QCD observables. A standard hadron is composed of a quark and an antiquark of the same color (called a meson) or of three quarks or antiquarks of different colors (called a baryon).

Confinement manifests at high energies through the process called hadronization or fragmentation. In particle colliders, color charged particles such as quarks can be produced fairly easily. However, confinement prohibits quarks from being asymptotically free states, and the result is a jet of high energy hadrons in the final state of the collision. Fragmentation is a collection of soft processes at the subconfinement scale that act to neutralize the color. This phenomenon is discussed further in the context of collider physics in Chapter 5.

1.2.9 The GSW theory of electroweak interactions

A crucial piece of the SM is contained in the idea that the electromagnetic force and the weak nuclear force are manifestations of a unified electroweak force, based on the gauge theory $SU(2) \times U(1)$. This electroweak force contains the electromagnetic force as described by QED and the phenomenological weak nuclear force. It quantifies interactions between fermions that change electric charge and flavor, and is responsible for many of the more exotic phenomena of particle physics. In low energy regimes, the electroweak gauge group appears to reduce to the effective weak interactions and the $U(1)$ gauge theory of QED. This electroweak symmetry breaking is discussed further in Section 1.2.11. This Section is primarily concerned with the fermionic currents of the electroweak theory, as they are required in the particle phenomenology used later in this thesis. Many topics are neglected or only briefly mentioned. As always, a more detailed treatment is available in the standard references [3, 4, 5].

The GSW theory was motivated by the desire to explain certain experimental phenomena using the language of QFT. It was observed that not only are there electromagnetic interactions, which can be explained by QED, but there are also interactions where charge is transferred between particles in the initial and final states, called charged current interactions. The standard example is the beta decay of the neutron, where one of the down quarks ($q = -1/3$) in the neutron decays into an up quark ($q = 2/3$), an electron ($q = -1$) and a neutrino ($q = 0$), leaving a proton along with the electron and neutrino in the final state. Interactions of this type were for a long time described with some accuracy by the 4-point Fermi theory, which described the interaction by a four-fermion vertex, but the theory had many theoretical flaws and lacked predictive power.

The preferred method to describe the interaction was by using a mediator particle associated with some gauge symmetry. Because the mediator needed to be charged, it needed to interact with photons, and hence the new gauge group must contain QED within it. To describe interactions that have both electromagnetic currents and charged currents using a gauge group, one needs at least three gauge fields (one with positive charge, one with negative charge, and the photon). The smallest continuous Lie group that has three generators is $SU(2)$. However, simply by examining the commutation relations of the phenomenological charged and electromagnetic currents, it can be seen that they do not form an $SU(2)$ algebra.

As well, the weak interactions appeared to have a universal coupling strength, characterized by the Fermi constant G_F, which is an indicator of a gauge theory. Moreover, it is an experimental fact that the weak force is short ranged, which means that, in the standard gauge theory description of forces, the mediator of the weak force must be massive.

The theory also needed the correct current structure when dealing with left handed fermions. It was observed experimentally that only left handed fermions were influenced by the weak interactions (that had been observed at that time), leading to maximal parity violation. The electroweak force relies on the notion of chirality, or 'handedness.' Particles in one of the spinor representations of the Lorentz group are left handed or right handed. More formally, chirality is the eigenvalue of the γ^5 matrix, and left handed (ψ_L) and right handed (ψ_R) spinors satisfy

$$\begin{aligned}\gamma^5\psi_R &= (+1)\,\psi_R,\ \bar{\psi}_R\gamma^5 = (-1)\,\bar{\psi}_R,\\ \gamma^5\psi_L &= (-1)\,\psi_L,\ \bar{\psi}_L\gamma^5 = (+1)\,\bar{\psi}_L.\end{aligned} \tag{1.76}$$

In the above, the spinors are Dirac spinors with two independent components.

These chiral spinors can be obtained from a 4-component Dirac spinor through the helicity projection operators

$$\begin{aligned}\psi_R &= \frac{1}{2}\left(1+\gamma^5\right)\psi = P_R\psi, \bar{\psi}_R = \psi\frac{1}{2}\left(1-\gamma^5\right) = \psi P_L,\\ \psi_L &= \frac{1}{2}\left(1-\gamma^5\right)\psi = P_L\psi, \bar{\psi}_L = \psi\frac{1}{2}\left(1+\gamma^5\right) = \psi P_R.\end{aligned} \tag{1.77}$$

Also useful are the relations

$$\bar{\psi}\psi = \bar{\psi}_L\psi_R + \bar{\psi}_R\psi_L \tag{1.78}$$

and

$$\bar{\psi}\gamma^\mu\psi = \bar{\psi}_L\gamma^\mu\psi_L + \bar{\psi}_R\gamma^\mu\psi_R. \tag{1.79}$$

These spinor constructions are required because the weak force treats left handed and right handed particles differently. They will be used in Chapter 6.

All of this experimental and theoretical evidence points to a more complicated gauge structure than pure $SU(2)$. The inclusion of neutral currents requires at the least another gauge field. A natural extension of $SU(2)$ is $SU(2) \times U(1)$.

Table 1.2: $SU(2) \times U(1)$ charges of left and right handed SM fermions

	T_3	Q	Y
ν_L	+1/2	0	-1
e_L	-1/2	-1	-1
u_L	+1/2	+2/3	+1/3
d_L	-1/2	-1/3	+1/3
e_R	0	-1	-2
u_R	0	+2/3	+4/3
d_R	0	-1/3	-2/3

The chirality structure of the theory can be implemented if the left handed currents generate an $SU(2)$ algebra, with the left handed fermions transforming in $SU(2)$ representations like

$$e_L, \nu_L = \frac{1}{2}\left(1 - \gamma_5\right) f \tag{1.80}$$

in which they form an $SU(2)$ doublet

$$\psi_L = \begin{pmatrix} \nu_L \\ e_L \end{pmatrix} \tag{1.81}$$

with certain $SU(2) \times U(1)$ charges. The right handed fermions e_R are $SU(2)$ singlets, and there are no right handed neutrinos in the SM. The charges are given in Table 1.2. The weak isospin is T_3, while the electromagnetic charge is Q and the hypercharge is $Y = 2(Q - T_3)$ (so $Y = 1$ for left handed particles, and $Y = 2$ for right handed particles).

The covariant derivative of an $SU(2) \times U(1)$ gauge theory is

$$D_\mu = \partial_\mu - i g_2 W_\mu^a \tau^a - \frac{i}{2} g_3 B_\mu \tag{1.82}$$

where $a = 1, 2, 3$ indexes the $SU(2)$ generators and the gauge fields are W_μ^a and B_μ. The charged currents can be mapped to the W^1 and W^2 fields, while the W^3 and B fields correspond to neutral currents.

The form of these interactions with fermions is somewhat complicated in the neutral sector, and a rotation to a more amenable (diagonal) basis is helpful in understanding what is happening. By defining

$$Z_\mu = \cos\theta_W W_\mu^3 - \sin\theta_W B_\mu \tag{1.83}$$

$$A_\mu = \sin\theta_W W_\mu^3 - + \cos\theta_W B_\mu \tag{1.84}$$

one can write the interactions cleanly in terms of the Z boson (a superposition of the W^3 and B gauge fields) and the A boson, which can be identified with the electromagnetic photon. The Weinberg angle θ_W, such that $\tan\theta_W = g_2/g_3$ in terms of the $SU(2)$ and $U(1)$ gauge parameters g_2 and g_3.

This gets us to the electroweak Lagrangian which describes a massless gauge theory invariant under $SU(2) \times U(1)$ transformations. The $SU(2) \times U(1)$ gauge theory predicts not only weak charged currents and the neutral electromagnetic current, but also weak neutral currents. That these currents have been observed provides further support for $SU(2) \times U(1)$ as the electroweak gauge group. The $SU(3)$ symmetry of the quarks and gluons can be included as well, since there are no gauge sector interactions between the electroweak sector and the color sector, though quarks feel the effects of both forces. In this way we can present the SM as the gauge field theory of $SU(3) \times SU(2) \times U(1)$. This theory is clearly incomplete, as we know that not only do the weak gauge bosons need nonzero masses, but the fermions also must be massive, which presents a problem with the electroweak symmetry as will be explored in Section 1.2.11. To include the mass terms and bring the SM to its complete form, we must introduce the formalism of spontaneous symmetry breaking, which is the subject of the next two Sections.

1.2.10 Symmetry breaking in classical field theory

We have been working with theories that have various symmetries; that is, Lagrangians that are invariant under various symmetry transformations. It turns out that the study of theories with symmetries that are explicitly broken can lead to highly interesting phenomena. We consider what happens when we include a term that breaks the symmetry of the Lagrangian. This is called, unsurprisingly, symmetry breaking, and when done explicitly like this is a part of the construction of the theory. Symmetries can also be broken by physical processes, leading to more natural symmetry breaking patterns. Mathematically, symmetry breaking is an operation that privileges certain generators of the symmetry group, obfuscating the full symmetry group behind a manifest subgroup and a relationship among the generators.

The following are illustrative examples of symmetry breaking that have been adapted from references [3, 5, 6, 15]. We first explore the simplest case of symmetry breaking in field theory and illustrate how the symmetry can be used to generate new dynamics. Consider the classical theory of a massless scalar field $\phi(x)$ in four dimensions with a quartic interaction. The Lagrangian takes the form

$$\mathcal{L} = \frac{1}{2}\partial^\mu\phi\partial_\mu\phi - \frac{\lambda}{4!}\phi^4. \tag{1.85}$$

This Lagrangian is trivially invariant under the discrete symmetry $\phi \to \phi' = -\phi$. Inclusion of a term proportional to ϕ^2 does not change this. If we were to add a term $-\frac{1}{2}m^2\phi^2$ to the Lagrangian (1.85) with $m^2 > 0$, this term would generate a mass for the ϕ field. Writing the massive Lagrangian explicitly in terms of kinetic and potential parts gives

$$\mathcal{L} = \frac{1}{2}\partial^\mu\phi\partial_\mu\phi - V(\phi) \tag{1.86}$$

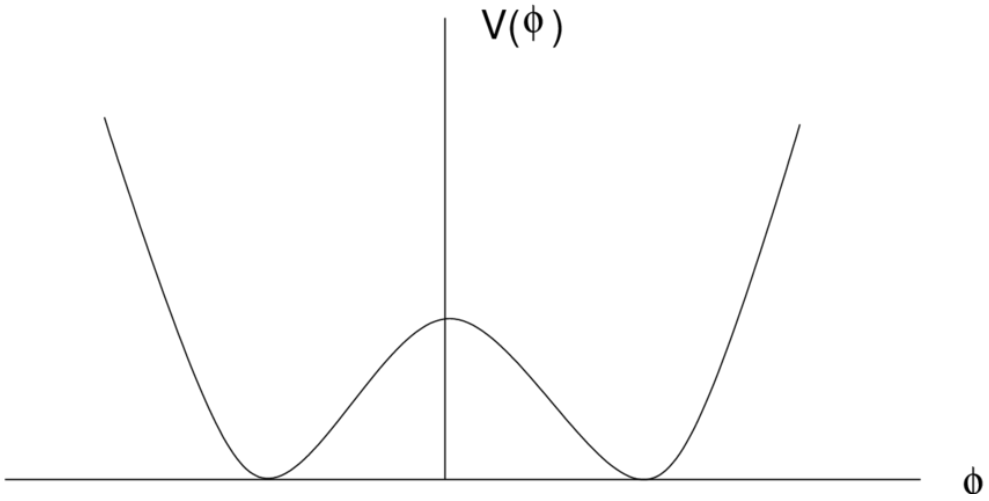

Figure 1.4: The potential $V(\phi)$ in Equation (1.88) as a function of the classical field ϕ. Note the distinct minima symmetric about zero.

where

$$V(\phi) = \frac{1}{2}m^2\phi^2 + \frac{\lambda}{4!}\phi^4. \tag{1.87}$$

This potential can be plotted as a function of ϕ, and it has a single minimum, at $\phi_0 = 0$. The field ϕ is still at this point a classical field, so it makes sense to think of it (and plot it) in this way as a function. In general, the same symmetry breaking techniques discussed in this Section for a classical field can be applied to quantum fields by using the formalism of the effective action. As the effective action is not explicitly required in this thesis, we refrain from exploring it here. It is discussed in detail in the standard references [3, 4, 5].

However, the situation changes when we consider instead a term $+\frac{1}{2}\mu^2\phi^2$, where $\mu^2 > 0$. This is equivalent to including a negative masslike term in the Lagrangian, or giving the ϕ field an imaginary mass $\mu = im$. The potential in this case takes the form

$$V(\phi) = -\frac{1}{2}\mu^2\phi^2 + \frac{\lambda}{4!}\phi^4. \tag{1.88}$$

This potential is plotted in Figure 1.4, and it has two minima which are found at

$$\phi_0 = \pm v = \pm\sqrt{\frac{6}{\lambda}}\mu. \tag{1.89}$$

To explore the dynamical behaviour of the theory, we expand about one of these minima. The choice of which of the minima to expand about is arbitrary, and it is this choice which breaks the symmetry. That there is more than one equivalent vacuum that can be chosen is why the symmetry breaking is called spontaneous. Note that the mechanism that makes the 'choice' is irrelevant here. We define a shifted field

by $\phi(x) = v + \sigma(x)$, where the minima occur at $\sigma = 0$. In terms of the shifted field, the Lagrangian takes the form

$$\mathcal{L} = \frac{1}{2}\partial^\mu\sigma\partial_\mu\sigma - \frac{1}{2}(2\mu^2)\sigma^2 - \sqrt{\frac{6}{\lambda}}\mu\sigma^3 - \frac{\lambda}{4!}\sigma^4 \tag{1.90}$$

where we have dropped constant terms that do not contribute to the equation of motion. Because we are expanding about a minimum, the coefficients of terms linear in σ must vanish as well.

This is a theory of a scalar field $\sigma(x)$ with mass $m_\sigma = \sqrt{2}\mu$ and cubic and quartic interactions. With the appearance of the cubic term, the reflection symmetry is no longer apparent, however is has left hints of its existence in the relationship between the interaction coefficients.

Now we move on to the case of spontaneous breaking of a continuous symmetry. Consider a complex interacting scalar field theory in four dimensions. If the theory has quartic interactions, the Lagrangian is of the form

$$\mathcal{L} = \frac{1}{2}\partial^\mu\phi\partial_\mu\phi^* - V\left(\phi, \phi^*\right) \tag{1.91}$$

where the potential contains the interaction term and a masslike term similar to the previous example:

$$V\left(\phi, \phi^*\right) = \frac{1}{2}\mu^2\phi^*\phi + \lambda\left(\phi^*\phi\right). \tag{1.92}$$

This Lagrangian is invariant under a phase shift of the field $\phi(x)$, which is a global $U(1)$ continuous symmetry:

$$\phi(x) \to \phi'(x) = e^{i\alpha}\phi(x). \tag{1.93}$$

As before, we consider the minima of the potential $V\left(\phi, \phi^*\right)$. Differentiation gives

$$\frac{\partial V}{\partial \phi} = \mu^2\phi^* + 2\lambda\phi^*\left(\phi^*\phi\right), \tag{1.94}$$

which we set to zero. For $\mu^2 > 0$, the minimum is at $\phi = \phi^* = 0$. For $\mu^2 < 0$, $\phi = 0$ is a local maximum, and there is a minimum at $|\phi|^2 = -\mu^2/2\lambda = a^2$. As illustrated in Figure 1.5, this minimum is actually a continuum of minima.

After quantization, the field ϕ takes on a nonzero vacuum expectation value of a. So ϕ has a degenerate vacuum with a rotational symmetry. The physical fields are then excitations above the vacuum, expansions around $|\phi| = a$. To exploit the rotational symmetry of the vacuum, write the complex field ϕ in polars:

$$\phi(x) = \phi_1(x) + i\phi_2(x) = \rho(x)e^{i\theta(x)} \tag{1.95}$$

In the discrete case, choosing a value for the vacuum entailed choosing the positive or negative root. Here, specifying the vacuum amounts to fixing a vacuum value for the continuous parameter $\theta(x)$. We choose

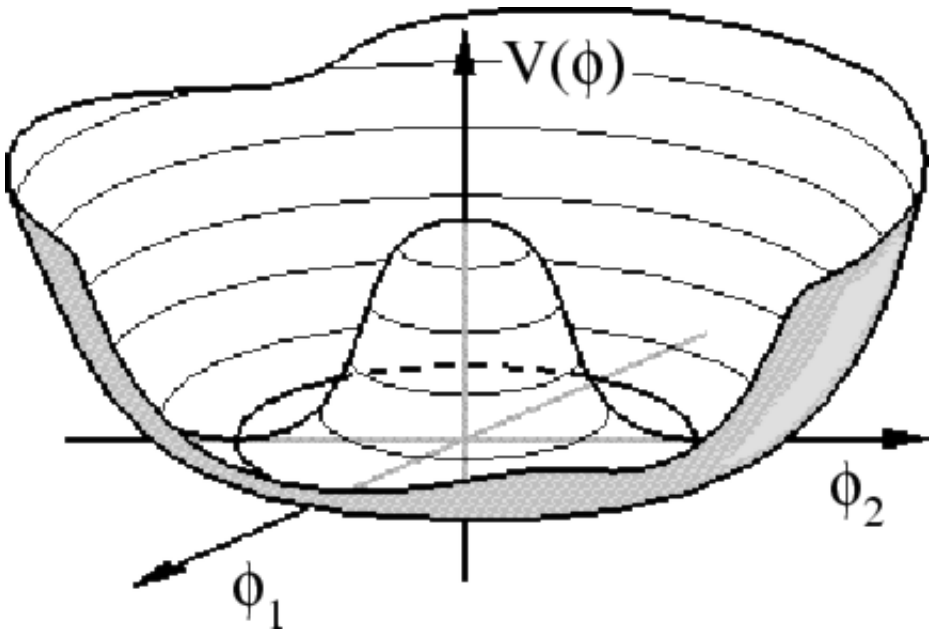

Figure 1.5: A plot of the 'Mexican Hat' potential $V(\phi_1, \phi_2)$ from Equation (1.92). Note the continuous minimum centered about the origin.

$\langle 0 \left| \theta \right| 0 \rangle = 0$. The vacuum expectation value of the component field ρ is a, so then by defining a $\rho' = \rho - a$, we have

$$\phi(x) = [\rho'(x) + a]\, e^{i\theta(x)}. \tag{1.96}$$

In terms of the field ρ', the potential can be written as

$$V = \mu^2 \rho'^2 + 2\mu^2 a\rho' + \mu^2 a^2 + \lambda\left(\rho'^4 + 4a\rho'^3 + 6a^2\rho'^2 + 4a^3\rho' + a^4\right)$$

$$= \lambda\rho'^4 + 4a\lambda\rho'^3 + 4\lambda a^2\rho'^2 - \lambda a^4$$

$$= \lambda\left(\left[\rho' + a\right]^2 - a^2\right)^2 - \lambda a^4$$

$$= \lambda\left(\phi^*\phi - a^2\right)^2 - \lambda a^4. \tag{1.97}$$

The kinetic term is

$$\left(\partial_\mu \phi\right)\left(\partial^\mu \phi^*\right) = \left(\partial_\mu \rho'\right)\left(\partial^\mu \rho'\right) + \left(\rho' + a\right)^2 \left(\partial_\mu \theta\right)\left(\partial^\mu \theta\right). \tag{1.98}$$

The full Lagrangian is then

$$\mathcal{L} = \left(\partial_\mu \rho'\right)\left(\partial^\mu \rho'\right) + \left(\rho' + a\right)^2 \left(\partial_\mu \theta\right)\left(\partial^\mu \theta\right) - \lambda\left(\phi^*\phi - a^2\right)^2 + \lambda a^4. \tag{1.99}$$

The term $4\lambda a^2\rho'^2$ acts as a mass term for the ρ' field, which we have seen in the discrete case. However, there is no such mass term for the θ field, leaving θ massless. This is a consequence of the fact that θ was used to parameterize the continuous symmetry of the degenerate vacuum.

Spontaneous breaking of a continous symmetry has taken two massless fields $\phi = \phi_1 + i\phi_2$ to a massive field ρ' and a massless field θ. The symmetry has been 'hidden' in a sense in the mass of the second field. The massless field θ is called the Goldstone boson of the system.

This specific example illustrates a general result: when a continuous symmetry of the Lagrangian is spontaneously broken, the degrees of freedom of the broken symmetry manifest in the Lagrangian as massless bosonic fields. This result is known as Goldstone's Theorem [16, 17].

In this Section we have demonstrated some of the features of spontaneous symmetry breaking in classical scalar field theories, in preparation for a discussion of the Higgs mechanism in the next Section. We have illustrated the both the case where a discrete symmetry is broken, resulting in a change in the Lagrangian and the apparent loss of the symmetry, and the case where a continuous symmetry is broken, which generates a new massless particle in the Lagrangian.

1.2.11 The Higgs mechanism

The final piece of the SM as it currently stands is electroweak symmetry breaking and the resulting activation of the Higgs mechanism to generate masses for the weak gauge bosons and the fermions. The requirement of symmetry under the $SU(2)_L$ gauge group introduces a problem when attempting to describe the mass terms of the fermions. It can be seen that the naive mass term $m^2\bar{\psi}\psi = m^2\left(\bar{\psi}_L\psi_R + \bar{\psi}_R\psi_L\right)$ is not invariant under $SU(2)_L$ transformations, as ψ_L and ψ_R transform differently under $SU(2)_L$, so some gauge invariant mechanism is required to generate fermion masses. Likewise, as a naive gauge boson mass term would alos violate the symmetry, there is no natural way to introduce mass terms for the electroweak gauge bosons.

In the previous Section, we discussed spontaneous breaking of a global continuous symmetry. The situation changes when a local or gauge symmetry is spontaneously broken. Consider as an example an Abelian gauge theory with a complex scalar field, which is essentially scalar quantum electrodynamics. The Lagrangian takes the form

$$\mathcal{L} = -\frac{1}{4}F^{\mu\nu}F_{\mu\nu} + |D_\mu\phi|^2 - V(\phi), \tag{1.100}$$

where the covariant derivative is $D_\mu = \partial_\mu + ieA_\mu$.

This Lagrangian is invariant under local gauge transformations

$$\phi(x) \to \phi'(x) = e^{i\alpha(x)}\phi(x), \tag{1.101}$$

$$A_\mu(x) \to A'_\mu(x) = A_\mu(x) - \frac{1}{e}\partial_\mu\alpha(x). \tag{1.102}$$

The potential is taken to be one which induces spontaneous symmetry breaking:

$$V(\phi) = -\mu^2 \phi^* \phi + \frac{\lambda}{2} (\phi^* \phi)^2 \tag{1.103}$$

where the parameter $\mu^2 > 0$.

As in the previous example, ϕ acquires a nonzero vacuum expectation value and the $U(1)$ symmetry is broken. The potential has a minimum at

$$V_{min} = \langle 0 \, | \phi | \, 0 \rangle = \phi_0 = \sqrt{\frac{\mu}{\lambda}}. \tag{1.104}$$

The field ϕ is then expanded into real and imaginary parts, with the vacuum expectation value made explicit

$$\phi(x) = \phi_0 + \frac{1}{\sqrt{2}} (\phi_1(x) + i\phi_2(x)) \tag{1.105}$$

which when inserted into the potential in Equation (1.103) gives

$$V(\phi) = -\frac{1}{2\lambda}\mu^4 + \frac{1}{2} 2\mu^2 \phi_1^2 + \mathcal{O}(\phi_i^3) \tag{1.106}$$

which includes a mass term for ϕ_1 of mass $m_1 = \sqrt{2}\mu$. The second field, ϕ_2 remains massless, and acts as the Goldstone boson of the model.

However, the local symmetry that has been introduced in the form of the covariant derivative causes a new complication. Under this field relabelling, the kinetic terms transforms as

$$|D_\mu \phi|^2 = \frac{1}{2} (\partial_\mu \phi_1)^2 + \frac{1}{2} (\partial_\mu \phi_2)^2 + \sqrt{2} e \phi_0 A_\mu \partial^\mu \phi_2 + e^2 \phi_0^2 A_\mu A^\mu + (\ldots) \tag{1.107}$$

where the $(\ldots)$ indicates interaction terms cubic and quartic in the fields ϕ_1, ϕ_2, and A_μ which are not pertinent to the result. The final term in the expression is a mass term for the gauge boson that gives a mass of $m_A^2 = 2e^2\phi_0^2$. It appears the spontaneous symmetry breaking has given the massless gauge boson a mass proportional to the vacuum expectation value of the scalar field.

Spontaneous symmetry breaking as implemented in the SM involves the nonabelian Higgs mechanism where, in contrast to the calculations earlier in this Section, the broken symmetry is a nonabelian gauge symmetry. The basic logic is the same, but there are some important consequences that result from the more complicated gauge group.

Consider a scalar field theory with an $SU(2)$ symmetry such that

$$H_i \to H_i' = (1 + i\alpha^a t^a)_{ij} \, H_j \tag{1.108}$$

where the generators $t_{ij}^a = \sigma^a/2$. The field H is a Lorentz scalar and an electroweak doublet. The gauge covariant derivative is

$$D_\mu H = \left(\partial_\mu - igA^a_\mu t^a\right) H = \left(\partial_\mu + gA^a_\mu T^a\right) H \tag{1.109}$$

which makes the kinetic term of the scalar field now

$$\frac{1}{2}\left(D_\mu H_i\right)^2 = \frac{1}{2}\left(\partial_\mu H_i\right)^2 + gA^a_\mu\left(\partial_\mu H_i T^a_{ij} H_j\right) + \frac{1}{2}g^2\left(T^a H\right)_i\left(T^b H\right)^i A^a_\mu A^{b\mu}. \tag{1.110}$$

If we let the scalar field H take on a nonzero vacuum expectation value $\langle H_i\rangle = (H_0)_i$ and we then expand about that minimum then, as in the Abelian case, the Lagrangian will acquire a term that acts as a mass term for the gauge bosons

$$\mathcal{L}_{m^i_A} = \frac{1}{2}m^2_{ab}A^a_\mu A^{b\mu} \tag{1.111}$$

where the masses are contained in the mass matrix $m^2_{ab} = g^2\left(T^a H_0\right)_i\left(T^b H_0\right)^i$. The masses should in general be positive for gauge bosons.

If any of the generators T^a leave the vacuum invariant, then $T^a H_0 = 0$ so that generator does not contribute to the mass matrix and the associated gauge boson A^a_μ remains massless. The vacuum solution is invariant under the $U(1)$ subgroup of $SU(2)$ generated by the third generator (W_3), so $SU(2)$ is spontaneously broken to $U(1)$. For any vector in the space, there will always be a tranformation that takes the vector into a subspace orthogonal to the Goldstone space. This is called unitary gauge, and it is in the unitary gauge that the SM Higgs scalar boson manifests as the Higgs doublet takes the form

$$H = \begin{pmatrix} 0 \\ \frac{h+v_h}{\sqrt{2}} \end{pmatrix}. \tag{1.112}$$

Explicitly in unitary gauge, the electroweak gauge sector of the SM becomes

$$\begin{aligned}\mathcal{L} = \mathcal{L}_{gauge} &- \frac{1}{2}h\left(\partial_t^2 - \nabla^2 + m_h^2\right)h - g\frac{m_h^2}{4m_W}h^3 - \frac{g^2}{32}\frac{m_h^2}{m_W^2}h^4 \\ &+ 2\frac{h}{v_h}\left(m_W^2 W^+_\mu W^-_\mu + \frac{1}{2}m_Z^2 Z^2_\mu\right) + \left(\frac{h}{v_h}\right)^2\left(m_W^2 W^+_\mu W^-_\mu + \frac{1}{2}m_Z^2 Z^2_\mu\right)\end{aligned} \tag{1.113}$$

where h is the physical Higgs boson field and v_h is the vacuum expectation value of the Higgs field. The gauge sector Lagrangian $\mathcal{L}_{gauge}$ has been suppressed for brevity, as it is very large and not particularly nice to look at. Thus the nonabelian Higgs mechanism has generated masses for the electroweak gauge bosons.

Using the Higgs doublet, one can also construct gauge invariant Higgs-fermion interaction terms that generate gauge invariant fermion mass terms after electroweak symmetry breaking. The fermion Yukawa sector is (before unitary gauge)

$$\mathcal{L} = -Y^\psi_{ij}\bar{\psi}^i_L H\psi^j_R + h.c. \tag{1.114}$$

summed over the fermions ψ. The Yukawa couplings are given by Y_{ij}, H is the SM Higgs doublet, and $h.c.$ indicates the Hermetian conjugate of the first term. These terms become couplings between the physical

Higgs field h and the fermions and fermion mass terms (proportional to $Y_{ij}/v_h\bar{\psi}\psi$) in unitary gauge. These terms are manifestly gauge invariant.

In this way, the Higgs mechanism allow the SM to behave as required by experiment. Observation of the physical Higgs boson in 2012 validates the SM as a theory.

1.3 Evidence for dark matter

This Section will provide an overview of the evidence for the existence of dark matter, evidence which can be said to make up the dark matter problem itself. There are two typical ways to present the evidence for dark matter: chronologically based on time of discovery and from small to large based on the scale of the phenomena. We have chosen here the latter, which better facilitates cohesion in a more technically detailed discussion. The smallest scale at which evidence of dark matter appears is the galactic scale, and we begin there, with a discussion of galatic rotation curves, before proceeding to the scale of galaxy clusters and then to the cosmological scale. See reference [18] for a review of the evidence for the existence of dark matter.

1.3.1 Galactic scale evidence

The scale of a single galaxy (hundreds of thousands of light years in diameter for the luminous disc) appears to be the smallest at which dark matter can be observed through its gravitational influence. In smaller scale systems, such as solar systems, dark matter is not concentrated enough to have a gravitational effect that can yet be measured, and no non-gravitational evidence for dark matter has yet been observed. Galactic scale evidence is also very important historically, as it led to the modern formulation of the problem of dark matter.

Galactic rotation curves

On the scale of galaxies, the most well known piece of evidence for the existence of dark matter is found in the rotation curves of spiral galaxies. A rotation curve is a plot of the rotational velocity of objects rotating about a central point against their radius. Spiral galactic rotation curves are governed by Newtonian gravity to a very good approximation, but observations produce results that indicate either the presence of invisible gravitating mass or the breakdown of Newtonian gravity.

The rotational velocity of an object in a stable gravitational orbit about an extended mass can be obtained from the balance equation

$$\frac{v_{rot}(r)}{r} = \frac{G_N M(r)}{r^2} \tag{1.115}$$

where the mass inside the orbit of radius r is $M(r)$ and G_N is Newton's gravitational constant. In terms of the density of the extended mass, one can write $M(r) = 4\pi \int \rho(r) r^2 dr$. Solving for the velocity, one obtains the prediction

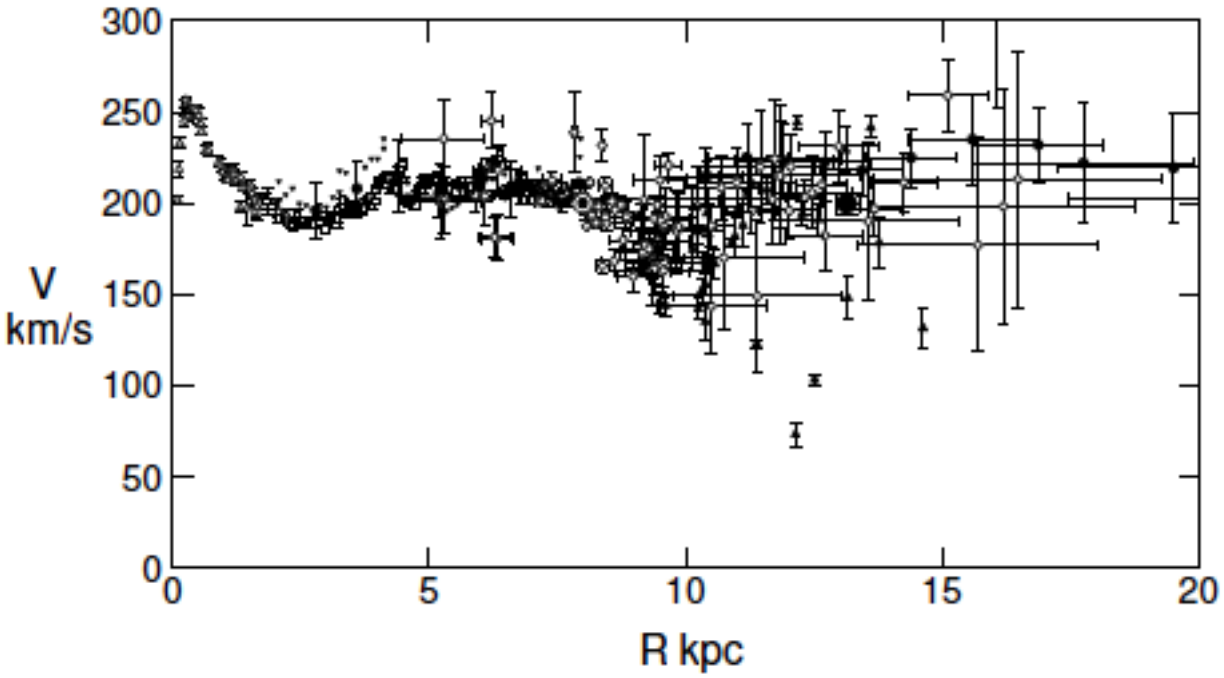

Figure 1.6: Rotation curve of the Milky Way, as reported in reference [19]. That it is roughly constant beyond about 3 kpc is strong support for the presence of dark matter.

$$v(r) = \sqrt{\frac{G_N M(r)}{r}}. \tag{1.116}$$

One can measure the rotational velocities of stars in galaxies by applying photometry techniques to tracer stars and measuring the Doppler shift of spectral lines, and combine together measurements of many stars at various radii to obtain a rotation curve for the galaxy.

Applied to a galaxy that consists solely of luminous mass, one expects that for r beyond the luminous part of the galaxy, the mass $M(r)$ should be constant, and hence that the rotational velocity should go like $v(r) \sim 1/\sqrt{r}$. However, observationally one sees $v(r) \sim$ const as far out as tracer stars can be distinguished. The rotation curve for the Milky Way has been reproduced in Fig 1.6. This behaviour can most simply be explained by simply assuming that there is a nonluminous mass component forming a spherical halo contributing to $M(r)$ with a density that goes like $\rho(r) \sim 1/r^2$, in which the luminous disk is embedded. This nonluminous mass is the manifestation of the dark matter problem in spiral galaxies.

The dark matter problem became accepted as a genuine problem as opposed to a curiosity by the scientific community following the work of Vera Rubin and collaborators [20, 21, 22], who measured the rotation curves of hundreds of spiral galaxies. While Rubin was not the first to notice the discrepancy (Babock did in 1939 [23]), she was the first to systematically study a large sample size with a high degree of rigor. That she was able to do so is due to the advances in optical astronomy, but that her study bore such incredible fruit was due to her painstaking personal efforts. Although the community was skeptical to begin with, the mounting

evidence forced acceptance of the accuracy of her work and the consequent implications.

A modern study of galactic rotation curves for over 1000 galaxies also exists, confirming the original findings [24] and reviewing the techniques involved. Galactic rotation curves remain an important part of the puzzle of dark matter, though their contribution tells us less than the evidence from gravitational lensing and cosmological observations in recent decades.

1.3.2 Cluster scale evidence

Some of the earliest and more recently, the strongest evidence for dark matter appears at the scale of galaxy clusters. These objects are groups of hundreds to thousands of galaxies that form a loosely bound gravitational system with a diameter of anywhere from 2-10 Mpc. Clusters as a whole have masses on the order of 10^{14}-10^{15} solar masses, and are composed of not only the galactic components but also of the hot gas that makes up the intracluster medium, which is x-ray emitting and has a temperature of 2-15 K. About 1% of the mass is in the galaxies, and about 9% is in the intracluster medium. The remaining 90%, as we will see in this Section, is made up of dark matter.

Gravitational lensing

Gravitational lensing was one of the main predictions of the general theory of relativity, and the observation of the effect was key in the acceptance of the theory. In general relativity mass, or more generally the stress-energy tensor $T_{\mu\nu}$, is related to the curvature of spacetime through the Einstein field equations

$$G_{\mu\nu} = 8\pi T_{\mu\nu}. \tag{1.117}$$

For a static system, the basic interpretation is that mass warps the flat spacetime close to it, generating a curved spacetime that acts on mass as a gravitational force. In flat spacetime, light will follow a straight line, but this is only a special case of the more general fact that light will follow the shortest path between any two points (this is known as Fermat's principle). In a curved spacetime, light will follow the geodesics, which are those paths that minimize the time it takes for light to travel between the two points. Consequentially, the presence of mass will cause light to follow curved trajectories, creating a lensing effect. This is the essential physics behind the gravitational lens.

As lensing cannot change the number of photons or the surface brightness of objects, the effects of gravitational lensing are directly related to the amount of matter (luminous or not) in the lensing system, which makes it a useful probe of dark matter distributions [25]. A massive object in the foreground will distort the light emitted by objects that appear near it in the background, which can create multiple images of the background objects or even a continous ring (known as an 'Einstein ring') depending on the geometry. This kind of gravitational lensing by what is effectively a point mass is known as strong lensing, and is capable of providing rough mass estimates for the foreground object, based on the amount of deflection the images

of the background object undergo. Observations of strong lensing have been used to estimate the mass of galaxies and galaxy clusters and provide support for the existence of additional nonluminous mass [26].

More usefully, strong lensing has been used to probe the MACHO (Massive Compact Halo Object) hypothesis of dark matter, in which dark matter consists of normal matter that is cold and hence dark in asteroid to planet sized bodies drifting through the galactic halo. Neutron stars and black holes are also thought to be MACHOs. MACHOs can be sought by looking for so-called microlensing events, where a MACHO passes in front of a star and briefly lenses the light of the star, causing a slight twinkle as the light is focussed. By searching for such events and noting their frequency, one can estimate the dark mass contribution of MACHOs to the galactic halo. After years of observations, the number of observed lensing events indicates MACHOs can make up at best 20% of galactic dark matter [27].

However, strong gravitational lensing is not the most useful tool for studying distributions of dark matter. Finding appropriate background objects to study for a distributed object like a cluster is difficult, and for a lens of insufficient strength it is difficult to separate lensing effects from the natural shape of the object. Extracting the nature of the mass that generates the lensing from pure observation is not straightforward, and usually involves comparison with numerical simulations and theoretical predictions. Weak gravitational lensing is the statistical study of the images of many objects viewed through a lens of extended spatial distribution. Lensing warps circular sources to appear elliptical, but without prior knowledge of the shape of the lensed object, this information is meaningless. As galaxies have an essentially random orientation with respect to our observations, it becomes difficult to determine how much of the ellipticity is due to lensing and hence how strong the lensing effect is. However, by considering lensed objects over a wide field of view, one can perform a statistical analysis to extract correlations in the shear distortion of the set of objects. This allows one to extract information about the collective lens, which in turn allows the construction of a map of the spatial distribution of gravitating matter in the lens. This includes dark matter, which means that weak lensing provides a window into the large scale structure of dark matter. Weak lensing has been used effectively not only with optical wavelengths, but also with infrared light, to observe objects that are very optically dim or optically obscured. For a detailed discussion of weak gravitational lensing and its use in observational cosmology, see reference [28].

One of the most important pieces of evidence for the existence of particle dark matter is the Bullet Cluster [29]. This cluster (1E0657-558), which actually consists of two galaxy clusters undergoing a collision, is at a distance of about 1.141 Gpc or 3.7 billion light years ($z = 0.296$). The mass distribution of the system was probed using weak gravitational lensing, and compared against the distribution of visible mass as observed with optical instruments and through the Chandra X-ray Observatory. The mass distribution was consistent with the hypothesis that the majority of gravitating mass in the system was nonluminous, and moreover has proven difficult to explain with non-particle explanations of dark matter, such as modified gravity theories. That the Bullet Cluster was actually caught in an observation is a very lucky event for the particle astrophysics community.

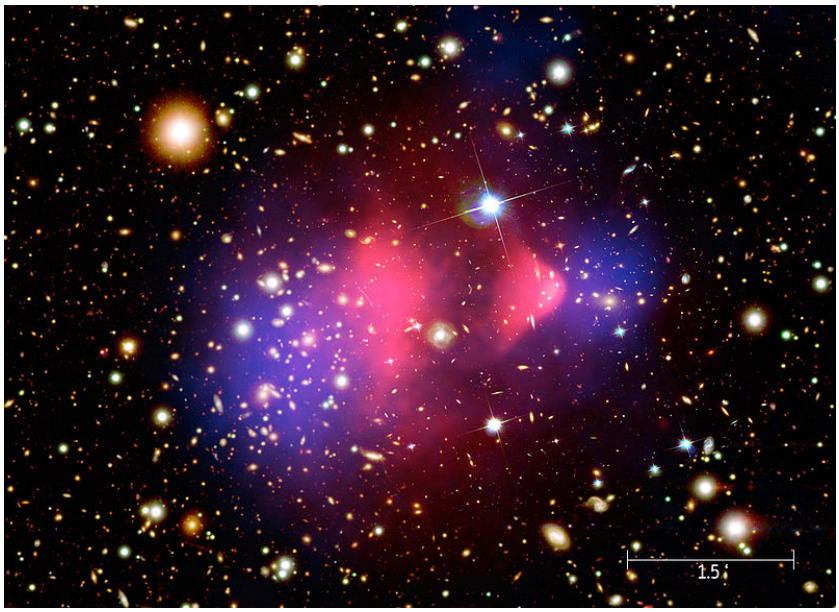

Figure 1.7: An overlay image of the Bullet Cluster (1E0657-558), as reported in reference [29]. The blue overlay is where the majority of the gravitating mass of the cluster is, while the red overlay is where the majority of the visible mass is. The discrepancy between the two indicates the majority of the mass of the cluster is nonluminous.

The classic summary image of the Bullet Cluster is included in Figure 1.7. The red and blue overlays are provided to show where the visible and dominant mass distributions are. To see how these observations are consistent with a particle dark matter interpretation, we consider how the main components of the cluster are affected by the collision. In a collision of this scale, the individual galaxies in the clusters are essentially collisionless, only being affected by gravitational tidal forces. They are simply too small to interact in any meaningful way. It is expected that the galaxies will then simply pass through the center of the collision, at least initially. The clouds of plasma will interact very strongly with each other, as they consist of charged particles, and will not pass through one another, instead becoming a combined cloud near the center of the collision.

So after the collision, considering only the visible components of the clusters, one expects to see the galaxies having passed through and beyond the center of the collision with the hot plasma remaining behind. Considering only visible mass, one would expect for a weak lensing analysis to put the the majority of the cluster mass in the plasma, at the center of the collision. This is not what is observed. It is in fact the case that the hot plasma (-red- overlay in Figure 1.7) contributes only $\sim 12\%$ of the mass of the clusters. The majority of the gravitating mass (the -blue- overlay in Figure 1.7) traces the galaxies, indicating that it is collisionless. This matches the predicted properties of dark matter. More technical details of the analysis are available in reference [29] and the literature cited therein. The Bullet Cluster is still studied in great detail [30, 31, 32, 33].

Velocity dispersions

For large scale objects such as galaxy clusters which are gravitationally bound, one can observe the motion of individual galaxies within the cluster and infer the gravitational potential that causes that motion. The gravitational potential, of course, is directly related to the mass distribution within the cluster. This allows measurements of the velocities of galaxies within a galaxy cluster to be used to estimate the total gravitating mass of the cluster. This was the method used by Zwicky in 1933 to examine the Coma cluster [34].

The virial theorem is a classical relation for a stable system that relates the average kinetic energy of the components of the system to the total potential energy, and it can be written

$$\langle T \rangle = -\frac{1}{2} \sum_{k=1}^{N} \langle \bar{F}_k \cdot \bar{r}_k \rangle. \tag{1.118}$$

For a central force, where the potential is proportional to powers of the radial distance $V(r) = ar^n$, the above relation simplifies to

$$2\langle T \rangle = n \langle V_{tot} \rangle \tag{1.119}$$

which becomes for the case of Newtonian gravity ($n = -1$):

$$\langle T \rangle = -\frac{1}{2} \langle V_{tot} \rangle. \tag{1.120}$$

The kinetic energy can be represented in terms of the velocities of component objects, which can be observed. These observations are done using Doppler measurements for the case of galaxy clusters. The potential energy of a gravitationally bound system thus is related to the total mass of the system. In this way, the observable velocities of objects in a bound system can be used to infer the total mass of the system. Note that though the virial theorem can provide a lower bound on the mass in the system, it cannot provide an upper bound. The masses estimated with the virial theorem are different from the masses of luminous sources observed. This indicates a significant dark component to the gravitational potential.

For this to provide a valid approximation in practice, certain conditions must be met. First, all bodies must be approximately the same mass compared to the total mass of the system. Second, a representative sample of the system must be obtained, typically requiring a large number of observations. Finally, the objects in the system must have an isotropic velocity distribution. Modern estimates of the fraction of baryonic matter in galaxy clusters from velocity observations that satisfy these conditions are $\Omega_b \simeq 0.2 - 0.3$ [35, 36, 37, 38].

Dwarf galaxies are small clusters of stars that exist around larger spiral galaxies. They are discussed in much greater detail in Chapter 4, as a possible gamma ray source for annihilating particle dark matter. Observations of stellar motion within these dwarf galaxies can serve as a predictor of the total gravitating mass in the galaxy. These observations indicate that dwarf galaxies have mass to light ratios that are the highest of any observed structure, indicating that they are incredibly rich in dark matter [39, 40].

One can also obtain mass estimates for clusters from the temperature of the gas in the intracluster medium, which is easily observed since it emits x-rays. The cluster gas is supported by its own pressure against gravitational collapse, and assuming hydrostatic equilibrium, one can infer a balance equation

$$\frac{dP_g}{dr} = -\frac{GM(r)\rho_g(r)}{r^2} \tag{1.121}$$

where $M(r)$ is the total mass inside the radius r and $\rho_g(r)$ is the gas density at radius r.

If we further assume that the gas obeys the ideal gas law, its pressure can be written

$$P_g = \frac{\rho_g kT}{\mu} \tag{1.122}$$

which can be combined with Equation (1.121) to give the following estimate of the gravitating mass of the cluster

$$M(r) = \frac{kT_g(r)r}{G\mu}\left[-\frac{d\ln\rho_g}{d\ln r} - \frac{d\ln T_g}{d\ln r}\right] \tag{1.123}$$

where in the above k is the ideal gas constant and μ is the mean mass per gas particle.

X-ray observations give us the temperature T_g, the density ρ_g and the chemical composition after some spectral analysis. With this information, Equation 1.123 can be used to estimate the total mass of the cluster, and these estimates are in agreement with those obtained from the observations of galaxy velocity distributions [37], providing further evidence of the existence of substantial gravitating dark matter in galaxy clusters.

1.3.3 Cosmological scale evidence

In recent years, observational cosmology has moved to the forefront of our queries into fundamental physics. Our study of cosmology relies on several sets of observations, but by far the most important are our decades of CMB observations. The CMB is the flux of photons that were emitted at the time of last scattering in the thermal history of the universe, when the primordial plasma had cooled to such a point that it became opaque, and the free ions and electrons combined to form hydrogen atoms. This event is discussed in slightly more detail in Chapter 2. The photons released carry information about the state of the universe at that time, including the distribution of matter, both baryonic (baryonic matter is massive SM matter in the context of astronomy) and dark.

CMB anisotropies

Some of the strongest evidence for particle dark matter as nonbaryonic comes from studies of the CMB. In fact, it is exceedingly difficult to model CMB observations without the inclusion of large amounts of non-baryonic matter. The CMB is about 3K in temperature, and about 400 photons occupy every cubic cm of space, with a flux of about 10^{13} photons per second per cm^3. The CMB sky is pictured in Figure 1.8.

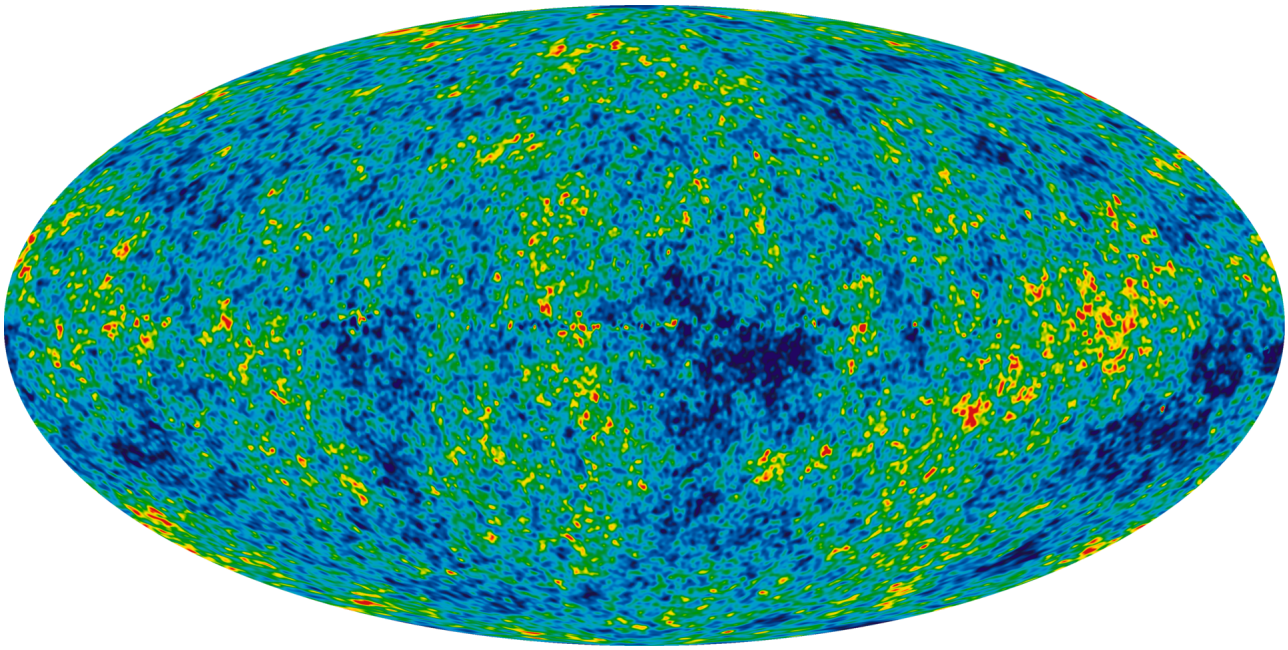

Figure 1.8: Image of the CMB mapped over the sky, as reported in reference [41]. Bluer regions are colder (photons from that direction are less energetic) while redder regions are hotter (photons from those regions are more energetic).

In the early universe, before the time when the first hydrogen atoms formed, there were acoustic oscillations propagating through the primordial baryon-photon plasma, with regions of slightly more and less compressed mass. The origin of these oscillations is not known, and is an area of active research [42]. They are thought to be the relics of fluctuations at a much earlier period, which were frozen in by cosmic inflation. There presence is not in doubt, however [41]. More compressed regions had slightly higher temperatures than less compressed regions, due to simple thermodynamics.

Eventually, the universe cooled enough that the photons and baryons decoupled, releasing what are essentially ionization photons. The above regions of differing temperature can be mapped to the mass distribution at the time of last scattering, when the CMB was generated. This is not only due to the slight temperature differences in the plasma communicating themselves to the emitted photons, but also due to the redshifting of the photons as they escaped the slightly deeper gravitational potential of the denser regions. The photon flux from the last scattering event has cooled as the universe has expanded, which it is now made up of microwaves, but the temperature fluctuations are still present, and observable, at levels of $\delta T/T \sim 10^{-5}$.

Temperature fluctuations in the CMB over the sky can be expanded in spherical harmonics

$$\frac{\delta T}{T} = \sum_{l=1}^{\infty} \sum_{m=-l}^{l} a_{lm} Y_m^l (\theta, \phi) \,. \tag{1.124}$$

The $l = 1$ dipole moment is due to the motion of the Earth with respect to the CMB, and is subtracted off. Averaging over value of m gives

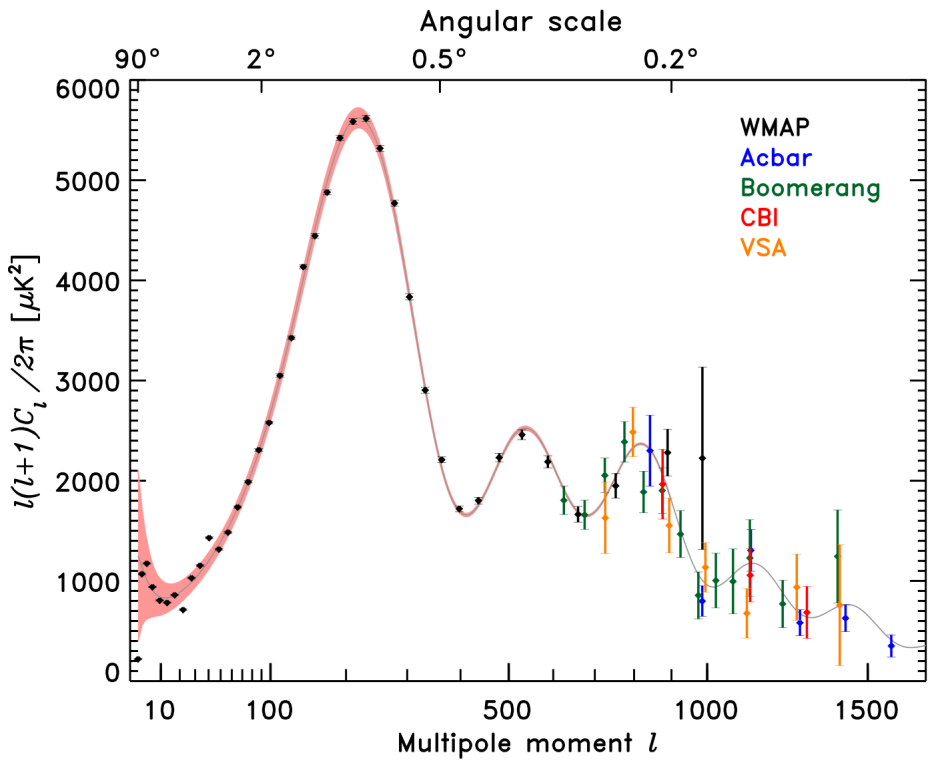

Figure 1.9: Power spectrum of the CMB as a function of multipole moment of expansion l. Information about the densities of the components of the universe can be extracted from the peaks (see text for more details). Figure originally published in reference [43].

$$C_l = \frac{1}{2l+1} \sum_{m=-l}^{l} |a_{lm}|^2 \,. \tag{1.125}$$

This quantity can be used to obtain the angular power spectrum of the CMB, which is

$$P = \frac{l\,(l+1)}{2\pi} C_l. \tag{1.126}$$

The value of the parameters C_l contain information about the distribution of matter at the time the CMB was emitted, and can be determined from observations.

The value of the first peak is related to the sonic horizon distance at the time of last scattering, which is largest spatial scale that could have responded to an acoustic wave. This is related to the propagation speed of acoustic waves, which is tied to the density of the medium. It essentially characterizes the size of the causal 'sound cone' of the medium. What value of l it appears at depends on the matter density of the universe $\Omega_0 = \rho(t)/\rho_c(t)$, where ρ_c is the critical density. The second peak, related to the maximum rarefaction, has a height less than that of the first peak, and the relative supression of the second peak increases as the cosmic fraction of baryons Ω_b increases. The third peak, which is related to the maximum compression, is sensitive to the dark matter fraction Ω_d. Thus, from the these three peaks, we can extract Ω_d.

The CMB has previously been studied by the succession of satellite-based instruments (COBE (1989-1993) [44] WMAP (2001-2010) [45], and PLANCK (2009-2013) [41]). The first two of these devices were single purpose instruments designed to to study the anisotropies in the CMB first reported by COBE in 1992 [46] (PLANCK having multiple other aims), and the combined program heralded the birth of precision cosmology.

Structure formation

Arguments for dark matter appealing to structure formation do not provide strong evidence for the existence of dark matter, but instead rely on consistency for their persuasive power. Mass in the observable universe is not distributed isotropically at scales smaller than 100 Mpc, but instead is clumped into regions of higher and lower density. Our understanding of the mechanism behind the initial asymmetries and their subsequent evolution as the universe expanded is far from complete. The basic picture is that the initial perturbations were generated by some unknown primordial fluctuations, and that the evolution was governed primarily by gravity with complications due to various thermodynamic effects. The basic solution for the evolution is density perturbations leading to an exponential growth in the amplitude of the waves, but this does not take into account pressure, which counters this growth. As pressure waves and gravity travel at different speeds, this leads to some interesting dynamics.

Dark matter has weak interactions with the SM, and hence decoupled from the primordial plasma relatively early on, and began to gravitationally evolve structure much earlier. As it is also non-interacting, it underwent gravitational collapse in a far different way that would happen with baryonic matter. Then, when the baryonic matter decoupled and began to undergo gravitational collapse later, it was drawn to the structure already in place from the collapse of the dark matter. This is reflected in the observations, and the universe would look very different if baryonic matter had collapsed without the influence of dark matter.

Hot (relativistic) dark matter cannot, in general, reproduce the observed large scale structure of the universe. It is simply moving too fast, and takes too long to collapse. If dark matter were hot, one would expect to see very old superclusters and very young galaxies, but this is the opposite of what we actually see. Galaxies have been around for over 13 billion years, and superclusters are a relatively recent phenomenon. There have been attempts to make hot dark matter with the observed structure, but such explanations are now disfavored by modern observations of high redshift galaxy distributions. This is not to say hot dark matter is ruled out completely, but it must make accommodations for structure formation.

These theories are tested by conducting N-body simulations of gravitational collapse, where N is in the billions [47, 48]. While these simulations are more or less in agreement with the predictions of the theory, providing a strong consistency argument, there are still unresolved questions, especially in the finer structures at the cluster scale and the galaxy scale, and only recently have the contributions of baryonic matter been taken into account.

1.4 Solutions to the dark matter problem

There have been many solutions proposed to address the dark matter problem. They fall into three broad categories: standard matter, exotic matter, and modifications to gravity. Of the three, the first is no longer considered viable, in large part due to its inability to describe the cosmological observations that were discussed in the previous Section. Explanations of that kind essentially posited that there was simply a large amount of normal (baryonic) matter out there that did not emit light, such as asteroids, planets, dust and brown dwarfs (see the discussion of microlensing in Section 1.3.2). This explanation is not supported by the analysis of CMB anisotropies. There were a number of observational studies done to observe nonluminous standard matter, but none were able to detect the amounts that would be required to address the dark matter problem in full at even the galactic scale.

The second class of explanations introduces new massive particles that are not part of the SM to account for dark matter. Generically, this is called particle dark matter, because such models usually admit a particle physics description of dark matter. It is the favored explanation among the astrophysics and particle physics communities. Examples of families of particle dark matter models are reviewed in this Section.

As evidence for the existence of dark matter is entirely gravitational, it is natural to ask if one can modify the theoretical description of gravity so that it is capable of reproducing the observations. The chief candidate of alternative gravity scenarios is discussed in Section 1.4.4.

1.4.1 Weakly interacting massive particles

At this point in time, the generic candidate for particle dark matter is the weakly interacting massive particle, or WIMP. Exact usage of the term WIMP has shifted over the decades, but in this thesis the term 'WIMP' will be used to describe any model of particle dark matter that was produced thermally in the early universe following the WIMP production paradigm as discussed in Chapter 2.

As mentioned above, the term 'WIMP' has been used to describe different things over the years, but the original usage was in the context of the supersymmetric (SUSY) WIMP. SUSY is an extended symmetry of spacetime, which can be obtained by extending the Poincaré Lie algebra into a graded Lie algebra. The transformations obtained in this extension map elements of a 'superfield' of particle fields into one another, where the elements of the superfield belong to different representations of the Lorentz group. More specifically, under SUSY transformations fermions are transformed into bosons and bosons into fermions. A consequence of this is that the existence SM particles indicates the existence of a set of partner superparticles, or sparticles, which complement the SM particles in the superfields. The reason SUSY has gained so much popularity is that these superpartners allow it to act as a custodial symmetry, solving the electroweak hierarchy problem. The radiative superpartner contributions to the Higgs boson mass can naturally cancel out the uncomfortable quadratic divergences that occur in the SM.

In additional to addressing the hierarchy problem, SUSY requires many new particles which can address

a number of other problems in particle physics, including the dark matter problem. In most SUSY theories, the lightest supersymmetric particle, which is the lightest particle that cannot decay into SM particles due to the conservation of R-parity (a conserved charge that is different between particles and sparticles), is both stable and neutral and so can act as dark matter. It will also typically interact with SM matter through the weak force, and SUSY scales tend to place its mass at around 100 GeV, which makes it a perfect candidate to fulfill the WIMP miracle (see Chapter 2). This lightest supersymmetric particle tends to be a neutralino, generally a linear combination of gauginos λ and Higgsinos $\tilde{H}^0$ (the superpartners of weak gauge bosons and the Higgs boson) [49]

$$\chi^0 = \alpha\lambda_B + \beta\lambda_W + \gamma\tilde{H}_1^0 + \delta\tilde{H}_2^0. \tag{1.127}$$

The literature pertaining to SUSY dark matter is vast, so we include only a handful of references [50, 51, 52, 53]. Further details are available in the reviews [54, 55] and the references therein. However, there has been no sign yet of SUSY at the LHC, which has placed very strong constraints on the parameter space of SUSY dark matter for the most natural models [56, 57, 58].

Another frequently considered candidate for dark matter is the lightest Kaluza-Klein particle [59], which occurs in theories with extra dimensions. In such theories, particles propagate in the additional spacetime dimensions as well as the usual four, which leads through quantization to an infinite tower of particle states with identical quantum numbers. The lightest of these states, which is often an excitation of the hypercharge gauge boson, is usually stable, and can act as cold dark matter in some cases. Such particles interact with SM matter through Higgs exchange and through exchange of other Kaluza-Klein particles. Kaluza-Klein theories of dark matter are less discussed at present than they were a decade ago, but still appear quite frequently in the literature.

Little Higgs models are another class of general beyond SM particle physics models that naturally admit dark matter [60, 61, 62, 63], and the currently popular twin Higgs model [64] is within this class. In this class of models, the SM Higgs boson is the pseudo Goldstone Boson of a spontaneously broken global symmetry at the TeV scale. The symmetry breaking term is constructed so as to naturally cancel contributions to the Higgs mass at loop order, resolving the fine-tuning part of the hierarchy problem in that approximation. It is intended to be the low energy effective theory of some higher UV completion that fully resolves the hierarchy problem. The basic construction requires a discrete parity-like symmetry that can function as a stabilizer for dark matter, preventing decays. The generic dark matter candidate [65] in the simplest variant of the theory is a heavy vector particle that interacts with the SM primarily through the Higgs-portal. For a review of the current experimental constraints on little Higgs dark matter, see reference [66].

1.4.2 Axion-like particles

The axion is a light pseudoscalar particle that was originally proposed to address a problem in QCD, but has become a somewhat common feature in beyond SM theories of particle physics. For several decades, it was

considered a strong candidate for dark matter, though current bounds on the QCD axion have almost ruled that possibility out. However, nonstandard axions, occasionally referred to as 'axion-like' particles, remain a family of strong candidates. There are several reviews of axion dark matter [67, 68, 69].

In the QCD Lagrangian, a gauge invariant term like

$$\mathcal{L}_\theta = \frac{\theta g^2}{32\pi^2} G^a_{\mu\nu} \tilde{G}^{a\mu\nu} \tag{1.128}$$

can appear. Indeed, there is no reason it should not appear. However, such a term would lead to CP violating processes in pure QCD, which have not been observed, placing stringent bounds [8]. That θ is so small (or zero) strikes many as unnatural without the involvement of some symmetry, and this unseemly smallness is known as the strong CP problem.

The strong CP problem can be solved if one postulates the existence of a classical global $U(1)$ symmetry of the QCD Lagrangian [70, 71], usually called the Peccei-Quinn symmetry after its creators. The $U(1)_{PQ}$ symmetry is spontaneously broken by the θ term in the QCD Lagrangian (1.128). The spontaneous breaking of a continuous symmetry generates a massless Goldstone boson, which is called the axion. The relevant Lagrangian is

$$\mathcal{L}_{\theta+a} = \left(\theta + \frac{a}{f_a}\right) \frac{g^2}{46\pi^2} G^a_{\mu\nu} \tilde{G}^{a\mu\nu} \tag{1.129}$$

The axion obtains a dynamical mass through loop order interactions with the gluon fields (anomalous interactions), or through the breaking of the PQ symmetry in some models. Masses for axions are highly model dependent, and range from 3×10^{-6} eV to 10 eV. Axions with larger masses are possible in some cases, but have lifetimes that are short on cosmological scales. The axion is characterized by the $U(1)_{PQ}$ breaking scale f_a, which is generally taken to be much larger than the electroweak breaking scale $v_h = 246$ GeV. A basic review of axion physics including current experimental results is available in reference [8].

The axion will couple to photons through a term generated by the mixing effect with the pions, by virtue of having the same quantum numbers,

$$\mathcal{L}_{a\gamma\gamma} = -g_\gamma \frac{\alpha_{em}}{\pi} \frac{a}{f_a} \mathbf{E} \cdot \mathbf{B} \tag{1.130}$$

where g_γ is some model dependent constant of $\mathcal{O}(1)$, and α_{em} is the electromagnetic fine structure constant. This term allows conversion of axions to photons in a strong magnetic field, which is the process sought in direct axion search experiments.

The axion interactions with SM fermions takes the form

$$\mathcal{L}_{a\bar{f}f} = i g_f \frac{m_f}{v} a \bar{f} \gamma_5 f \tag{1.131}$$

where v is the PQ scale and as above, g_f is a model dependent constant of $\mathcal{O}(1)$. The nonobservation of the decay channels opened by this term also place fairly weak bounds on the axion mass.

Bounds on the QCD axion are now quite strong [8], which has precipitated a drop in the volume of discussions of axion dark matter. However, the QCD axion is not the only possible kind of axion. Axion-like particles can arise in a beyond SM theory in which a global $U(1)_{PQ}$ symmetry is broken (through a PQ mechanism). The generic axion-like particle has nonzero $U(1)_{PQ}$ charge, a large vacuum expectation value, is scalar or pseudoscalar, and is an electroweak singlet. This last property means it will interact with the SM only through the $U(1)_{PQ}$ symmetry. The exact nature of the interaction is model dependent.

The strongest constraints on the axion parameter space come from observations of stellar life cycles. The presence of axions would increase the rate at which stars cool, accelerating their evolution significantly. This is because axions interact very weakly in comparison to other particles like photons, and so the energy of any axion produced is essentially lost to the star, as the axion will likely pass out of the star without scattering and depositing any of the energy back. This is clearly not the case for photons, which take much longer to reach the surface due to many scattering events. This can be thought of as a standard star radiating energy only from its surface area, while a star that produces axions is radiating energy from its entire volume. The most important processes involving axions that would occur in stars are Compton scattering ($\gamma e \to ae$), axion bremsstrahlung ($Ne \to Nea$), and the Primakoff effect ($\gamma N \to aN$). Comparison of observations to standard stellar evolution models constrains the couplings involved in each of these axion processes. Observations of red giants in particular rule out many models of axions in the mass range 200 keV $\geq m_a \geq$ 0.5 eV.

Additionally, the supernova SN1987a rules out axions in the mass range 3×10^{-3} eV $\geq m_a \geq$ 2 eV. These bounds come from the required consistency of observations with theories of supernova core cooling being entirely due to neutrinos, leaving no place for axion contributions. This constraint is independent of the axion model.

Axion production in the early universe is far outside of the standard WIMP paradigm. Thermal production of axions requires the couplings to the gluon leave the axion in thermal equilibrium until the QCD phase transition at around $T \sim \Lambda_{QCD}$ [72] (see Chapter 2 for more details). This analysis is complicated by the axion decay channel to photons, and pion conversion effects [73]. Hot axion dark matter was considered for a long time, though those models are less favored by other constraints on the axion parameter space [74]. Cold axions are more promising, primarily because of the vacuum realignment mechanism [75, 76, 77] that can generate an axion with interesting properties. Essentially, near the QCD phase transition, topological effects can generate a dynamical restoration of the PQ symmetry, generating an axion condensate which can act as cold dark matter. Axion dark matter is frozen out of the vacuum. These cold axions were never in thermal equilibrium, and so cannot be constrained by cosmological observations in the same way as generic thermal WIMPs can.

1.4.3 Right handed neutrinos

Of the SM fermions, neutrinos are unique in that they exist only in the left-handed chirality state. Additionally, in the basic SM, neutrinos are massless, which has been experimentally determined to be incorrect

[78]. This second fact is perhaps the only definitive piece of evidence from within particle physics itself that the SM is incomplete. The existence of right handed counterparts to the SM neutrinos has been considered many times as a way of generating neutrino masses, and they have also been consistently considered as a dark matter candidate [79, 80, 81, 82, 83, 84, 85, 86, 87, 88, 89]. See also reference [90] for a detailed review. It is known that the SM neutrino is too light and moves too quickly to account for the observed dark matter abundance, but a heavier neutrino could do so. In the literature, the right handed neutrino is called by that name if it has a mass on the GeV scale or larger, and if it has a mass on the keV scale it is called 'sterile' (in contrast to the active left handed SM neutrinos). The distinction is one of common usage, not definition, however, and as neutrinos are not the focus of this thesis we use the two terms interchangeably. Some sources include the neutrino dark matter candidates under the umbrella of WIMP, but we prefer to treat them as a separate category in this thesis, because of the specification we have made that the term 'WIMP' is associated with the freeze-out thermal production mechanism. While some neutrino models involve WIMP-like thermal production, many do not, and we prefer to group the neutrinos together for this brief survey.

A generic model of sterile neutrinos has a Lagrangian [91] that looks something like

$$\mathcal{L} = \mathcal{L}_{SM} + i\bar{\nu}_R \partial \nu_R - \bar{L}_L F_{\nu_R} \tilde{H} - \bar{\nu}_R F^{\dagger}_{\nu_R} L_L \tilde{H}^{\dagger} - \frac{1}{2}\left(\bar{\nu}^c_R M_M \nu_R + \bar{\nu}_R M^{\dagger}_M \nu^c_R\right) \tag{1.132}$$

where H is the SM Higgs doublet and F_{ν_R} is the matrix of the Yukawa couplings for the right-handed neutrinos ν_R. A Majorana mass term is generated by the Majorana mass matrix M_M, and $\nu^c_R = C\bar{\nu}^T_R$, where C is the charge conjugation matrix. The right-handed neutrinos are SM gauge singlets, and the only interactions with the SM sector are through the Yukawa couplings, which allow interactions with the Higgs and facilitate mixing effects with the left-handed lepton doublets. The Yukawa terms also generate a Dirac mass term in unitary gauge through the Higgs mechanism below the electroweak scale. These mass parameters are mostly free parameters of the model, and can be constrained in a number of ways depending on the overlying theory (including either parameter being set to zero).

The mixing between left and right handed neutrinos would allow for right handed neutrinos to decay into $\nu_L\gamma$ final states, which have not been observed, setting upper limits of $\sim$ keV masses on right handed neutrinos that can so decay. Variants that cannot decay in that manner can be much heavier. Other decays, such as those to $\nu_L\nu_L\nu_L$ final states, can cause the lifetime of the right handed neutrino to drop, but the decays happen so rarely in most models that the lifetime is not reduced below what is acceptable for dark matter (dark matter need not be absolutely stable if it decays slowly enough that the present day abundances can be matched to the abundance at the time of last scattering). There are several scenarios for the thermal production of heavy neutrinos in the early universe depending on model specific factors and the mass hierarchy. Thermal production through mixing effects in the neutrino sector also must be considered.

Right handed neutrinos are sought by a variety of experiments. These include x-ray searches for decaying light right handed neutrinos in the universe [92], searches for neutrinoless $\beta\beta$ decays [93, 94] (which require Majorana neutrinos, possibly right handed), and electron capture experiments (also known as inverse β

decay) in dark matter direct detection experiments, and in the SHiP high intensity beam dump experiment [95]. These experiments are mostly general neutrino physics experiments, not specifically focussed on dark matter.

Right handed neutrinos remain a promising candidate to consider for beyond SM physics, whether or not they account for particle dark matter. They are further discussed in Chapter 6, in the context of vector-portal dark matter.

1.4.4 Modified theories of gravity

While the predominant paradigm to explain the dark matter problem is particle dark matter, it is important to consider possible alternatives, especially since the existence of dark matter can only be inferred indirectly from gravitational phenomena. The natural place to look for explanations for gravitational discrepancies is in the laws of gravity. While it has fallen out of favor, the leading candidate for a theory of modified gravity that can resolve certain aspects of the dark matter problem is Modified Newtonian Dynamics (MOND) [96, 97, 98].

The basic principle of MOND is to modify the Newtonian gravitational potential so that the gravitational force law reads

$$F_N = ma\mu \tag{1.133}$$

where $\mu = \mu(a/a_0)$ is called the interpolating function. The function $\mu(x)$ is chosen so that $\mu(x) \sim x$ for $x \ll 1$ and $\mu(x) \sim 1$ for $x \gg 1$. Common choices for $\mu(x)$ are $\mu(x) = 1/(1+x^{-1})$ or $\mu(x) = \sqrt{1/(1+x^{-2})}$. MOND is an observational law that has proven very successful in describing the rotation curves of spiral galaxies. After inserting this modified force law into the balance equation (1.115), one can solve for the velocity to obtain $v^4 = GMa_0$ for large distances, which produces a constant rotation curve as observed if one takes the mass M constant at that point.

A value of $a_0 = 1.2 \times 10^{-8}\text{cm/s}^2$ has been found from a fit to the rotation curves of ~ 100 galaxies [99], which agrees with values obtained from the Tully-Fisher law, which is an empirical relation between the rotation speed of spiral galaxies and the amount of luminous mass they contain [100]. MOND has had a great deal of phenomenological success on the galactic scale [101, 102], but virial theorem studies of cluster scale dynamics indicate that a factor of 2-3 more mass than is visible is still required in the MOND paradigm to reproduce observations [101].

As mentioned above, basic MOND is an observational law. Theoretical interpretations are varied, though the most popular of the attempts to extend MOND into a complete relativistic theory of gravity is the tensor-vector-scalar theory (TeVeS) [103, 104], which is a modification of the more standard extensions of general relativity which incorporate a scalar (see, for example, reference [105] for a discussion of scalar-tensor gravity). Modifying the basic scalar-tensor theory in include MOND-like effects resulted in issues with superluminal propagation of the scalar, which was resolved by the inclusion of the vector field.

TeVeS has had some phenomenological successes and some failures. It can reproduce certain strong lensing observations [106], but weak lensing results are less satisfactory [107]. The cosmology of the theory has been studied in great detail [108], and it can account for much of the cosmological evidence usually used to support particle dark matter [109], but there are some difficulties.

Additionally, analysis of the Bullet Cluster as discussed in Section 1.3.2 indicates alternative gravity models that incorporate gravitational lensing (such as TeVeS), require at least 2.4× the amount of baryonic matter in nonluminous mass to reproduce the observations [29]. This requirement weakens the ability of alternative gravity theories of this type to explain dark matter, and has led to the slow decline of their popularity in the community. While MOND and its relativistic extensions still have a number of adherents, most astrophysicists have accepted that reality disfavors the explanations these theories provide.

Chapter 2

Thermal Relic Dark Matter

The study of particle dark matter is inextricably related to the study of cosmology, and in particular, to the study of the thermal history of the universe. If the solution to the dark matter problem is in fact the presence of a fundamental particle, and not one of the other possibilities, that particle was somehow produced in the early universe. Assuming particle dark matter roughly follows the same behaviour as SM particles, one can model the interactions of the dark matter in the early universe. Many of the properties of particle dark matter can be related to its decoupling from the primordial plasma, and over the last few decades a window into that epoch has been opened for us by the COBE [46], WMAP [45], and PLANCK [41] satellite observations of the CMB. With the advent of precision observational cosmology, models of dark matter can be constrained by cosmological observations, providing much needed restrictions to the vast parameter space of particle dark matter. This Chapter is a discussion of the most prevalent scenario for dark matter production in the early universe: thermal freeze-out from the primordial plasma.

The Chapter opens with a rapid review of the thermal history of the universe in Section 2.1 to provide background for the discussion that follows. In Section 2.2 is an introduction to the basic statistical mechanics of fundamental particles in the setting of the early universe, which is the formalism used for calculations of the thermal production of dark matter. The mechanism of freeze-out itself in the case of cold dark matter is discussed in detail in Section 2.3, and Section 2.4 is an application of the freeze-out scenario to the simple example of scalar Higgs-portal dark matter.

2.1 Thermal history of the universe

To put the following discussion of the thermal production of dark matter in the early universe into context, this Section provides a brief overview of the thermal history of the universe. Deeper treatments that contain the full mathematical explanations are readily available. The text of Weinberg [28] in particular is very thorough, and that of Kolb and Turner [110] is recommended as well.

The history of the universe, as we currently understand it, is illustrated in the standard graphic that appears in Figure 2.1. At time $t = 0$ was the event known as the Big Bang, about which we know essentially nothing, which was followed by what is known as the inflationary period during which the universe expanded rapidly due to some unknown mechanism. The physics behind inflation is an area of active research [111, 42],

and many models tie the mechanism of inflation to fluctuations of a primordial scalar field [112, 113, 114]. Inflationary cosmology is outside of the author's area of expertise, so we leave our discussion at that and move on.

After the inflationary period, more standard thermodynamics and particle physics takes over. At this time of $t \sim 10^{-38}$ s, when the universe was a temperature of $T >\sim 10^{16}$ GeV, the temperature of the universe is high enough that all particles may be created easily and all species are in thermal equilibrium. At high temperatures, the average collision energy of particles is higher, which leads to a higher collision rate. When the collision rate is larger than the Hubble expansion rate, it can be assumed that the universe is in thermal equilibrium, with a common temperature-energy. In natural units, as discussed in Appendix A, one can express temperature in units of energy, and the conversion factor is that 1 GeV of temperature is equivalent to 1.16 $\times 10^{13}$ K. This is the epoch of the primordial plasma, which is a radiation dominated epoch (as all species of particle are highly relativistic).

Standard expansion according to the Friedmann equation has taken over after the cessation of inflation, and the universe expands according to standard solutions to the Friedmann equation [28]. This expansion can be written in terms of the Hubble factor $H(t) = \dot{a}(t)/a(t)$, where $a(t)$ is the scale factor of the universe.

The universe expands, and thermodynamics implies that it should cool as it does. So as time t increases, temperature T decreases, and for a well defined rate of expansion, temperature and time become equivalent ways of describing how old the universe is. The conversion factor will depend on the epoch, or which term in the Friedmann equation is dominant. During this period of the history of the universe, that is radiation. As the universe expands and cools, the plasma that comprises it also cools, following basic thermodynamics, and undergoes a number of phase transitions. The first phase transition is the hypothesized grand unified theory (GUT) phase transition, which occurs around $10^{14} - 10^{16}$ GeV. To understand this phase transition, which may actually be a series of phase transitions, requires knowledge of the UV completion of the SM of particle physics, which we do not have. The GUT phase transition is where, essentially, the SM decoupled from the higher energy theory in which it is presumed to be embedded. In this context, decoupling means that the interaction timescales of particles in the higher energy theory are larger than the local Hubble time, which means those interactions only occur very rarely. The nature of the GUT phase transition is highly dependent upon unknown particle physics, but what comes after is more clear.

At a temperature of $\sim$ 300 GeV, the electroweak phase transition occurs, and the electroweak force separates into the short range weak force and the long range electromagnetic force. Matter gains explicit mass through the Higgs mechanism, and the weak gauge bosons decouple from the plasma. After this, down to the next scale, the heavy fermionic content of the SM (t, b, c quarks and τ leptons) gradually decouples from the plasma, the heavier fermions first.

When the universe has cooled to $100 - 300$ MeV, at $t \sim 10^{-5}$ s, the QCD phase transition occurs, color confinement becomes active, and free quarks hadronize out of the quark-gluon plasma. At this point, the active particle species of the universe include hadrons (protons, neutrons, and some mesons such as the pion

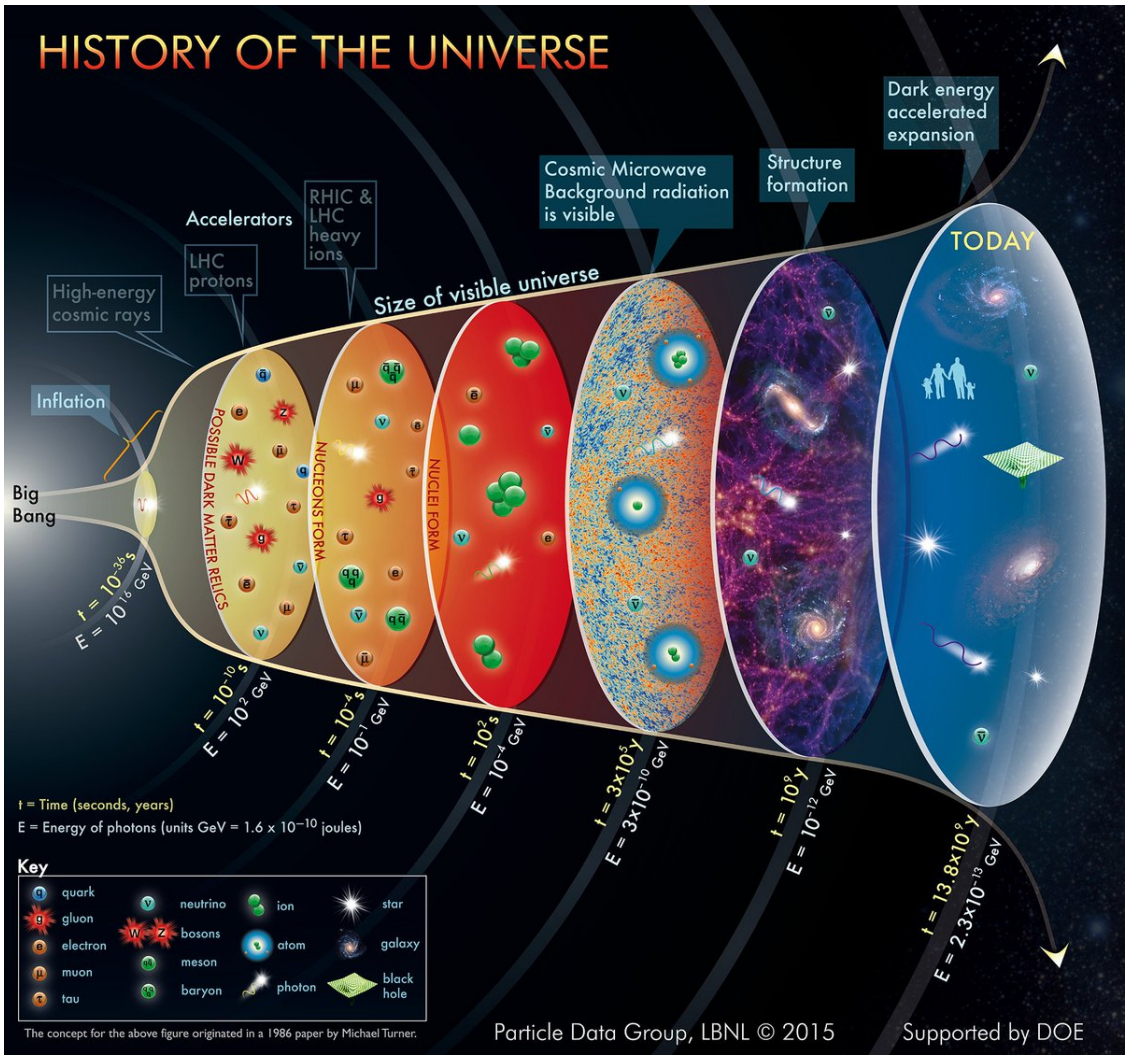

Figure 2.1: A schematic of the thermal history of the universe, courtesy of the Particle Data Group [8].

for a short time), electrons, muons for a short time until they too decouple, the neutrinos (which decouple in the massive case at around $T = 1$ MeV), and photons. At this period, the universe can still be considered radiation dominated.

Primordial nucleosynthesis occurs from $t \sim 10^{-2} - 10^{-3}$ s or $T \sim 10 - 0.1$ MeV, and some of the free protons and neutrons bind to form the first atomic nuclei. As the abundances of various species of nuclei that formed at this time should be very close to current abundances, this is the earliest possible period that can be probed by observations. At $t = 10^{11}$ s is the point usually taken to be the end of the radiation dominated epoch and the beginning of the matter dominated epoch, when the nonrelativistic particle density contributes roughly the same as the relativistic particle density, and the matter term in the Friedmann equation dominates. It is also around this time that structure formation, as discussed in Chapter 1, begins.

At around $t = 10^{13}$ s recombination and last scattering occur, as was discussed briefly in Chapter 1, and the CMB is generated. The free electrons and protons bind to neutral hydrogen, and stop freely exchanging energy with photons. Estimates place the temperature at the last scattering at around 3000 K. At this point matter and radiation have decoupled, and the universe proceeds on to the present without any other phase transitions. There is occasional scattering between matter and the remaining photons, but there is little energy transfer.

After this point, the universe continues to evolve, but the evolution is driven primarily by gravity and possibly magnetic fields. Particle physics effects are negligible, and we end the overview at this point. The next Section provides a technical description of particle behaviour during these early periods.

2.2 Particle statistical mechanics in the early universe

This Section will introduce the basic formalism for describing the number density of a particle species in the early universe, when both thermal effects and expansion effects are important.

A gas of non-interacting particles in a changing volume $V = a^3(t)$ will have a constant particle number N, as non-interaction implies particles will not be created or annihilate. In terms of the number density $n(t)$, this relation can be written $N = n(t)a^3(t) = const.$ This implies the following differential equation is satisfied:

$$\frac{d}{dt}\left(n(t)R^3(t)\right) = 0. \tag{2.1}$$

In the standard expanding universe, this equation can be written in terms of the Hubble parameter $H = \dot{a}(t)/a(t)$, which describes the expansion of the universe, as

$$\frac{dn}{dt} + 3nH = 0. \tag{2.2}$$

The Hubble factor $H(t)$ changes is time, and generally goes like t^{-1}. The Hubble time or radius H^{-1} describes the scale of the expansion.

The assumption of non-interacting particles is not sufficient to describe particle physics in the early universe, where the temperature was large enough that all particles can be assumed to be in thermal equilibrium, and hence interacting. A particle will be in thermal equilibrium with a plasma it is in contact with if the temperature of the plasma is large enough, allowing it to be freely created (ie $T > 2m$). More formally, for $\Gamma = n\langle\sigma v\rangle$ the interaction rate per particle in terms of the total thermal annihilation cross section, the particle species is in thermal equilibrium if $\Gamma > H(t)$. If a particle is in thermal equilibrium, it can be created and can annihilate, leading to changes in the total particle number. These creation and annihilation processes must be incorporated into the balance equation (2.2). The number density evolution of particles in thermal equilibrium is described by a complicated system, the governing equation of which we will now derive. In contrast, once a particle species has decoupled, its evolution is simple, governed only by the expansion of spacetime (and possibly self-annihilations for a time). For a completely decoupled and non-interacting species, the number density goes like $\sim 1/a^3$, and momentum goes like $\sim 1/a$.

To take these terms into account, we consider the phase space distribution function of the particles $f(p^\mu, x^\mu)$, described by the Boltzmann equation. The phase space distribution describes the probability that the system will be found in the infinitesimal phase space volume $f(p^\mu, x^\mu)d^4pd^4x$. In general operator form, the Boltzmann equation is [110]

$$\hat{L}\left[f\right] = \mathcal{C}\left[f\right], \tag{2.3}$$

where $\hat{L}$ is the Liouville operator describing the time evolution of the phase space distribution, and $\mathcal{C}$ is the collision operator, which will be defined shortly. The covariant, relativistic Liouville operator is, in the Robinson-Walker spacetime that describes the expanding universe in standard cosmology,

$$\hat{L}\left[f\right] = E\frac{\partial f}{\partial t} - \frac{R'}{R}\left|\hat{p}\right|^2\frac{\partial f}{\partial E}. \tag{2.4}$$

The number density can be written in terms of the phase space distribution through

$$n(t) = \frac{g_*}{(2\pi)^3}\int d^3p f(E,t) \tag{2.5}$$

where g_* is the number of degrees of freedom of the plasma. The relativistic number of degrees of freedom is dependent on the numbers of fermions (g_f) and bosons (g_b) in the theory:

$$g_*(T) = \sum_b g_b + \frac{7}{8}\sum_f g_f. \tag{2.6}$$

Integration by parts of Equation (2.5) and substitution into Equation (2.3) gives the differential form of the Boltzmann equation:

$$\frac{dn}{dt} + 3nH = \frac{g_*}{(2\pi)^3}\int d^3p\frac{\mathcal{C}\left[f\right]}{E}. \tag{2.7}$$

The collision term is in general a very complicated object [110]. In contrast to the noninteracting Boltzmann equation, which says groups of particles maintain phase space density as they travel through phase space, the collision term modifies the phase space density. It encapsulates all possible interactions that can change particle number. A more detailed discussion can be found in references [110] and [115].

In general, the Boltzmann equations are a set of coupled integral-partial differential equations, with one equation for each particle species in the plasma. Such equations are naturally very difficult to solve, even before the quantum field theory inputs to the collision operator are examined in much detail. A simplifying assumption that is usually made, known as the decoupling assumption, is to assume most particle species have equilibrium phase space distributions, which reduces the system of equations down to a single equation for the species of interest. By using T invariance and by making the assumption that the species of interest obeys Maxwell-Boltzmann statistics, the collision operator side of the equation can be simplified further.

One would like to solve the Boltzmann equation to determine the current abundance of the species of interest. This requires determining when the collisional term stops contributing; that is, when the species decouples from the plasma. When a species decouples, the particle number (up to potential self-annihilation; see the next Section) ceases to change, as the term on the right-hand side of Equation (2.7) is now zero. The current number density can then be obtained by subjecting the number density at decoupling to the dilution effect due to the expansion of spacetime. This process is called 'freeze-out.' It was formalized by Lee and Weinberg [116] for the abundances of heavy neutrinos in the early universe, and their basic approach and approximations are used to this day.

There are, however, no general closed form solutions for the Boltzmann equation. Approximate solutions are obtained through analytic approximations or numerical methods. In what follows, we can begin referring to the species of interest as 'dark matter.' There are several additional assumptions that can then be made. We assume a stable dark matter particle, with only $2 \leftrightarrow 2$ annihilation/production processes changing particle number density. Most dark matter models require a certain stability to reproduce the observed abundance, and for most quantum field theory models, $2 \leftrightarrow 2$ processes dominate production and annihilation, though there are a handful of exceptions. Assume as well that the SM particle species have thermal distributions with zero chemical potential, which they effectively are at this period.

The most common approximation made is to decide at what temperature range the species of interest decouples from the plasma. The choices are hot and cold, describing whether or not the particle species decouples at relativistic or nonrelativistic energies. For a particle species that freezes out hot, when the average particle has a kinetic energy comparable to or larger than the rest mass of the particle, the final value of the number density is insensitive to the exact temperature at which the decoupling occurs, depending only on the number density at the time of freeze-out. Hot thermal relics are typically very light ($\sim$ eV scale masses), and cosmological bounds on hot dark matter exist [117]. The classical model for hot dark matter was the axion, though as discussed in more depth in Chapter 1, different production mechanisms are now favoured for axion dark matter. Hot dark matter is beyond the scope of this thesis, and so we do not discuss

it any further.

The alternative is a cold thermal relic, which occurs when a particle species freezes out with an average particle energy far less than the particle rest mass, called the nonrelativistic regime. Unlike hot thermal relics, the abundance of cold relics at freeze-out is very sensitive to the temperature at which decoupling occurs. When this process is applied to a dark matter model, we call the thermal relic cold dark matter, and these models typically decouple some time after the electroweak phase transition, but before the QCD phase transition. The WIMP is a class of models of cold dark matter, and we discuss the details of the freeze-out process and how it can be used to constrain the properties of cold dark matter in the next Section.

2.3 Freeze-out of cold dark matter

The standard WIMP paradigm has dark matter in thermal equilibrium with the primordial plasma during the early universe until the Hubble expansion causes the temperature to drop below some critical value, at which the WIMP is said to 'freeze out.' The abundance of the WIMP at freeze-out is directly related to the current abundance. Observations of the current abundance can then be used to constrain the properties of the WIMP related to the freeze-out process. Practically, this results in a constraint on the WIMP annihilation cross section. The idea of the 'WIMP miracle' that has driven so much of the dark matter experimental effort follows from this. A particle with a mass of $\mathcal{O}(100\,\mathrm{GeV})$ and an annihilation cross section of $\langle\sigma v\rangle \sim 10^{-26}\,\mathrm{cm}^3/\mathrm{s}$ will reproduce the observed dark matter abundance with only minor tweaking [118]. This is the natural scale for weakly interacting particles, leading to the term 'WIMP.' The term was originally used to describe a supersymmetric particle, which naturally occurred in certain variants of SUSY with the correct properties, but usage has since expanded to include any particle dark matter with a GeV-TeV scale mass and an annihilation cross section within a few orders of magnitude of $10^{-26}\,\mathrm{cm}^3/\mathrm{s}$ which can reproduce the observed abundance with minimal fine-tuning. To reiterate from Chapter 1, we use 'WIMP' in this thesis to refer to any particle produced by the freeze-out process described below.

The standard treatment of thermal WIMP production follows. The number density $n(t)$ of WIMPs in the early universe is governed by the rate equation, which is the Boltzmann equation for cold dark matter. It can be written in terms of the equilibrium number density When the WIMP is in thermal equilibrium with the rest of the universe, as it is assumed to be at some early time, the number density is constant. This is simply a consequence of the definition of thermal equilibrium. We can resolve the collisional term through many simplifications [110] into a production term and an annihilation term. The annihilation term is simply $\langle\sigma v\rangle n^2$; which is proportional to n^2, because two WIMPs are required to cause an annihilation event. Inserting a constant number density into the Boltzmann equation lets us set the left hand side to zero, which allows us to write the thermal production term in equilibrium as

$$dN_{th} = \langle\sigma v\rangle n_0^2 a^3 \tag{2.8}$$

where n_0 is the thermal equilibrium number density of the WIMP. The function $a(t)$ is the Robinson-Walker scale factor. This leads to the rate equation becoming

$$\frac{dn}{dt} + \frac{3n}{2t} = -\langle \sigma v \rangle \left(n^2 - n_0^2 \right). \tag{2.9}$$

where $\langle \sigma v \rangle$ is the velocity weighted thermally averaged total annihilation cross section of the dark matter particle. This equation is simply a statement of conservation of number density. The change in the number of WIMPs is the number produced less the number that annihilate in a given unit of time. Alternatively, it can be written in terms of the Hubble factor H:

$$\frac{dn}{dt} + 3nH = -\langle \sigma v \rangle \left(n^2 - n_0^2 \right). \tag{2.10}$$

The equation is now in a form that is amenable to solution.

That the Boltzmann equation can be written in this form, in terms of the equilibrium number density, is perhaps not obvious. This formulation follows from something known as the principle of detailed balance. The principle claims that whenever all species but one are in thermal equilibrium, the creation process can be obtained from the destruction process by the substitution of n_{eq}, the equilibrium number density of the target species, for n, the number density, in the Boltzmann equation. This is simply a more specific statement of the conservation of particle number when a species is in thermal equilibrium.

During the radiation dominated epoch, where the temperature T of the universe is much larger than any mass scale relevant for WIMP production ($T \gg m$), T can be related to the (cosmic) time t by

$$t = \frac{b}{T^2} \tag{2.11}$$

where the numerator is

$$b = \frac{3\hbar M_{pl} c^2}{\pi k_B^2} \sqrt{\frac{5}{2g_*(T)}}. \tag{2.12}$$

In the above, M_{pl} is the Planck mass and $g_*(T)$ is the number of relativistic degrees of freedom of the plasma at temperature T, as mentioned in the previous Section. For $m_b < T < m_W$, which is the usual scale of freeze-out temperatures for $\mathcal{O}(100$ GeV) WIMP dark matter, and assuming no non-SM particles lighter than the temperature, $g_*(T) = 91.5$. Note that the standard treatment ignores terms proportional to dg_*/dt, which are nonzero if the number of contributing particles changes over the temperature range being integrated over. For temperatures on the GeV scale, these changes may occur for a handful of SM particles with masses in that range, and possibly for beyond SM particles at higher temperatures, but all such changes will be negligible in WIMP scenarios. A new particle or two will not change the results.

The relation in Equation (2.11) allows reframing of the rate equation (2.9) in terms of the temperature

$$\frac{d}{dT}\frac{n}{T^3} = 2b\langle \sigma v \rangle \frac{n^2 - n_0^2}{T^6}. \tag{2.13}$$

To solve this equation, the equilibrium number density n_0 needs to be known. The standard treatment of this problem uses the analytic approximation of Lee and Weinberg (LW) [116] for the equilibrium number density

$$n_0(T) = \frac{1}{2\pi^2 (\hbar c)^3} \int_0^\infty dK \frac{\left(K + m_\chi c^2\right) \sqrt{K\left(K + 2m_\chi c^2\right)}}{\exp\left[\left(K + m_\chi c^2\right)/k_B T\right] \pm 1}. \tag{2.14}$$

where the ± 1 is determined by whether the particle obeys Fermi statistics or Bose statistics (+ for fermions, - for bosons). The kinetic energy is K. Note that we have made factors of $\hbar$ and c explicit in this equation, and this continues to the end of the Section.

This approximation remains valid until the WIMP drops out of thermal equilibrium; that is, until the temperature reaches a freeze-out temperature T_f satisfying

$$\frac{d}{dT}\frac{n_0(T)}{T^3}\bigg|_{T=T_f} = 2b\langle\sigma v\rangle \frac{n_0^2(T_f)}{T^6}. \tag{2.15}$$

This can be taken as the definition of freeze-out temperature. For standard WIMPs, values are typically $T_f \lesssim 0.05 m_\chi$ [118]. After the freeze-out temperature is reached at time t_f, the annihilation term dominates the rate equation, leading to (where we have transformed back to the variable t again)

$$\frac{dn}{dt} + \frac{3n}{2t} = -\langle\sigma v\rangle n^2 \tag{2.16}$$

with the initial condition that $n(t_f) = n_0(T_f)$. This equation describes a cloud of particles in expanding space that are continually self-annihilating. After some time t_{eq} is reached, the annihilation rate becomes negligible and the expansion term begins to dominate. Equation (2.16) no longer holds, and the solution to the rate equation for $t > t_{eq}$ can now be written

$$n(t) = n(t_{eq}) \left(\frac{a(t_{eq})}{a(t)}\right)^3. \tag{2.17}$$

Defining the dimensionless variable $\zeta = m_\chi c^2/k_B T_f$, the LW condition (2.14) takes the form

$$\exp(\zeta) = \frac{2bk_B^2 m_\chi c^2}{\left(\sqrt{2\pi}\hbar c\right)^3} \langle\sigma v\rangle \frac{\sqrt{\zeta}}{\zeta - 3/2}. \tag{2.18}$$

Integration of Equation (2.16) over its range of validity from t_f to t_{eq} gives for GeV scale T_f:

$$n(t_{eq}) \simeq \frac{n(t_f)}{1 + 2n(t_f)\langle\sigma v\rangle t_f} \left(\frac{t_f}{t_{eq}}\right)^{\frac{3}{2}}. \tag{2.19}$$

In terms of ζ, t_f can be written

$$t_f = \frac{b}{T_f^2} = \frac{bk_B^2}{m_c hi^2 c^4}\zeta^2. \tag{2.20}$$

From the nonrelativistic limit of Equation (2.14) (which is valid for $T_f \ll m_\chi$), we can then write

$$n(t_f) = \frac{m_\chi^2 c^4}{2bk_B^2\langle\sigma v\rangle}\frac{\zeta - 3/2}{\zeta^2}. \tag{2.21}$$

Evolution of the number density from t_{eq} to the present time t_0 is expressed in terms of the expansion factor

$$n(t_0) = \frac{n(t_{eq})}{z_{eq}}. \tag{2.22}$$

The current energy density for single component dark matter can be expressed as

$$\varrho_{DM} = n(t_0)m_\chi c^2 \tag{2.23}$$

which we know from observation is equal to 1265 eV/cm^3.

Using (2.19) for $n(t_{eq})$, (2.21) for $n(t_f)$ and (2.20) for t_f gives

$$\varrho_{DM} = \frac{2\zeta - 3}{2\zeta - 1}\zeta\frac{k_B\sqrt{b}}{2\langle\sigma v\rangle t_{eq}^{3/2} z_{eq}^3}. \tag{2.24}$$

Between Equation (2.24) above and the LW condition (2.14), we have two equations for the three unknowns m_D, $\langle\sigma v\rangle$, and $\zeta \approx m_D/T_f$. By eliminating $\langle\sigma v\rangle$, we can obtain a condition that fixes the freeze-out temperature T_f for a given mass m_D:

$$m_D c^2 = \frac{\zeta - 1/2}{\zeta^{3/2}}\exp(\zeta)\frac{\varrho_{DM}}{C}. \tag{2.25}$$

where C is a numerical constant. The values obtained for T_f can then in turn be used to fix the cross section $\langle\sigma v\rangle$ for a mass m_D

$$\langle\sigma v\rangle_{Th}(T_f) = \frac{2m - 3T_f}{2m - T_f}\frac{2.075m \times 10^{-24}\text{cm}^3/\text{s}}{\varrho_{DM}\,[\text{eV/cm}^3]\,T_f}. \tag{2.26}$$

Usually, these constraints on the cross section are used to reduce the parameter space of the dark matter model, either by directly constraining the cross section or, in simpler models, by converting the cross section constraint into a constraint on the coupling. This is illustrated in Figure 2.2. The larger the annihilation cross section, the longer it takes for the WIMP to freeze out of the plasma, and the lower the predicted present day abundance. To match the observed current abundance therefore will require a specific thermal cross section, as quantified by Equation (2.26).

The thermally averaged annihilation cross sections $\langle\sigma v\rangle$ as functions of freeze-out temperature can be computed in a number of ways. In this thesis they are computed using the integral expression of Gondolo and Gelmini [119, 120]:

$$\langle\sigma v\rangle(T_f) = \frac{1}{8m^4 T_f K_2^2(m/T_f)}\int_{4m^2}^{\infty} ds\sigma(s)K_1\left(\frac{\sqrt{s}}{T_f}\right)\sqrt{s}\left(s - 4m^2\right). \tag{2.27}$$

In this expression $K_1(x)$ and $K_2(x)$ are the modified Bessel functions of the first and second order respectively. The mass m is the mass of the annihilating particle and the relativistic cross section as a

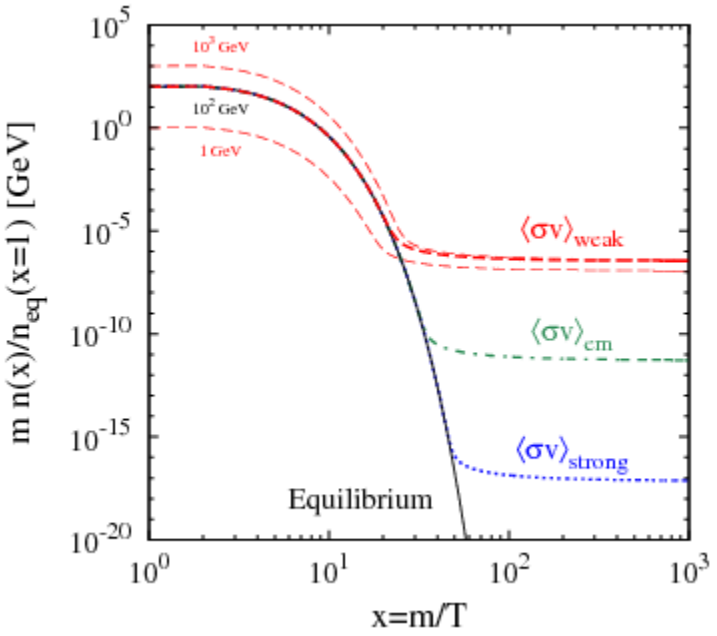

Figure 2.2: Freeze-out of thermal dark matter for various values of the annihilation cross section $\langle\sigma v\rangle$. Larger cross section values lead to the WIMP dropping out of thermal equilibrium later and having a smaller abundance at the present time. Image from [118].

function of the Mandelstam variable s is $\sigma(s)$. Note that this expression is not valid if the dominant part of the cross section is not a function solely of the center of mass energy squared s, which is a consequence of certain variable choices made in the derivation. There is no equivalent expression for t or u channel dominated annihilation cross sections. While many models can get away with considering only s-dependent annihilation cross sections, exceptions are not difficult to find. For an example, see Section 2.4, where the Higgs-portal model requires some additional care in certain regions of the parameter space.

Evaluation of this integral will generally need to be done numerically for all but the most trivial cross sections. If the cross section has resonances, care must be taken with the numerical treatment, but most adaptive quadrature routines are capable of handling singularities of that kind. It is more dangerous when the cross sections are not unitary, and increase without bound as s increases, as is occasionally the case in partially complete models. In such models, the field theory is not wholly internally consistent by design, which allows for embedding in higher energy theories.

If the annihilation cross sections violate unitarity, the integral may diverge. In this case, the velocity expansion method of thermal averaging [121] will prove more useful. The velocity weighted cross section can be expanded in powers of velocity squared, and the resulting series can be truncated and thermally averaged. This method is useful in some situations such as the unitarity violating scenario mentioned above or the case of annihilation cross sections that depend on not only s, and allows one to avoid the potentially troublesome integral, but will break down when the expansion is no longer valid. The expansion will typically fail near resonances in the annihilation cross sections or near thresholds, where new annihilation channels

open. However, in these regions, the integral becomes more difficult to evaluate as well.

By far the most commonly considered mechanism for the production of particle dark matter in the early universe is freeze-out, which gained popularity due to the WIMP miracle, as discussed above. However, WIMP dark matter is strictly constrained, and for certain models these constraints are quite strong. In many cases, the particle physics model cannot accomodate WIMP dark matter. The freeze-out scenario also only allows a certain range of masses and couplings near the weak scale. Now that the SUSY neutralino no longer enjoys overwhelming popularity as a dark matter candidate, the attachment to the weak scale interactions is much weaker, though it is still quite phenomenologically attractive. The weak scale is, of course, an energy region within the reach of our current experiments.

There are a number of alternative production scenarios that have been discussed in the literature, many of which are discussed frequently enough to obtain their own acronyms [122]. One such alternative scenario for the thermal production of dark matter in the early universe is known as the 'freeze-in' scenario [123], and the particle that freezes in is known as a Feebly Interacting Massive Particle (FIMP). We consider the FIMP here briefly as an alternative to the WIMP. The basic premise behind FIMP freeze-in is that the dark matter particle is not in thermal equilibrium with the primordial plasma. The FIMP interacts very weakly, and never achieves the number density required to self-annihilate. The FIMP number density thus obeys a slightly different Boltzmann equation than the one obeyed by the WIMP number density, where no annihilation term is present. Production from the thermal plasma proceeds as usual, increasing the number density, until the universe cools enough that the production process can no longer occur. At this point the FIMP number density remains roughly constant, leading to the descriptive name of the process being freeze-in.

FIMP models are generally as simple and predictive as WIMP models, but by virtue of the small interaction strength, tend to be out of phenomenological reach. This is both a curse and a blessing, as they cannot be observed, but they also cannot be excluded. FIMP dark matter is generally most useful in a model that predicts a very weakly interacting stable particle for other reasons. The FIMP scenario can then be used to provide an additional constraint on the model. For a simple example of the application of the scenario to Higgs-portal scalar dark matter, see reference [124].

2.4 Example - Higgs-portal scalars

If one makes the assumption that the entirety of observed dark matter is made up by a single species, one can use the observed abundance to constrain the parameter space of the model. In the case of simple models, such as the Higgs-portal scalar (fully detailed in Appendix B), the reduction of the parameter space can be very useful. The Higgs-portal scalar model of dark matter, in its simplest form, extends the SM by only two additional parameters: the mass of the new scalar field m_S, and its coupling to the Higgs boson η_S, called the Higgs-portal coupling. By applying the constraint that Higgs-portal scalars make up all of the current

abundance of dark matter, we can constrain one of these parameters (usually η_S) in terms of the other.

The thermally averaged annihilation cross section required of the WIMP for it to account for the observed thermal abundance appears in Equation (2.26). We note that our result agrees with the approximate general results of reference [118], of $\sigma v \sim 2.2 \times 10^{-26}$ cm^{3}s^{-1}.

If we assume the dominant component of the Higgs portal scalar annihilation cross section are proportional to η_S^2 (which they are when s-channel processes dominate, which is in turn true in the perturbative regime), one can use the different expressions for the thermally averaged cross section to extract an explicit constraint on η_S^2. By forming a ratio of the expressions in Equations (2.27) and (2.26), one has obtained a ratio of the difference between the particle physics model prediction (Equation (2.27)) and the observational constraint from the abundance on the WIMP annihilation cross section (Equation (2.26)), which leads to a constraint on η_S^2:

$$\eta_S^2 = \frac{\langle \sigma v \rangle_{Th}}{\langle \sigma v \rangle / \eta_S^2}. \tag{2.28}$$

As both the expressions for the cross section depend only on the mass of the scalar m_S, Equation (2.28) is an expression for an η_S^2 that satisfies the observed abundance constraint in terms of m_S.

Figure 2.3 plots the thermally constrained values for η_S^2 as obtained from the ratio in Equation (2.28) against the mass of the Higgs-portal singlet for a mass range of phenomenological interest.

Note that this treatment requires that the dominant part of the annihilation cross section is proportional to η^2, which means only s-channel (or pointlike) processes are significant. For scalar Higgs-portal models this may not be the case, as the full annihilation cross section to Higgs bosons includes contributions from u and t-channel processes (the Mandelstam variables u and t are defined in Equation (1.5)), which are typically subdominant and thus neglected:

$$\begin{aligned}\sigma_{SS\to hh}(s,t,u) = \frac{1}{16\pi s}\sqrt{\frac{s-4m_h^2}{s-4m_S^2}}\Bigg[\eta_S^2\left(\frac{6v_h^2 m_h^2}{s+m_h^2} - \frac{v_h^2}{4} - \frac{36 m_h^4 v_h^2}{s^2+m_h^4+m_h^2\Gamma_h^2}\right) \\ +\eta_S^3\frac{v_h^3}{4}\left(\frac{1}{t+m_S^2}-\frac{1}{u+m_S^2}\right)\left(\frac{1}{4}+\frac{3m_h^2}{s+m_h^2}\right) - \eta_S^4\frac{v_h^4}{16}\frac{u-t}{(t+m_S^2)(u+m_S^2)}\Bigg].\end{aligned} \tag{2.29}$$

These contributions go like η^4 or η^3 for interference terms, and can be safely neglected in the highly perturbative regime. For convenience, the Mandelstam variables t and u are included in Chapter 1, where notations and conventions are established. However, when the theory becomes less perturbative, and the subdominant contributions begin to have significant effects, this treatment is no longer valid. Figure 2.4 shows the thermally constrained coupling up to above 30 TeV to illustrate that, at some mass value, the coupling will reach the point where perturbation theory formally breaks down, at $\eta_S = 4\pi$. This occurs as approximately $m_S =$ 27.5 TeV. Of course, higher order terms will begin to have significant effects far before that point, and would need to be taken into account to obtain any meaningful predictions, and the full annihilation cross section to Higgs bosons 2.29 would need to be used to find the abundance. We note as well that this also occurs near

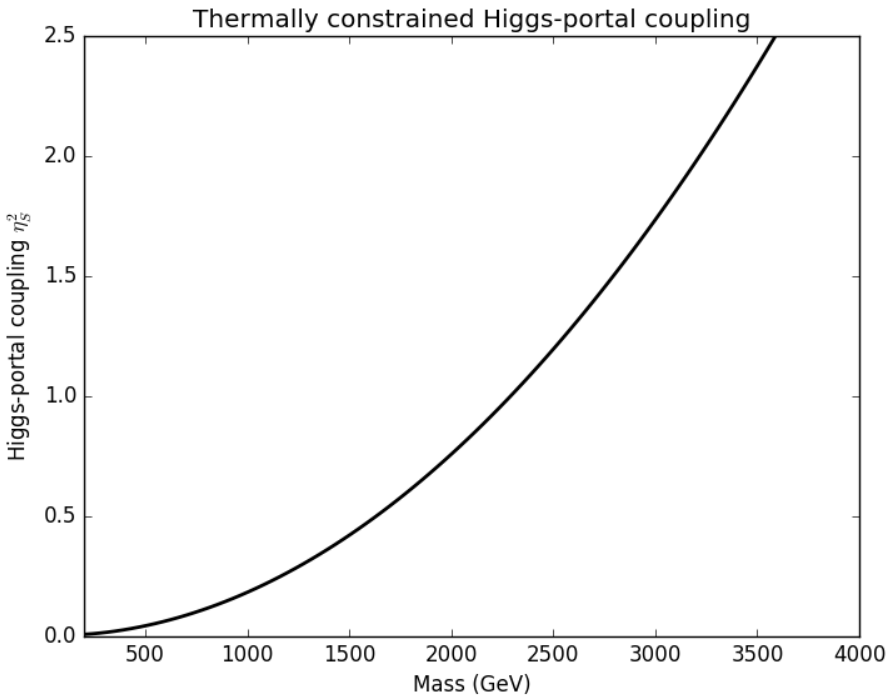

Figure 2.3: The thermally constrained Higgs-portal coupling η_S for scalar Higgs-portal dark matter, as a function of dark matter mass for the range m_S =200 GeV to 4000 GeV. Values obtained from Equation (2.28).

the resonance that occurs when $m_S = m_h/2$. Near this point as well, the approximations we have employed in our treatment of the thermal relic calculations break down.

It is important to remember that the cross sections that go into the thermal average (2.27) are only some finite number of terms in the perturbative expansion, and are approximations to the full cross sections. In fact, only the leading order term is typically used. A natural question to ask to ask is whether or not higher order contributions to the cross section have any effect on the solution to the Boltzmann equation. Because the cross section enters the Boltzmann equation linearly, we expect the perturbative expansion to apply to the solution to the Boltzmann equation as well, but with the additional effect of the velocity weighting and thermal averaging it is worth looking into. Additionally, the annihilation processes are taking place in an active thermal background, which means that one should take thermal effects into account at the 1-loop level and beyond. This amounts to performing the calculation using the formalism of thermal field theory or finite temperature field theory [125, 126].

These calculations have been done for the case of the minimal SUSY WIMP [127, 128], and show that the effects of NLO and finite temperature corrections are small in comparison to theoretical and experimental uncertainties and so can be ignored. While it is not rigorous, dark matter models tend to be similar enough that it is probably safe to assume a simple WIMP model like the scalar Higgs-portal model has similar finite temperature corrections. There has also been work that verifies the Boltzmann formulation is still valid when formal aspects of the quantum field theory are taken into account in a thermal environment [129]. This

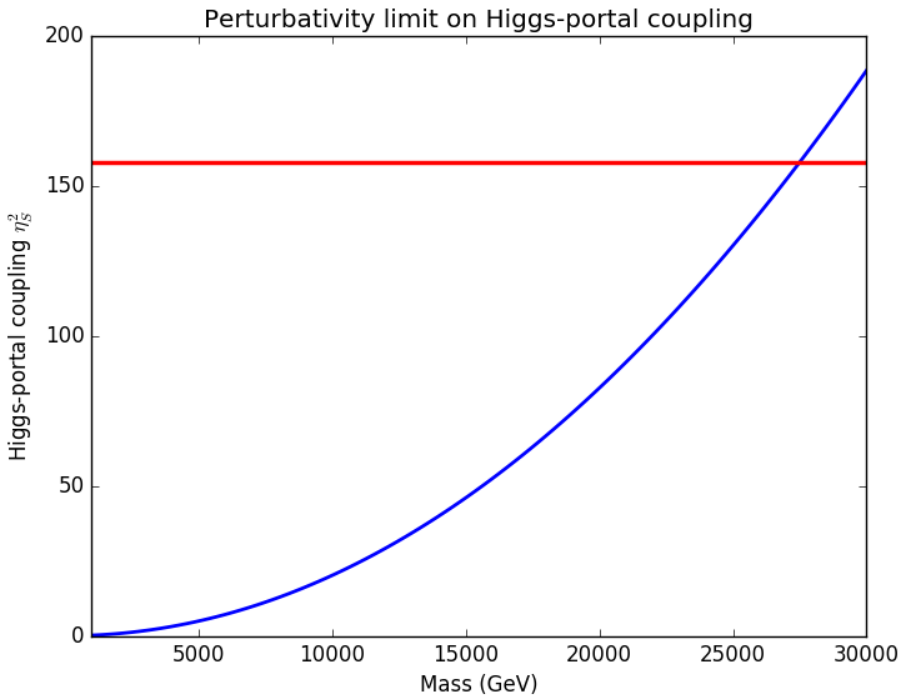

Figure 2.4: The thermally constrained Higgs-portal coupling η_S compared against the perturbativity bound of $16\pi^2$. The coupling crosses over the bound at $m_S \sim 27500$ GeV, though perturbative approximations will lose their predictive power far before that point, as well as the thermal constraint breaking down.

includes the effects of the IR divergences that result from soft and collinear terms in the process, which are important effects to consider when evaluating the validity of calculated results.

Chapter 3

Direct Detection of Dark Matter

The primary means of searching for particle dark matter is through direct detection. The basic principle is one of a passive detector in an external particle flux, in this case the ambient dark matter in the galactic halo. The detector is a volume of some responsive material, and one looks for atomic nuclei in the target volume recoiling from something that is not observed. This is the expected signal of particle dark matter, and by observing the behaviour of the recoiling nucleus, certain properties of the dark matter particle can be inferred. Direct detection measurements, which have not to this date been confirmed, would give valuable information about dark matter masses and interaction strengths with SM matter. This Chapter describes the basic physics behind direct detection and remarks briefly on the current status of the field.

To confirm the presence of a signal, a detailed understanding of the entire system is required, from the level of particle physics through hadronic and nuclear physics, materials physics, and up to astrophysics. This Chapter cannot be exhaustive in its discussions, but missing details can be found in the extensive references. In Section 3.1, we review the fundamental concepts behind the calculation of event rates in a dark matter direct detection experiment. Section 3.2 contains a brief discussion of the experiments that are currently taking data, as well as some in the construction or planning phases. The current state of dark matter direct detection is summarized in Section 3.3, and the techniques of the Chapter are applied to the example of scalar Higgs-portal dark matter in Section 3.4.

3.1 Event Rates

A direct detection experiment is passive, counting events over time. The rate of fundamental interactions per unit time is called the event rate R, and measurement of this quantity for WIMP interactions with atomic nuclei is the goal of the direct detection experiment. It is estimated that the local flux of WIMPs is $\sim 10^5 \ (100\,\mathrm{GeV}/m_{DM}) \ \mathrm{cm}^{-2}\mathrm{s}^{-1}$. Direct detection experiments attempt to measure the scattering of this flux of WIMPs from the detector nuclei.

The basic techniques required to compute an expected event rate for a model of WIMP dark matter are not particularly complicated, but the details are fraught with uncertainties from a variety of sources. An experimental collaboration will compute an expected event rate under certain assumptions, and then compare the expected rate against the observed event rate. When no events are seen, as is typically the case, these

expected rates are used to place upper bounds on a possible physical event rate at some statistical confidence. Bounds on event rates can then be converted into bounds on generic or model-specific nuclear recoil cross sections or other parameters. This Section reviews how an expected event rate is calculated for a standard direct detection experiment.

3.1.1 Basic recoil physics

The differential event rate with respect to the recoil energy E_R per unit volume is [130]

$$\frac{dR}{dE_R} = \frac{\rho_0}{m_A m_{DM}} \int_{v_{min}}^{\infty} dv \left[v f(v) \frac{d\sigma_{NR}}{dE_R}(v, E_R) \right]. \tag{3.1}$$

The cross section $d\sigma_{NR}/dE_R$ is the differential nuclear recoil cross section with respect to recoil energy, which is dependent on the particle physics model of dark matter. Velocities are small enough (on the order of hundreds of km/s) that this cross section should be computed in the nonrelativistic limit. The velocity distribution of the dark matter flux in the frame of the detector as it passes through the detector volume is $f(v)$, and is discussed further in Section 3.1.4. The masses m_A and m_{DM} are the nucleus mass and dark matter mass respectively, and ρ_0 is the local dark matter energy density. Since ρ_0/m_{DM} gives the local dark matter number density, this is essentially a count of the dark matter particles passing through the detector. Results are typically reported in units of $\text{kg}^{-1}\text{day}^{-1}\text{keV}^{-1}$. Simple inspection of Equation (3.1) indicates that larger dark matter masses and small interaction cross sections combine to create a very low event rate. For a generic model, event rates generally go like $1/m_{DM}$.

The lower bound of integration is the minimum velocity v_{min}, which is the dark matter particle velocity associated with the minimum energy that will cause a recoil of energy E_R

$$v_{min} = \sqrt{\frac{2E_{min}}{m}} = \sqrt{\frac{m_A E_R}{2\mu_A^2}}. \tag{3.2}$$

Recoil energies for elastic scattering of dark matter masses in the range 10-1000 GeV are expected to be in the 1-100 keV range [130]. Event rates are $\sim 1/100\text{kg} \cdot \text{day}$. The recoil energy can be related to the momentum transfer q^2 between the dark matter particle and the nucleus through [130]

$$E_R = \frac{\mu_A^2 v^2 \left(1 - \cos\theta^*\right)}{m_A} = \frac{q^2}{2m_A}, \tag{3.3}$$

where θ^* is the scattering angle in the center of mass frame and $\mu_A = m_{DM} m_A / \left(m_{DM} + m_A\right)$ is the reduced mass of the WIMP-nucleus system.

Integration of Equation (3.1) over recoil energy E_R yields the event rate

$$R = \frac{\rho_0}{m_N m_{DM}} \int_{E_T}^{\infty} dE_R \int_{v_{min}}^{\infty} dv \left[v f(v) \frac{d\sigma_{NR}}{dE_R}(v, E_R) \right], \tag{3.4}$$

where E_T is the threshold energy of the detector. Below the threshold energy, not enough momentum is transfered during the recoil event to register in the detector.

This part of the calculation is well understood, but the next Sections address the effects of nuclear physics, particle physics, and astrophysics on the event rate. These effects introduce most of the uncertainties and assumptions required for event rate calculations.

3.1.2 Recoil cross sections

The particle physics and nuclear physics contributions to the event rate enter through the quantity $d\sigma_{NR}/dE_R$, the differential nuclear recoil cross section, which is the microscopic quantity describing the recoil event. A nuclear recoil cross section can be divided into two parts, labelled by whether or not they interact with the spin of the nucleus. The part of the cross section that does not interact with nuclear spin is the spin independent (SI) part, while the part that depends on nuclear spin is the spin dependent (SD) part.

$$\frac{d\sigma}{dE_R} = \left(\frac{d\sigma}{dE_R}\right)_{SD} + \left(\frac{d\sigma}{dE_R}\right)_{SI} \tag{3.5}$$

For values of momentum transfer q such that the particle wavelength is comparable in size to the nuclear radius, the cross section σ will drop as q increases. Dependence on the recoil energy can be factored out for small values of momentum transfer q, and the above expression can be written in terms of the zero momentum transfer (fully nonrelativistic) cross sections $\sigma_0^{SI,SD}$ and recoil energy dependent form factors $F_{SI,SD}(E_R)$, which are discussed further in Section 3.1.3:

$$\frac{d\sigma}{dE_R} = \frac{m_A}{2\mu_A^2 v^2}\left(\sigma_0^{SI} F_{SI}^2(E_R) + \sigma_0^{SD} F_{SD}^2(E_R)\right). \tag{3.6}$$

In Equation (3.6), the quantities σ_0^{SI} and σ_0^{SD} are the zero momentum transfer limit cross sections for WIMP-nucleus scattering, in the spin independent and spin dependent cases, respectively. This scattering is usually a tree level effect, though that is not always the case, and is typically a t-channel process. The calculation of the cross section is usually straightforward, but depending on the model there may be a number of contributions.

For the spin independent case, the cross section can further be simplified, and expressed at the level of a WIMP-nucleon scattering cross section:

$$\sigma_0^{SI} = \sigma_p \frac{\mu_N}{\mu_p}\left(Z f_p + (A - Z) f_n\right)^2 \tag{3.7}$$

where μ_p is the reduced mass of the WIMP-proton system, Z is the charge number of the nucleus, and A is the atomic mass number of the nucleus. The factors f_n and f_p are the 'WIMP charges' of the neutron and proton, respectively. For most models, $f_n = f_p$ and the spin independent nuclear cross section scales with the proton cross section like $\sigma_N \simeq A^2 \sigma_p$ for a nucleus of atomic mass number A. This is because the scattering is mostly coherent for q smaller than the nucleus size, as is the case for nonrelativistic scattering. It is in terms of these WIMP-nucleon cross sections are how experimental collaborations typically report their results.

As mentioned above, it is generally assumed that $f_p = f_n$ and that the dark matter couples the same to both protons and neutrons, but models of isospin-violating dark matter have been studied [131].

The above analysis is also specific to the case of elastic scattering. For inelastic scattering, where the dark matter can absorb some of the recoil energy and become somehow excited or the nucleus itself becomes excited, the situation changes [132, 133, 134]. Inelastic dark matter is treated generically through the use of parameterizations that affect the kinematics terms in the cross section and the minimum velocity in the event rate. Several direct detection experiments have considered inelastic dark matter signals [135, 136, 137, 138]

The matrix element of an interaction between a dark matter particle and a SM fermion (usually a quark or nucleon) can be factorized in terms of Dirac structure:

$$O = \Gamma_{DM}\Gamma_{SM}F(s,t,u) \tag{3.8}$$

The terms Γ_{DM} and Γ_{SM} represent Dirac bilinears characterized by the Lorentz structure of the interaction on the dark matter side and the SM side, respectively. The scalar function F is a form factor parameterizing the interaction depending on the Mandelstam variables s, t, and u. It will also contain the particle model details, such as the coupling values and mediator propagator, and the nuclear form factors. The form factor will be constant for a pure contact interaction.

These operators behave differently in the nonrelativistic limit, which leads to contributions of different orders of magnitude. The simplest example is nuclear spin dependence, but different operators can be suppressed by one or more powers of relative velocity or momentum transfer (which are very small in the nonrelativistic limit), leading to very small cross sections. For some models, however, these highly suppressed contributions are in fact dominant. A highly detailed discussion of these operators is given in reference [139], including conveniently tabulated results.

The spin dependent part of the cross section can be written in terms of nuclear spin J_N

$$\sigma_N^{SD}(E_R) = 32\mu_A^2 G_F^2 \left[\frac{J_N+1}{J_N}\right] \left[\langle S_p\rangle a_p + \langle S_n\rangle a_n\right]^2 F_{SD}^2(E_R) \tag{3.9}$$

where the Fermi constant is G_F and μ_A is the reduced mass of the WIMP-nucleus system. The a_n and a_p are effective couplings to the neutron and proton, and the expectation values are of nuclear spin operators. Spin dependent form factors are moderately complicated, typically split into isoscalar and isovector components, and require several experimental inputs [140, 55]. Taking the nonrelativistic limit of this cross section yields the velocity dependence through the spin operator expectation values as fully detailed in references [140, 139]. Because of this velocity dependence, spin dependent cross sections are typically smaller than spin independent cross sections. Combined with the weaker bounds, which will be discussed in Section 3.3, this makes spin dependent cross sections of use only for those models which have highly suppressed spin independent cross sections (see Chapter 6 for examples from the literature with spin-1 mediators).

3.1.3 Nuclear physics effects

The nuclear form factors appearing in Equation (3.6) parameterize the response of the atomic nucleus to the scattering event. In the $q^2 \to 0$ limit, spin independent scattering is coherent, allowing the parameterization

in terms of form factors. The standard paramterization for the spin independent form factor is the Helm form factor [141]

$$F_{SI}^2(E_R) = \left(\frac{3j_1(qr_0)}{qr_0}\right)^2 e^{-s^2q^2} \tag{3.10}$$

where $q^2 = 2m_N E_R$ and $j_1(qr)$ is the first order spherical Bessel function

$$j_1(qr) = \frac{\sin(qr) - qr\cos(qr)}{(qr)^2} \tag{3.11}$$

and s is the nuclear skin thickness of ~ 1fm. The effective nuclear radius r_0 can be approximated by

$$r_0 \simeq \sqrt{\left(1.2 \text{ fm } A^{1/3}\right)^2 - 5s^2}. \tag{3.12}$$

The form factors act to further suppress the already small event rate.

There have also been studies of the possibility of electron recoil dark matter search experiments [142, 143, 144, 145], where the dark matter particle interacts preferentially with electrons. For some time this has been considered as a possible solution to the discrepancy between the DAMA annual modulation searches and the nonobservation of a signal from the remainder of the direct detection experiments [143], though recent results seem to disfavor this explanation [146]. This situation is further discussed in the context of the experimental results in Section 3.3.3.

3.1.4 Astrophysical parameters

The event rate is proportional to the local dark matter energy density ρ_0, which is usually taken to be the canonical value of 0.3 GeV cm^{-3} [147]. The dark matter density is not strongly constrained, however, and a range of values have appeared in the literature [148], different by factors of up to 3. Due to the strong effect of the local dark matter density on the event rate, understanding ρ_0 and any errors associated with it is of paramount importance when interpreting the results of direct detection experiments.

Dark matter in the galactic halo is assumed to have a Maxwellian velocity distribution, given by

$$f(\mathbf{v}) = \frac{1}{\sqrt{2\pi}\sigma_v} \exp\left(\frac{-|\mathbf{v}|^2}{2\sigma_v^2}\right) \tag{3.13}$$

where $\sigma_v = \sqrt{3/2}v_c$ is the standard deviation, and $v_c = 220$ km/s is usually used [149]. Practically, the integral over velocity in Equation (3.1) is truncated on the upper end at the escape velocity of the galaxy, which is usually taken to be 544 km/s from observations made by the RAVE survey [150], though there are statistical uncertainties present.

While the velocity distribution taking Maxwellian form is an assumption, it is a well justified approximation. Particle dark matter is nonrelativistic and highly diffuse, as well as being very weakly self-interacting, making contact induced deviations from a Maxwellian distribution negligible. A more likely cause of deviations would be the dark matter halo not being isotropic, which is indicated to some extent by both observations and numerical simulations. Of particular interest are the triaxial models [151, 152].

3.1.5 Directional searches

Aside from the standard directionless searches, a new type of experiment exists that aims to retain information about the direction of the nuclear recoil, allowing more information about the dark matter distribution and the kinematics of the interaction to be extracted. These searches are called directional searches, and they have somewhat different event rates.

Differential event rates in a directional detector go like [153]

$$\frac{dR}{dE_R d\cos\gamma} \sim \exp\left\{-\frac{\left[\left(v_E + v_\odot\right)\cos\gamma - v_{min}\right]^2}{v_c^2}\right\} \tag{3.14}$$

The halo circular velocity is defined to be $v_c = \sqrt{3/2}v_\odot$. The angle γ is between the recoil and the mean direction of solar motion within the galactic halo. A more detailed expression for the event rate appears in reference [154]. As can be seen from the above expression, the integrated rate of scattering events in the forward direction will exceed those in the backward direction by an order of magnitude [153]. This also allows for exceptional background discrimination [155]. Some further details about the experimental aspects of directional searches are included in Section 3.2.2.

We discuss directional searches here only to provide some perspective about what the future of direct detection as an experimental field is headed. We do not use directional searches in any of the phenomenology sections.

3.2 Direct detection experiments

This Section will discuss some important aspects of the experimental side of dark matter direct detection. A basic understanding of how the experiments work is a crucial part of proper dark matter phenomenoloy. There are a number of review articles that exist, though due to the fast progression of the field they tend to become out of date within less than a decade. This Section can be supplemented by references [156, 157] and in particular reference [158], which has been consulted extensively. For reference, a list of dark matter direct detection experiments has been included in Table 3.1, along with some details about their materials, detection channels, and years of operation.

3.2.1 Detection channels

After a scattering event has occurred within the detector volume, it must be observable by the detector instruments in some way. There are three basic mechanisms by which the experiment can register that a nuclear recoil has occurred. The energy deposited by the recoil disperses into the surrounding medium, and can be measured as phonons (or heat in a gas), photons, or electrons.

Phonons are quantized acoustic waves on a lattice, the quantum analogue of an acoustic wave in a gas. They are a common way for energy to propagate through a solid state medium. The recoil could also excite the

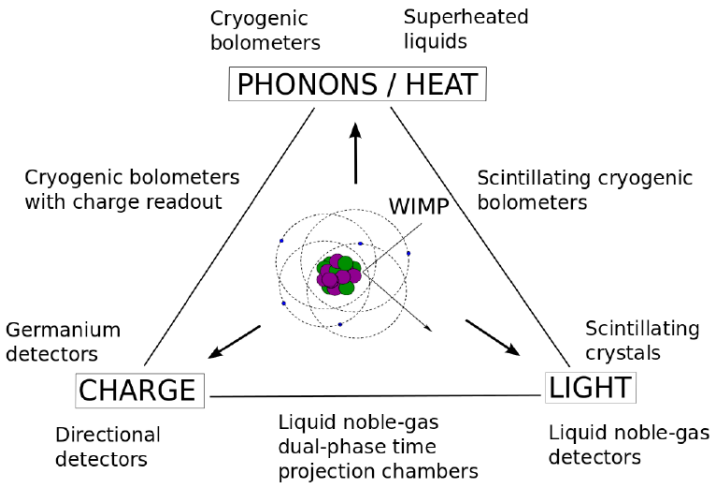

Figure 3.1: Detection channels for direct detection of particle dark matter, including dual-channel systems. Image originally appears in [158].

nucleus, which would then emit a scintillation photon as it fell back into the ground state. Depending on the material, 1-10% of the recoil energy can become scintillation photons [158]. As well, the recoil could ionize the atom, causing an electron to carry off some of the recoil energy. Electrons ionized by nuclear recoils propagate through the medium and further ionize it, and these charges can be collected by an external electric field, allowing reconstruction of the original recoil. These three signals are more or less easy to observe depending on what the detector material is. Experiments will rely on one, or use two in such a way that they can complement each other and provide additional information about the event. These dual channel detectors have better background discrimination, in particular being able to tell whether an event was an electron recoil or a nuclear recoil due to the different features of the recoil across the channels. For example, electron recoils can be distinguished from nuclear recoils by the ratio of scintillation energy to phonon energy in a dual-channel detector.

These detection channels have influenced the choice of target materials, as is discussed in Section 3.2.2. Ionization can be used in crystal detectors constructed of semiconductors such as germanium, and also in low pressure gases such as those in directional detectors. Scintillation can be used in certain crystals, as well as being the primary mechanism in noble liquid detectors. Acoustic waves are detectable in superheated gases and as phonons in semiconductor crystals. Several of the noble liquid collaborations have included a layer of noble gas above the liquid bulk which allows use of the ionization signal as well, creating a dual-phase detector [159, 160, 161, 162]. This is discussed further in Section 3.2.2. These different channels are summarized in the schematic that appears in Figure 3.1.

3.2.2 Detector materials

The materials chosen to construct the detectors are chosen because they satisfy certain requirements for signal generation and propagation. Heavier WIMPs will require heavier target nuclei to generate a signal,

while for light WIMPs, the event rate above the detector threshold may be small, due to the exponential decay of the energy spectrum with increasing recoil energy. Threshold energies are typically 5-40 keV. A lower threshold energy naturally allows an increased event rate. This Section discussed several classes of detector material, including their uses and drawbacks, as well as what channels they allow.

Semiconductor crystals

The original dark matter direct detectors were repurposed from neutrinoless double beta decay experiments. Because the technology was fairly well developed and the expertise existed, the majority of early direct detectors were crystal based. Crystal detectors lend themselves to all three detection channels, depending on the species of crystal.

Perhaps the most common material used for solid state detectors is germanium (Ge), which is usually used as a scintillator. In fact, the first limits on nuclear recoil signals of dark matter were obtained in 1987 using a germanium ionization detector [163]. Germanium, when cooled, has a low threshold energy for excitation, which allows for probing lower mass regions, and lends itself to good energy resolutions, which allows for better identification of background events. Germanium is also exceptionally radio-pure, reducing internal backgrounds, which will be discussed in the next Section.

Aside from the pure germanium detectors, there are also the cryogenic bolometers, composed of a variety of materials, which rely primarily on phonon signals. Because phonons have no lower energy limit, a phonon signal has very low energy thresholds and a good energy resolution. Measurement of these phonons generally occurs by connecting the detector to a thermal bath through which temperature changes can be detected. These detectors will frequently also use a charge or scintillation signal, with the energy dependence of how the secondary signal quenches being used to discriminate between nuclear and electron recoils.

Noble liquids

Noble liquid detectors are those whose detector material is a volume of the liquid phase of a noble gas, usually xenon or argon, though neon is being considered [164]. These detectors have a few advantages. Noble liquids have a very high scintillation and ionization yield compared to other detector target candidates. As the liquids are highly homogenous, they allow a considerably simplified detection analysis. As well, an outer layer of the detector volume can be used as a high density liquid shield, and events within the shield volume are neglected, leaving the interior volume of the detector (the fiducial volume) as the actual detection space. Common xenon isotopes tend to be spin sensitive, allowing the detector to probe both spin independent and spin dependent interactions. Noble liquid nuclei are heavy, which makes them suited for probing larger WIMP mass ranges.

The simplest noble liquid detector will only detect scintillation photons using photomultiplier tubes at the edge of the tank. These detectors typically use a method called pulse-shape discrimination to distinguish between electron recoils and nuclear recoils, where the different response of the excited states to different

recoils is measured. More modern dual-channel designs, however, can capture the ionization signal as well [165]. The primary scintillation signal is used to set the energy scale for particle interactions, while the ionization signal allows discrimination between electron recoils and nuclear recoils. The ionized charge either immediately recombines to produce more scintillation light, or is extracted by applying an electric field across the liquid target, which causes the charge to drift to an end of the tank. There, they leave the liquid and are accelerated through a layer of gaseous phase detector material, which generates a secondary scintillation signal that can be measured. Because of the presence of both the gaseous phase and the liquid phase of the same noble element, detectors of this type are often referred to as dual-phase detectors. For a detailed analysis of nuclear recoils in liquid xenon, see [166].

Superheated gas

The basic principle behind the superheated gas dark matter detector is the same as the one behind the old bubble chamber experiments of the early days of particle physics. The target material is a gas that is superheated to slightly below the boiling point. Recoil interactions deposit a tiny amount of energy, which induces a local phase transition, causing bubbles to appear. These bubbles can then be observed, and details about the interaction can be inferred from their behaviour. Of course, the recoil energy must be large enough to create a bubble. Events are recorded using CCD cameras, and the bubble location can be determined to mm accuracy. The detector must be rested to the initial state after every event, making operation somewhat more expensive than the more passive noble liquid detectors.

The high temperature of the detector renders the thermal backgrounds that trouble low temperature detectors irrelevent. However, alpha particles and neutrons still pose problems, and need to be dealt with in the standard ways (See Section 3.2.3). Acoustic signals can be used to discriminate against alpha particles [167], but neutrons remain troublesome.

Superheated fluid detectors are not competitive for spin independent cross section bounds, but are very competitive for spin dependent bounds. The PICO experiment in particular provides some of the current strongest spin dependent limits [168].

Directional search experiments

The physics of directional dark matter searches was described in Section 3.1.5. This Section provides an overview of the experimental aspects of these searches. The basic principle behind the directional search is that the recoil track of the nucleon is measured, which allows information about the kinematics of the scattering event to be obtained. The detectors are ionization-based, where a nuclear recoil causes ionization charge, which is caused to drift to the edge of the detector by a homogenous electric field. The recoil can then be reconstructed. The lengths of the tracks produced by the charged particles can be used to distinguish between nuclear and electron recoils, as the electron tracks re about ten times longer.

The detectors are gaseous time projection chambers [169, 170, 171], in which the gas is both the detector

and the target material. Gases that have been used include CS_2 and CF_4 [172] among others. Many directional detectors use a mixture of gases to exploit their different properties. For example, ions of one gas drift differently from ions of another, which allows further inference about the recoil event depending on which ions are collected.

Novel designs

There are also several experimental designs that do not neatly fit into the above categories and are still in the planning phase. These systems are still untested, but are promising. We discuss each of these briefly.

Solid xenon has been considered [173]. The solid state has the advantage of increased light collection in comparison to the liquid phase, as well as allowing much faster electronic drift speeds. Because the detector would be solid, a phonon signal could also be studied, leading to a possible triple channel detector. Obviously, maintaining the solid state is a technological hurdle.

The DAMIC [174] collaboration is examining the possibility of a detector constructed of silicon CCDs. Such a detector would have extremely low energy thresholds due to the lack of electronic noise, which would allow the probing of very low WIMP mass ranges. NEWS [175] is a spherical gas detector intended to probe low mass regions of the WIMP parameter space as a nonstandard bubble chamber.

3.2.3 Backgrounds

Direct detection experiments look for signals on the order of a few keV, which renders them exceptionally susceptible to false signals from background radiation. In the energy range expected of a WIMP recoil, an unshielded germanium detector would have an event rate of around $10^4\,\mathrm{keV}^{-1}\mathrm{kg}^{-1}\mathrm{day}^{-1}$ [156]. Background particles that can produce signals similar in shape to that expected of a WIMP, and therefore are important to consider, are gamma rays, neutrons, and neutrinos. In general, neutrons are the greatest problem. Neutrinos are mostly irrelevant, however see Section 3.3.4 for a discussion of what happens when neutrinos do become important. Background fluxes can be divided into two general kinds: those from sources external to the detector, and those from internal sources. External backgrounds are more or less the same for every detector, but internal backgrounds depend on the detector material and the construction parameters of specific experimental setups. The number of measured background events will scale with target mass, and detectors using heavier elements need to account for this as well.

There are a handfull of ways to deal with backgrounds. At the physical level, there are different kinds of shielding that can be used, and certain kinds of event tagging that allow discrimination between background and signal events. This tagging can be done through precise measurement of a specific parameter, for example electron recoils or multiple scattering events, which are not expected of WIMPs. Also, known backgrounds can be subtracted from the signal, but this requires a very good understanding of said backgrounds, typically obtained through extensive calibration runs. Calibration runs usually expose the detector to a radioactive source with an understood output, and compare recorded event rates with Monte Carlo simulations of the

source and known backgrounds. Looking for annual modulation signals (Section 3.3.3) is also a way to separate signal from background. Directional detectors, as discussed in Section 3.2.2, are able to use the diurnal modulation of the flux to separate signal from background.

For a detailed discussion of background radiation in dark matter direct detection experiments, see reference [176]. Uncertainties in the astrophysical inputs to the analysis lead to difficulties in background analysis, but ways of compensating for these uncertainties is being studied [177, 178].

External backgrounds

External gamma ray backgrounds come mostly from the decay of naturally occurring uranium and thorium, as well as some less common isotopes such as potassium and cobalt, in the surrounding material. These gamma rays strike the detector bulk and cause photoelectric effect events, Compton scattering, and production of e^+e^- pairs. This background can be reduced by taking care when obtaining construction materials, but cannot be avoided completely. The remainder is reduced by shielding with lead or water, which can reduce background induced events by 4-5 orders of magnitude. An analysis technique that is used to discriminate against the charged products of these gamma ray interactions is to veto multiple scattering events, as a WIMP is highly unlikely to multiply scatter. Noble liquid experiments can also use self-shielding to reduce these effects, as described in the discussion of fiducial volumes above.

External neutrons interact with nuclei in the detector bulk through elastic scattering, which produces a recoil signature that is nearly identical to that of a WIMP. Neutrons can be produced by the interaction of high energy cosmic ray muons with surrounding material, and those produced in this way can have energies of up to the GeV scale [179]. Another source of neutrons is from naturally decaying material, which produces radiogenic neutrons. Radiogenic neutrons can be avoided to an extent by careful selection of material and purification of radioactive elements. Cosmic ray interactions can be reduced by going as far underground as possible. Estimates indicate that the cosmic ray muon flux is reduced by roughly an order of magnitude for every 2 km of depth [179]. Active vetoing of events is also used. If a muon is observed by external detectors surrounding the experiment, coincident events in the detector are vetoed, as they may have been caused by an associated neutron. Shielding with water or polyethylene is also used, as are the basic data analysis techniques that are used for gamma rays (like the fiducial volume).

Internal backgrounds

Internal backgrounds are dependent on the type of detector, though a common feature across all detector materials is contamination of the material by radioactive components.

Generally, the growth process for the crystals used in semiconductor detectors forces out impurities. A more concerning problem is surface contamination from the decay products of ambient atmospheric radon. Events from surface contamination can be potentially identified and vetoed by placing electrodes on the surface of the crystal that allow for a positional identifier [180, 181]. This can be done for scintillating crystal

detectors as well [182]. While the crystal is inert after growth and when construction of the detector starts, it is possible that high energy cosmic rays interact with it during the construction phase and activate some nuclei. This cannot be avoided until the detector is underground, but the effect can be studied and quantified [183, 184] so that the background events can be accounted for.

Cosmic activation is also a problem for gas and liquid-based detectors. One method used by the DarkSide experiment to avoid this is to use argon that has been mined from underground sources [185]. This argon has a naturally lower proportion of radioactive isotopes due to its lack of exposure to cosmic rays. The problem is less pronounced for xenon-based experiments, as radioactive xenon isotopes are either too short lived or too long lived to affect the data collection of the detector. Similar to surface contamination of crystals, contamination of the bulk by other parts of the detector that are less clean is common (krypton and radon from the atmosphere in particular). This contamination induced background is carefully measured and accounted for.

3.2.4 Experimental collaborations

There are a number of direct detection experiments that are currently operational, and a number of older experiments that have either ceased taking data, or have been merged into a newer experiment. There are also a number of experiments that have been recently proposed, have had funding approved and are in the planning phase, or are already under construction or testing.

Noble liquid detectors, due to the high nuclear masses of their target nuclei, are the most important for high mass WIMPs. The current strongest bounds are set by the XENON [161], PandaX [186], LUX [162], and DEAP [187] collaborations. Each of these experiments is planning an upgrade within the next few years, and the strongest projected sensitivities over a very large mass range are expected to be set by the DARWIN experiment [188], which is in the planning phase. In the lower mass range of 1 GeV to a few 10s of GeV, the crystal detectors are dominant. The current strongest limits in this region are set by the CRESST [189] experiment. Both EURECA [190] and SuperCDMS [191] are expected to probe deeper into the parameter space.

Bubble chamber detectors provide strong spin dependent limits, particularly the PICO [168] experiments, which was recently formed by a merger of the COUPP [192] and PICASSO [193] experiments. Directional detectors, such as DRIFT [172], are also an important part of the future of direct detection. Finally, there are those proposed experiments discussed in Section 3.2.2, which do not fit into any of the above categories.

In Table 3.1 a list of dark matter direct detection experiments/collaborations has been provided. It includes target materials, detection channel, years of operation, and a reference. The reference is to design documentation if published, or to the published first results of the experiment. For longer running or larger experiments, a review article is occasionally cited. Further technical details are available in the associated references, and general summaries for both scientists and the public are typically provided on the individual collaboration websites, though those for inactive experiments tend to not be maintained. These websites

will nonetheless usually contain the most information and a list of publications, presentations, and reports relevant to the experiment.

3.3 Current exclusion limits

As mentioned in Section 3.1, no statistically significant nuclear recoil signal has been observed, which has led to experimental collaborations publishing exclusion bounds on nuclear recoil cross sections. The calculation of the reported exclusion limits is a delicate affair. As a positive signal is expected to be on the order of a few scattering events per year, statistics are very important. A highly detailed treatment of the statistical methods appears in reference [216]. Basically, a signal region in recoil energy-expected event rate space is chosen where the signal to background ratio is expected to be high, and the background in this region is estimated through calibration or simulation (or both). The techniques for low event likelihoods developed by Feldman and Cousins [217] that have become very popular in particle physics are applied to generate one-sided confidence intervals (for exclusion bounds) or two-sided confidence intervals (for error regions on a possible signal).

This Section provides an overview of current direct detection exclusion limits as reported by the various experimental collaborations. The discussion of current exclusion limits is divided into spin dependent and spin independent components.

3.3.1 Spin dependent limits

Spin dependent direct detection exclusion bounds are currently in the range of 10^{-33} cm^2 to 10^{-41} cm^2 depending on the WIMP mass. Currently the most stringent bounds are reported by the PICO collaboration [168]. Other competitive bounds are reported by XENON [218], LUX [219], and PandaX [220]. Future bounds are likely to be placed by the next generation noble liquid detectors such as LZ [207] and XENONnT [161], but projected limits have not yet been reported for the spin dependent case.

Due to the extra difficulty inherent in handling spin effects in the scattering events, spin dependent bounds are much weaker than spin independent bounds. This has led to the interesting situation where direct detection experiments do not always provide the most stringent bounds on nuclear recoil cross sections. For example, by translating the exclusion limits on dark matter production at the LHC, the CMS and ATLAS collaborations have been able to provide effective nuclear recoil limits for a set of models [221, 222]. More details on this are available in Chapter 5. Additionally, as will be discussed briefly in Chapter 4, the IceCube neutrino telescope in Antarctica has been able to provide competitive spin dependent nuclear recoil exclusion limits based on nonobservation of a neutrino annihilation signal from the Sun [223].

Because it is possible that WIMPs couple differently to protons and neutrons, and because spin dependent experiments are capable of providing bounds on these different channels due to material selection, exclusion

Table 3.1: Direct Detection Experiments

Experiment	Material	Detection channel	Years of operation	Reference
DAMA	NaI(Tl)	Scintillation	1995-2013	[194]
CoGeNT	Ge	Ionization	2009-present	[195]
NAIAD	NaI(Tl)	Scintillation	2001-2003	[196]
CDEX	Ge, NaI(Tl)	Ionization	2010-present	[197]
CDMS	Ge, Si	Phonons, Ionization	1990-present	[198]
EDELWEISS	Ge	Phonons, Ionization	2000-present	[199]
CRESST	$CaWO_4$	Phonons, Scintillation	2000-present	[200]
EURECA	$CaWO_4$, Ge	Undecided	Future	[190]
ROSEBUD	Various	Scintillation	1997-2012	[201]
KIMS	CsI(Tl)	Scintillation	2000-2012	[202]
XENON	Xe	Scintillation, Ionization	2005-present	[159, 160, 161]
PandaX	Xe	Scintillation, Ionization	2009-present	[186]
XMASS	Xe	Scintillation	2010-present	[203]
DarkSide	Ar	Scintillation, Ionization	2012-present	[204]
DEAP	Ar	Scintillation	2007-present	[187]
CLEAN	Ar, Ne	Scintillation	2011-present	[205]
ZEPLIN	Xe	Scintillation, Ionization	2000-2011	[206]
LZ	Xe	Scintillation	Future	[207]
WARP	Ar	Scintillation, Ionization	2008-2011	[208]
ArDM	Ar	Scintillation, Ionization	2006-present	[209]
LUX	Xe	Scintillation, Ionization	2009-present	[162]
DARWIN	Xe	Bubble chamber	Future	[188]
COUPP	CF_3I	Bubble chamber	2006-2013	[192]
PICASSO	C_4F_{10}	Bubble chamber	2012-2014	[193]
SIMPLE	C_2ClF_5	Bubble chamber	2000-2012	[210]
PICO	C_3F_8	Bubble chamber	2013-present	[211]
DRIFT	CF_4, CS_2, O_2	Directional	2003-present	[172]
MIMAC	CF_4, CHF_3, C_4H_{10}	Directional	2012-present	[212]
NEWAGE	CF_4	Directional	2007-present	[213]
DMTPC	CF_4	Directional	2010-present	[214]
D^3	Ar, CO_2	Directional	Future	[215]

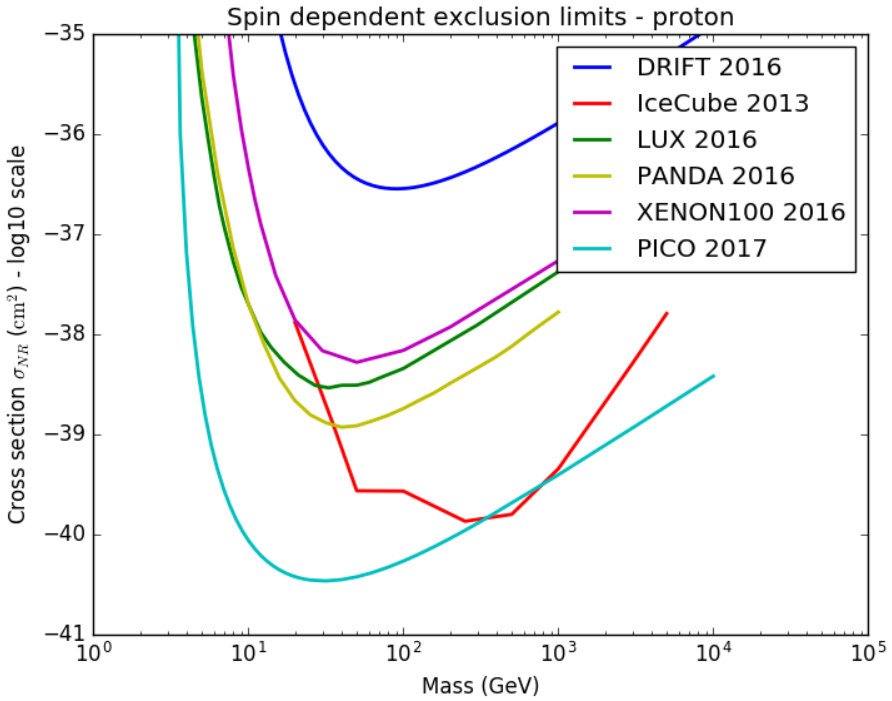

Figure 3.2: Current spin dependent exclusion limits for WIMP scattering from protons. Results reported by XENON100 [218], LUX [219], PandaX [220], PICO [168], and DRIFT [224]. Older IceCube limits included for comparison [223].

limits are generally reported separately for proton and nucleon scattering. Current limits for a selection of publicly available spin dependent exclusion bounds appear in Figure 3.2 for the proton coupling case, and in Figure 3.3 for the neutron coupling case. The IceCube exclusion limits from 2013 have been included for comparison.

3.3.2 Spin independent limits

Limits on spin independent nuclear recoil cross sections are in the range of 10^{-38} cm^2 to 10^{-47} cm^2 depending on the WIMP mass, and the next generation will hit 10^{-49} cm^2. These sensitivities are rapidly approaching what is called the neutrino floor, which is an irreducible background caused by the solar and cosmic neutrino flux passing through the solar system (see Section 3.3.4 for further discussion and a comparison to current and projected exclusion limits).

Limits for the most relevant of modern spin independent exclusion bounds are presented in Figure 3.4. A selection of projects in the planning phase that have reported predicted sensitivities have limits that appear in Figure 3.5. Note that the most recent results from XENON, LUX, DEAP3600 and DARWIN have not been made available to the public in pure data form, and so we are unable to include them here.

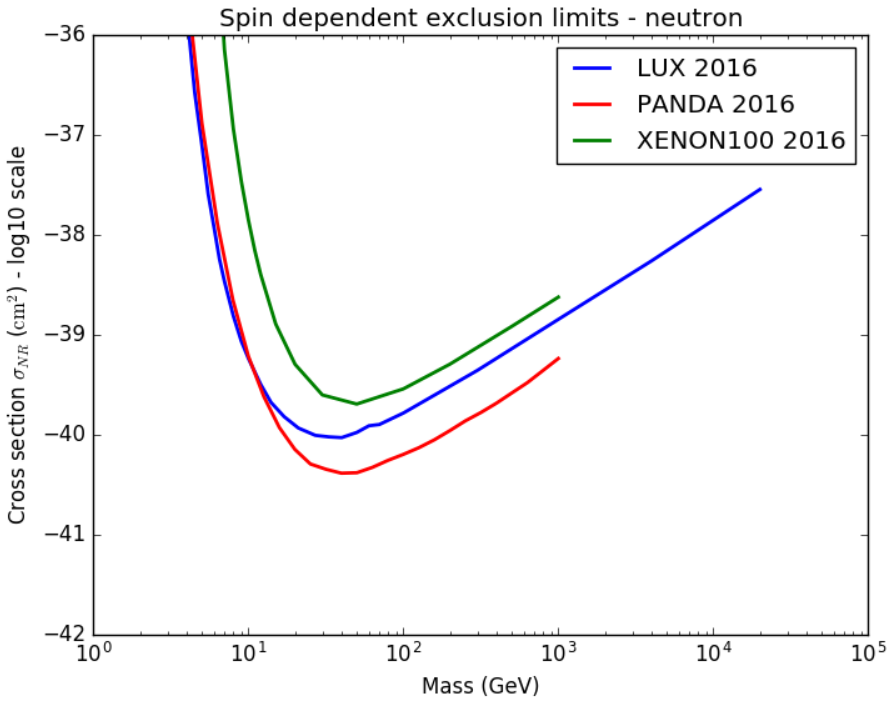

Figure 3.3: Current spin dependent exclusion limits for WIMP scattering from neutrons. Results reported by XENON100 [218], LUX [219], PandaX [220].

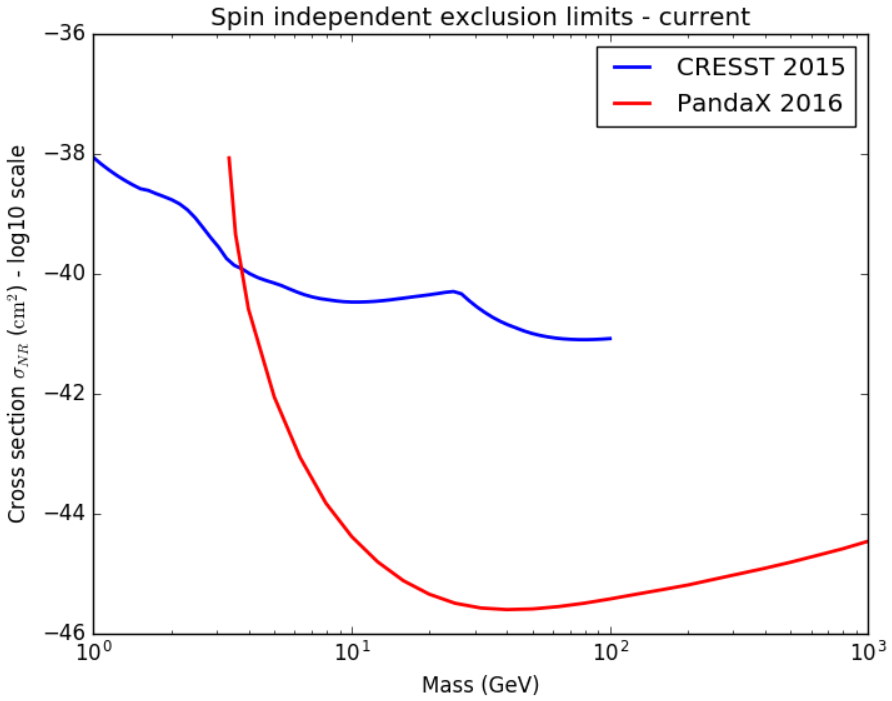

Figure 3.4: Currently reported spin independent nuclear recoil exclusion limits. Results from PandaX [225] and CRESST [189].

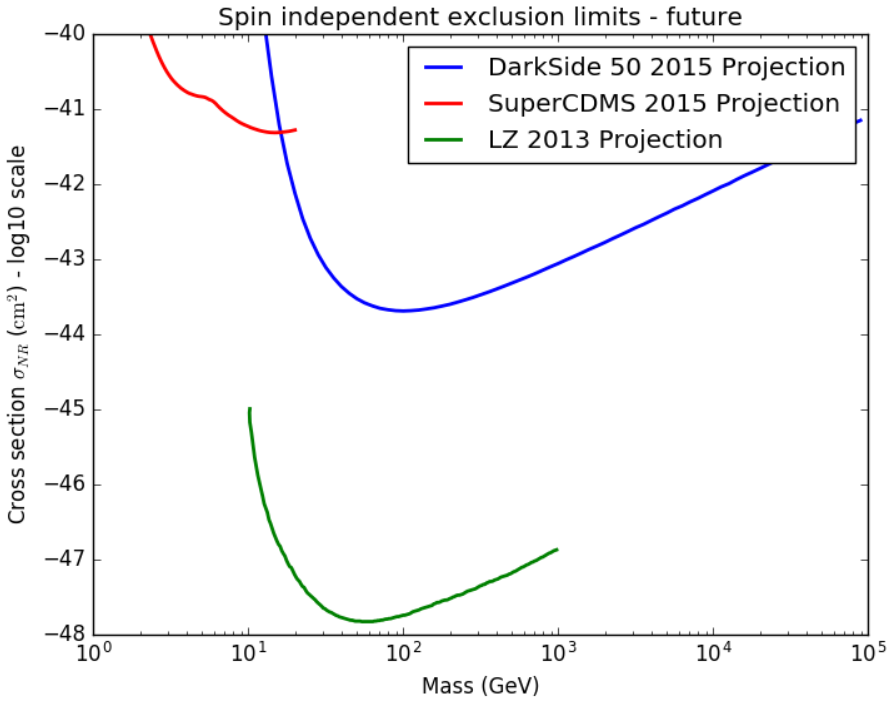

Figure 3.5: Currently reported spin independent nuclear recoil projected sensitivities. Results from DarkSide [185], SuperCDMS [191], and LZ [207].

3.3.3 Annual modulation signals

An approach taken by the long-running DAMA family of experiments is to search for annual variations in the number of background events observed. This allows them to draw conclusions with much lower sensitivities than other experiments, as they do not need to subtract backgrounds because their signal is on top of the backgrounds. It is expected from the Earth's motion in the galactic halo that the number of events will be largest in June and smallest in December [226].

There is a reported signal in a region of the parameter space $m_{DM} \approx 10 - 15$ GeV and $m_{DM} \approx 60 - 100$ GeV, depending on scintillation efficiency. The most recent report of the signals observed by DAMA/LIBRA are available in reference [227]. It should be noted that the observed signal is in disagreement with exclusion bounds reported by other experiments, including XENON100 [228], and has been for some time. Other possible causes for these signals include [229, 230] atmospheric muons (from atmospheric modulation) and background neutron variation.

The XENON collaboration has recently reported a modulation signal analysis of the entirety of live time for the XENON100 experiment [146]. They have been able to exclude axial vector WIMP electron scattering events as a cause of the observation signal reported by DAMA/LIBRA to 5.7σ significance.

3.3.4 The neutrino floor

It is known that WIMP direct detection sensitivities cannot increase much further due to the presence of the predicted so-called 'neutrino floor.' The neutrino floor was first seriously considered nearly a decade ago [231, 232], when the second generation of direct detection experiments had seen nothing, and the particle astrophysics community realized that dark matter might have nuclear recoil cross sections well below what was expected from the SUSY WIMP. The next generation of direct detection experiments that are in the planning phase and anticipated to come online within a few years [161, 188] will reach the neutrino floor in the spin independent sector.

In Section 3.2, the neutron background was discussed. Neutrons are dangerous because, as neutral particles, their recoil signatures are very similar to those predicted for WIMP dark matter. Special care is taken to shield against neutrons and purge radioactive material from the environment. Similarly, coherent neutrino-nucleus scattering events will generate a signal that is very similar to that that would be generated by WIMP dark matter. Direct detection experiments will soon have sensitivities that can detect such scattering events from the natural neutrino background flux. This background cannot be shielded against, as there is no effective way to shield against a neutrino flux. The sensitivities at which these neutrino scattering events become relevant is called the neutrino floor, as it is a hard lower bound on WIMP direct detection experiments, at least in the current search paradigm. Essentially, any WIMP nuclear recoil signal that is smaller than the expected uncertainties in the neutrino nuclear recoil spectrum cannot be with statistical confidence observed or excluded. Even if dark matter is discovered above the neutrino floor, precision studies of the properties of dark matter will require increased sensitivity, so considering the neutrino floor is unequivocally important. The neutrino floor as well as several current and projected direct detection exclusion limits appear in Figure 3.6.

The differential cross section of neutrinos off of an atomic nucleus with respect to recoil energy E_r is given by the expression

$$\frac{d\sigma}{dE_r}\left(E_r, E_\nu\right) = \frac{G_F^2}{4\pi} Q_W M_N \left(1 - \frac{M_N E_r}{2E_\nu^2}\right) F^2\left(E_r\right), \tag{3.15}$$

where the energy of the incoming neutrino is E_ν, G_F is the Fermi constant, M_N is the atomic nucleus mass, and $F(E_r)$ is a nuclear form factor. The weak charge of the nucleus is $Q_W = (A-Z)-(1-4\sin^2\theta_W)Z$, where Z is the number of protons in the nucleus, $A-Z$ is the number of neutrons, and θ_W is the Weinberg angle. This cross section is due to a neutral current process, generated at tree level by Z boson exchange between the neutrino and the valence quarks of the nucleons in the nucleus. However, the momentum transfer is small enough that the Z boson wavelength is larger than the diameter of the nucleus, leading to the coherent scattering of the neutrino off of all the nucleons. This coherency allows the use of the effective nuclear coupling used in the above cross section. It is interesting to note that coherent neutrino-nucleus scattering is a SM prediction that has never been observed in a dedicated experiment, which provides a connection between

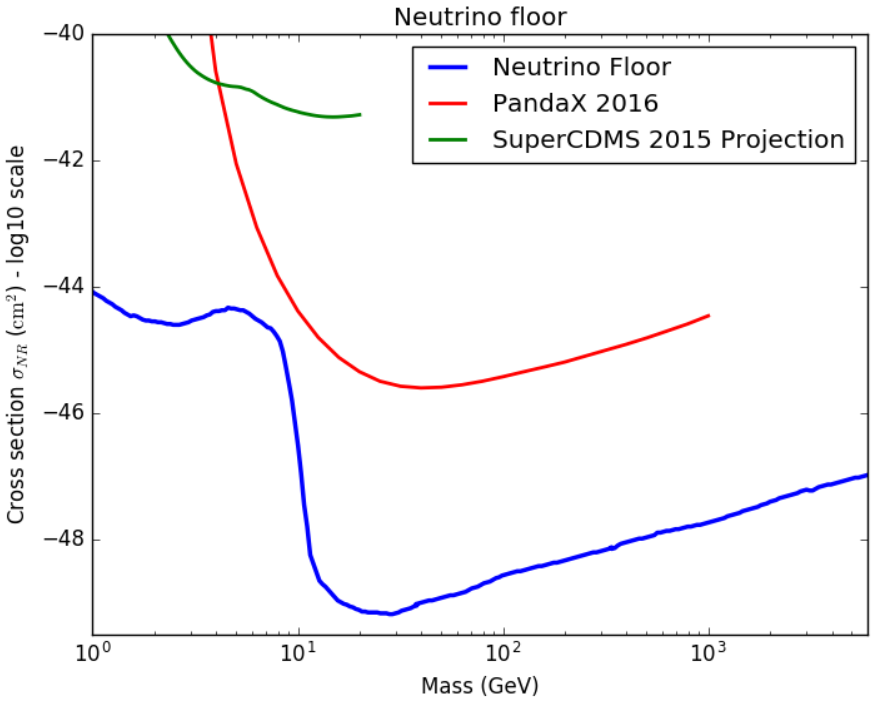

Figure 3.6: The neutrino floor, as reported in [233], against several current and projected nuclear recoil exclusion limits and sensitivities. Reported results and projections include PandaX [225] and SuperCDMS [191].

the current dark matter direct detection experimental effort and neutrino physics (see reference [234] for a theoretical discussion of some of the neutrino physics prospects).

The neutrino flux that generates the neutrino floor is produced primarily by nuclear processes in the Sun, by high energy cosmic rays striking the upper atmosphere and by supernovae. Geo neutrinos, which result from the decay of radioactive elements in the Earth, have been shown to have a negligible effect [231]. Solar neutrinos mimic the recoil spectrum of a ∼6 GeV WIMP, and atmospheric neutrinos generated by cosmic rays will mimic a ∼100 GeV WIMP. Neutrinos from the diffuse supernova background, which is the isotropic and constant flux of neutrinos produced by supernovae, can mimic WIMPs in the 10-30 GeV mass range. The incident neutrino flux is displayed for informational purposes in Figure 3.7.

The neutrino recoil events are individually indistinguishable from WIMP recoil events. In principle, given enough exposure, the signal of WIMP nuclear recoils can be distinguished from that of neutrinos, as there are predicted differences in the high energy tails of the recoil energy distributions. The required exposures are, however, unrealistically large. Yet direct detection searches are a crucial part of the experimental effort searching for dark matter, and to lose them completely would be difficult. This has led to a number of studies that consider ways to avoid the neutrino floor. We will conclude this section by providing a brief outline of some of the main ideas that have appeared in the literature.

In principle, the neutrino background can be distinguished from WIMP signals by using the predicted WIMP annual modulation signal. Solar neutrino events are not expected to exhibit such a modulation, so

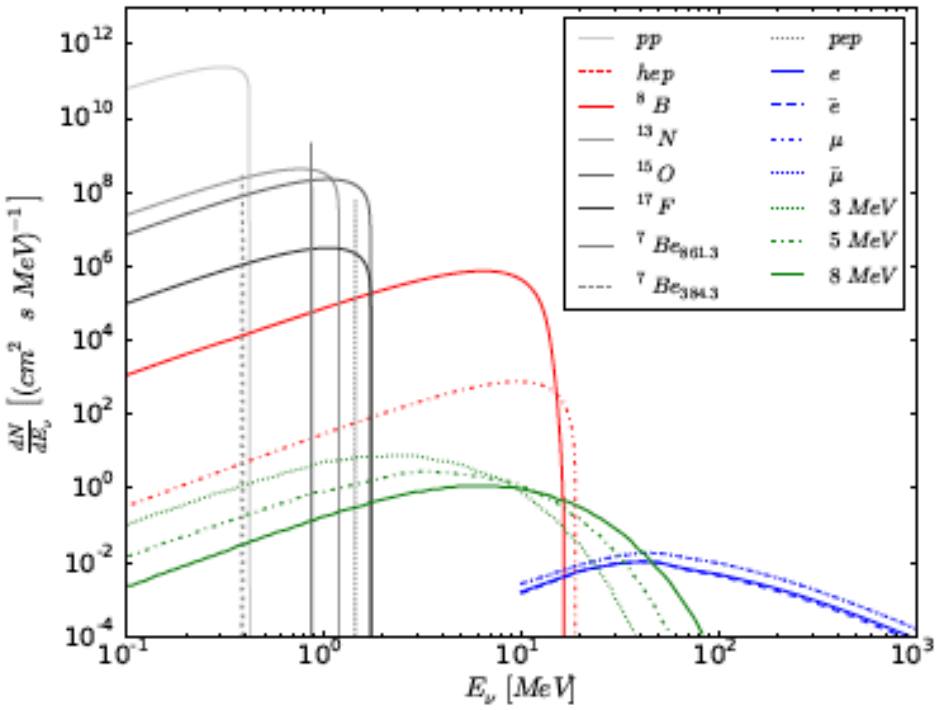

Figure 3.7: Neutrino flux as a function of neutrino energy for a variety of processes. Figure from reference [235]

several groups have considered using this phase difference as a tool for discrimination [236, 233]. Directional detectors, being sensitive to both direction and recoil energy, have been suggested as a way to probe at higher sensitivities [235, 237]. This would require a significant amount of exposure time, however. There are also attempts to theoretically extract distinguishing features from the different spectra using effective field theory techniques [238]. The variety of these approaches indicates that the community is taking the problem posed by the neutrino floor very seriously.

3.4 Example: Scalar Higgs-portal dark matter

To illustrate how the material that has been covered in this Chapter is used by a phenomenologist, we will discuss the example of scalar Higgs-portal dark matter. The model is described in further depth in Appendix B. The basic approach, which is more or less the same for all models, is to find the nuclear recoil cross section and to compare it with the current exclusion limits, and then to decide whether or not the model is still viable. That is what we do here.

The scalar Higgs-portal model, being essentially a two-scalar Yukawa theory, has the simplest possible direct detection phenomenology. When the Higgs-singlet coupling η_S of the model has been fixed by the thermal abundance constraint (see the previous Chapter for this discussion), the model has only the singlet mass m_S as a free parameter. The mediator is well understood, as it is a SM particle, and the only major uncertainty on the SM side is in the parametrization of the Higgs boson interaction with the nucleon. This Section is an adaptation and extension of work that appears in references [239, 240], of which the author of this thesis is an author.

The nuclear recoil cross section in the nonrelativistic limit takes the form [239, 240, 241]

$$\sigma_{NR} = \frac{g_{hNN}^2 \eta_S^2 v_h^2}{4\pi m_h^4} \frac{m_N^2}{(m_S + m_N)^2} \tag{3.16}$$

where the masses of the SM Higgs, the nucleon, and the dark matter singlet are m_h, m_N and m_S respectively. As usual, the Higgs vacuum expectation value is $v_h = 246$ GeV, and the singlet-Higgs coupling parameter is η_S. The quantity g_{hNN} parameterizes the interaction between the Higgs boson and the nucleon. In our calculations, we use the values $m_h = 125.9$ GeV and $m_N = 0.9305$ GeV.

The effective Higgs-nucleon coupling g_{hNN} is a parameterization of the interaction between a composite nucleon and the Higgs boson field. The standard calculation is found in the work of Shifman, Vainstein and Zakharov [242], and is discussed in further detail in Appendix B. The numerical inputs to that calculation require consideration.

As discussed in the Appendix, the primary property of interest that contributes to the Higgs-nucleon coupling is the nucleon strangeness content, characterized by

$$y_N = \frac{2\langle N | \bar{s}s | N \rangle}{\langle N | \bar{u}u + \bar{d}d | N \rangle}. \tag{3.17}$$

The initial work in reference [242] assumed zero strangeness in the nucleon, but later work demonstrated that strangeness could have a considerable effect [243]. Using the estimates of the nucleon strangeness content available at the time, it was found the estimated strangeness could alter the coupling by factors of up to 2.5. The calculations in reference [243] in 1988 used a strangeness of $y_N = 0.47$, which is much higher than modern estimates. Lattice gauge theory results indicate a strangeness of $0 \leq y_N \leq 0.14$ [244, 245, 246, 247, 248, 249, 250].

Further experimental constraints can be included if one uses the nucleon-pion sigma factor $\sigma_{\pi N}$, defined by

$$\sigma_{\pi N} = \frac{m_u + m_d}{2} \langle N \left| \bar{u}u + \bar{d}d \right| N \rangle \tag{3.18}$$

which can be extracted from pion-nucleon scattering experiments. Reported results indicate that the sigma parameter is ≤ 70 MeV [244, 251, 252].

Using both the nucleon strangeness y_N and the sigma parameter $\sigma_{\pi N}$, the Higgs-nucleon coupling (scaled by the Higgs vacuum expectation value) can be written

$$g_{hNN} v_h \simeq \frac{7}{9} \left(1 + \frac{m_s y_N}{m_u + m_d} \right) \sigma_{\pi N} + \frac{2}{9} m_N. \tag{3.19}$$

By considering the allowed range for the input values y_N and $\sigma_{\pi N}$, we can restrict the allowed range for values of $g_{hNN} v_h$ to 210 MeV $\leq g_{hNN} v_h \leq$ 365 MeV. The lower bound correspond to $y_N = \sigma_{\pi N} = 0$ while the upper bound is $y_N = 0.14$ and $\sigma_{\pi N} = 70$ MeV. In terms of the actual coupling, this range is $0.853 \times 10^{-3} \leq g_{hNN} \leq 1.484 \times 10^{-3}$. As this quantity enters the nuclear recoil cross section squared, this amounts to an uncertainty of a factor of about 3 in the final cross section. We note our results agree with those of reference [253], and with the results of more recent lattice gauge theory calculations [254]

In Figures 3.8, 3.9 and 3.10 we plot the nuclear recoil cross section for the scalar Higgs-portal model beside experimental and projected direct detection exclusion limits for several relevant mass ranges. The possible range of the Higgs-nucleon coupling g_{hNN} is indicated by the shaded region. As is noted in Chapter 5 and in Appendix B, limits on the invisible Higgs decay width rule out Higgs-portal scalars with masses below $m_h/2 \simeq 63$ GeV. Because of this, we do not consider scalars in that mass range.

Figure 3.8 is the lower mass region from $m_S = 63$ GeV to 250 GeV. This region is clearly excluded by recent PandaX, LUX, and XENON1T limits, though this was not the case in 2015 when these results were originally published [240]. The sudden spike in the theoretical cross section near 63 GeV is due to the resonance in the Higgs-portal annihilation cross sections that were used to obtain the thermally constrained Higgs-portal coupling η_S. As m_S approaches $m_h/2$, the coupling required to generate the current abundance climbs to the nonperturbative regime. Results for $m_S \leq 65$ GeV are unreliable at best, as the approximations going into the thermal relic calculations begin to break down (see Chapter 2 for more details).

Figure 3.9 is the higher mass region of $m_S = 250$ GeV to 2000 GeV. The Higgs-portal model is excluded by the 2016 reported limits in this mass range as well, not to mention future projected limits. Figure 3.10

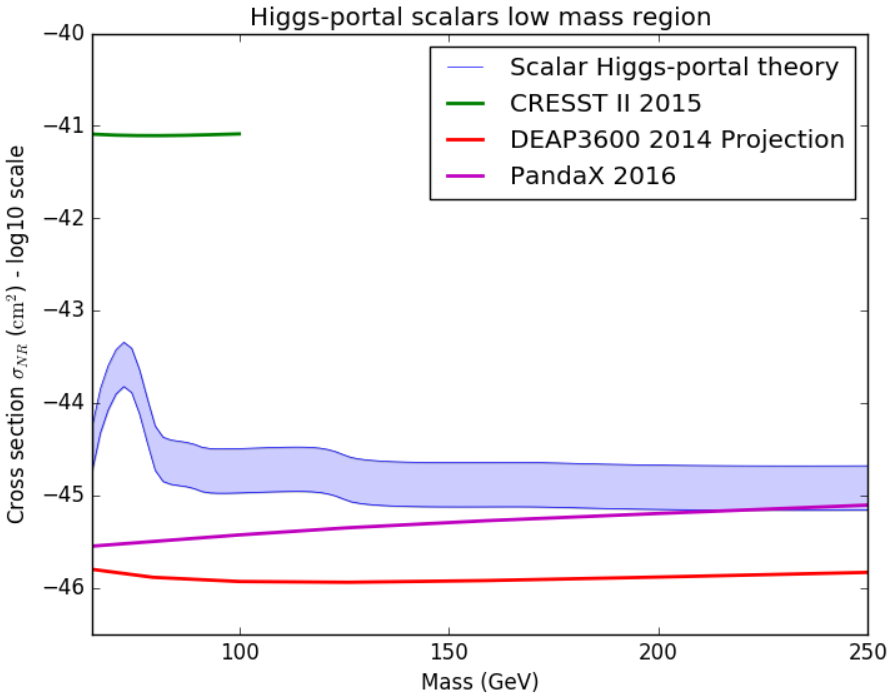

Figure 3.8: Theoretical nuclear recoil cross section for scalar Higgs-portal dark matter in the mass range of 63 GeV to 250 GeV with a thermally constrained coupling. Higgs-nucleon coupling values in range discussed in text. Theoretical cross sections compared to reported results from CRESST [189], DEAP3600 [255], and PandaX [225].

covers the extreme mass region of 1.5 TeV to 15 TeV. This extends beyond the range of any current bounds, but future experiments are projected to probe this region. In any case, the perturbative assumption for a thermally constrained Higgs-portal scalar begins to break down in this region [240].

The above Figures clearly show that scalar Higgs-portal dark matter is out of parameter space. To avoid current experiments, the model needs masses that are on the order of several TeV, which is large enough that to account for the observed relic abundance, the Higgs-portal coupling η needs to be approaching the limit of where perturbation theory is valid. And if the coupling is so large, the approximations used in the thermal production analysis break down, making the high mass region of the Higgs-portal model nonpredictive.

For these reasons, it is reasonable to say that the scalar Higgs-portal model in the simplest case is effectively excluded. The obvious way to extend the model to retain viability is to relax the constraint that scalar Higgs-portal dark matter produced by thermal freeze-out must account for the entirety of the observed abundance. This would allow for smaller values of the Higgs-portal coupling η_S to be used, and lower the cross sections below the exclusion bounds. Of course, this may not be the most natural approach.

The most basic way to do this is to assume multi-component dark matter, where the Higgs-portal component does not comprise the whole of dark matter. Such variants are discussed in [256, 257], though using them without theoretical motivation is perhaps unmotivated. Additionally, multi-component dark matter complicates the situation by including more particles, the lack of which was one of the primary draws of the

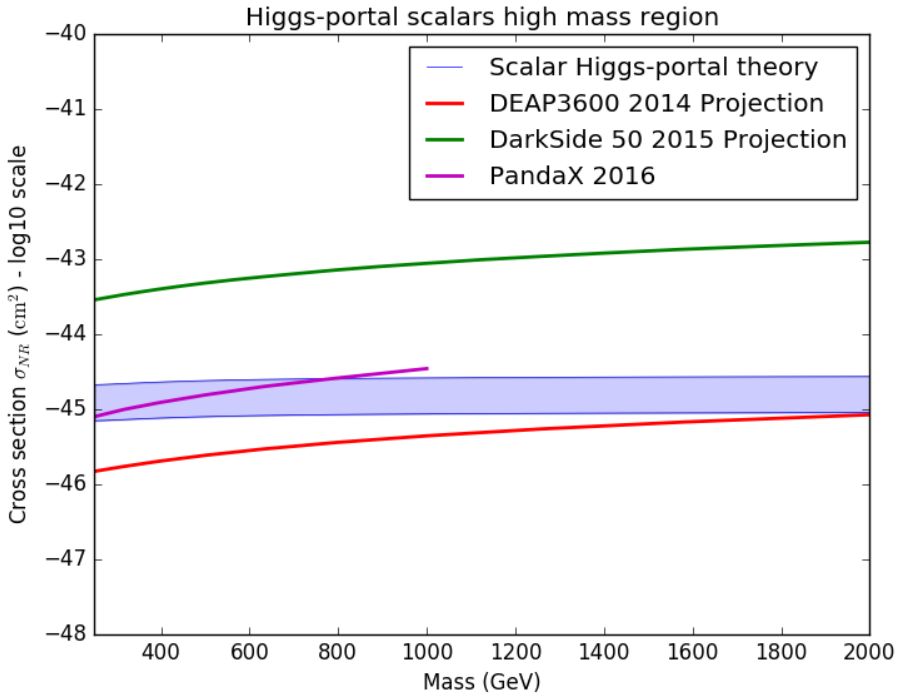

Figure 3.9: Theoretical nuclear recoil cross section for scalar Higgs-portal dark matter in the mass range of 250 GeV to 2000 GeV with a thermally constrained coupling. Higgs-nucleon coupling values in range discussed in text. Theoretical cross sections compared to reported results from DarkSide [185], DEAP3600 [255], and PandaX [225].

Higgs-portal model to begin with. It also becomes necessary to ask the question of where in the expanded parameter space the additional dark component becomes dominant for detection purposes. Additional constraints must be found and applied, leading to further complication. Another possibility, which has been discussed in reference [124], is to assume Higgs-portal scalars are produced not by freeze-out during the early universe, but by some alternative mechanism. Such mechanisms are discussed briefly in Chapter 2.

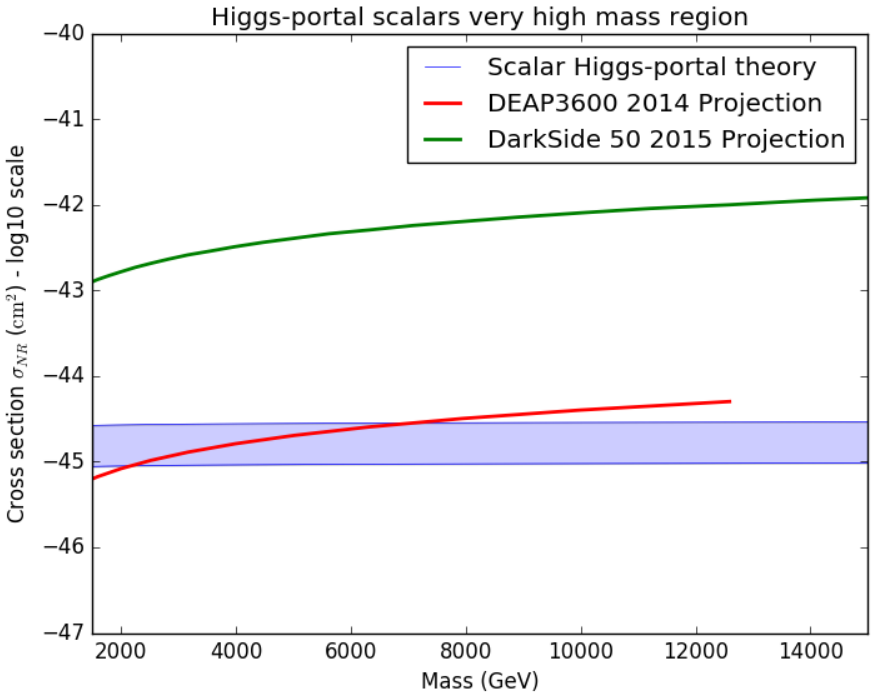

Figure 3.10: Theoretical nuclear recoil cross section for scalar Higgs-portal dark matter in the mass range of 1500 GeV to 15000 GeV with a thermally constrained coupling. Higgs-nucleon coupling values in range discussed in text. Theoretical cross sections compared to reported results from DarkSide [185] and DEAP3600 [255].

Chapter 4

Indirect Detection of Dark Matter

If dark matter was thermally produced as in the WIMP paradigm, it has an annihilation cross section at freeze-out of around 3×10^{-26} cm^3/s. For most WIMP masses, the dark matter halo has a high enough number density that one expects annihilation of present time nonrelativistic halo WIMP particles at a rate $\sim \sigma_{ann} v \rho^2/m^2$. Indirect detection of dark matter is the detection of the products of these annihilations. It is a complementary approach to the direct detection of dark matter that was discussed in the previous Chapter, and the collider production of dark matter that will be discussed in the Chapter immediately following.

While indirect detection is promising, it suffers from certain drawbacks. The first is that only a few particles resulting from the annihilation of dark matter are suitable as a detectable signal. This is primarily because most annihilation products, particularly in annihilations of high mass particles, tend to be unstable and rapidly decay. There are only four stable particle species that live long enough to reach the Earth from an arbitrary point in the dark matter halo.

The second major difficulty is extraction of an annihilation signal from everything else out there. There are many high energy astrophysical processes that produce these stable particles, some with spectral signatures similar to what one expects from dark matter annihilation. Confirming any positive signal in general requires a detailed understanding of the other processes that are producing these particles. Such an understanding is currently beyond us for most astrophysical processes.

The most promising indirect detection channel is the gamma ray channel, which consists of high energy photons (> 100 MeV). Photons are stable, so they will reach our instruments, and are fairly easy to detect. They also have the advantage of being produced in nearly every SM decay path, so they will, in general, comprise a significant portion of the final state of any annihilation cascade. Another advantage they have over charged particles in particular is that they travel in straight lines (if minor gravitational lensing effects are ignored), allowing targeted searches of specific regions of space, meaning a gamma ray signal can provide both spatial and spectral information about its source. In contrast, charged particles such as electrons and protons are deflected by the galactic and interplanetary magnetic fields, propagating in such a complicated way that their point of origin cannot be known.

The main drawback of the gamma ray signal is the opposite side of one of its advantages. Since gamma rays are produced so easily, every astrophysical process will produce them in large numbers. This makes extraction of any specific signal from the gamma ray sky very difficult. Nonetheless, the advantages outweigh

the drawbacks, and the gamma ray signal remains the best indirect search avenue, having been referred to as the 'golden channel.'

For this reason, while the Chapter is titled 'Indirect Detection of Dark Matter,' the focus will be on gamma ray signals. In Section 4.1, we discuss the basics of the detection of cosmic gamma rays, including calculation of the photon flux from the annihilation of particle dark matter. A brief overview of the instruments used to detect cosmic gamma rays is also provided in Section 4.2. Sections 4.3 through 4.6 consider different means of searching for gamma ray signals of annihilating dark matter. Section 4.3 concerns the isotropic gamma ray flux of mostly unknown origin, and possible contributions from annihilating dark matter. Section 4.4 discusses a potential dark matter explanation for the observed gamma ray excess in the galactic core. Section 4.5 considers bounds on dark matter annihilations derived from observations of dwarf galaxies, small clusters of stars with very high dark matter densities. Section 4.6 describes searches for monochromatic gamma ray lines, a signal unique to annihilating dark matter.

There are also possible indirect signals from annihilating dark matter in antimatter cosmic rays and in the neutrino flux. In Section 4.7, these two other channels will be touched on. Finally, we will explore the gamma ray detection prospects for the simple example of a Higgs-portal scalar. Each of the above search targets will be considered in turn.

4.1 Gamma ray signals

This Section covers some of the fundamentals of the study of gamma ray signals of annihilating dark matter. It is expected that the ambient dark matter in some region of the galactic halo will annihilate at a rate proportional to its number density and annihilation cross section, and that the resulting annihilation products will propagate away from the annihilation zone. The long lived of those annihilation products, including photons, will generate a flux that can be calculated from the parameters of the particle physics model of dark matter and the astrophysics of the dark matter distribution in the region of interest. This theoretical flux, the construction of which is discussed in great detail in Section 4.1.1, can then be compared against the observations of the gamma ray sky as reported by gamma ray telescopes such as the Fermi space telscope and the ground based Cherenkov telescopes. Most of the subsequent Sections of this Chapter will be spent considering specific regions of interest or flux generation mechanisms.

4.1.1 Prompt photon spectra

This Section is concerned with the so-called prompt photon spectrum: that is, the spectrum of photons produced immediately, either directly from the annihilation of dark matter particles or, more likely, through the immediate decay of SM particles produced in the annihilation, as well as radiative corrections to those processes. The main distinction between prompt photons and the secondary photons discussed in Section 4.1.3 is the time between the annihilation event and the emission of the photons. Basically, prompt photons

can be described in principle by a single QFT process, though a potentially very complicated one, while the time scales between the annihilation event and the production of secondary photons are large enough to prohibit that.

The differential gamma ray flux per energy and solid angle from annihilating dark matter is given by [258]

$$\frac{d\Phi_\gamma}{d\Omega dE} = \frac{1}{2}\frac{r_\odot}{4\pi}\left(\frac{\rho_\odot}{m_{DM}}\right)^2 \times J \times \left(\sum_f \langle\sigma v\rangle_f \frac{d\mathcal{N}_\gamma^f}{dE}\right). \tag{4.1}$$

There will be an additional multiplicative factor of $1/2$ when the annihilating dark matter is not self-conjugate (ie is not its own antiparticle). It is typical in the literature to divide this expression into two factors, distinguished by their uncertainties. The final factor, with the annihilation cross section, is the particle physics term, because it is determined by the particle physics model of dark matter. The other factor, including the J-factor, is called the astrophysical factor, and depends on the macroscopic dark matter distribution in the halo, being agnostic to the particle physics nature of the dark matter.

The velocity weighted annihilation cross section of dark matter to final state f is $\langle\sigma v\rangle_f$. This cross section can in general be computed once the details of the particle model of dark matter are determined. The quantity $d\mathcal{N}_\gamma^f/dE$ is the differential photon number density with respect to energy that is produced by final state f, and has contributions from a number of complicated processes. It describes the number of photons generated per energy interval for an annihilation event to the final state f. How to handle it in calculations is discussed in Section 4.1.2. We note that the above expression in Equation (4.2) is presented in terms of annihilation cross sections to final state f. In the literature, one frequently comes across an alternative presentation, where the total annihilation cross section $\langle\sigma v\rangle = \sum_f \langle\sigma v\rangle_f$ is used. In this convention, the particle physics factor is written

$$\sum_f \langle\sigma v\rangle_f \frac{d\mathcal{N}_\gamma^f}{dE} = \langle\sigma v\rangle \sum_f \mathrm{Br}_f \frac{d\mathcal{N}_\gamma^f}{dE}, \tag{4.2}$$

where Br_f is the annihilation branching fraction to final state f, given by $\mathrm{Br}_f = \langle\sigma v\rangle_f/\langle\sigma v\rangle$. These two conventions are equivalent, but we have chosen to work with the former because there is less ambiguity about unknown or neglected final states. It is important to note that while the velocity weighted cross section discussed here in the context of indirect detection is formally the same quantity as the one discussed in Chapter 2 in the context of the thermal abundance calculations, these two contexts are quite different. In this Chapter, we are using the present day cross section, which is for the annihilation of nonrelativistic dark matter, where $v \simeq 300$ km/s. In Chapter 2, freeze-out occurs at $T_f \simeq m_{DM}/20 \to v \simeq 0.4c$, which means the numerical values for the cross sections in these regimes are orders of magnitude apart. In particular, this means that approximations that can be used in the nonrelativistic regime (like expansion in powers of velocity) do not necessarily apply in the freeze-out regime.

The astrophysical J-factor is given by

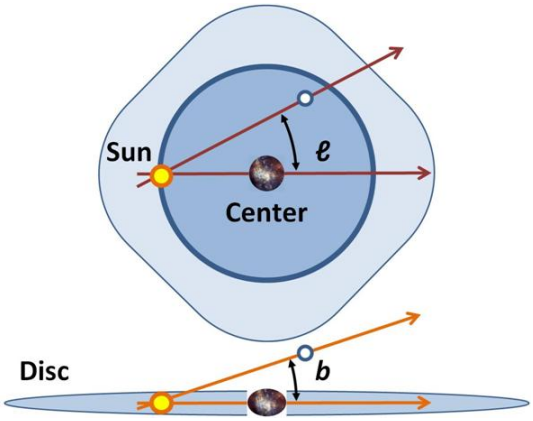

Figure 4.1: Illustration of the galactic coordinate system, as described in the text.

$$J = \int_{l.o.s} \frac{ds}{r_\odot} \left(\frac{\rho\left(r\left(s,\theta\right)\right)}{\rho_\odot} \right)^2 . \tag{4.3}$$

It is an integral along the line of sight (parameterized by variable s) of the dark matter density profile $\rho(r)$ (See Appendix D for further discussion of the dark matter profile). Essentially, it counts the number of dark matter annihilations that will occur along a given line of sight. The factors of the solar system position $r_\odot$ and local dark matter density $\rho_\odot$ are included by convention, to make J a dimensionless quantity. The coordinate system is set up so that the radial variable $r\left(s,\theta\right)$ is

$$r\left(s,\theta\right) = \sqrt{r_\odot^2 + s^2 - 2 r_\odot s \cos\theta}. \tag{4.4}$$

The angle θ is the aperture angle between the line of sight and the axis that connects the Earth to the Galactic center. This is illustrated in Figure 4.1. Spherical symmetry of the halo is assumed, so J is invariant under rotations in θ.

These variables can be related to the galactic polar coordinates (d, b, l) which are defined by $x = d\cos b\cos l$, $y = d\cos b\sin l$ and $z = d\sin b$. Our solar system is at $x = y = z = 0$ so that the Galactic center is at $x = r_\odot$, $y = z = 0$. The angle θ can be expressed as $\cos\theta = x/d = \cos b\cos l$.

In general, the integrals involved in the computation of J must be numerically evaluated. Numerical values for many of the more common regions of interest can be found in the literature, but not all possible ones. While the integrations are not necessarily difficult, integration of profiles that involve $1/r^2$ terms have complications. Basic numerical integration techniques tend to fail to converge when the upper boundary of the s integration is placed at infinity. More advanced techniques may successfully converge, but the singularity in the core region must be handled with care. Stable techniques that are able to handle quadratic singularities within the region of integration and also infinite boundaries are actually very rare. We found that it was best to simply apply an upper cutoff on s of some tens of times the scale radius of the profile, and then use a fixed grid Gauss-Legendre quadrature. This introduced errors in the core region, but profile uncertainties are large there as well. A grid with 1024 points was used for the integration over s. Individual parameter

sets should be tested for stability, but physically beyond this point the galactic halo is small enough that it is safe to ignore.

The factor J defined in Equation 4.3 is the number of annihilation events expected in an infinitesimal solid angle $d\Omega$. To obtain a more useful quantity that counts annihilations in a finite solid angle, such as a region of observation or the angular resolution of a telescope, we integrate over an angular region $\Delta\Omega$ to obtain the averaged J factor

$$\bar{J}\left(\Delta\Omega\right) = \frac{1}{\Delta\Omega}\left(\int_{\Delta\Omega} J d\Omega\right). \tag{4.5}$$

For more commonly considered regions $\bar{J}$ takes one of the following forms [259]:

Disk:

$$\Delta\Omega = 2\pi\int_0^{\theta_{max}} d\theta\sin\theta \Rightarrow \bar{J}\left(\Delta\Omega\right) = \frac{2\pi}{\Delta\Omega}\int_0^{\theta_{max}} d\theta\sin\theta J(\theta), \tag{4.6}$$

Annulus:

$$\Delta\Omega = 2\pi\int_{\theta_{min}}^{\theta_{max}} d\theta\sin\theta \Rightarrow \bar{J}\left(\Delta\Omega\right) = \frac{2\pi}{\Delta\Omega}\int_{\theta_{min}}^{\theta_{max}} d\theta\sin\theta J(\theta), \tag{4.7}$$

$b \times l$ region in galactic coordinates:

$$\Delta\Omega = 4\int_{b_{min}}^{b_{max}}\int_{l_{min}}^{l_{max}} dbdl\cos b \Rightarrow \bar{J}\left(\Delta\Omega\right) = \frac{4}{\Delta\Omega}\int_{b_{min}}^{b_{max}}\int_{l_{min}}^{l_{max}} dbdl\cos b \times J(\theta(b,l)). \tag{4.8}$$

The disk and annulus are symmetric about the galactic center. The $b \times l$ region is for one quadrant of the sky ($b > 0^o$, $0^o < l < 90^o$) and an additional factor of 4 is required to extend to all quadrants.

For a specific angular region of interest $\Delta\Omega$, the differential flux from that region is then

$$\frac{d\Phi_\gamma}{dE} = \frac{1}{2}\frac{r_\odot}{4\pi}\left(\frac{\rho_\odot}{m_{DM}}\right)^2 \times \bar{J}\Delta\Omega \times \left(\sum_f \langle\sigma v\rangle_f \frac{d\mathcal{N}_\gamma^f}{dE}\right) \tag{4.9}$$

with, as before, an extra factor of 1/2 for non-self-conjugate particles.

4.1.2 Photon spectral functions

As mentioned above, the differential photon spectra $d\mathcal{N}_\gamma^f/dE$ are the number of photons per unit energy generated by an annihilation to the SM final state f. This quantity is in general very difficult to compute, primarily due to the hadronization effects that occur. Analytic approximations exist [260], but the standard approach is now to rely on precomputed spectra that are available for public use. These spectra are typically generated using the collider physics Monte Carlo event generation stack, occasionally modified to include additional physics. The primary drawback to this approach is the presence of inaccuracies in the collider stack at low energies [259], which become important for nonrelativistic annihilations of dark matter. Nonetheless, no better alternative has appeared.

There are a number of different sets of pregenerated spectra. We have chosen to work with the set provided by the group of Marco Cirelli in the PPPDMID package [259], which includes tabulated values

easily accessible in Mathematica. The underlying Monte Carlo calculations that produced the tabulated values were done using a modified version of PYTHIA [261]. An important point to note is that this set of spectra includes electroweak corrections implemented at the Monte Carlo simulator level, which are not included in the basic PYTHIA implementation. These corrections are significant for the yields of leptonic and photonic final states for energies $E \ll m_{DM}$, leading to differences of up to 20% [262]. Bremsstrahlung of weak gauge bosons leads to additional hadronization effects that alter the final spectra, in turn leading to logarithmic enhancements of up to order $\left[\ln\left(\frac{m_{DM}}{m_{Z,W}}\right)\right]^n$, independent of the dark matter model. Polarization issues also affect the results, to a smaller degree.

Results are provided in the package for $f = e, \mu, \tau, u, d, s, c, b, t, W, Z, h$. The spectra are reported as $d\mathcal{N}/d\log x$ for $x = K/m_{DM}$, where K is the kinetic energy of the final state in the rest frame of the collision. The dark matter mass range provided is from $m_{DM} = 5$ GeV to $m_{DM} = 100$ TeV, though for $m_{DM} \gg m_Z, m_t$ the spectra $d\mathcal{N}/d\log x$ are largely insensitive to the dark matter mass. It is the small x regions which are the most important phenomenologically, because they are where the largest numbers of photons are produced. In Figures 4.2 and 4.3 we plot the photon spectra from the annihilations of a generic dark matter particle of mass 200 GeV and 2000 GeV respectively. These plots include a set of channels that appear in the annihilation spectra of Higgs-portal scalars, discussed in Section 4.8. The key feature of these spectra is the rapid fall off with energy, illustrating that the vast majority of photons will be produced at tiny fractions of the rest mass of the annihilating particle.

These results contain prompt photons only. Those include photons produced immediately, those from final state showers, those from hadronic decays, and those from external state QED and weak bremsstrahlung. Photons from internal bremsstrahlung (ie emission of photons from charged loop particles) are not included, as they are model dependent, but are expected to be subdominant in general.

4.1.3 Secondary photon spectra

In addition to the prompt photon spectra discussed above, annihilating dark matter also leads to the production of the so-called secondary photon spectrum [259, 263]. Prompt photons are the direct products of dark matter annihilations, but secondary photons are those emitted by charged particles that are themselves a primary annihilation product. These secondary photons are emitted by a variety of processes as the charged particles propagate through space, and span the energy spectrum from the gamma to the radio. A secondary photon signal is, in general, much more difficult to model theoretically and to extract from data than the prompt signal.

Secondary emission is usually from electrons or positrons, which are both stable and light enough that most of their energy is in their velocity rather than their rest mass. As they propagate, the electrons and positrons lose nearly all of their energy to photons. The main source of energy loss is due to inverse Compton scattering of the charged particles with photons in the diffuse flux such as CMB photons or starlight. Inverse Compton scattering accounts for a significant fraction of the cosmic gamma flux, and when modelling the secondary

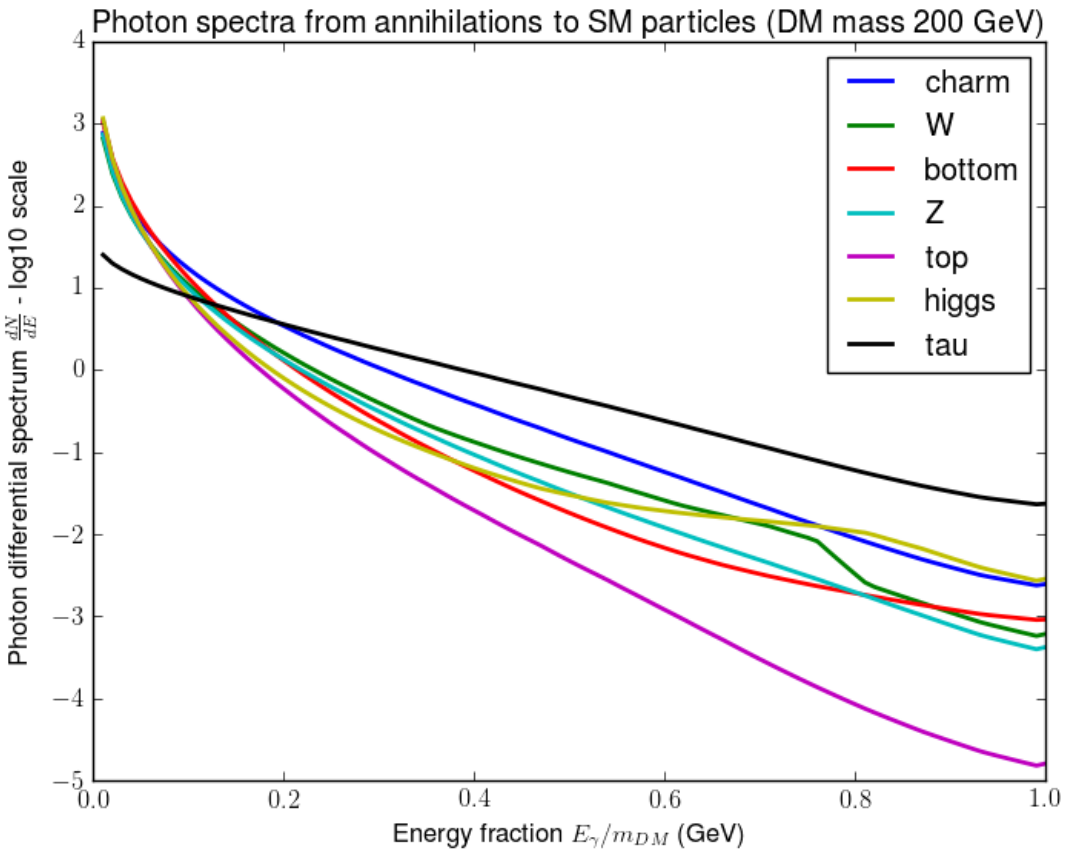

Figure 4.2: Plot of prompt photon spectra $\frac{d\mathcal{N}}{dE}$ for generic annihilating dark matter of mass 200 GeV, to the final states charm, W boson, bottom, Z boson, top, Higgs boson, and tau lepton. Plot is of the number of photons per energy interval on a logarithmic scale, as tabulated in the PPPC ID Mathematica package [259].

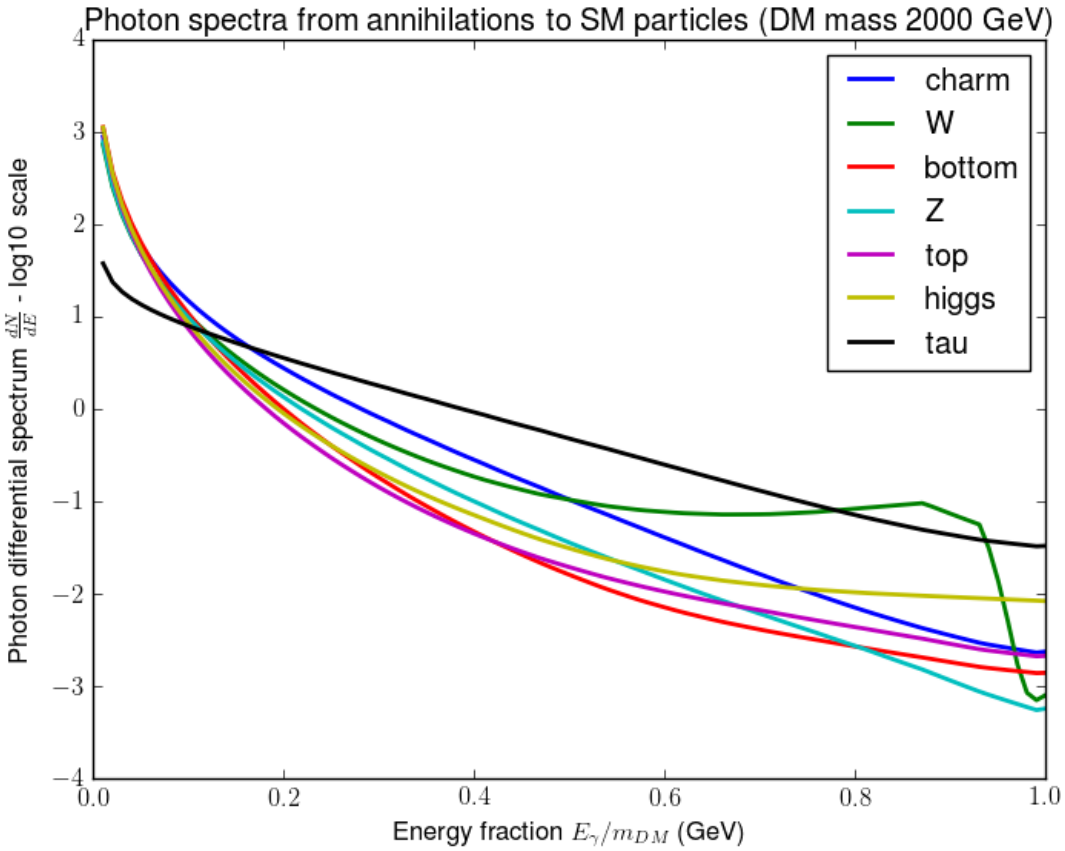

Figure 4.3: Plot of prompt photon spectra $\frac{d\mathcal{N}}{dE}$ for generic annihilating dark matter of mass 2000 GeV, to the final states charm, W boson, bottom, Z boson, top, Higgs boson, and tau lepton. Plot is of the number of photons per energy interval on a logarithmic scale, as tabulated in the PPPC ID Mathematica package [259].

flux from dark matter annihilations, including only inverse Compton scattering with CMB photons is a reasonable approximation [264]. Also a contributor is synchrotron radiation emitted by the charged particles as they travel through magnetic fields. More technical details about the synchrotron radiation component of the flux are available in references [265, 266]. Subdominant contributions from bremsstrahlung effects due to interactions with ionized gas clouds and the emissions of hadronic annihilation products can also be considered. These contributions tend to be too low to justify the added complication of their inclusion.

A signature can be calculated by following a basic procedure. First, the prompt electron and positron production spectra must be computed, and converted to a steady state contribution to the cosmic ray flux. This is, of course, highly dependent on the particle physics model of dark matter. One can then compute the expected photon emissions from the propagation of the steady state flux, the physical mechanisms of which are fairly well understood, but which are governed by parameters that are poorly constrained. Finally, one computes the observation rate for an instrument such as Fermi or one of the radio telescopes. Calculation of emissions and propagation can be done with a numerical package such as GALPROP [267, 268], or one can use the results of reference [259], conveniently available precomputed in a Mathematica package. There is also the possibility of semi-analytically fitting to composite black body spectra [264], which is obviously more involved.

4.2 Instruments and analysis

The preeminent instrument used for gamma ray studies of dark matter is the Fermi space telescope [269], discussed in brief in Section 4.2.1. We also consider data provided by several ground based Cherenkov telescope arrays, including VERITAS [270], MAGIC [271], and HESS [272], which are discussed in Section 4.2.2.

The statistical analysis performed on the data to extract bounds is highly technical; see reference [216] for a review of statistical methods in the indirect detection of dark matter. In this thesis, we do not go into detail concerning the statistical methods used by the collaborations to determine their reported results, only using said results.

4.2.1 Fermi space telescope

The Fermi-LAT is a satellite telescope that was launched in 2008, and observes gamma ray events from about one fifth of the sky. The Fermi-LAT can detect photons with energies of 20 MeV to over 300 GeV [269], and contains active background discrimination and rejection against cosmic rays, Earth albedo photons, and radiation trapped in the Earth's magnetosphere. The instrument has an effective area of about 8000 cm^2 at normal incidence and has a field of view of 2.4 sr.

Gamma rays enter into the tracker and hit a layer of tungsten foil that converts them into e^+e^- pairs. For gamma rays of large energies $E_\gamma \gg m_e$, the produced pair will have a low transverse momentum and

so continue largely in the same direction as the source gamma ray. The pair is then tracked further in the instrument by a series of silicon strip detectors. The information from these trackers is used to construct the direction of the original gamma ray. Finally the pair hits a calorimeter, where the energy can be measured. In this way, estimates of both the direction and energy of an incident gamma ray can be obtained.

Contamination of the signal by charged particles, either cosmic rays or the result of cosmic rays interacting with the Earth's atmosphere, is a serious concern. Similar signals can be generated by charged cosmic rays striking the foil, so an anticoincidence system is implemented to allow vetos of charged particles. Backsplash is likewise reduced by taking direction into account in the veto. The signals generated by the instrument allow reconstruction of both particle trajectory and energy, which allows discrimination between charged particles and photons. Rigorous calibration runs are also done.

Simulations are used to realize the data given a hypothesized sky model, and are a part of the parameter fitting process. The physical sky model is folded through the simulated detector response to calculate the expected counts. After analysis, background contamination from residual unaccounted for sources is estimated to be under 10%. The final results are typically made available electronically and with supporting scripts to extract the data in useful ways.

4.2.2 Ground Cherenkov telescopes

Ground Cherenkov gamma ray telescopes are Earth-based instruments for the detection of gamma rays. As indicated by their name, they observe the Cherenkov radiation produced when a high energy photon enters the Earth's atmosphere. The Cherenkov telescopes have large collection areas of 100s of m^2, much larger than the smaller areas of space telescopes, because they use the Earth's atmosphere itself as a detection medium. More properly, the Cherenkov telescope images the Cherenkov radiation emitted by the cascade of charged particles that is produced when a high energy photon hits the Earth's atmosphere, some 10s of km in the sky. VERITAS is a four telescope array that can detect photons with energies between 85 GeV and 30 TeV. HESS is a five telescope array, with an energy range of 30 GeV to 100 TeV, and MAGIC is a two telescope array with an energy range of 25 GeV to 30 TeV.

The photons that are detected are produced by bremsstrahlung and decays of unstable products of the initial high energy interaction. Due to the height and energy of the initial interaction, the Cherenkov flash covers an area of hundreds of square meters at the surface of the Earth. That the full instrument is an array of telescopes spread out over hundreds of meters allows discrimination against other cosmic rays events, such as muons, which have a much narrower cone, as well as drastically improving the angular and energy resolution of the system. Significant backgrounds to ground Cherenkov telescopes include hadronic showers, starlight, moonlight, and cosmic ray generated muons.

Table 4.1: IGRB fit parameters

Foreground model	α	I_{100} (MeV^{-1} cm^{-2} s^{-1} sr^{-1})	E_{cut} (GeV)
A	2.32 $\pm$ 0.02	0.095 $\times 10^{-7}$ $\pm$ 0.08 $\times 10^{-7}$	2.79 $\pm$ 52
B	2.28 $\pm$ 0.02	1.12 $\times 10^{-7}$ $\pm$ 0.08 $\times 10^{-7}$	206 $\pm$ 31
C	2.26 $\pm$ 0.02	0.78 $\times 10^{-7}$ $\pm$ 0.07 $\times 10^{-7}$	233 $\pm$ 41

4.3 Diffuse gamma rays

Observations of the gamma ray sky show the existence of a diffuse flux of high energy photons, extending well into the gamma range of the spectrum. This flux was first observed by the SAS-2 satellite [273], and later confirmed by the EGRET instrument [274]. This diffuse flux has many known contributions, including active galactic nuclei [275, 276, 277] now confirmed by Fermi [278], star-forming galaxies [279, 280], merging galaxy clusters [281], millisecond pulsars [282, 283], ultra high energy cosmic ray scattering [284, 285], as well as numerous other unresolved sources. Most point sources contribute anisotropically, so their contribution to the diffuse flux is small [286, 287]. Once the contributions of the known sources have been subtracted off, the remaining part of the diffuse flux is called the Isotropic Gamma Ray Background (IGRB).

Annihilations of dark matter particles in the galactic halo and beyond can contribute to this flux [288], and if dark matter is present, it would be exceedingly odd if there was no contribution. One can then use the observed flux to place bounds on the properties of annihilating dark matter. In fact, for WIMP scale dark matter annihilation cross sections, predicted halo fluxes from dark matter annihilations are comparable to the observed IGRB, allowing for meaningful comparisons to be made.

The Fermi-LAT instrument is uniquely capable of measuring the diffuse low energy gamma spectrum. The discrimination between charged particles and gamma rays that an instrument such as Fermi allows enables the measurement of the diffuse flux, which is notoriously difficult to do with ground-based Cherenkov telescopes [289] due to charged particle backgrounds, but which makes up the majority of gamma rays detected in the LAT. We consider results reported by the Fermi collaboration after some 50 months of observations with the LAT instrument [290] in the 20 MeV to 300+ GeV range. These observations have identified thousands of gamma sources.

Due to the high intensity of the galactic plane, measurements of the IGRB focus on the off-plane regions of the sky at high latitudes. The Fermi-LAT collaboration parameterizes [290] the IGRB spectrum for $|b| > 20^o$ by a power-law with exponential cutoff:

$$\frac{d\mathcal{N}}{dE} = I_{100} \left(\frac{E}{100 \text{ MeV}} \right)^{-\alpha} \exp\left(-E/E_{cut}\right). \tag{4.10}$$

The parameters I_{100}, α and E_{cut} are presented in Table 4.1, obtained from reference [290] where they were obtained by a χ^2 regression fit to the data. The fit is plotted for the three foreground models in Figure 4.4.

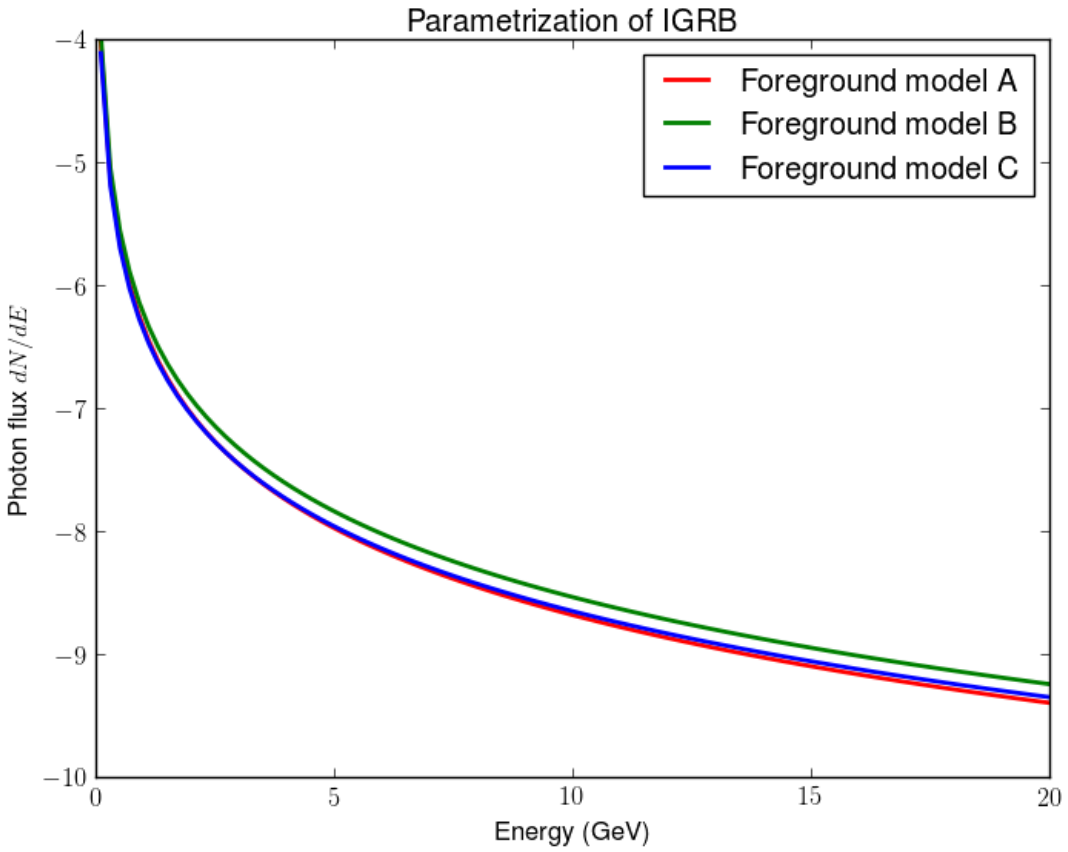

Figure 4.4: Plot of the functional parameterization of the IGRB photon flux $\frac{d\mathcal{N}}{dE}$ by the Fermi collaboration in reference [290] for each of the three foreground models. The expression is presented in Equation (4.10), and the numerical values of the parameters are reproduced in Table 4.1. The main point that is illustrated by this Figure is that the foreground models introduce little variation in the parameterized IGRB.

The foreground models A, B and C are different emission models of the contributions of diffuse sources including contributions from interactions between cosmic rays and interstellar gas, inverse Compton scattering of cosmic electrons in the solar radiation field, and emission from catalogued gamma sources. In general, the effects of the foreground models can have very important effects on the derived bounds [291] (see also Appendix A of reference [292] for explicit details).

With the above observed IGRB flux, one can do analysis to obtain exclusion limits for various models of particle dark matter. Fermi has done an analysis [292] searching for the annihilation signals of a generic WIMP in the IGRB, finding nothing of note. They have noted that the IGRB is a difficult place from which to extract a signal, as so much information is lost in the required integration over the sky to obtain event rates. There are, however, other ways of extracting information from the IGRB.

There is also the possibility of looking for signatures of annihilating dark matter in the anisotropies of the IGRB [264, 293], observations of which have been reported by Fermi [294]. The IGRB is expected to be primarily isotropic. Anisotropies in the IGRB are mostly due to point sources, primarily blazars, but there is the possibility that regions of different dark matter density in the galactic halo, called subhalos, may produce them as well. There is also an expected anisotropy (a dipole) from dark matter annihilation in the direction of the galactic core, due to the higher predicted dark matter density in that region (see Section 4.4), but because of the large number of gamma sources in the core, such an anisotropy is much more difficult to extract. The basic means to search for IGRB anisotropies is to expand the flux in spherical harmonics to get the power spectrum. One can take a dark matter annihilation signal and subhalo distributions obtained from numerical simulations (ie Aquarius [295]) to calculate the resulting contribution to the power spectrum [296] and compare against the observed power spectrum. A general procedure to perform this analysis for a generic particle physics model of dark matter is found in reference [264]. The main weakness in this approach, aside from the obvious low signal strength that is inherit in all dark matter searches, is the reliance on simulations of dark matter subhalo structure, a field which is so far entirely theoretical. The limits imposed by this technique are weak so far, but they will become stronger as more data on the IGRB is obtained and analyzed.

4.4 Galactic core excess

It is obvious that regions of higher dark matter density will produce a stronger gamma ray signal from annihilations. In fact, the gamma ray flux will depend quadratically on the dark matter density along a given line of sight. This makes sense, as annihilation requires a pair of particles. Targeted searches then should look at regions of higher local dark matter density, and the galactic core region is one such. In fact, due to the expected high dark matter density in the core region and its proximity to Earth, the galactic center is expected to be the brightest source of gamma rays from annihilating dark matter in the sky [297].

The core region is very bright in the gamma sky, due to the number of high energy processes involving

compact objects that happen there. In addition to their direct gamma yields, the charged products of these processes produce secondary gamma rays due to their interactions with interstellar gas and the strong radiation fields in the core region. There is also the presence of the Sagittarius A source. The presence of this background and possible foreground makes extraction of any diffuse spectrum hard.

An independent analysis of Fermi-LAT data by Goodenough and Hooper [298, 299] noted the existence of a spatially extended gamma ray emission component on top of the understood astrophysical gamma ray background sources. This excess is spherical in space, and the energy spectrum can be modelled by a power law $\sim r^{\Gamma}$ with Γ around 2.2-2.4, with a peak at a few GeV ($\sim$ 2-3). These features are consistent with a generic dark matter annihilation signal.

This analysis has since been repeated by a number of groups [300, 301, 302, 303], including the Fermi collaboration [304], who have all confirmed the presence of the excess to high statistical significance. Whether or not it is actually due to annihilating dark matter, however, is less certain. Popular alternative explanations include gamma ray millisecond pulsars [305] and interactions of high energy cosmic rays with interstellar gas [306], though more recent studies indicate that no more than 5-10% of the excess could be caused by millisecond pulsars [307, 308]. There are also numerous other non-exotic astrophysical explanations [309, 310, 311]. In the context of dark matter annihilations, the excess has been studied extensively in the literature [300, 299, 312, 313, 306, 304, 314].

The excess appears to exist, but all analysis depends on the validity of the Fermi background models [304]. In their analysis, the Fermi collaboration explored multiple specialized interstellar emission models to analyze the excess [304]. The excess is generally the same between various publications and foreground/background models, though the spectral shape and normalization of the excess is dependent on galaxy modelling parameters [302]. The extent of this dependence is being explored further. A new analysis of the gamma ray signals of galaxy clusters is reported to provide constraints, under certain assumptions, on dark matter annihilation cross sections that rule out a dark matter interpretation of the galactic core excess [315]. As well, observations from dwarf spheroidal galaxies (see Section 4.5) appear to be in conflict with the excess [316, 317], though these can be avoided if the dark matter annihilation cross sections depend strongly on the velocity [318].

A number of fits to the excess have been provided in the literature, though usually without reporting the normalization factors. We choose to work with the parameterization provided in reference [319], which includes all relevant quantities.

Figure 4.5 is a plot of the excess above the standard diffuse emission models. It has a peak at 1-3 GeV and a tail that continues out to over 100 GeV. There are large uncertainties in the excess, which become even larger in the tail. Multiplication by E^2 when plotting and presenting astrophysical fluxes is traditionally used to emphasize features in steeply falling spectra. The position of the peak in the photon spectrum scales linearly with the mass of the annihilating dark matter particle.

Reference [319] includes fits to a log-parabola spectrum

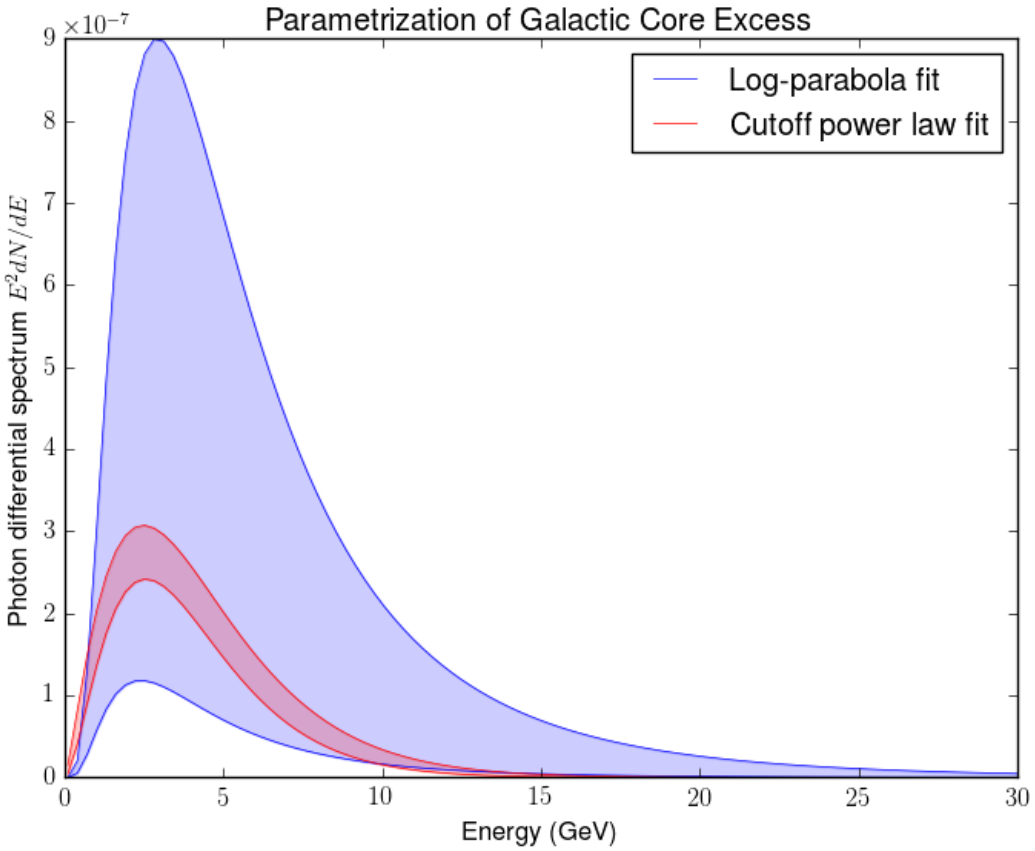

Figure 4.5: Plot of the functional fits to the galactic core excess from reference [302], where the shaded regions enclose the error bars on the fit parameters. Numerical values for the parameters are reproduced in Table 4.2, and the expressions themselves appear in Equations (4.11) and (4.12) in the text.

Table 4.2: Galactic core excess fit parameters

Parameter	Log-parabola fit	Power law fit
N_0 (MeV^{-1} cm^{-2} s^{-1} sr^{-1})	$1.20 \times 10^{-12} \pm 0.46 \times 10^{-12}$	$1.03 \times 10^{-9} \pm 0.56 \times 10^{-9}$
α	-4.28 $\pm$ 0.18	-
β	0.959 $\pm$ 0.026	-
γ_c	-	0.45 $\pm$ 0.21
E_b (MeV)	100	-
E_c (GeV)	-	1.65 $\pm$ 0.20
E_0 (MeV)	-	100

$$\frac{d\mathcal{N}}{dE} = N_0 \left(\frac{E}{E_b}\right)^{-(\alpha+\beta \ln(E/E_b))} \tag{4.11}$$

and a power law spectrum with exponential cutoff

$$\frac{d\mathcal{N}}{dE} = N_0 \left(\frac{E}{E_0}\right)^{-\gamma_c} \exp\left(-E/E_c\right). \tag{4.12}$$

Numerical values for both of these fits are provided in Table 4.2, including errors. The functions themselves are plotted, with error regions included, in Figure 4.5. The region of interest is a $7^o \times 7^o$ box centered on the center of the galaxy ($|b| < 3.5^o$, $|l| < 3.5^o$ in terms of galactic coordinates). They use a modified NFW profile with parameters as described in the reference. The reference finds a best fit to dark matter of mass 39.4 GeV annihilating to $\bar{b}b$ with an annihilation cross section of $\sigma v \simeq 5.1 \times 10^{-26}$ cm^3/s.

The fit is to Fermi-LAT data obtained from the period of August 2008 to May 2013. The observations are modelled including the diffuse background as observed by Fermi, a set of catalogued point sources, a handful of extra point sources, as well as the effects of Sgr A* and a potential new diffuse component. Diffuse emission is modelled with GALPROP [268]. Each of these contributions is modelled separately, and in various combinations. Also considered are bremsstrahlung emissions from molecular gas interactions with high energy electrons [320], which are a large contributor to galactic center gamma rays. The parameters in Table 4.2 are for the full model with all the above sources included.

The excess can be fit by a generic dark matter particle annihilating to photons through SM channels with a mass in the 10s of GeV. In particular for WIMP scale cross sections ($\sigma v \simeq 3 \times 10^{-26}$ cm^3/s), if the dominant annihilation channel is $\tau^+\tau^-$, a 10 GeV mass provides the best fit, and a 30-60 GeV particle provides the best fit if annihilating dominantly to $\bar{b}b$ quark pairs, as mentioned above. It should be noted that the dark matter annihilating dominantly to leptons is now disfavoured by data from the cosmic positron spectrum [309].

A dark matter model can be tested against the galactic core excess simply by computing the expected spectrum of the model in the galactic core region and then comparing with one of the fits. A full analysis

requires a fit against the actual data, but a preliminary examination is possible with one of the parameterizations that have been reported, such as Equation (4.11) or Equation (4.12). Any dark matter candidate in this mass range must satisfy the direct detection bounds (see Chapter 3) as well, a prospect that is becoming increasingly difficult for non specialized models.

4.5 Dwarf spheroidal galaxies

Some of the more promising targets for dark matter annihilation searches are dwarf spheroidal galaxies (dSphs), which are small clusters of stars that orbit larger spiral galaxies. While small and lacking significant astronomical activity, dSphs are possibly the most common type of galaxy in the universe, and are believed to be relics of the formation of spiral galaxies. They have very old stellar populations and large separations between stars. They are almost empty of visible gas and dust, which means they do not significantly emit scattered x-rays like most extended astronomical bodies. Satellite galaxies of the Milky Way in particular are close enough to be observed in detail, as are some dSphs of other local group galaxies [321].

Dwarf satellites are good targets for dark matter searches for a few reasons. First, they are relatively sterile. They lack many of the conventional mechanisms for the production of gamma rays [322, 323] They are also generally far from the galactic disk in the sky, which means they are far from the high gamma foreground it produces. Finally, they have a very large dark matter content. Indeed, dSph light-to-mass ratios are some of the smallest of observed astronomical objects [324], indicating up to $\mathcal{O}(10^3)$ more dark matter than baryonic matter. These properties make them a perfect place to look for annihilating dark matter.

The mass of a dSph can be accurately estimated from only stellar velocity measurements [39, 40]. Using orbital physics, one can obtain the required mass to keep the dwarf galaxy stable from the stellar velocities. The dynamics of dSphs are similar to that of globular clusters, but the dwarf galaxies occupy a much larger spatial extent, which indicates a much higher ratio of gravitating mass to light than is found in globular clusters.

In general, a telescope will observe photon events from the region of interest, and so the fundamental observational quantity of gamma ray astronomy is the number of photon events N_γ. By using knowledge of the instrument, we can convert the number of events into information about the photon flux. Then, using the details discussed previously in Section 4.1, one can use this information about the photon flux to extract information about the theoretical particle physics model that contributes to the flux, such as the annihilation cross sections.

This process is described further here for a Cherenkov telscope. The number of events with an energy greater than some minimum value E_{min} observed by a Cherenkov telescope is given by

$$N_\gamma\left(E \geq E_{min}\right) = T_o \int_{E_{min}}^{\infty} dE \mathcal{A}_{eff}\left(E\right) \frac{d\Phi_\gamma}{dE} \tag{4.13}$$

where T_0 is the observation time, and $\mathcal{A}_{eff}\left(E\right)$ is the energy dependent effective area of the telescope. As

Table 4.3: Astrophysical J values for dSphs

Dwarf	$\log_{10} J$
Segue I	19.5±0.29
Draco	18.8±0.16
Leo II	17.6±0.8

usual $d\Phi_\gamma/dE$ is the differential photon flux per unit energy, which will depend on the annihilation rate in the target, as discussed in Section 4.1.

The effective area is essentially the detection cross section of the instrument to a uniform photon flux. In general, it will rise as a power law function of energy. The effective area is in general different for each individual observation, as changes in observation angle and target location in the field of view have significant effects, and numerical values are almost impossible to obtain from the literature. Collaborations will estimate the effective area from Monte Carlo calculations of the detector response to simulated air showers. The effective area can be expressed in terms of both true energy of the photon and the reconstructed energy of the event. The gamma flux from a source is estimated from the number of excess events passing the selection cuts for a particular data set using the effective area of the instrument.

Fermi [316] has reported results from the observation of a number of dSphs near the Milky Way. They have observed no significant excess in any of them. Reported bounds are approaching the canonical thermal cross section limit but are not yet there.

When the instrument collaborations report their results, they generally include the astrophysical J values used in their calculations. See also [325] for those used by in the Fermi calculations. We include the J factors in Table 4.3 for some dwarfs that are considered in Section 4.8.

It should be mentioned that a potential signal was found in the Milky Way satellite Reticulum II by an independent collaboration analyzing Fermi data [326] with a 3.7σ significance. The analysis found that a basic WIMP with the standard annihilation cross section channels and a mass of 50-100 GeV, up to uncertainties in the astrophysics of the dSph, could account for the excess. However, subsequent observation by Fermi [327] revealed that the excess was no longer significant, and Reticulum II observations have since been used to calculate upper limits on the dark matter annihilation cross section [328].

4.6 Monochromatic line searches

The ideal gamma ray signal of dark matter annihilation would be a monochromatic line. That is, a peak in the gamma ray spectrum above the background at a characteristic energy due to the resonance of direct dark matter annihilation to high energy photons. Such a signal would be very strong evidence for the annihilation of an exotic component of the target region, as no signal of this kind is expected from standard astrophysical processes. No such signal has yet been confirmed as being exotic in origin, but the searches continue. This

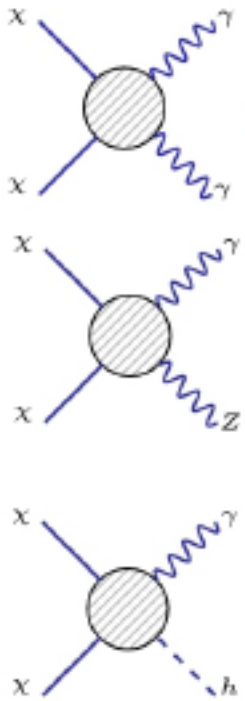

Figure 4.6: Effective field theory diagrams illustrating annihilation processes by which monochromatic photon lines can be produced. Generally, the blob represents a loop order process of some kind. The $\gamma\gamma$ case is of primary interest.

Section discusses searches for line signals by Fermi and the Cherenkov telescopes and the bounds on the dark matter annihilation cross section that result from that nonobservation.

We note that the monochromatic line is a special case of the photon spectrum, distinct from the more generic diffuse fluxes that have been discussed until now. The line searches discussed in this Section also differ from dSph studies as they consider a much larger region of the sky.

As WIMP dark matter is not expected to interact with the electromagnetic force at tree level, the direct annihilation to photons would need to be a loop order process, meaning a suppression factor of 1-4 orders of magnitude compared to a tree level annihilation cross section. The internal structure of the process is model dependent, but likely would involve a loop of electromagnetically charged particles, such as SM fermions. Analysis of such a signal is carried out for a specific model in Section 4.8. In general, one can expect to look for both $\gamma\gamma$ and γX final states, where X is a neutral particle, usually the Z boson or the SM Higgs. In models with a larger beyond the SM sector, this could also be a new particle. These processes are illustrated in an effective field theory approach in Figure 4.6.

The direct annihilation will produce photons of energy

$$E_{\gamma\gamma} = m_{DM} \tag{4.14}$$

for annihilation to two photons of equal energy ($\gamma\gamma$ channel, in the rest frame of the annihilation), or

$$E_{\gamma X} = m_{DM}\left(1 - \frac{m_X^2}{4m_{DM}^2}\right) \tag{4.15}$$

for annihilation to the γX channel, where m_X is the mass of the X particle. The line signal can be described by a Dirac delta convolved with the energy dispersion introduced by the instrument, which is usually modelled by a Gaussian:

$$\mathcal{G}(E_\gamma, \omega, E_0) = \frac{1}{\sqrt{2\pi}E_0\omega}\exp\left(-\frac{(E_\gamma - E_0)^2}{2E_0^2\omega^2}\right) \tag{4.16}$$

where $\omega = \zeta/w$ with ζ being a measure of the detector energy resolution, varying between 0.1 and 0.01 for GeV photons, and $w = 2\sqrt{2\log 2}$ the full-width half-max of the Gaussian.

HESS looks at the core region and the region off the galactic plane [329, 330]. Fermi [331] looks at a 20^o $\times$ 20^o square around the galactic core with point sources removed and at the sky at angles $|b| > 10^o$, away from the galactic plane and its heavy background. Fermi presents 95% confidence upper limits [331] on the flux

$$\frac{d\Phi_\gamma}{dE} = \frac{1}{8\pi}\frac{\langle\sigma v\rangle_{\gamma\gamma}}{m_{DM}^2}2\delta\left(E_\gamma - E\right)\int\frac{dJ}{d\Omega}d\Omega \tag{4.17}$$

and the resulting bounds on the annihilation cross section to photons $\langle\sigma v\rangle_{\gamma\gamma}$. The dark matter profile is an input to these bounds, and unlike the case of dSph bounds, the profile is important. It has been found that limits computed using the Einasto profile are generally stronger than limits computed using the NFW profile.

An example of what a potential line signal might look like is the 130 GeV Fermi line, appearing in Fermi data of the region near the galactic core [332, 333, 334]. The line generated a great deal of excitement, as there was negligible foreground in the field of view, indicating a conventional explanation to be unlikely. However, further observations and analysis led to a lower statistical significance of the signal [335], and eventually a statement by the Fermi collaboration that there was no longer enough evidence to support the line's existence [331]. Nonetheless, the Fermi line provoked the development of a variety of theoretical techniques to match particle dark matter models to the signal, which will no doubt prove useful if a non-vanishing line signal is ever observed.

While the 'smoking gun' is the observation of a distinct monochromatic line, there are also other indications of dark matter annihilations directly to photons. Gamma lines are accompanied by a lower energy continuum flux from radiative corrections and prompt decays of other final state particles. This flux is more pronounced for the case of dark matter annihilations to γX final states, where the X decays electroweakly, producing many photons along the way. Fermi and HESS look for this continuum as well as the monochromatic line, but obviously bounds are much less stringent for such a weak signal.

This continuum allows exploration of dark matter mass ranges otherwise inaccessible, however. In reference [336], the authors have performed an analysis on Fermi and HESS data that uses the expected continuum

to probe for dark matter annihilations whose monochromatic line would be well out of the range of even the ground based Cherenkov telescopes. Their limits extend up to 100 TeV, though they are very weak (on the order of $10^{-22.5}$ for annihilations to $\gamma\gamma$ and 10^{-23} for the γZ and γh channels). Despite their weak constraints, these bounds are among the only experimental limits on dark matter at that mass scale.

4.7 Other indirect signals

As mentioned at the beginning of this Chapter, the gamma ray signal is not the only possible signal of the annihilation of dark matter in the halo. There are other potential channels which are being actively studied, though they provide much weaker constraints than the gamma ray signal. In this Section, a basic overview of each of these secondary indirect detection signals is provided, with the reader referred to the literature for a more complete discussion.

4.7.1 Antimatter signals

A significant component of charged cosmic rays are antimatter; primarily positrons and antiprotons, but also containing light anti-nuclei such as deuterium and helium. It is possible that a dark matter annihilation signal is present in the flux of cosmic antimatter, as dark matter is generically expected to respect the CP symmetry in its annihilations (that is, is is expected to favor neither matter nor antimatter in its annihilation products). Antimatter signals of dark matter annihilations have been considered for decades [337, 338, 339]. Such antimatter signals are sought [340, 341, 342], and have been considered in all of the above mentioned channels (positrons, antiprotons, antideterium, antihelium).

The main instruments of interest in the search for antimatter signals of annihilating dark matter are PAMELA [343] (2006-2016) and its sucessor aboard the ISS, AMS-02 [344] (2011-present). As well, the GAPS balloon experiment will begin taking data shortly [345]. Both PAMELA and AMS are magnetic spectrometers that measure the direction and energy of charged particles passing into them, though the latter is a much more sophisticated device.

The basic strategy is more or less the same as the case of searching for a gamma ray signal. Annihilation cross sections to final states are computed and using spectral functions for the relevant final states, a source term can be generated. The positron case is the simplest one, and source spectra for composite antimatter particles are more complicated, requiring models for hadronization [259] and for nucleation (see [346] for details). Nucleation in particular relies on many simplifying assumptions.

In contrast to the case of gamma rays however, the source spectra do not propagate intact to instruments on the Earth (or in Earth orbit). The galaxy contains numerous magnetic fields on a variety of scales, which alter the propagation of charged particles through many mechanisms, most of which are poorly understood. More details are available in the literature [347, 259, 348]. Several of these effects produce the diffuse secondary gamma rays which were discussed in Section 4.1.3. Propagation of charged particles in the galaxy

can be approximately modelled by a diffusion-convection equation, which is derived from the Fokker-Planck description of particle transport, with a number of terms introduced to account for various effects:

$$\nabla \cdot \left[K(\mathbf{x}, E)\nabla\psi(\mathbf{x}, E, t) - \bar{V}_c(\mathbf{x}, E)\psi(\mathbf{x}, E, t)\right] - \Gamma_{ann}(E)\psi(\mathbf{x}, E, t) + \mathcal{Q}(\mathbf{x}, E, t)$$

$$+\frac{\nabla \cdot \bar{V}_c(\mathbf{x}, E)}{3}\frac{\partial}{\partial E}\left[\frac{p^2}{E}\psi(\mathbf{x}, E, t)\right] - \frac{\partial}{\partial E}\left[b_{ion}(E) + b_{Col}(E)\psi(\mathbf{x}, E, t)\right]$$

$$-\frac{\partial}{\partial E}\left[\frac{1+\beta^2}{E}K_{pp}(E)\psi(\mathbf{x}, E, t)\right] + \frac{\partial}{\partial E}\left[\beta^2 K_{pp}(E)\psi(\mathbf{x}, E, t)\right] = \frac{\partial}{\partial t}\psi(\mathbf{x}, E, t). \quad (4.18)$$

In the above are, without going through a term by term description, contributions from diffusion, convection, particle annihilation and production, and energy loss through various mechanisms such as collisions. The propagation of cosmic rays is discussed in detail in the monograph [348], and in the review [347]. One generally assumes isotropic spatial diffusion, a homogenous diffusion coefficient, and a diffusion volume in the shape of a cylindrical block. Only specific interactions between the most important particle species are taken into account. This equation generally requires numerical solution for anything but the most trivial cases, using a variety of special purpose software packages (such as GALPROP [268]). Reported results generally use a number of approximations, and semianalytic solutions are also possible by approximating the Green's functions of the equation.

The source spectra can be convolved with the solution to the propagation equation to obtain the local spectra of antimatter at Earth. As in the case of gamma rays, local fluxes for generic WIMP models have been computed and are available through the PPPIDM project [259]. All types of charged particles appear to have a power law spectrum.

Antimatter studies of dark matter are regularly published, though not nearly as frequently as gamma ray studies. After the recent observations of the antiproton spectrum by AMS, and the older positron excess [349], there have been a number of studies discussing various models of dark matter [350, 351, 352, 353]. Nothing significant has been noted. Nonetheless, the possibility of an antimatter signal of annihilating dark matter is an exciting one that will continue to draw attention.

4.7.2 Neutrino signals

A more speculative indirect signal of the annihilation of dark matter is the neutrino signal, which was first proposed in the late 90s [354]. For a generic WIMP, this signal is more difficult to detect than potential gamma or antimatter signals, and has at least as much uncertainty. It has been studied much less, though it has become more popular now that the IceCube neutrino telescope has begun operation.

Dark matter annihilation cross sections are of the order 10^{-26} cm^2, leading such low event rates that it is very difficult to extract a signal from even small amounts of background. To boost the potential signal to noise ratio, it would be beneficial to target a region where the dark matter density is higher relative to

background generating sources. This is the motivation for targeting dwarf spheroidal galaxies, as discussed in Section 4.5. There are however options which are much closer.

Cold dark matter in the galactic halo has so little energy that it is possible for it to become captured in massive bodies. For a detailed discussion of this process, which is mostly glossed over here, see reference [355]. While in general massive bodies such as stars or planets pass through the halo without interaction, there will be the occasional scattering event of a dark matter particle off of the atomic nuclei making up the body. These scattering events may transfer enough energy to the body that the dark matter particle becomes unable to escape the gravitational potential well of the body, becoming captured.

As this occurs, over time the body will accumulate a population of dark matter particles orbiting its center of gravity. The dark matter particles will also annihilate at a rate that is proportional to their number density, with increasing frequency as the local abundance rises:

$$\frac{dN}{dt} = \Gamma_{capt} - 2\Gamma_{ann} - \Gamma_{evap} \tag{4.19}$$

After some time, the capture rate and the annihilation rate will balance out and there will be a stable equilibrium population, generating an equilibrium annihilation signal. For most astronomical bodies, a generic WIMP with standard weak-scale interactions will have an equilibrium annihilation rate significantly higher than its halo annihilation rate.

The annihilation rate can be written

$$\Gamma_{ann} = \frac{1}{2} C_{ann} \tanh^2 \left(\sqrt{C_{ann} A} t \right) \simeq \frac{1}{2} C_{ann} \tag{4.20}$$

where A is a numerical value and the quantity C_{ann} is approximately for standard WIMP dark matter

$$C_{ann} \simeq \langle \sigma v \rangle \left(\frac{G_N m_{DM} \rho_{sun}}{3 T_{sun}} \right)^{3/2} \tag{4.21}$$

where the solar density and temperature are near the center of the Sun. The capture rate is proportional to the ratio of the dark matter density ρ_{DM} and mass m_{DM}, and the spin dependent and spin independent nuclear recoil cross sections σ_{SD} and σ_{SI}:

$$\Gamma_{capt} \sim K \frac{\rho_{DM}}{m_{DM}} \left(A \sigma_{SD} + B \sigma_{SI} \right) \tag{4.22}$$

In the above K, A, and B are numerical constants. The evaporation rate Γ_{evap} describes how frequently WIMPs fee themselves from the trapping gravitational potential, and can usually be neglected.

The majority of annihilation products will be lost in the capturing body, but neutrinos have a very small interaction cross section with matter, and so a sizeable fraction of the neutrino flux will escape. Detection of this neutrino flux can then proceed by standard means using neutrino telescopes on Earth. The neutrino spectrum at production is different from the spectrum of the flux that arrives at our detectors here on Earth, and that needs to be taken into account. These differences arise primarily from neutrino oscillations.

It has been known for some time that neutrino mass eigenstates and flavor eigenstates are different, and this manifests as an apparent nonconservation of flavor, or oscillation between flavors of a flux of neutrinos travelling between a source and a detector. Taking oscillation effects into account is crucial to predicting the correct flux, though it is not a particularly complicated procedure [356, 357]. These effects are typically taken into account by the simulation software.

Both the Earth [358] and the Sun have been considered as potential capturing bodies. They each have disadvantages. The Earth is comparatively small, and hence has a small equilibrium annihilation rate. This is not quite compensated for by the low background proximity in comparison to the Sun. The Sun is further away, and produces its own high energy neutrino spectrum from internal fusion processes, as reproduced in Figure 4.7. The energy ranges of solar neutrinos are similar to those from the annihilation of dark matter for much of the reasonable WIMP parameter space. Analysis of any potential solar signal thus requires a detailed understanding of the solar neutrino spectrum and the ability to extract an anomalous signal from the observed flux. In addition to the Earth and Sun, neutrino signals from annihilating dark matter in a number of sources have been studied, including the galactic halo [359, 360], the galactic core [361], and from beyond the galaxy [362].

There are a handful of other contributions to the overall neutrino flux that can act as backgrounds to any potential dark matter signal. These include the dominant solar and atmospheric neutrinos, but also geo neutrinos, cosmic neutrinos, and reactor neutrinos. Of these, reactor neutrinos, resulting from heavy concentrations of decaying isotopes, typically found in nuclear reactors, are negligible, as are cosmic neutrinos. Geo neutrinos, produced by nuclear processes within the Earth, are too low energy to provide a measurable background to a potential neutrino dark matter annihilation spectrum. The real backgrounds are from solar neutrinos, produced by the Sun's fusion processes, and atmospheric neutrinos, produced when high energy cosmic rays hit the atmosphere and initiate a particle cascade. These backgrounds can only be accounted for by careful modelling of their spectra. Understanding these spectra is of great importance for the progression of a number of fields of physics. One can look for an excess of neutrinos in a region of the spectrum that should not contain as many solar or atmospheric neutrinos and try to fit the excess to an annihilation spectrum of some kind. Given the expected event rates for the detection of dark matter neutrinos, this is a long and painstaking process.

Theoretical calculations are complicated by incomplete knowledge of the annihilation cascades which produce neutrinos and how they are altered by the stellar medium. Processes involving hadronization and the subsequent electroweak decays of hadrons in the solar plasma are a particular issue. The neutrino spectra from dark matter annihilations at the source are usually computed using standard Monte Carlo simulation packages [364, 365], which take these secondary effects into account. Neutrino oscillations also need to be taken into account when simulating the local flux at the detector after propagation from the production region [366, 356, 357]. In practice, oscillation calculations are combined with the software simulating production to provide a final flux at the detector.

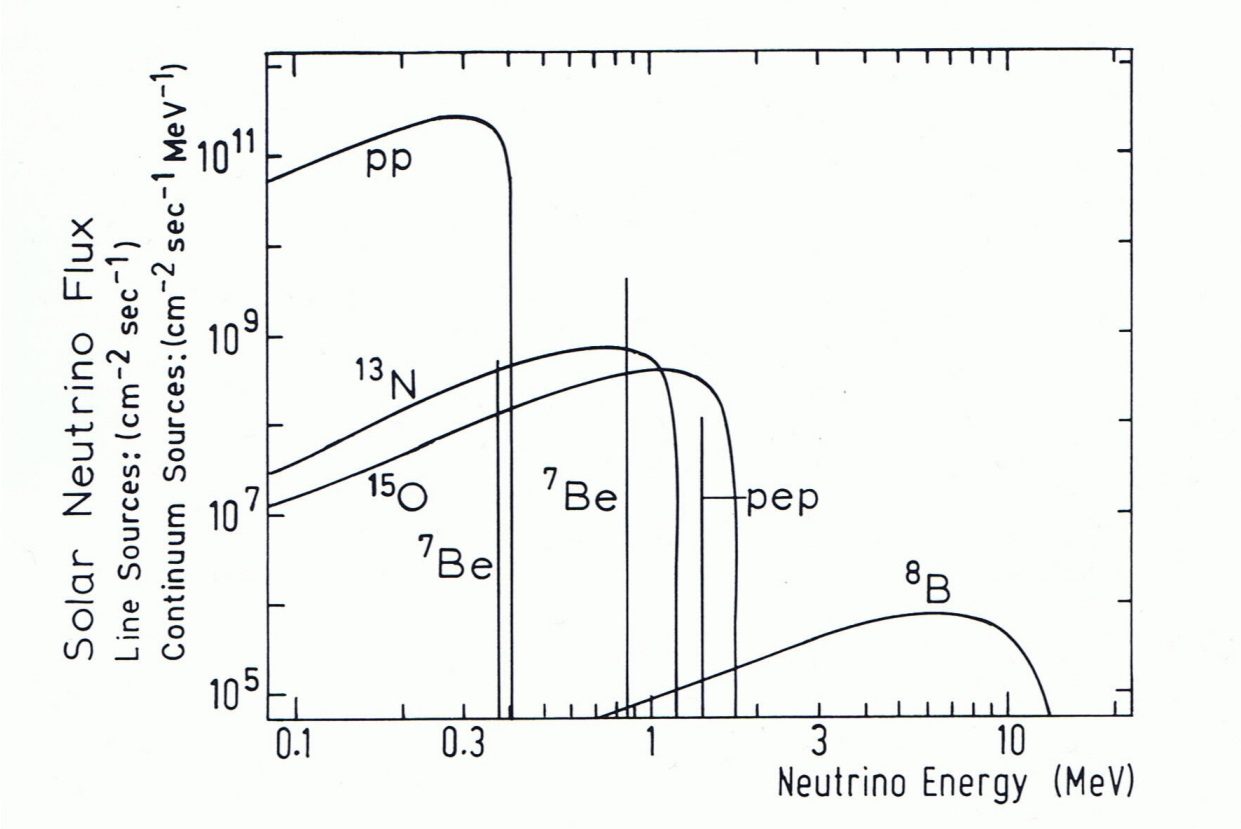

Figure 4.7: Neutrino flux from a variety of processes occurring in the sun. Figure originally appeared in reference [363].

IceCube [367], and its predecessor AMANDA [368], are neutrino telescopes near the South Pole. They use the Antarctic ice sheet as their detection medium. The basic principles behind their functioning are as follows. Neutrinos passing through matter interact with that matter with a very low rate, but through those weak force interactions, various leptons can be produced. In particular, through charged current interactions, a neutrino with a specific weak flavor may produce a charged lepton with that flavor. These charged particles then continue to propagate through the medium and, if they have enough energy, they will emit Cherenkov radiation. This radiation is obviously absorbed almost instantly, unless the medium is near transparent, such as highly pure Antarctic ice. The IceCube telescope consists of several arrays of optical detectors arranged deep within the ice, designed to pick up this Cherenkov radiation. The arrays are distributed so that they can pick up multiple photons emitted by the same charged particle and so determine the direction of travel of the particle as well as its energy. This allows discrimination against background events, such as charged particles from cosmic rays and other sources. To further distinguish these events from neutrino events, only upward going charged particles are counted. This is because downward going particles could have come from anywhere, while upward going particles would have had to be produced by something that could propagate through the entire volume of the Earth, such as a neutrino. These telescopes search for a neutrino flux from dark matter annihilations in the Sun, among other things.

SuperKamiokande [369] is a liquid water based neutrino telescope that operates on much the same principles as the ice based telescopes discussed above. Neutrinos that pass through the bulk of the detector occasionally interact with it, and if those neutrinos are muon neutrinos, this interaction will produce a muon that can be observed by its Cherenkov radiation. The Kamiokande family of experiments was constructed with the goal of solving the solar neutrino problem, which it did in the late 1990s [370], providing evidence to support flavor oscillations of neutrinos. Since, the SuperKamiokande experiment has also sought an excess over the expected solar neutrino flux, an excess which could be due to dark matter annihilations as described above. No such excess has been observed [371].

While observations of the neutrino flux can be used to place bounds on the dark matter annihilation cross section, these observations can also be used to place bounds on the dark matter nuclear recoil cross section discussed in Chapter 3. This is because in the standard model of WIMP capture, the annihilation rate is proportional to the capture rate, which depends on the nuclear recoil cross section. The bounds on the nuclear recoil cross section tend to be more useful than bounds on the annihilation rate, which is subject to greater theoretical uncertainty. In fact, while bounds from the neutrino flux on the spin independent cross section are much weaker than current bounds from direct detection experiments, the spin dependent bounds reported by IceCube are competitive. This is because of the comparatively weaker bounds that direct detection experiments are capable of providing in the spin dependent sector. The bounds report by IceCube are included for comparison in Chapter 3.

4.8 Example: scalar Higgs-portal dark matter

As an example of the application of these techniques to a real (albeit simple) example, we consider the case of Higgs-portal scalar dark matter. The model is described in full detail in Appendix B. In this section, we will analyze the potential for the observation gamma ray signals from the annihilation of Higgs-portal scalars in the galactic halo.

Bounds on the annihilation cross sections from observations of dwarf spheroidal galaxies (Section 4.5) are obtained, as are bounds from non-observation of a spectral line due to direct annihilation to photons (Section 4.6). We also analyze whether a gamma ray signal could be hiding in the IGRB (Section 4.3). Finally, we consider whether or not the annihilation of Higgs-portal scalars could account for the observed gamma ray excess from the galactic center (Section 4.4).

Higgs-portal dark matter has been discussed in the context of gamma ray annihilation signals for years [260, 372], and also in the context of antimatter signals [341] and neutrino signals [373]. Many additional references also appear in the remainder of this Section.

4.8.1 Photon fluxes

The prompt photon fluxes from the annihilation of Higgs-portal scalars are computed from the nonrelativsitic annihilation cross sections as described in Section 4.1. The cross sections themselves are provided in Appendix B. We include only the channels t, b, c, τ, W, Z, h, as the others are subdominant. Of these, the t, W, Z, and h channels dominate when they are kinematically available. In this Section, we use the photon spectra as provided in reference [259].

4.8.2 Bounds on annihilation

We discuss possible observations of the annihilation of Higgs-portal scalars in signals from dSph galaxies, monochromatic lines, and the IGRB.

Dwarf spheroidal observations

This Section contains a comparison of predicted signals from annihilation of Higgs-portal scalars in a selection of dSphs.

First, we consider observations of the Segue I dwarf by VERITAS [374, 375, 376] and MAGIC [377, 378]. The Segue I dwarf galaxy was discovered in 2006 at a distance of 23±2 kpc from the solar system, at a latitude well above the galactic plane. Stellar velocity observations indicate it contains a great deal of dark matter [379], and it is close enough to be an attractive target, having a mass-to-light ratio of around 3400 [380]. VERITAS observed Segue I from Jan 2010 to May 2011, and observing no dark matter annihilation signal was thus able to place upper bounds on the flux of dark matter produced gamma rays [375, 376]. An overview of standard techniques used by VERITAS in their analysis is provided in reference [381]. We use

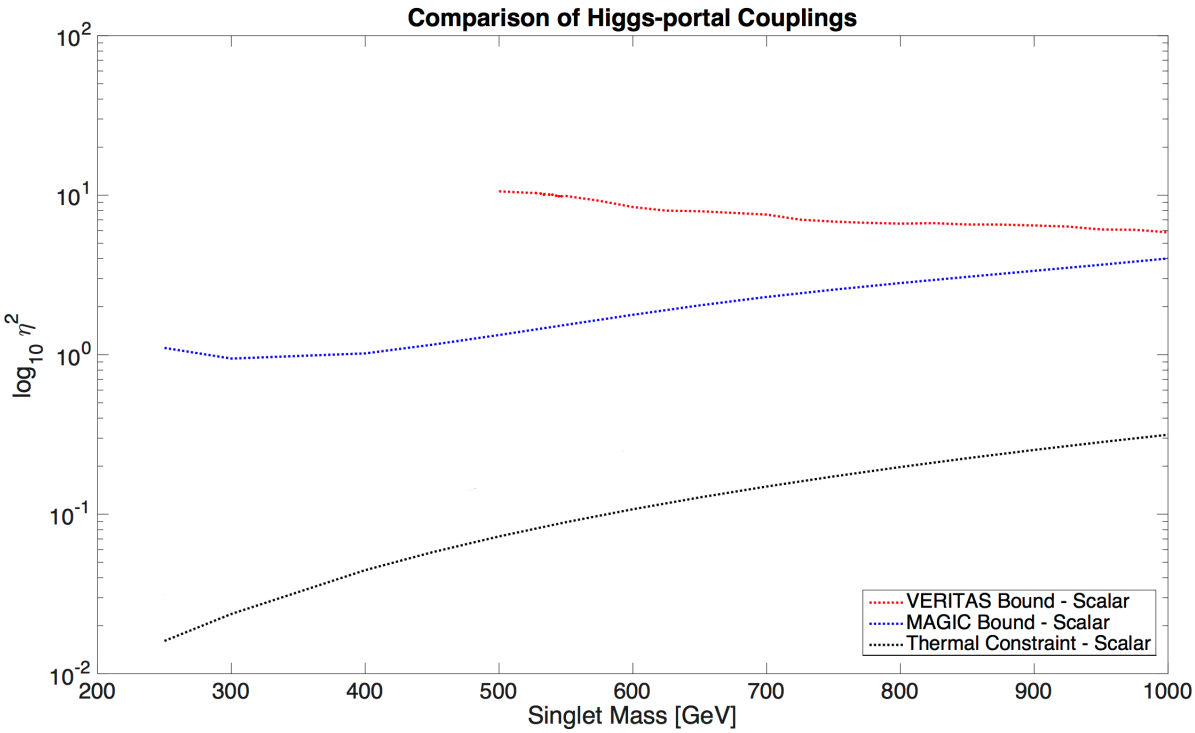

Figure 4.8: Bounds from Segue I on Higgs-portal scalar couplings derived from observations by VERITAS [375] and MAGIC [377]. Thermally constrained couplings over the same mass range are included for comparison.

Equation (4.13) as detailed in reference [376], with a value of $E_{min} = 300$ GeV. Because VERITAS is largely insensitive to energies below 300 GeV, scalar masses below 500 GeV are neglected. The relation (4.13) can be inverted and by inserting the reported event rates, one can place a bound on the annihilation cross section. The effective areas for the VERITAS Segue I observations were obtained through a request made to the VERITAS Collaboration. The MAGIC collaboration has reported bounds on dark matter for a variety of channels [378] based off of 158 hours of Segue I observations [377]. The modified statistical procedure applied and details of the astrophysical models used are available in reference [378].

The Higgs-portal annihilation cross sections are proportional to the Higgs-portal coupling η^2, which provides a convenient means of presenting exclusion bounds. We extract the dependence on the coupling from the cross section and present the exclusion bounds derived from the VERITAS and MAGIC observations on the Higgs-portal coupling in Figure 4.8. These bounds were calculated as described above from VERITAS event numbers and derived from MAGIC data using the Higgs-portal annihilation spectra, rather than generic annihilation channels. We note that the bounds presented for the VERITAS data are consistent with those reported for the annihilation cross section of a generic WIMP [375].

The bounds form observations by MAGIC are stronger than those provided by VERITAS for the mass range considered, while the thermally constrained couplings are clearly much smaller. This leads us to con-

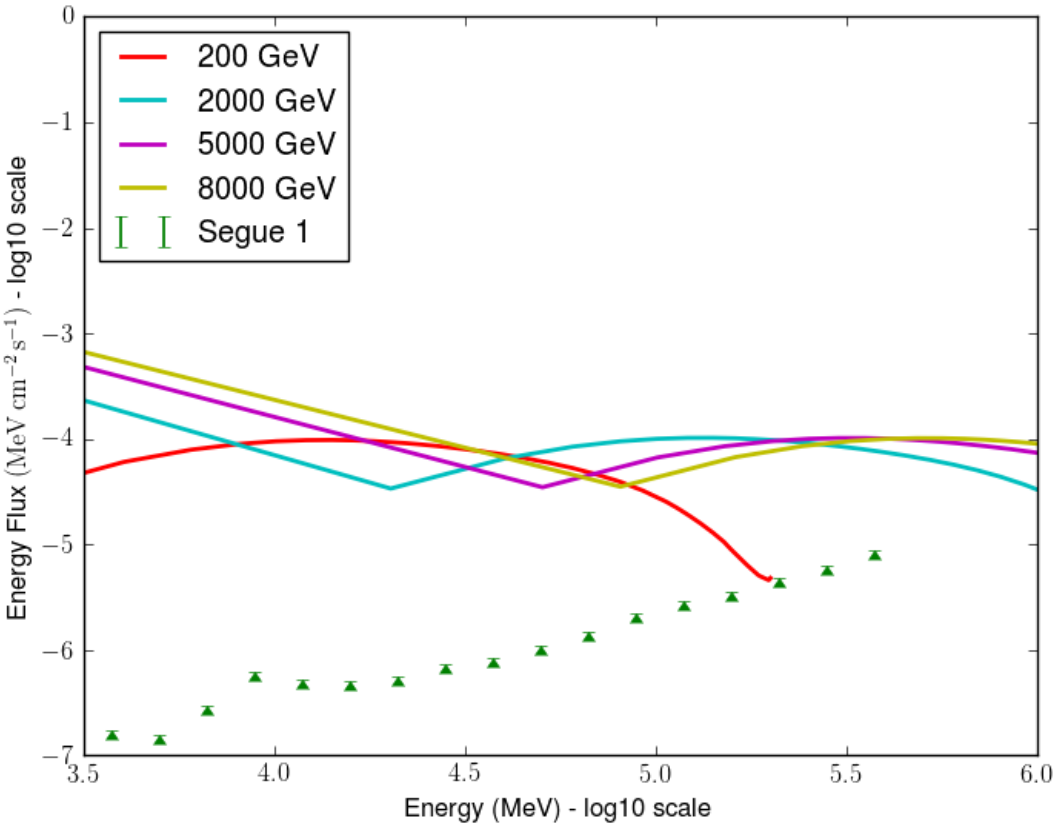

Figure 4.9: Observed limits from Fermi [316] on the energy-scaled flux $E^2 \frac{d\mathcal{N}}{dE}$ for dwarf galaxy Segue I compared against the predicted flux from Higgs-portal scalar annihilations for thermally constrained scalars of mass 200 GeV, 2000 GeV, 5000 GeV and 8000 GeV. Both axes are logarithmic.

clude that neither VERITAS nor MAGIC can constrain the Higgs-portal scalar model form dSph observations (as Segue I provides the strongest bounds of any dwarf for both of these instruments).

Now we consider observations made by Fermi.

Fermi also finds no significant signal, and so reports 95% confidence upper bounds on the cross section, assuming annihilation to $\bar{b}b$ or $\tau^+\tau^-$. Their data is provided at various stages of the analysis, so different models can be considered and one is not forced to accept their cross section bounds. We exploit this here, using instead their bound on the photon flux. The most recent Fermi results use an updated statistical treatment that combined results from several dSphs into a single joint likelihood function that is then used to compute bounds. Note that Fermi dark matter annihilation calculations are done assuming no Higgs annihilation channel [325], making the final results not immediately usable for Higgs-portal models.

We have computed the theoretical differential flux $E^2 d\Phi/dE$ for thermally produced Higgs-portal scalars with masses of 200 GeV, 2000 GeV, 5000 GeV, and 8000 GeV annihilating in three different dSphs (Segue I, Leo II, and Draco, chosen for their wide range of J factors). The astrophysical J-factors are independent of profile for dSphs [382, 379]. We use the results calculated in [383] for the J-factors of the dSphs. See also reference [384] for a review of J-factor calculations and profile differences. These differential fluxes for

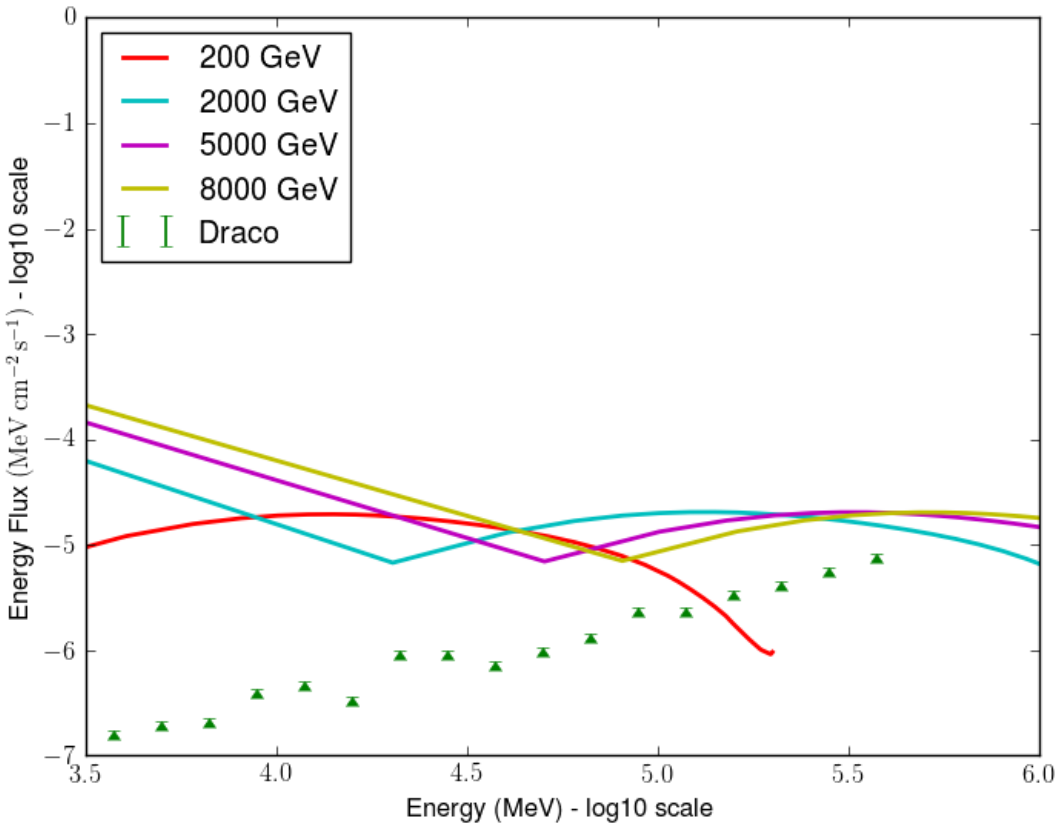

Figure 4.10: Observed limits from Fermi [316] on the energy-scaled flux $E^2 \frac{dN}{dE}$ for dwarf galaxy Draco compared against the predicted flux from Higgs-portal scalar annihilations for thermally constrained scalars of mass 200 GeV, 2000 GeV, 5000 GeV and 8000 GeV. Both axes are logarithmic.

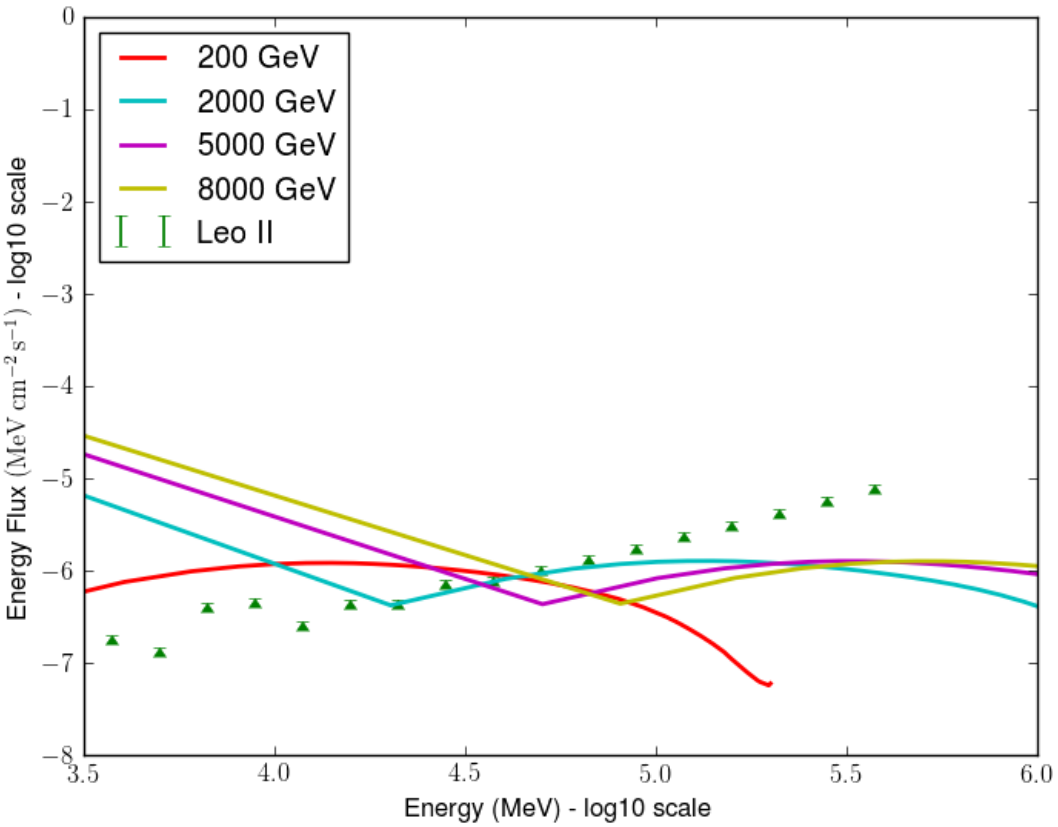

Figure 4.11: Observed limits from Fermi [316] on the energy-scaled flux $E^2 \frac{d\mathcal{N}}{dE}$ for dwarf galaxy Leo II compared against the predicted flux from Higgs-portal scalar annihilations for thermally constrained scalars of mass 200 GeV, 2000 GeV, 5000 GeV and 8000 GeV. Both axes are logarithmic.

low energies are plotted in Figures 4.9, 4.10, and 4.11. Also in these Figures are plotted the bounds on that differential flux as reported by Fermi in reference [316]. The bounds differ for each of the dwarfs, but basic visual analysis reveals that thermally produced Higgs-portal scalar dark matter is not consistent with Fermi observations of these dSphs.

Monochromatic line searches

The cross section for annihilation of Higgs-portal scalars to photon lines involves a 1-loop process. Full expressions for this cross section, which is somewhat complicated, appear in Appendix B. As an alternative, we have computed as well the cross section $\sigma_{SS\to\gamma\gamma}$ using an effective $h\gamma\gamma$ vertex, also detailed in the Appendix. Both cross sections are plotted in the nonrelativistic limit for a range of scalar masses in Figure 4.12. We note the discrepancy between the two cross sections, which is caused by the effective vertex being pushed beyond the range of its validity. The vertex relies on being able to assume the top and W boson masses are very large with respect to the energy scale of the process, which is clearly not the case here.

Also plotted with the cross sections in Figure 4.12 are the bounds on the annihilation to $\gamma\gamma$ as reported by Fermi [331]. From the Figure, it appears that the Fermi observations do not constrain the Higgs-portal model much beyond the resonance region near $m_S = m_h/2$. Limits on $Z\gamma$ lines are available [385], but we do not consider them, as the $\gamma\gamma$ line bounds are universally stronger. The HESS bounds are in a less convenient form than the Fermi bounds, and are comparable or weaker in Fermi's range, so we include only results from Fermi.

Line searches for Higgs-portal scalars are considered in reference [386], which considers the $\gamma\gamma$ and $Z\gamma$ channels near the half Higgs mass resonance region, though they do not address the conflict with the direct detection exclusion limits. Line bounds on scalar Higgs-portal dark matter are also considered in reference [330]. The authors compare against Fermi limits in for the mass values of $m_S = 62.5$ GeV, 150 GeV, 316 GeV, and 500 GeV. They consider both monochromatic lines and detection of the continuum resulting from final state radiation. They include full expressions for the cross sections they use, which is a valuable contribution we take advantage of. For more information on final state radiation and its uses in dark matter indirect detection, see references [387, 388]. As well, reference [302] considers the indirect detection of thermal Higgs-portal scalars, and our results roughly agree with theirs. They make a point that we would like to emphasize, regarding the boost in the thermal cross section that occurs in the resonance region near $m_S = m_h/2$, and that if the singlet mass is too far from this resonance region, a monochromatic gamma ray peak would be too broad to be picked up by Fermi with its current instrument resolution. The authors also consider the case, which we find somewhat forced due to the necessary deviation from minimality required, of annihilation primarily to the Higgs boson.

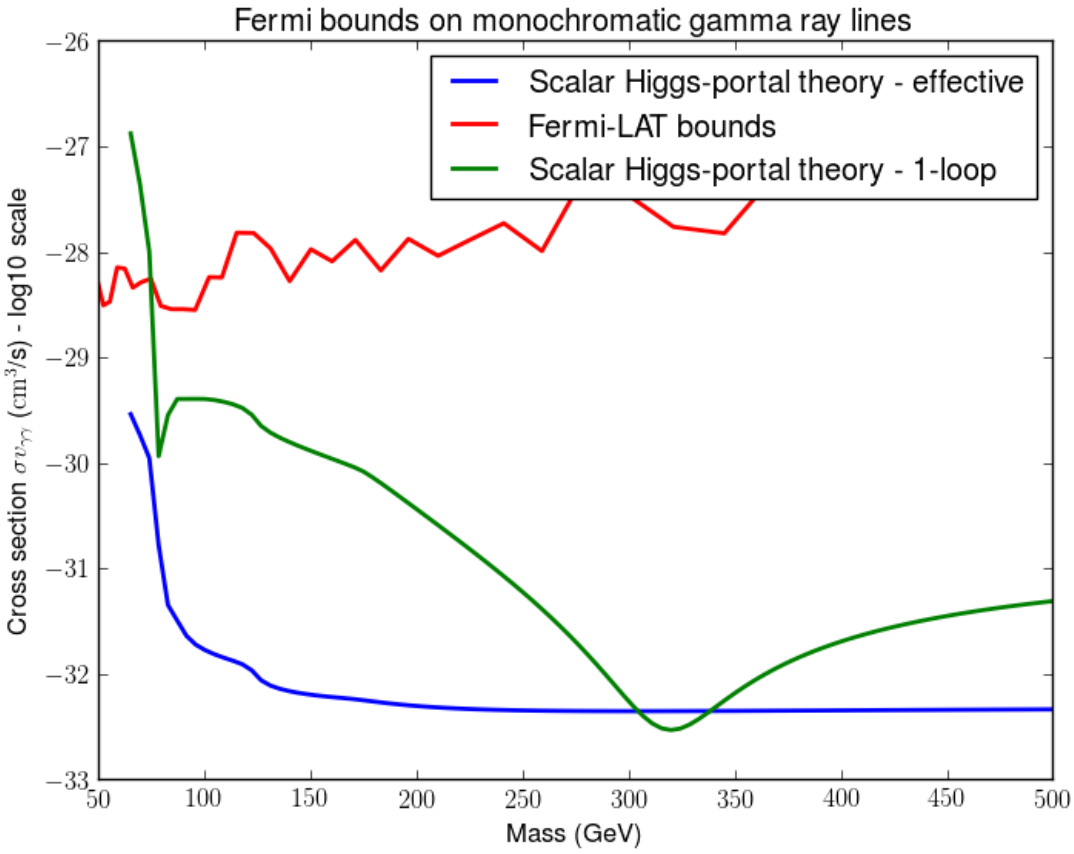

Figure 4.12: Bounds on the dark matter annihilation cross section to $\gamma\gamma$ as reported by Fermi [331] and discussed further in the text. Comparison is made to the scalar Higgs-portal model for two different calculations of the annihilation cross section, one using an effective Higgs-photon vertex and the other using the 1-loop expression for the cross section, which are both described in Appendix B. The Higgs-portal model is unconstrained for both methods, aside from the low mass region near the half Higgs mass resonance.

IGRB bounds

The gamma ray annihilation signals of scalar Higgs-portal dark matter were first considered with rigor in reference [260], which compared predictions against the IGRB. Much has changed since that study, with current IGRB observations comparable to predicted fluxes from dark matter annihilations.

We consider first the contributions to the IGRB from the annihilations of Higgs-portal scalars near the half Higgs mass resonance. To see if scalar Higgs-portal dark matter is consistent with the IGRB, we compute the ratio $\left(d\Phi_\gamma^{Fermi}/dE\right) / \left(d\Phi_\gamma^{Theory}/dE\right)$. If this ratio is larger than one, the predicted flux from the annihilating scalars is less than the observed IGRB and could make up some part of it. When the ratio is less than one, the predicted flux is larger than the observed IGRB and so Higgs-portal dark matter is disfavoured by the data.

In Figure 4.13, we plot this ratio for a thermal Higgs-portal scalar with a mass of 65 GeV. To illustrate as well the effects of astrophysical uncertainties, we have plotted the ratio for three values of the dark matter density, taking the standard value with standard error of 0.3 ± 0.1 as our values. The variation is striking, and for more extreme values, as have been postulated [389], the differences become even more pronounced. The Figure considers the Fermi observations with foreground model A, though using a different foreground model does not appreciably alter the conclusion. From the Figure, it can be seen that there is some tension between the IGRB as observed by Fermi and Higgs-portal scalar dark matter.

In Figure 4.14 we have plotted the ratio of fluxes $\left(d\Phi_\gamma^{Fermi}/dE\right) / \left(d\Phi_\gamma^{Theory}/dE\right)$ for a set of masses with the standard density value of 0.3 GeV/cm^3. In this Figure, the regions of the spectrum where the theoretical flux is larger than the observed flux are marked with x's. For most of the masses, the predictions of the Higgs-portal model are consistent with the IGRB, with some variability due to the Fermi foreground model. It can be noted that the 250 GeV mass Higgs-portal scalar might be soon extractable from Fermi observations in the 15-25 GeV range, if the sensitivity increases proceed as expected. The wide variability in the tails of the model is simply a consequence of the Figure having been plotted with a dimensionless ratio as the x-axis. The ratio is scaled by annihilating dark matter mass, and so the fact that larger masses are more poorly constrained at higher energies by the data set than smaller masses should be expected. In fact, Fermi is incapable of detecting IGRB photons with energies in the tail end of the annihilation spectra for some of the heavier scalars included in the Figure.

In comparing our results quantitatively to those reported in [292], we notice several of the same features. Heavier annihilating particles are ruled out by the higher fluxes in the high energy regions, and lighter annihilating particles run into trouble in the low energy regions, due to the $\bar{b}b$ channel.

4.8.3 Galactic core excess

In this Section, we consider whether or not Higgs-portal scalar dark matter could account for the galactic core excess. We compute the expected flux from the annihilation of Higgs-portal dark matter and compare

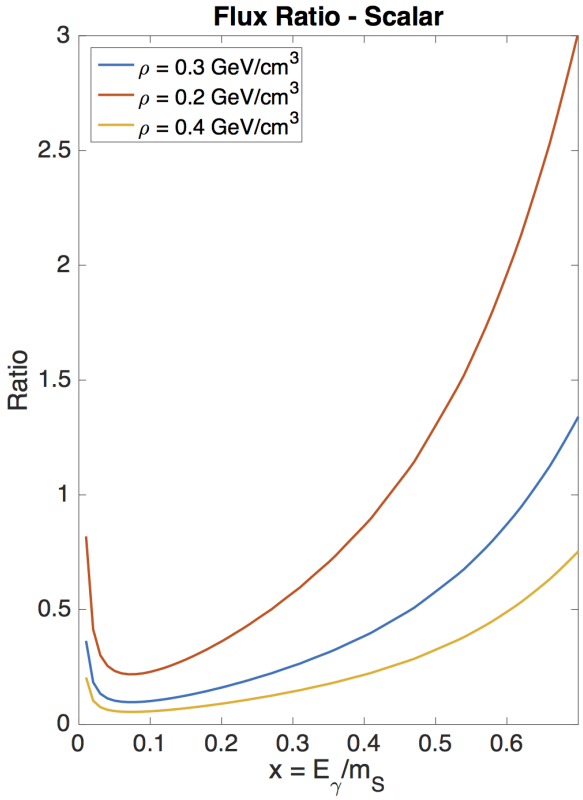

Figure 4.13: The ratio $\left(d\Phi_\gamma^{Fermi}/dE\right) / \left(d\Phi_\gamma^{Theory}/dE\right)$ plotted as a function of the dimensionless energy ratio $x = E_\gamma/m_S$. This plot illustrates the case of a 65 GeV Higgs-portal scalar, using the IGRB foreground model A for the fit. The three lines represent different values of the dark matter density $\rho_\odot$, demonstrating the effects of astrophysical uncertainties on the ratio. Figure originally reported in reference [631].

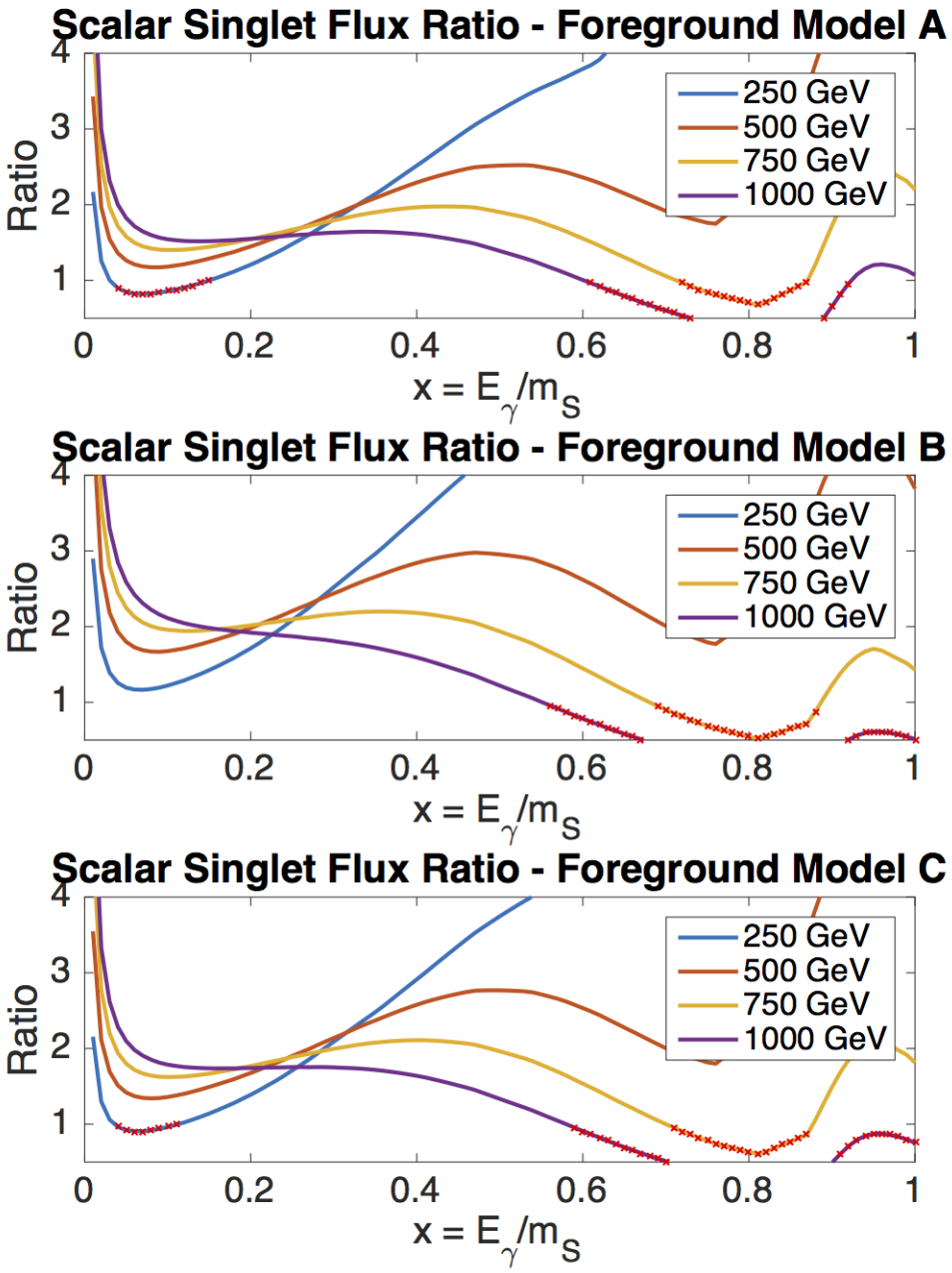

Figure 4.14: The ratio $\left(d\Phi_\gamma^{Fermi}/dE\right) / \left(d\Phi_\gamma^{Theory}/dE\right)$ plotted for each of the IGRB foreground models as a function of the dimensionless energy ratio $x = E_\gamma/m_S$. Masses are chosen to illustrate the regions where the theoretical flux is not consistent with the observed flux. Such regions are marked by the red 'x's. Figure originally reported in reference [631].

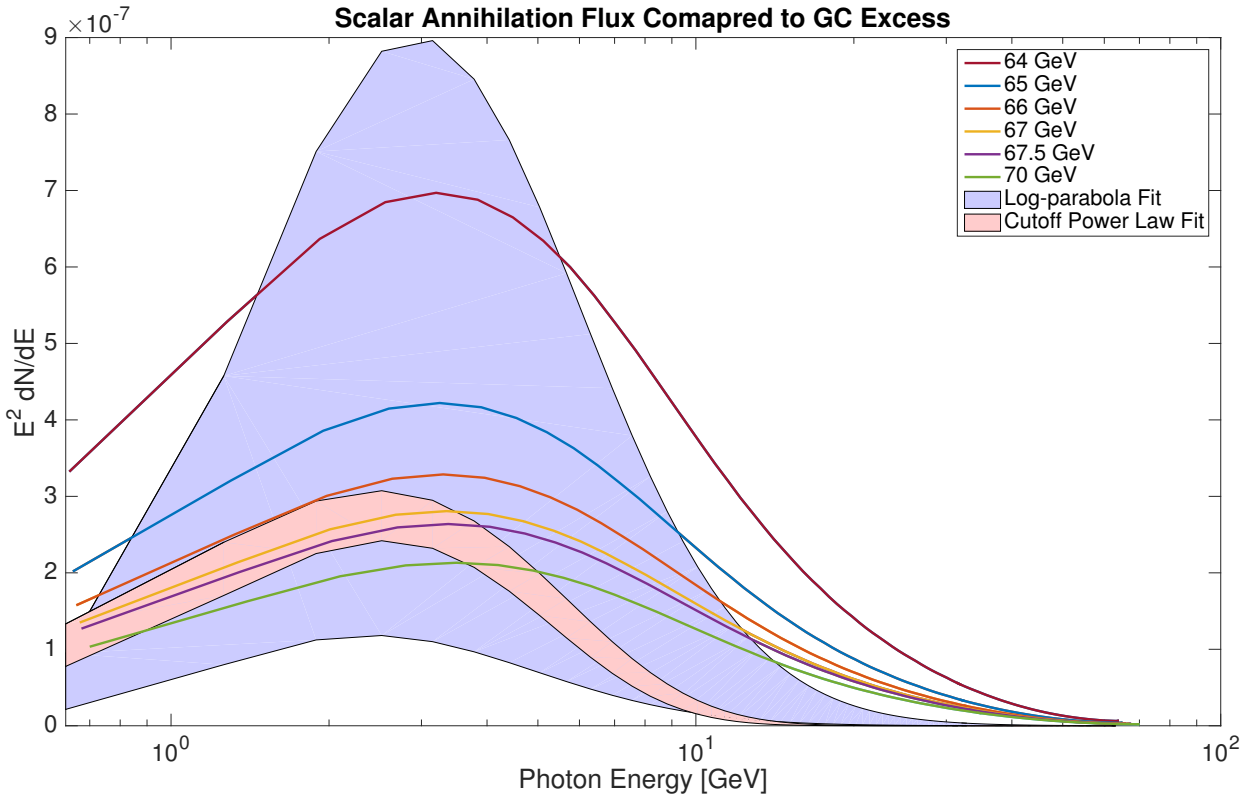

Figure 4.15: Flux produced by the annihilation of Higgs-portal scalars of masses in the range 64 GeV to 70 GeV in the $7^o \times 7^o$ region of interest around the center of the galaxy, compared against two functional fits to the galactic core excess with shaded error regions as reported in reference [302]. See Section 4.4 for further details. Figure originally reported in reference [631].

it to the observed galactic core excess as described in Section 4.4.

As discussed in Section 4.4, the excess peaks at a few GeV in energy, and if it is caused by annihilating dark matter that produces prompt photons through the decay of SM final states, then the dark matter must have a mass in the tens of GeV. Generally, the excess is fit assuming annihilation to $\bar{b}b$ pairs. Once the annihilation channels to the electroweak bosons open up, the electroweak cascades from the decays of these particles makes fits to the excess much more contrived.

As Higgs-portal scalars have a strong constraint on their masses from the invisible Higgs decay width below the half Higgs mass of $\sim$ 62.5 GeV (see Chapter 5 for more details), we consider masses only above that value. Values of 64, 65, 66, 67, 67.5 and 70 GeV are considered, as we have found that 63 GeV is too close to the s-channel resonance in the annihilation cross section, leading to flux predictions an order of magnitude too large. The fluxes for each of these masses are plotted alongside the excess in Figure 4.15. A 66-67.5 GeV mass scalar fits the excess better than any of the other options, with the chief difference from the excess being in how rapidly the tail falls off. As can be seen from the rapid fall off in flux even at 70 GeV, to match the observed excess a certain proximity to the resonance is required, for thermal Higgs-portal

scalars at least. Of course, as discussed in Chapter 3, these mass values are not consistent with bounds from direct detection experiments.

Our results agree more or less with the results of [302]. The model is considered in the context of the galactic core excess in reference [390], and a vector variant is as well in reference [391]. The authors explore the resonance region near $m_S = m_h/2$ and higher mass regions. While our results agree broadly with theirs, their results regarding the direct detection bounds and related effects on the parameter space disagree with our findings. There are also differences between our treatments of the thermal abundance calculations. Higgs-portal scalars are also discussed as a potential cause of the galactic core excess in reference [314]. The analysis is similar to the one presented here, and our results agree insofar as the best fit appears to be near the half Higgs mass resonance, but we find that for their value of $m_S = 62.7$ GeV, the approximations going into the thermal abundance calculations break down, and predictivity is lost without modifying the analysis. The authors also curiously fail to address the conflict between this mass value and the direct detection bounds. The reference also suggests the interesting idea that uncertainties in the astrophysical J factor can be used to allow reconciliation between the galactic core excess and the bound on the annihilation cross section set by dSph observations.

Modified distribution assumptions

The Galactic core excess is in a region of the parameter space that has been excluded by direct detection experiments for the majority of models, including the Higgs-portal scalar model discussed in the example. However, as discussed in Chapter 3, there are a number of assumptions that go into the calculation of the nuclear recoil bounds that are reported. Many of these assumptions deal with the astrophysical properties of the dark matter distributions, and have large uncertainties associated with them. This has led to the analysis reported in [392], which attempts to retain the dark matter explanation of the Galactic core excess.

The basic argument is that WIMP distribution parameters that go into the reported nuclear recoil bounds are to some degree incorrect. By assuming that the Galactic core excess is caused by the annihilation of WIMP dark matter, and then using the excess to modify the WIMP halo distribution parameters, different bounds on the nuclear recoil cross section can be obtained. The article [392] works with the LUX 2013 data set [393], which has since been superseded [394]. We briefly show using Figure 4.16 that this analysis is incapable of reconciling the Higgs-portal scalar explanation of the Galactic core excess with the LUX 2013 exclusion bounds. Needless to say, the stronger bounds that have been reported more recently also rule out the Higgs-portal scalar explanation of the Galactic core excess.

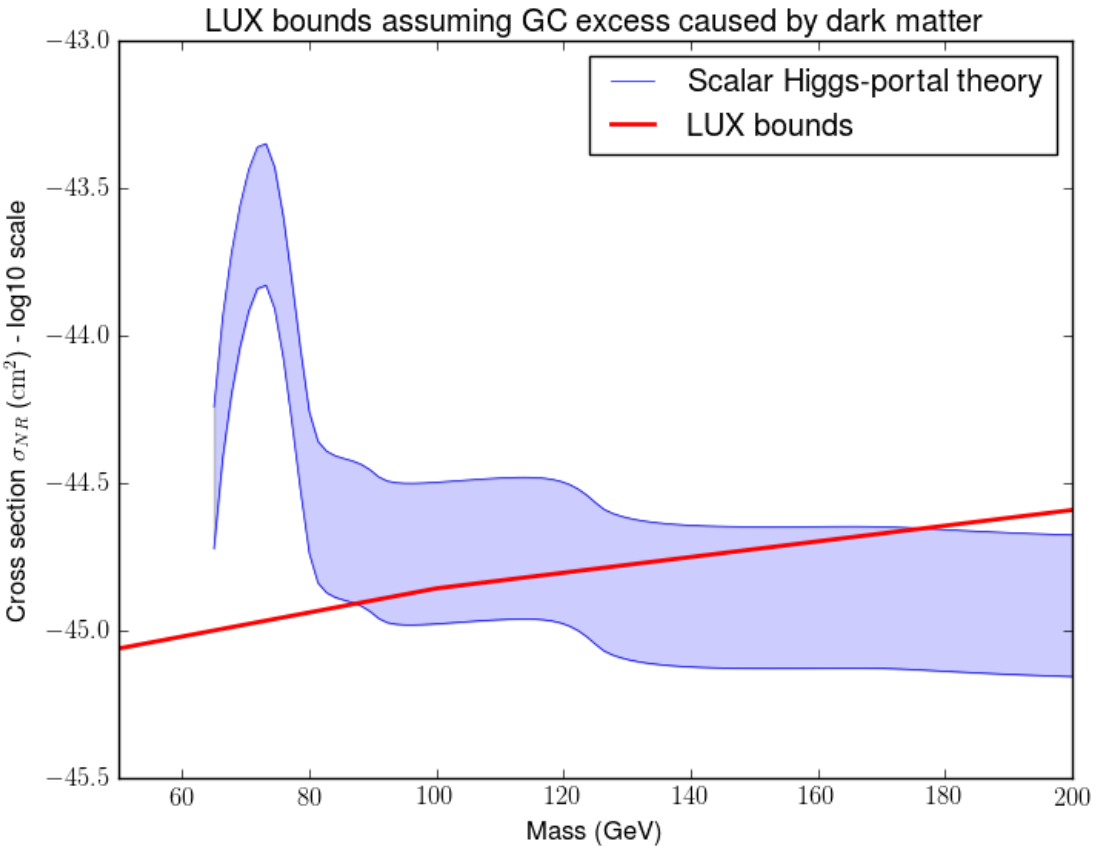

Figure 4.16: Comparison of the direct detection cross section for thermal Higgs-portal scalar dark matter against LUX bounds computed using nonstandard dark matter distribution assumptions as described in the text and reference [392]. While the modified bounds admit slightly more of the parameter space than the standard bounds, they are still not relaxed enough to admit a Higgs-portal scalar explanation for the galactic core excess.

Chapter 5

Collider Signatures of Dark Matter

In the previous two Chapters, purely observational methods of dark matter detection were considered. Both direct detection and indirect detection techniques, for all their use, are ultimately passive. In this Chapter, we will consider the only existant controlled laboratory technique to search for dark matter: the particle collider search.

For a significant portion of the time particle physics has existed as a field, new discoveries were made exclusively through particle collider experiments. It is not surprising, then, that many people in the community are hopeful that particle dark matter might be first observed in a particle collider. The logic is sound. If particle dark matter interacts with SM matter and forces to some degree, it should be produced in some amount at a particle collider that has collisions of sufficient energy. With several years worth of LHC data available at the time of this writing, as well as proposals for higher energy collider experiments in the future, it is expected by much of the community that dark matter will be observed shortly. Of course, even observing it, let alone extracting meaningful information about its properties, is certain to be very difficult. This difficulty is the reason a very strong collider phenomenology program with a focus on dark matter exists. It is also true that much of the research program for beyond the SM particle physics is reliant on particle colliders, which leads to a fortuitous alignment of research priorities between particle astrophysics and more traditional particle physics. Aspects of this program that the author is familiar with will be the primary focus of this Chapter.

In Section 5.1, several of the basic aspects of collider physics relevant to the phenomenology of dark matter will be reviewed. This allows a proper emphasis to be placed on important parts of what is a vast field in particle phenomenology, as well as establishing language and conventions for what follows. Section 5.1 will cover some essential properties of particle colliders (Section 5.1.1), a detailed discussion of cross section calculations within the parton model (Section 5.1.2) and a brief discussion of the narrow resonance approximation (Section 5.1.3), which is important in beyond SM collider physics calculations. Section 5.2 will discuss bounds placed by collider data on mediators to dark sectors, which tend to be more stringent than bounds on the dark sectors themselves. More proper searches for dark matter at colliders, the missing energy and mono-X searches, are discussed in Section 5.3. Finally, Section 5.4 contains an example of the techniques discussed in the preceding Sections applied to a simple model of particle dark matter, the by now familiar scalar Higgs-portal model.

5.1 Fundamentals of Collider Physics

The study of modern particle physics depends heavily on the experimental results provided by particles colliders. In fact, it would not be out of place to say that particle physics itself was born in tandem with particle colliders. Nearly all of the important discoveries of particle physics have been made because of collider experiment results. Due to this intimate connection, it is important to discuss some of the basic aspects of experimental and phenomenological particle collider physics before proceeding to dark matter searches. For a standard treatment of the basic aspects of collider physics, suitable for both experiment and theory, see references [395] and [396].

Particle colliders exploit physics that appears at high energies. Following from the basic principles of QFT, particle number is not a conserved quantity, and so a collision of particles with a large enough total energy has a chance of producing new particles that were not originally present. The probability of this occurring for a given process can be calculated in the form of the cross section for that process using the techniques of QFT. In this way, particles that are unstable or too heavy to naturally appear can be produced and studied.

This is the purpose of a particle collider experiment. Stable and easily produced particles are accelerated until they reach a certain energy, one large enough produce the target process or particle, and then are projected onto a target. The accelerated particles, known as the beam, interact with the particles of the target in a variety of ways, producing final state particles which can be observed and studied. The particle collider is the primary laboratory experiment of high energy physics, and any particle physicist should be well acquainted with it.

5.1.1 Particle colliders

A particle collider is a device that uses electromagnetic fields to accelerate and collide a beam of particles with a target at high energies. For particle physics effects to appear, the energies of the particles in the beam must be firmly in the relativistic regime, such that the relativistic dispersion relation $E^2 = m^2 + p^2$ applies. The spatial resolution of processes that can be studied is limited by the wavelength of the particles involved in the process. As wavelength is inversely proportional to momentum for massive particles, a larger momentum implies that smaller spatial extents can be probed, where higher energy physics is.

Additionally, in colliders particles can be observed if they are produced in a collision event and particles may only be produced if the center of mass energy of the collision is large enough to produce them. To produce a pair of particles of mass m, we require a center of mass energy of $E_{cm}^2 \geq 4m^2$. For massive particles such as WIMPs, this can be very large.

Most modern particle colliders designed to reach high center of mass energies are constructed so that two beams of particles are interacting. This is for reasons of energy efficiency, as illustrated by the following argument.

Consider a beam of particles directed at a fixed target. In this case

$$E_{cm} = \sqrt{m_1^2 + m_2^2 + 2E_1 m_2} \simeq \sqrt{2E_1 m_2} \tag{5.1}$$

assuming $E_1 \gg m_1, m_2$.

Now consider the case where the target is itself a beam of particles travelling in the opposite direction. The above relation becomes

$$E_{cm} = \sqrt{m_1^2 + m_2^2 + 2E_1 E_2 + 2p_1 p_2} \simeq \sqrt{4E_1 E_2} \tag{5.2}$$

which goes like $\sqrt{4E^2} \simeq 2E$ if $E_1 \simeq E_2$. It is clear then that E_{cm} scales much more effectively with two beam systems, and hence that the two beam system is desirable when examining processes which primarily require high energies.

The need for a high E_{cm} is what has driven much of the development of collider physics over the last few decades. In particular, the LHC required a large center of mass energy if it was to be capable of what was asked of it, including finding the Higgs boson and signs of beyond SM physics. While the first of those has been observed, no new physics has yet appeared. This has led the community to propose a variety of larger future colliders with higher center of mass energies [397, 398, 399, 400, 401]. Such colliders are necessary to probe the energy ranges immediately above the SM scale, though they too will be insufficient if new physics lurks at the 100 TeV scale or beyond.

When a specific particle physics process is of interest, as is frequently the case in collider experiments, there is no way to guarantee that that process will occur. Particle physics processes occur at scales which are deep in the quantum regime. Whether or not a specific process will occur is probabilistic, and moreover there can be significant interference effects from different contributions to the same quantum process. The quantum nature of these particle physics systems means that the only way to obtain results of any value is through statistics.

The vast majority of interactions that occur in a particle collider are trivial scattering events. Processes of interest that may involve new physics are much rarer. Particle colliders will use beams that are made up of large numbers of particles to generate large numbers of events, which increases the odds that a specific process will occur and be observed. An important quantity is the luminosity $\mathcal{L}$ of a particle collider. The luminosity is the flux of the incident beam of particles multiplied by the mean target density. It has units of inverse time $\times$ inverse area, and the quantity $\mathcal{L}\sigma$ is the event rate in a collider of luminosity $\mathcal{L}$ for a process with cross section σ. The total number of events can be obtained by integrating the event rate over time:

$$\mathcal{N}(t) = \int_0^t \sigma \mathcal{L}(t) dt. \tag{5.3}$$

Pulling the constant in time cross section σ outside of the integral gives the integrated luminosity, with units of inverse area. For the LHC, instantaneous luminosities are on the order of $10^{34}\,\mathrm{cm}^{-2}\,\mathrm{sec}^{-1}$, and integrated luminosities for 2017 exceeded 50 fb^{-1}.

In the next Sections, we will discuss various signatures of particle dark matter. In this context, a detector signature is a set of observables that are used to tag or identify potentially relevant events. These observables are usually associated with some process of interest. Processes that are not the one of interest but produce the same signature are called background processes.

Before moving on, we will briefly discuss the basic kinds of particle colliders. By this, we mean the types of particles that make up the beams. Currently, the only particle colliders that exist are electron-positron (e^+e^-), proton-proton (pp) and nucleus-nucleus, and electron-proton (e^-p) colliders. Examples of the first include LEP [402], among others. The well-known LHC [403] is a proton-proton collider, as was the Tevatron [404] that preceded it. HERA is a fixed target electron-proton collider [405]. These are just a few of the more well known examples. Several other kinds of collider have also been considered, though none have been constructed, including muon colliders [406, 407] and photon colliders [408, 409, 410], among others. High energy particle physics is mostly done using e^+e^- and pp colliders.

5.1.2 Calculations with the parton model

Most of the basic calculations of collider processes take place within the parton model [411], which is a model that describes the behaviour of hadrons at large momenta where QCD perturbation theory applies.

The parton model is a relatively simple way of describing the fairly complex dynamics of composite particles in collisions. The basic effect of the parton model is that, in a high energy collision, one can treat a hadron as being made up of pointlike noninteracting constituents called partons. A scattering event involving the hadron can then be described in terms of scattering events of the individual partons. That this can be done seems somewhat intuitive, but that it works to any degree in a strongly bound state is actually an important consequence of some deep pieces of quantum field theory.

Otherwise impossible calculations can be done with relative ease in the parton model. Naturally, the parton model is only an approximation to the full field theoretic result, and there are regimes where it cannot be applied. Nonetheless, it is one of the most useful tools in collider physics. This Section covers some of the background necessary to do basic calculations in the parton model.

Deep inelastic scattering

The formalism of the parton model follows naturally from an examination of deep inelastic scattering processes, in which leptons (charged in this case) scatter from target nucleons through electromagnetic or weak interactions. Deep inelastic scattering is an experimental phenomenon, in which the momentum transferred from the electron to the hadronic system is enough to disintegrate the hadron. In this process, the fundamental components of the hadron, the partons, are detectable. The basic discussions in this Section have been adapted from the classic textbook treatments of Cheng and Li [5], Barger and Philips [395], and Peskin and Schroeder [3], though many other references exist [412, 413, 396].

Consider the case of electron-nucleon deep inelastic scattering [414],

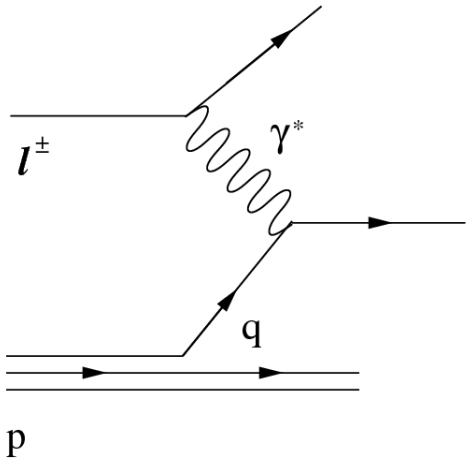

Figure 5.1: Basic diagrammatic representation of deep inelastic scattering in the electromagnetic channel. The lepton state $l^{\pm}$ imparts a large amount of energy to one of the partons of the hadronic state p through the photon γ_*, essentially disintegrating the hadron.

$$e(k) + N(p) \to e(k') + X(p_n), \tag{5.4}$$

illustrated in Figure 5.1. The label X indicates some hadronic final state the exact details of which are unimportant.

The useful kinematic variables are

$$q = k - k',\ \nu = p \cdot q / m_N \tag{5.5}$$

and we work in the lab frame, where the nucleon is initially at rest:

$$p_\mu = (m_N,\ 0,\ 0,\ 0)\,,\ k_\mu = (E,\ \mathbf{k})\,,\ k'_\mu = (E',\ \mathbf{k}')\,. \tag{5.6}$$

For a small lepton mass $m_l \ll m_N$, the momentum transfer q can be written

$$q^2 = (k - k')^2 = -4EE' \sin^2 \frac{\theta}{2} \leq 0,\ Q^2 = -q^2, \tag{5.7}$$

where θ is the lepton scattering angle after the collision. We are considering deep inelastic scattering, where the 'deep' implies that the momentum transfer Q is very large with respect to the momentum of the constituents of the hadron.

The transition amplitude for this process is given by

$$T_n = e^2 \bar{u}(k',\ \lambda')\gamma^\mu u(k,\ \lambda)\frac{1}{q^2}\langle n \left| J^{em}_\mu(0) \right| p, \sigma\rangle \tag{5.8}$$

in which $\bar{u}$ and u are the lepton spinors and J^{em}_μ is the nucleon electromagnetic current. This leads to the differential cross section

$$d\sigma_n = \frac{1}{|\mathbf{v}|}\frac{1}{2M}\frac{1}{2E}\frac{d^3k'}{(2\pi)^3 2k_0'}\prod_{i=1}^{n}\left[\frac{d^3p_i}{(2\pi)^3 2p_0'}\right]\frac{1}{4}\sum_{\sigma,\lambda,\lambda'}|T_n|^2(2\pi)^4\delta^4(p+k-k'-p_n), \tag{5.9}$$

and summation over all possible hadronic final states yields the inclusive cross section

$$\frac{d^2\sigma}{d\Omega dE'} = \frac{\alpha^2}{q^4}\left(\frac{E'}{E}\right)l^{\mu\nu}W_{\mu\nu}. \tag{5.10}$$

In the above, $l^{\mu\nu}$ is the leptonic tensor, and $W_{\mu\nu}$ is the hadronic tensor, both of which are useful quantities for describing deep inelastic scattering processes. The exact forms of these structures are not necessary for this discussion, but it is important to note that from conservation of electromagnetic current ($\partial^\mu J_\mu^{em} = 0$) it can be shown that

$$q^\mu W_{\mu\nu} = q^\nu W_{\mu\nu} = 0. \tag{5.11}$$

Using this fact and the knowledge that $W_{\mu\nu}$ is symmetric and depends only on the momenta p_μ and q_μ, a decomposition into Lorentz structures can be found:

$$W_{\mu\nu}(p,q) = \left[-W_1\left(g_{\mu\nu} - \frac{q_\mu q_\nu}{q^2}\right) + \frac{W_2}{M^2}\left(p_\mu - \frac{p\cdot q}{q^2}q_\mu\right)\left(p_\nu - \frac{p\cdot q}{q^2}q_\nu\right)\right]. \tag{5.12}$$

The functions $W_1(q^2,\nu)$ and $W_2(q^2,\nu)$ are the Lorentz invariant structure functions of the nucleon, with ν defined in Equation (5.5). For the special case of electron-nucleon scattering, where the final state X is also a nucleon, these structure functions reduce to the well-known Pauli and Dirac electromagnetic form factors $F_1(q^2)$ and $F_2(q^2)$, which appear in the nucleon electromagnetic current

$$\langle N(p')\left|J_\mu^{em}(q^2)\right|N(p)\rangle = \bar{u}(p')\left[\gamma_\mu F_1(q^2) + i\sigma_{\mu\nu}q^\nu\frac{F_2(q^2)}{2M}\right]u(p). \tag{5.13}$$

At $q^2 = 0$, $F_1(q^2)$ and $F_2(q^2)$ measure the total charge and anomalous magnetic moment of the nucleon, respectively. These form factors are also known as structure functions, and describe the response of the hadronic system to electromagnetic probes. They are discussed in detail in any basic text on quantum field theory [3, 4]. The structure functions must be extracted from experimental data, as a theoretical derivation would require an understanding of the interior of the hadron that is not available.

This current, which appears in electron-proton scattering for example, generates an elastic scattering cross section that falls off at large q^2. In the case of deep inelastic scattering events, where the final state nucleon in Equation (5.13) is replaced by some hadronic state, there is a different dependence on q^2. This experimentally observed dependence led to the theoretical construct known as the parton model, and is illustrated in Figure 5.2.

To explore the q^2 dependence in deep inelastic scattering, we define the dimensionless Bjorken scaling variable [415]

$$x = \frac{-q^2}{2M\nu} = \frac{Q^2}{2M\nu} \tag{5.14}$$

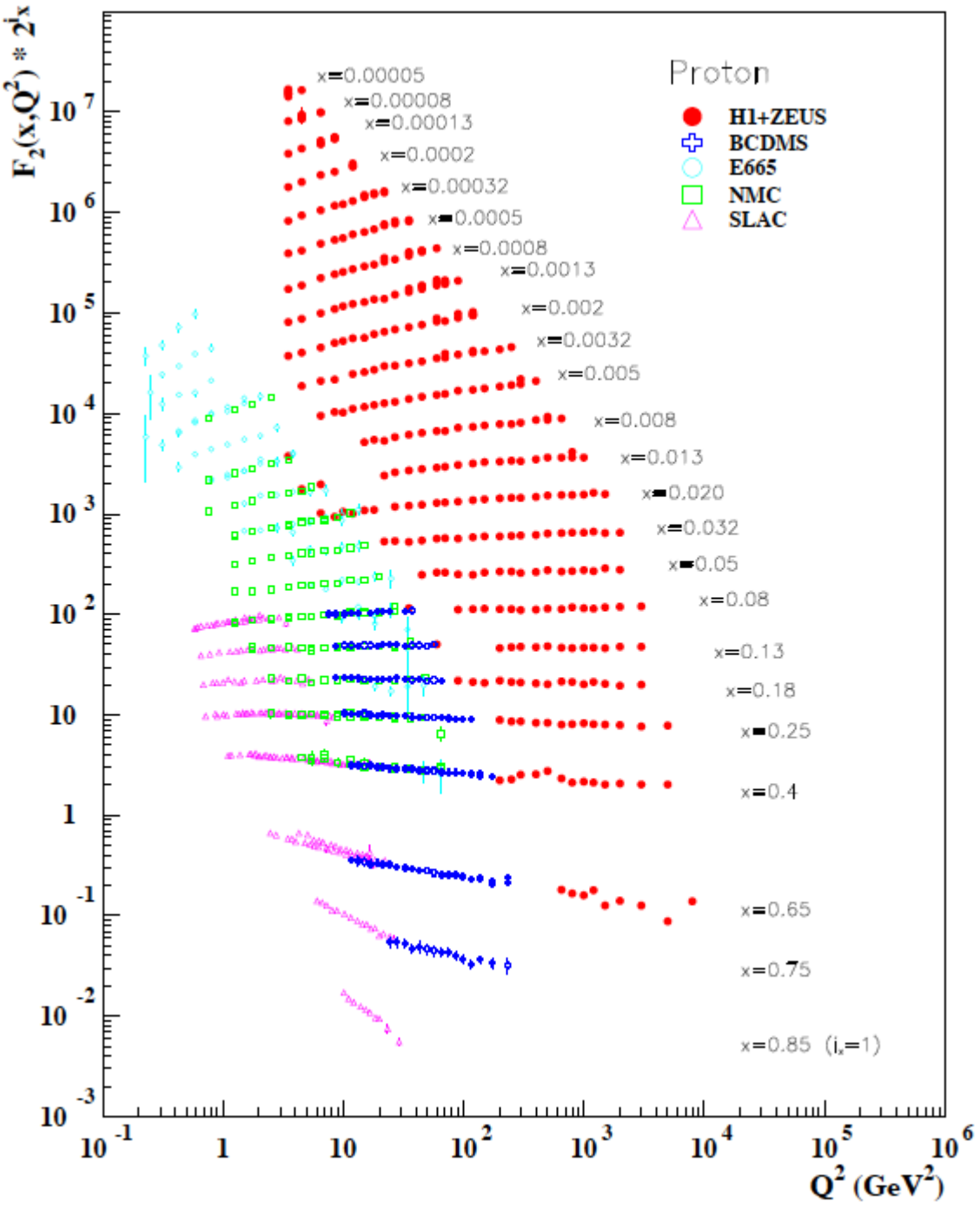

Figure 5.2: Plot of data points for the proton structure function $F_2(x, Q^2)$ against Q^2 for a variety of values of the Bjorken scaling variable x. For large regions of the parameter space, F_2 is nearly independent of Q^2 while depending strongly on x, providing experimental evidence for the statement in Equation (5.15). Figure reproduced from reference [8].

where $0 \leq x \leq 1$. That x must be in this range is simply a statement of conservation of energy. One could consider x a measure of the inelasticity of the collision, with $x = 1$ corresponding to the elastic case.

The experimental phenomenon of Bjorken scaling, as illustrated in Figure 5.2, is the statement that in the large Q^2 limit with fixed x the structure functions F_i depend only on x. More formally

$$\lim_{|q^2|\to 0,\ fixed\ x} F_i\left(x, \frac{q^2}{M^2}\right) = F_i(x). \tag{5.15}$$

Partons as constituents of hadrons

By Fourier transforming the distribution, it can be seen that the charge distribution of the scattering target inside the nucleon takes the form of a Dirac delta; that is, the photon interacts with a pointlike charge within the nucleon. This implies that the mediator (a photon for basic deep inelastic scattering) interacts with approximately pointlike particles, which are called 'partons.' This can be justified using the time-energy uncertainty principle. At high energies, the mediator 'acts' in a short amount of time, which can be thought of as being due to time dilation. The Lorentz frame of the hadron sees the mediator as highly dilated, meaning it seems to 'act' quickly. This provides a reasonable description of the wavefunction of a composite particle in a highly boosted Lorentz frame, and is known as the impulse approximation.

This allows processes involving hadrons to be split into partonic processes, which can be described by perturbative QCD, and processes which are nonperturbative. This separation is called factorization. The basic line of reasoning that justifies factorization is as follows: in highly perturbative deep inelastic scattering, the momentum transfer Q^2 is very large, which means the photon (for standard electromagnetic deep inelastic scattering) is very off-shell or highly virtual, carrying a lot of energy. The photon thus 'acts' very quickly (on a shorter scale), much more quickly than the gluons that bind the hadron together. The result is that the photon 'sees' the individual partons as free, in an instant where they are effectively unbound. This is, of course, only an approximate way of thinking about it.

There is a necessary assumption, that the transverse momentum of the parton is negligible, and that the momentum of the parton can be expressed entirely as some fraction of the momentum of the parent hadron ($p = xP$). Considering the experimental success of the parton model, this appears to hold. However, theoretical justification of this assumption requires QCD. For large energies where $E_{cm} \gg m_H$ the hadron mass m_H is negligible, and the hadron thus has a very large momentum aligned with the collision axis. To give a parton a large transverse momentum in this scenario requires the exchange of a gluon between partons, as partons interact through the strong force in the hadronic bound state. However, this gluon must be hard, carrying a large amount of energy (with respect to the hadron binding energy). However, gluon exchange processes are suppressed by the QCD running coupling α_s at large energy scales. Thus partons rarely interact and gain transverse momentum, and the assumption that parton momentum is collinear with hadron momentum is accurate.

It is accepted that the partons, which are experimentally observable, are identifiable with the quarks of

QCD, which are a theoretical construct. A complete derivation of the parton model from first principles QCD requires an understanding of the gauge theory that is beyond our reach at this time. What this means practically is that many of the inputs for QCD calculations involving hadrons need to be obtained experimentally.

It should be emphasized that the parton model only applies when α_s is very small, in the perturbative region of QCD. A formal discussion of this appears in reference [412], where the details of QCD factorization are discussed in full rigor. A basic assumption of the parton model is that the partons carry some fraction of the transverse momentum of the hadron. The number of partons of species i in hadron h with a momentum fraction inside the range x and $x + dx$ is given by

$$f_{i/h}(x)dx \tag{5.16}$$

where $f_{i/h}(x)$ is called the parton distribution function. The parton distributions functions depend on the nonperturbative quantum structure of the hadron, and so cannot be calculated in perturbation theory. They are determined experimentally [8].

Parton distribution functions are constrained by the quantum numbers and other observables of the hadron. For example, for the proton

$$\int_0^1 dx \left[(u_p(x) - \bar{u}_p(x)) - \left(d_p(x) - \bar{d}_p(x)\right) \right] = 1 \tag{5.17}$$

and

$$\int_0^1 dx \left(s_p(x) - \bar{s}_p(x)\right) = 0. \tag{5.18}$$

where the functions $u_p(x)$, $d_p(x)$ and $s_p(x)$ describe the parton distribution functions of the up quark, down quark and strange quark in the proton, respectively, and $\bar{q}(x)$ is the antiquark parton distribution function of quark flavor q.

These constraints are known as sum rules, and are often used to normalize the parton distribution functions. There are a number of other sum rules, which are derived from theoretical considerations and have been verified experimentally. This strong experimental support is evidence that the quark-parton model is a very good approximation to reality.

A sum rule that has an impact on the production of beyond SM particles, such as dark matter, in colliders is the momentum sum rule. Put simply, if the quarks were to carry all the momentum of the hadron (in this case, the nucleon), one would expect

$$\sum_j \int dx \left(x f_j(x)\right) = 1 \tag{5.19}$$

where the sum is over all of the valence quarks. The contributions from the sea quarks are expected to cancel.

However, experimentally $\int dx \left(x f_u(x) + x f_d(x)\right) \simeq 0.38$ for the nucleon. This implies that the u and d quarks only carry slightly over a third of the total momentum of the nucleon. In turns out that most of the

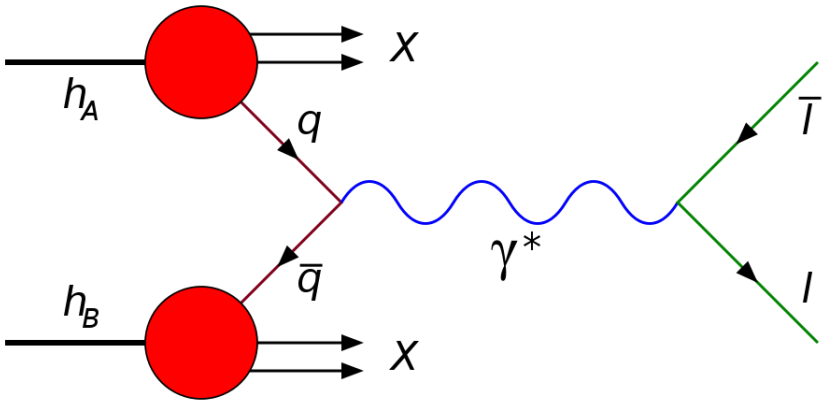

Figure 5.3: Basic diagrammatic representation of Drell-Yan scattering, where two protons $h_{A,B}$ collide and their component partons interact through the electromagnetic force. Here, a quark q and an antiquark $\bar{q}$ annihilate into a pair of leptons $l^{\pm}$. In general, there are many such processes that contribute.

rest is carried by the gluons. As will be discussed in Section 5.4, this has very important implications for Higgs production and associated physical phenomena.

The impulse approximation

The basic assumption that parton level processes are a good approximation for the hadronic process is called, as has been mentioned, the impulse approximation. One calculates the parton level cross section and then convolves that cross section with the parton distribution functions to obtain the hadron level cross section. For the case of deep inelastic scattering as discussed above, the impulse approximation would generate a cross section

$$\sigma_{eA\to eX} = \sum_q C_a \int dx_a f_{q/A}(x_q) \times \hat{\sigma}_{eq\to eX} \tag{5.20}$$

where $\hat{\sigma}_{eq\to eX}$ is the cross section for the parton level process of electron-quark scattering. This cross section is convolved with the parton distribution function for the quark q in hadron A and the total cross section is the sum over all the partons.

For the more complicated case of hadron-hadron scattering (Drell-Yan scatting for the case of nucleon-nucleon scattering), partons from both hadrons need to be taken into account. The hadron level cross section can be represented

$$\sigma_{AB\to cX} = K \sum_{a,b} C_{ab} \int dx_a dx_b \left[f_{a/A}(x_a) f_{b/B}(x_b) + (A \leftrightarrow B \text{ if } a \neq b) \right] \times \hat{\sigma}_{ab\to cX}. \tag{5.21}$$

In this convention, the parton level cross section $\hat{\sigma}$ is summed over initial and final colors, and the initial state color averaging factor is made explicit in C_{ab}. Basic values are $C_{qq} = C_{\bar{q}q} = 1/9$, $C_{qg} = 1/24$, and $C_{gg} = 1/64$. We have introduced here the K factor that is to correct for higher order QCD effects on the cross section. It is an estimate of the difference between the theoretical and experimental values of the cross section, and can be from 1.3 to 1.5 or higher depending on the process and energy scales involved. It is usually safe to use $K = 1.3$ for LHC processes, though K is expected to be larger for Higgs physics processes [416]. Formally, it is defined as

$$K = \left.\frac{d\sigma}{dm^2}\right|_{\text{exp}} / \left.\frac{d\sigma}{dm^2}\right|_{\text{theor}} \tag{5.22}$$

where m^2 is the invariant mass of the process [417]. We take the factor to be implicit in all subsequent equations.

For $|\bar{p}| \gg m$, we have $p_a = x_a p_A$ and $p_b = x_b p_B$ for 4-momenta relations. This means the center of mass energy squared of the ab partonic system $\hat{s}$ can be written in terms of the center of mass energy squared of the AB hadronic system s as $\hat{s} = x_a x_b s = \tau s$.

By eliminating x_b in favor of τ, the hadronic cross section becomes

$$\sigma = \sum_{a,b} C_{ab} \int_0^1 d\tau \int_\tau^1 \frac{dx_a}{x_a} \left[f_{a/A}(x_a) f_{b/B}\left(\frac{\tau}{x_a}\right) + (A \leftrightarrow B \text{ if } a \neq b) \right] \times \hat{\sigma}(\hat{s} = \tau s) \tag{5.23}$$

$$\Rightarrow \frac{d\sigma}{d\tau} = \sum_{a,b} \frac{d\mathcal{L}_{ab}}{d\tau} \hat{\sigma}(\hat{s} = \tau s) \tag{5.24}$$

with the frequently useful parton luminosity

$$\frac{d\mathcal{L}_{ab}}{d\tau}(\tau) = C_{ab} \int_\tau^1 \frac{dx_a}{x_a} \left[f_{a/A}(x_a) f_{b/B}\left(\frac{\tau}{x_a}\right) + (A \leftrightarrow B \text{ if } a \neq b) \right]. \tag{5.25}$$

There is an important concept that requires a brief introduction here, as it will be used in later Sections of this Chapter. In collisions between hadrons, such as those that occur at the LHC, most of the interactions at the parton level are soft. That is, they have a small transverse momentum component p_T (transverse to the axis of the collision). Small p_T means that the final states of the scattering process are nearly collinear to the initial states and hence are basically inside the incoming beam. Low p_T final states are essentially impossible to analyze, both because they are very messy and because they tend to be primarily directed toward a region with no detectors (inside the incoming beam). Soft processes also mean a large α_s and nonperturbative QCD, which means they cannot be analyzed theoretically either. Most of the processes in a hadron collision are soft, and therefore intractable.

Occasionally, however, a large p_T process will occur. For such a process, the final state momenta will be at larger angles from the beam axis, leading to more easily detected states. As well, the momentum transfer will be hard, rendering the process amenable to perturbation theory, and allowing the parton model approximations to be applied. Such processes are the ones which are studied at hadron colliders, and they are usually described in terms of their p_T. Examples of this characterization will follow in the next Sections.

Another convenient variable in a hadronic collision is the rapidity y, which is related to the parton momentum fractions $x_{a,b}$ by

$$y = \frac{1}{2} \ln \left(\frac{x_a}{x_b} \right). \tag{5.26}$$

This relation can be inverted to give

$$x_{a,b} = \sqrt{\tau} e^{\pm y}. \tag{5.27}$$

If one considers boosts as rotations into the time direction in Minkowski space, rapidity is the hyperbolic angle of those rotations. The rapidity is a convenient way of expressing the relative motion of particles produced in a collider. We use the rapidity in Chapter 6, which is why it is introduced here.

The differential cross section (5.24) can be written in terms of the rapidity as

$$\frac{d\sigma}{dyd\tau} = \sum_{a,b} C_{ab} \left[f_{a/A}(\sqrt{\tau} e^{y}) f_{b/B} \left(\sqrt{\tau} e^{-y} \right) + (A \leftrightarrow B \text{ if } a \neq b) \right] \tag{5.28}$$

With Equation (5.21), it is possible to calculate leading order production cross sections for various particles at the LHC. This is the first step to exploring dark matter production.

The improved parton model

The parton model that we have discussed so far is what is called the naive parton model. It can be considered a fixed energy or leading order approximation. The parton model can be extended, or improved, to include momentum transfer dependent effects from higher order contributions. These effects are crucial in obtaining accurate predictions of events in hadron colliders, and are the bare minimum for modern collider physics phenomenology. They are also required to deal with the mass singularities that appear due to the emission of soft gluons.

The basic principle behind that improved parton model is the inclusion of higher order QCD effects on the quark side of deep inelastic scattering. A full technical discussion is beyond the scope of this thesis, but it is a standard topic in texts on quantum field theory [5, 3, 4] and collider physics [395, 396]. The subject of formal perturbative QCD is treated in great detail in the monograph of Collins [412].

Higher order QCD corrections are necessarily Q^2-dependent, and must be incorporated into the hadronic tensor in Equation (5.12). To do so is nontrivial, and care is required when dealing with the resulting divergent contributions. Momentum transfer dependent corrections to the parton distribution functions can be quantified, but one needs to solve a system of coupled differential equations for the modifications. The equations are known as the DGLAP equations, the acronym comprised of the initials of the individuals who contributed most heavily to the analysis of the equations. Formulation of the DGLAP equations is a complicated calculation, and their solution is generally done numerically. One must generally use at least the NLO improved parton distribution functions to have any confidence in one's results, but NNLO solutions exist and can be used when great precision is required.

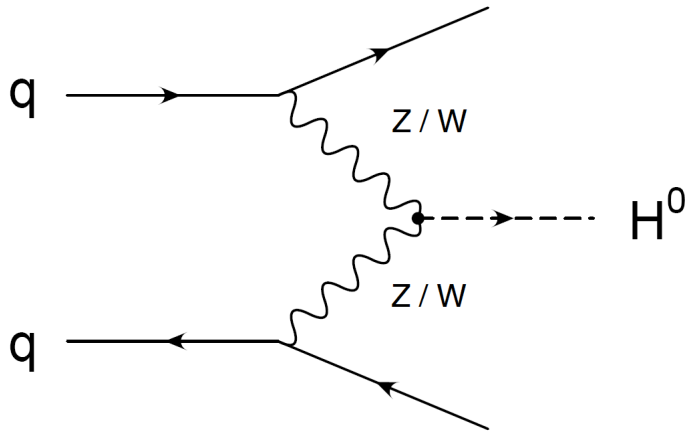

Figure 5.4: Feynman diagrams representing the production of the Higgs boson through the vector boson fusion mechanism in the partonic quark model. Diagram from reference [421].

The basic effect of working in the improved parton model as opposed to the naive parton model is that the parton distribution functions gain Q^2 dependence. This means that simple parameterizations do not exist and that one must use the precomputed grids of results reported by others. The standard parton distribution function sets are made available by the MSTW [418], ABM [419], and CTEQ/CT [420] collaborations, and are generally compared against one another for accuracy. Deviations between these collaborations generally only occur in the very small x region, which is usually only of concern to precision studies of perturbative QCD processes. For the purposes of dark matter detection, the parton distribution functions reported by these collaborations are equivalent.

The functions themselves are stored as grids in $x - Q^2$ space, and a variety of programs that can extract from these grids are provided. Calculations in this thesis use the NLO MSTW grids, reported in reference [418], due to the convenience of the supported Mathematica interfaces. Details on the calculations involved in obtaining these grids, as well as on the assumptions that were made, are available in the reference.

The effective vector boson approximation

It is frequently useful to consider a parton-style analysis of particles that are not classic QCD partons (quarks and gluons). Many processes that are studied at hadron colliders are generated primarily through the interactions of particles that are not usually considered constituents of hadrons, though they do appear within them due to higher order effects. It simplifies calculations considerably to be able to treat these intermediate particles as partons. This is especially useful at LHC energies.

For example, at the LHC, the second most dominant mechanism for Higgs production is through vector boson fusion (VBF) (see Section 5.4.2 for more explicit detail), in which two W or Z bosons annihilate to produce a Higgs boson. More properly, this process appears in a hadron collision most frequently when the weak gauge bosons are emitted by quarks in the hadrons, as illustrated in Figure 5.4.

The full cross section for the process $\sigma(pp \to hX)$ could be computed considering the process in Figure

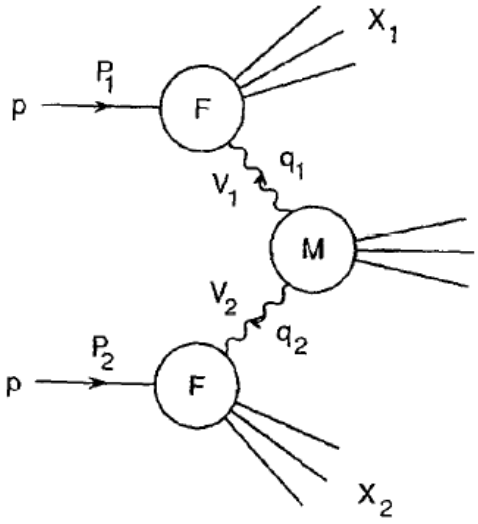

Figure 5.5: Schematic Feynman diagram representation of the process of vector boson fusion in a proton collision. Figure originally appeared in reference [422]. The blobs marked by F are nonperturbative processes whose contributions can be approximated by electroweak boson parton distribution functions. The blob M describes some electroweak boson annihilation process. The X_i are hadronic jet final states.

5.5 as the parton level process and using the quark parton distribution functions, but the three body final state and multiple vertices complicate the calculation significantly even for this relatively simple problem. To be able to consider the weak gauge bosons as partons would allow use of the simple tree level annihilation process of a pair of weak vector bosons as the parton level process, and convolution with the weak gauge boson 'parton distribution functions' would provide the complete cross section. This is analogous to the effective photon approximation for highly relativistic electrons. This analysis is known as the Effective Vector Boson (EVB) approximation, and was first considered a few decades ago in anticipation of the LHC coming online [423, 424].

We follow reference [422] for the weak gauge boson parton distribution functions. Weak vector boson scattering in proton collisions can be represented in terms of the charged and neutral current hadronic structure functions. The analysis of reference [422] requires a factorization of scales to be possible to order α_s, which requires assuming no parton level interference and no interference between similar final states of the scattering process. At LHC energies, these conditions are usually taken to be satisfied. When the invariant mass of the parton level process is larger than the weak gauge boson mass ($\hat{s} \gg m_V^2$), the cross section is dominated by $Q^2 \ll m_V^2$, and one can then derive a set of vector boson distribution functions that can be used in the usual way:

$$f_T(x) = \frac{g_V^2}{32\pi^2}\frac{1}{x}\int_x^1 \frac{dy}{y}\left[F_2\left(y, m_V^2\right)\left(1-\frac{x}{y}\right) + F_1\left(y, m_V^2\right)\frac{x^2}{y}\right]\ln\left(1+\frac{sy\left(y-x\right)}{m_V^2}\right), \tag{5.29}$$

for transversely polarized vector bosons and

$$f_L(x) = \frac{g_V^2}{32\pi^2}\frac{1}{x}\int_x^1 \frac{dy}{y}\left[F_2\left(y, m_V^2\right)\left(1 - \frac{x}{2y}\right)^2 - \frac{1}{2}F_1\left(y, m_V^2\right)\frac{x^2}{y}\right] \tag{5.30}$$

for longitudinally polarized vector bosons. The center of mass energy squared of the process is s, and $F_{1,2}^p(x, Q^2)$ are the proton structure functions as discussed above. The weak coupling for the vector boson is g_V, where $g_W = g_2$ and $g_Z = g_2/\cos\theta_W$, and θ_W is the Weinberg angle. The weak coupling parameter g_2 is related to phenomenological parameters through the relation

$$\frac{G_F}{\sqrt{2}} = \frac{g_2^2}{8m_W^2}. \tag{5.31}$$

As usual, G_F is the Fermi constant of the weak force.

A convenient parameterization of the proton structure function $F_2^p(x, Q^2)$ is given by [425, 426]

$$F_2^p\left(x, Q^2\right) = (1 - x)\left[\frac{F_P}{1 - x_P} + A(Q^2)\ln\left(\frac{x_P}{x}\frac{1 - x}{1 - x_P}\right) + B(Q^2)\ln^2\left(\frac{x_P}{x}\frac{1 - x}{1 - x_P}\right)\right] \tag{5.32}$$

where the scaling point is $x_P = 0.09$ and at this value $F_2^p(x_P, Q^2) = F_P \sim 0.41$ for all values of Q^2 probed in the range $0.11 \leq Q^2 \leq 1200\,\text{GeV}^2$. This joint fit to x and Q^2 was obtained from an analysis of ZEUS data.

The dependence on Q^2 has been parameterized in terms of the functions $A(Q^2)$ and $B(Q^2)$, which have been expanded in powers of $\ln Q^2$ [426]:

$$A(Q^2) = a_0 + a_1 \ln Q^2 + a_2 \ln^2 Q^2,$$

$$B(Q^2) = b_0 + b_1 \ln Q^2 + b_2 \ln^2 Q^2. \tag{5.33}$$

The numerical coefficients resulting from the fit appear in Table 5.1. The Callan-Gross relation [427] $F_2(x, Q^2) = 2xF_1(x, Q^2)$ holds to leading order in QCD, meaning we can use the above parameterization for both F_2^p and F_1^p. It should be noted that, strictly speaking, the parameterizations in Equations (5.32) and (5.33) are possibly outside of their range of validity at LHC energy scales. Their use in such situations can be justified by noting that the dependence on Q^2 is logarithmic at worst, meaning any errors introduced by the parameterization will grow very slowly, and are likely subdominant to NLO corrections.

To illustrate the behaviour of the weak gauge boson parton distribution functions in Equations (5.29) and (5.30), they are plotted in Figure 5.7 on a logarithmic scale. From the Figures, it can be seen that the W and Z boson distribution functions are nearly the same at LHC scales. This is simply because the mass difference between the two bosons is very small compared to the energy scale.

Formally, use of the parton distribution functions to generate a hadronic cross section from the partonic cross section as illustrated in Equation (5.21) requires integration over the region $0 \leq x \leq 1$. This presents a problem for experimental parameterizations of parton distribution functions, however, including this effective vector boson distribution. The problem is, of course, that $x = 0$ is experimentally inaccessible, and there

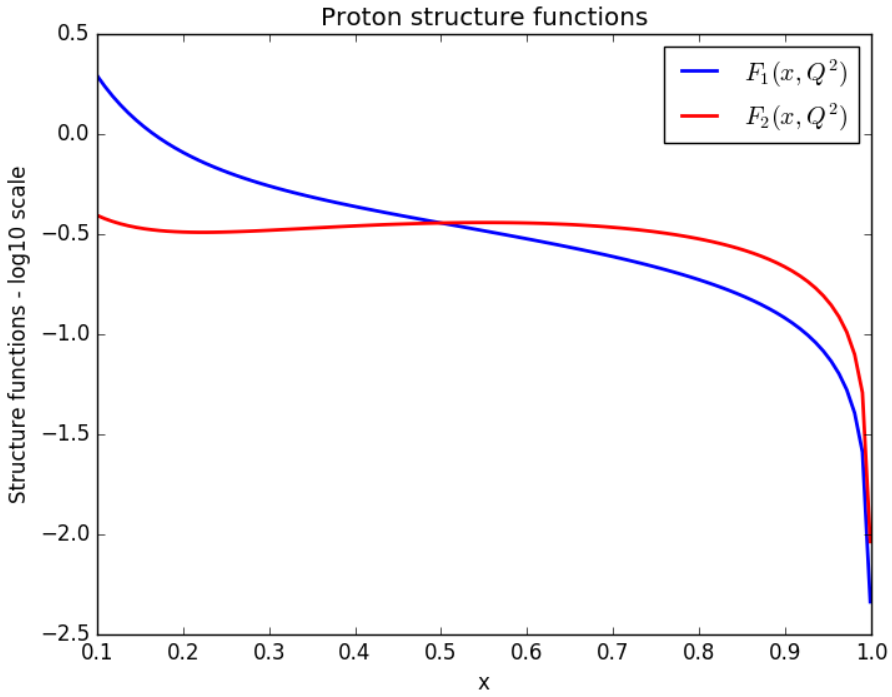

Figure 5.6: Structure functions $F_1(x, Q^2)$ and $F_2(x, Q^2)$ for the proton on a base 10 logarithmic scale calculated according to the parameterization from reference [426].

will always be a δ such that there is no data for $0 \leq x \leq \delta$, which means the parton distribution functions are incomplete and, practically, the integral must be truncated from below at δ. This holds for QCD, and is part of the reason for precision studies of low-x parton distributions. The approximations used for both the structure functions and the effective parton distribution functions themelves are valid only for $x > 0.1$ or so.

It is a practical limit on the integration, but clearly the parton model nonetheless works to some degree. The question, then, is what is the error introduced by this truncation? The effects of the truncation on well understood QCD quantities was considered in reference [428], where the strong coupling α_s is considered. It is found that % level errors are introduced into α_s for lower cutoffs in the 0.03-0.1 range. Further details about the methodology and the assumptions made are available in the reference.

Reference [428] explores a QCD scenario that has been thoroughly studied in comparison to the effective parton distribution functions that concern us here. There is no real alternative but to truncate the integral and accept that there is some error, but we will refrain from attempting to estimate that error. We will take the results of reference [428] to indicate that, while such errors exist, they are manageable, if unknown. With this in mind, we present our vector boson fusion results that use these effective parton distribution functions as first approximations only.

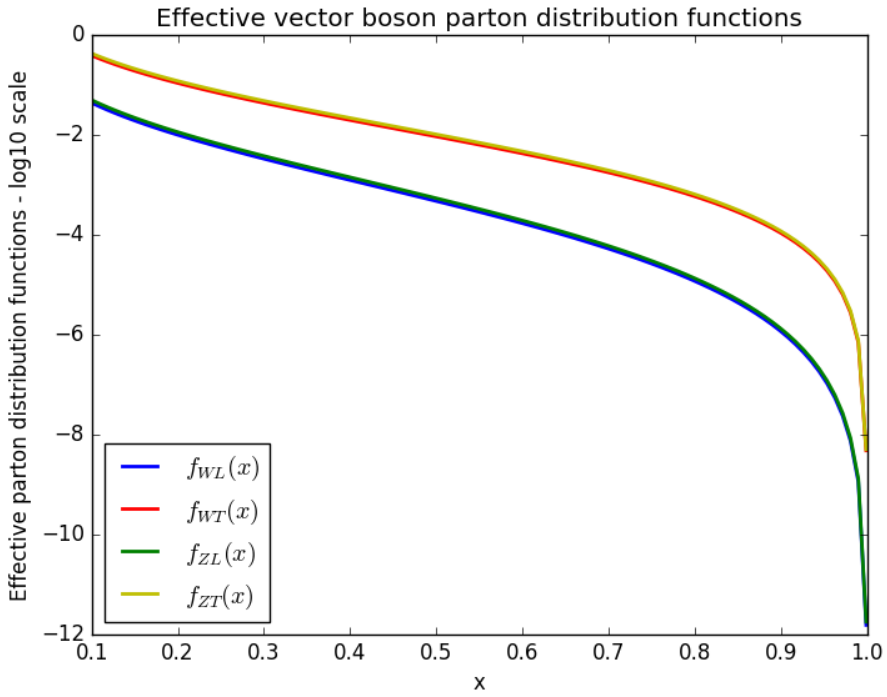

Figure 5.7: The effective parton distribution functions for the electroweak vector bosons in the proton, with both longitudinal (L) and transverse (T) parts included. Calculated over the range $0.1 \leq x \leq 1.0$ using the parameterization from reference [422]. Note that there is little difference in the functions between the two bosons.

Table 5.1: Structure function coefficents

Parameter	Fit value
a_0	$-5.381 \times 10^{-2} \pm 2.17 \times 10^{-3}$
a_1	$2.034 \times 10^{-2} \pm 1.19 \times 10^{-3}$
a_2	$4.999 \times 10^{-4} \pm 2.23 \times 10^{-4}$
b_0	$9.955 \times 10^{-3} \pm 3.09 \times 10^{-4}$
b_1	$3.810 \times 10^{-3} \pm 1.73 \times 10^{-4}$
b_2	$9.923 \times 10^{-4} \pm 2.85 \times 10^{-5}$

5.1.3 Narrow resonance approximation

The narrow resonance or narrow width approximation is an approximation that can be used to factorize the cross sections of processes that have certain properties, making them much simpler to calculate. It is used frequently in collider physics. A solid introduction to the approximation appears in reference [7], and there is also an example of the approximation applied to Z boson physics in reference [395].

The basic principle that the approximation follows from is that nonresonant contributions to the amplitude can be neglected near the resonance. For an s-channel process, the matrix element will be proportional to the denominator of the propagator $\sim 1/(p^2 - m^2 + i\epsilon)$. For values of $p^2 \simeq m^2$, this contribution will dominate all other contributions to the matrix element, generating a resonance in the cross section.

By careful analysis of the contributions to the matrix element, one can factor the cross section as

$$d\sigma(a+b \to X+Y) = \frac{\Gamma(A \to X)}{\Gamma(A \to all)} \left[\frac{1}{\pi} \frac{m\Gamma}{\left(s-m^2\right)^2 + m^2\Gamma^2} \right] \sqrt{\frac{\bar{p}^2 + m^2}{\bar{p}^2 + s}} d^3p ds. \tag{5.34}$$

The decay rates to various channels are denoted by Γ, and $\bar{p}$ is a three-momentum. The important term is

$$\mathcal{W} = \frac{1}{\pi} \frac{m\Gamma}{\left(s-m^2\right)^2 + m^2\Gamma^2}. \tag{5.35}$$

This is the relativistic Breit-Wigner resonance formula. If Γ is small compared to $d\Gamma/dE$ and $d\sigma^{prod}/dE$, we can use the following representation of the Dirac delta distribution:

$$\delta(x) = \lim_{\epsilon \to 0} \left[\frac{1}{\pi} \frac{\epsilon}{x^2 + \epsilon^2} \right] \tag{5.36}$$

to write the resonance contribution as a Dirac delta

$$\mathcal{W} \simeq \delta\left(s - m^2\right). \tag{5.37}$$

Inserting this approximation into the differential cross section (5.34) and using the Dirac delta to evaluate the integral gives the following expression for the cross section:

$$\sigma(a+b \to X+Y) = \sigma^{prod}(a+b \to A+Y) \frac{\Gamma(A \to X)}{\Gamma(A \to all)} \tag{5.38}$$

This means that, in the narrow resonance approximation, the production and decay of the resonance can be factored. The full cross section can be thought of, in a way that dangerously agrees with our intuition, as the production of a real particle followed by its decay. There will be no interference effects between the production and decay processes, as a consequence of the unitarity of cross sections for physical processes. We are thus able to assume that the intermediate state is produced on mass shell, and is nearly asymptotic and so we can treat its decay as a separate process from its production.

It also follows that cross sections can be calculated in terms of production rates:

$$\sigma(a+b\to X)=\frac{16\pi m^4}{N_\psi\lambda(m^2,m_a^2,m_b^2)}\frac{\Gamma(A\to X)\Gamma(\bar{A}\to\bar{a}+\bar{b})}{\left(s-m^2\right)^2+m^2\Gamma^2} \tag{5.39}$$

where $\lambda(x,y,z)=x^2+y^2+z^2-2xy-2xz-2yz$. In general, the narrow resonance approximation will introduce errors of order $\mathcal{O}(\Gamma/m)$.

The narrow resonance approximation is a powerful tool, which allows great simplifications to be made during cross section calculations. It is, however, not infrequently applied outside of its range of validity. The approximation has been shown to work very well inside the SM, but there are concerns about its accuracy in beyond SM physics [429, 430]. In particular, reference [431] provides a detailed discussion of the regions in which the approximation is valid and the errors that using it introduces.

The narrow resonance approximation can be applied safely if the following conditions hold. First, the resonance decay width must be small with respect to the resonance mass ($\Gamma \ll M$). This is usually the only condition that is considered when the approximation is applied in the literature. However, there are additional conditions. The final state particles must be much less massive than the resonance ($m \ll M$), and the scattering energy must be much larger than the resonance mass ($M \ll \sqrt{s}$). Also, there must be no significant interference with non-resonant processes (ie t and u-channel diagrams with the same initial and final states), and the resonance propagator must be separable from the matrix element. These latter two conditions are rarely considered, but can be very important. When these conditions are satisfied, one can integrate the propagator over the momentum to obtain the approximation.

If the approximation is used beyond where it is justified, errors that scale with energy (that can be devastating in collider physics) can be introduced, as well as unaccounted for interference effects. The lesson is to take care when using the narrow resonance approximation.

The narrow resonance approximation is strained when applied to Higgs mediated beyond SM processes, as will be discussed further in Section 5.4. We use the approximation in Chapter 6, when discussing the production of a Z' boson at the LHC.

5.2 Bounds on Mediators

In many cases, the strongest bounds on dark matter production in particle colliders are not those placed on the dark matter particle itself, but those placed on the mediator particle that facilitates its communication with the SM. This is because a mediator particle that couples to SM fields and can be directly produced in a particle collider is much easier to detect than a dark matter particle with highly suppressed couplings to SM fields. The most obvious example of this is that if a mediator can be produced in parton annihilation and has a mass larger than the light quarks, it can decay into partons, producing a characteristic dijet signal. The dijet, and other similar signals, are far easier to identify and extract from the LHC data than the missing energy signatures of dark matter which are discussed in Section 5.3.

When considering the phenomenology of a new model of particle dark matter, an examination of the

bounds on the mediator is very important. The results reviewed in this Section will be used in Chapter 6 to provide constraints on the model discussed there. This Section first provides a basic overview of a class of models known as hidden sector models (Section 5.2.1), which are those models most stringently and cleanly constrained by bounds on mediator fields. The subsequent Sections are brief descriptions of the bounds on scalar (Section 5.2.2) and vector (Section 5.2.3) mediators to hidden sectors as reported by the ATLAS and CMS collaborations.

5.2.1 Hidden sector Dark Matter

A common general family of models that frequently appears in the dark matter literature are the 'hidden sector' models [432]. These models contain field content that is hidden from (does not directly interact with) the SM or visible sector. Particles in the hidden sector do not have charge under the SM gauge groups (they are SM gauge singlets), and interaction between the two sectors proceeds generically through a mediator field of some kind that interacts with both sectors. The natural place to put dark matter is in the hidden sector, and the natural first constraint on a hidden sector model is on the properties of the mediator. We discuss hidden sector models here because both of the example models considered in this thesis (the scalar Higgs-portal model and the vector-portal model discussed in Chapter 6) are hidden sector models.

Hidden sector models are adaptable and, to a certain extent, generic. They are complete theories but as the connection to the SM is through a single or small number of mediator fields, phenomenological bounds can usually be translated between similar models. The basic 'classes' of hidden sector dark matter models are divided according to the type of mediator. The requirement of a renormalizable coupling limits the number of interactions to a handful of 'portals.' One thus has the scalar portal, the vector portal, and the less commonly studied neutrino portal. The Higgs portal that has been used as an example throughout this thesis is an example of a scalar portal model, and the 'portal' terminology was coined to describe the Higgs portal [433]. In scalar-portal models, the mediator is a scalar particle, and in vector-portal models, the mediator is a spin 1 massive boson, usually the gauge boson of some extended symmetry. In Chapter 6, we consider an example of vector-portal dark matter. The neutrino portal is somewhat more complicated to implement than the other two, and relies on interactions between the Higgs field and leptonic fields. It is closely related to the problem of neutrino masses and mixings, and as such has a large overlap with neutrino physics. Neutrino-portal dark matter is studied in references [434, 435, 436].

5.2.2 Scalar mediators

Models with scalar mediators to hidden sectors are very common [437], as are extensions of the SM that include additional scalars. This has led to a great deal of effort being put into searches for new scalars at colliders. The primary search channel for new scalars is the diphoton channel, which is a pair of high energy photons. Diphoton events would occur when the new scalar is produced and then decays through some process into a pair of final state photons. This channel is important despite the fact that most new scalars

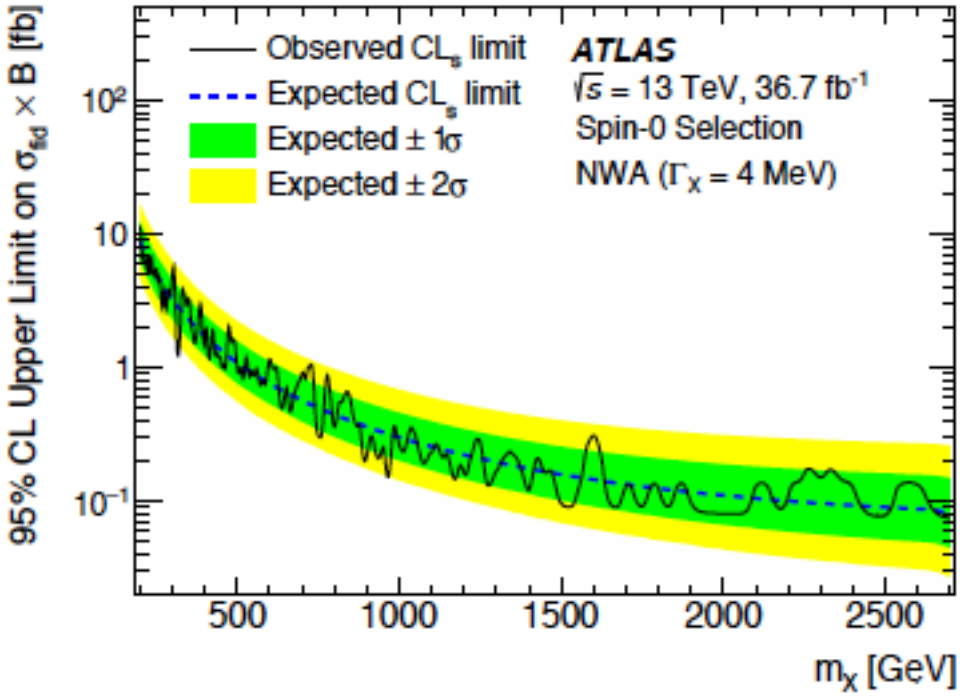

Figure 5.8: Bounds on scalar resonances from cross section × branching ratio to the diphoton channel. Values above the line are excluded with 95% confidence. Figure originally published in reference [438]

are expected to couple only very weakly to photons because of the advantages of the diphoton final state. The diphoton signature is electromagnetic, and so free of many QCD effects, and current technology allows for excellent energy resolution. The diphoton signature also has comparatively low backgrounds.

Figure 5.8 displays the current bounds on new scalars, including those which could be mediators to hidden sector dark matter, as reported in reference [438]. The bounds were derived from 36.7 fb^{-1} of data at the 13 TeV LHC. A variety of models with additional scalars are included in the plot, including extended Higgs sectors. The bounds exclude scalars that have a cross section × diphoton branching ratio above the indicated value in the mass range of 200-2400 GeV with a 95% confidence. More details on the event selection, data analysis and background simulation are available in the reference.

For masses below a few hundred GeV, these bounds are strong, and pose problems for many models. The bounds weaken at higher masses, due to lower expected numbers of events as the kinematic limit is approached. It should be noted that no statistically significant excess has been observed.

Earlier search results in 2015 reported a potential signal [439, 440] that could indicate a scalar resonance in the diphoton channel at approximately 750 GeV. Though the excess was small, with a local significance of 3.9/3.4 σ (ATLAS/CMS), far below the threshold of acceptance as an observed phenomenon, it nonetheless generated a great deal of excitement, and hundreds of articles were written on the theoretical implications (see reference [441] for a review of the developments). It was later reported that the excess was not confirmed, and had reduced in statistical significance [442, 443]. While this anecdote is perhaps depressing, it demonstrates

the importance of the diphoton channel for the discovery of new scalar mediators.

5.2.3 Vector mediators

Nearly all of the favoured extensions of the SM include extended gauge symmetries, and because of the group theory involved in the resulting symmetry breaking patterns, these models will almost always contain at least one additional $U(1)$ symmetry. Phenomenologically, this will typically lead to the prediction of a new massive spin-1 boson, usually denoted Z'. The Z' has been studied for decades [444, 445], and theories that use the particle to act as a portal to hidden sectors are a natural extension [446, 447]. Bounds on Z' particles from colliders have been considered with great detail, and are well understood. For a review of Z' phenomenology, see reference [448].

While there are a variety of channels that can be used to place bounds on new vector bosons, the ones that currently provide the strongest constraints are the dijet channel and the dilepton channel. Generically, the dilepton bound is stronger because the dilepton channel is much cleaner than the dijet channel, which is a consequence of how messy QCD becomes. However, there are enough specialized models that have a stronger dijet signature that the two searches are complementary.

The following Figures were originally published in references [449] (dijet) and [450] (dilepton). The dijet data was obtained from 37 fb^{-1} of integrated luminosity at the 13 TeV LHC, and the dilepton data was obtained from 36 fb^{-1} of integrated luminosity at the 13 TeV LHC. Figure 5.9 contains 95% exclusion limits on the cross section times branching ratio for a Z' resonance of a specific type in the dijet channel, and Figure 5.10 contains upper limits on the cross section times branching ratio for a vector resonance in the dilepton channel with 95% confidence. The specific model considered in the dijet case is a leptophobic Z' that has axial-vector couplings to SM quarks and Dirac fermionic dark matter. It is described in reference [451]. The other models considered in these publications include primarily generic Z' and W' models, though other more exotic possibilities, like quantum black holes and excited quarks, are also considered.

No significant excess is observed in either of these channels, and so we take them as upper limits on cross section times branching ratio for models that predict new vector bosons. It should be noted that above 3.5 TeV or so, the expected signal cross section falls rapidly due to the kinematics of the process, and bounds become much weaker. This fact will be important in Chapter 6.

5.3 Dark Matter Searches

The previous Section described the bounds on mediators to dark sectors, which are usually the first line of attack when analyzing the collider phenomenology of a new model of particle dark matter. However, for some models the mediator is not easily constrained or, as in the case of the Higgs-portal model, has known properties. In these cases, as well as in cases where additional analysis of the model is warranted, direct collider searches for dark matter are carried out.

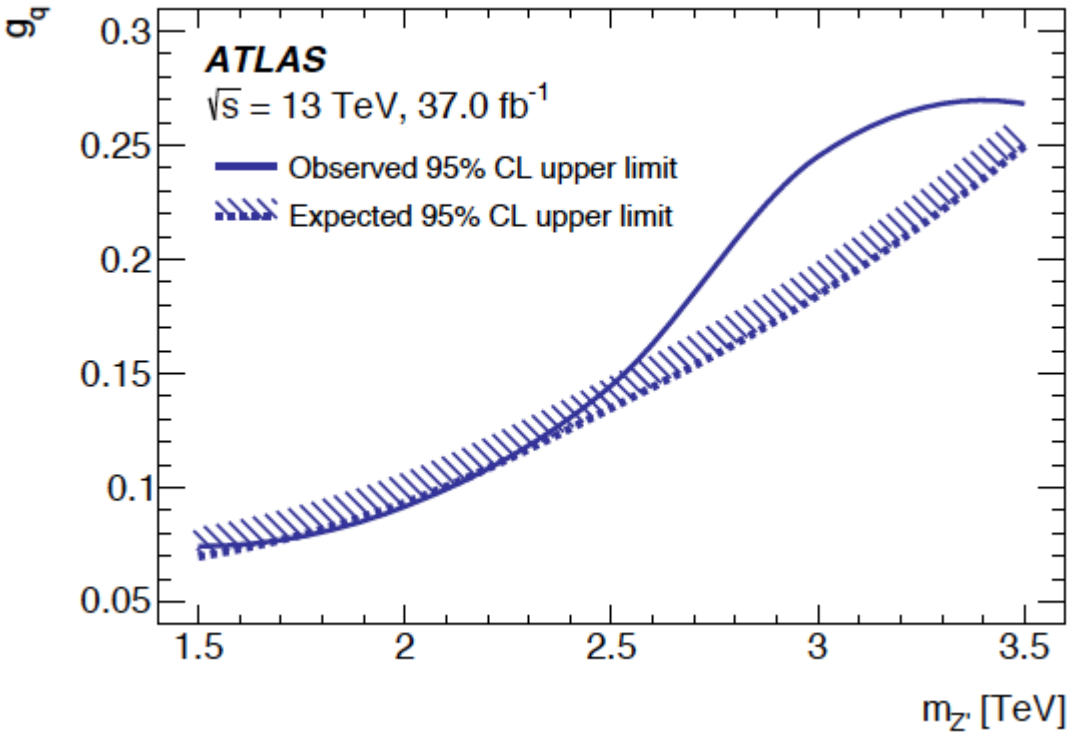

Figure 5.9: Bound on the coupling g_q between quarks and a Z' vector resonance in the dijet channel. Values above the line are excluded with 95% confidence. Further details on the model considered are included in the text. Figure originally published in reference [449]

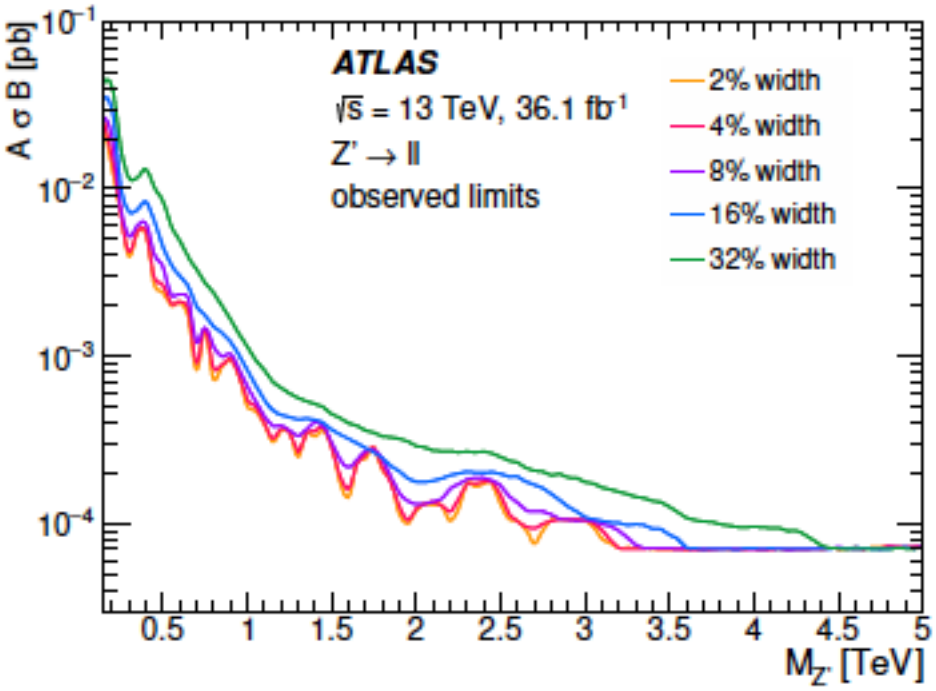

Figure 5.10: Bounds on vector resonances from cross section × branching ratio to the dilepton (dielectron and dimuon) channels for a range of resonance widths. Values above the line are excluded with 95% confidence. Figure originally published in reference [450]

Of course, no particle collider will run for the sole reason of searching for dark matter. Recently, however, there has been a strong push in the collider community to place more emphasis on dark matter searches. This push has no doubt been in part motivated by the absence of any signals in the passive direct detection experiments discussed in Chapter 3. The current state of the field at the time of this writing is summarized in reference [452].

As mentioned in Section 5.1, colliders are the only controlled laboratory experiment available to us that might allow the study of the properties of particle dark matter. That control implies reproducibility is something that cannot be overemphasized. As well, collider experiments can probe the interactions of particle dark matter with SM matter with much better accuracy than either direct detection experiments or indirect detection experiments, where astrophysical uncertainties dominate. It has been a frequently emphasized point in the literature that the direct, indirect and collider channels for the detection of dark matter are complementary. Each brings to the table a potential piece of the puzzle, which helps provide a picture of particle dark matter.

This Section will provide a status update on missing energy searches for dark matter at colliders. We have included discussions of the strict missing energy signature, as well as the mono-X searches, where a SM observable is produced along with the missing energy signal. A recent review of mono-X signatures [453] is one of the primary references followed. While we will provide bounds and some technical discussion of

backgrounds, much of the discussion will be qualitative, as the full details of the analyses that go into the calculation of these bounds from the available data is far beyond the scope of this thesis (or, indeed, any single thesis). This Section aims to provide the basic information that will allow a phenomenologist to get a grip on the basic searches and to provide relevant references for those who seek a deeper understanding.

5.3.1 Current research

Collider physics is messy, and extraction of a missing energy signal is complicated, especially when the invisible particle carrying off the energy has unknown properties, as in the case of dark matter. Recently, the collider physics community has begun to focus more on dark matter than in the past, resulting in three distinct approaches that attempt to make the analysis of collider data more tractable. The reason behind this surge in popularity is that with the new analysis techniques shaped by Run I of the LHC, it has become feasible to search for dark matter signatures in the mess that is collider data. This was not possible even a decade ago.

The first approach is the original one, which is to perform an analysis of data for each separate particle physics model of dark matter. This has only ever really been done for certain variants of SUSY dark matter (see reference [454] for a review). This approach has the advantage of dealing with a complete model with theoretical motivations that provides a fairly straightforward way to interpret the data. This approach is ideal, but is very labor intensive, especially with the current explosion of viable models, which has led collaborations to adopt the following two approaches.

Analysis is more useful to the community if it is as model-independent as possible. The second way of analyzing dark matter at colliders is by using effective field theories (EFTs). Cross sections can avoid complicated kinematic dependence if they are computed with respect to some energy scale of importance Λ. By integrating out heavy fields in a complete model, one can reduce more complicated interactions in the theory down to point interactions in a nonrenormalizable effective theory, usually categorized by the mass dimension of the associated operators, which are proportional to the scale Λ. Experimental bounds on Λ as a function of dark matter mass are fairly easy to produce.

A typical interaction between dark matter and SM particles in the effective theory is represented in terms of dimensionful operators $\mathcal{O}$ and several examples include [455]

$$\mathcal{O}_V = \frac{1}{\Lambda^2} \left(\bar{\chi}\gamma_\mu \chi\right) \left(\bar{q}\gamma^\mu q\right), \tag{5.40}$$

$$\mathcal{O}_A = \frac{1}{\Lambda^2} \left(\bar{\chi}\gamma_\mu \gamma_5 \chi\right) \left(\bar{q}\gamma^\mu \gamma_5 q\right), \tag{5.41}$$

$$\mathcal{O}_g = \frac{\alpha_s}{\Lambda^3} \left(\bar{\chi}\chi\right) \left(G_a^{\mu\nu} G_{\mu\nu a}\right), \tag{5.42}$$

$$\mathcal{O}_S = \frac{m_q}{\Lambda^3} (\bar{\chi}\chi) (\bar{q}q) , \tag{5.43}$$

$$\mathcal{O}_{\tilde{S}} = \frac{m_q}{\Lambda^3} (\bar{\chi}\gamma_5\chi) (\bar{q}\gamma_5 q) . \tag{5.44}$$

These operators govern the interaction of dark matter χ (here a Dirac fermion) with SM quarks q or gluons $G_{\mu\nu}$. Interactions can be characterized according to their Lorentz structure. Presented are the vector (V), axial vector (A), scalar (S), and pseudoscalar ($\bar{S}$) operators, as well as the scalar gluonic operator (g).

The cross sections become much simpler to calculate, and can easily be represented in terms of the EFT operators. Bounds can then be placed on these operators or the mass scales they contain, which allow study of particle dark matter generically at particle colliders [456, 457, 458, 459, 460, 461]. These results can also be translated into constraints on complete theories. The EFT approach has versatility in that collider bounds on EFT operators can be translated between the three main dark matter detection channels (collider, direct, indirect) with relative ease. Details of data modelling, event construction and selection are available in the individual ATLAS and CMS publications. Higher order SM effects on the searches have been considered as well [455].

However, the EFT approach has drawbacks. For significant regions of the parameter space probed by the LHC the EFT approximation breaks down [460, 461, 462, 463, 464, 465, 466, 467]. This will occur when the center of mass energy s is close to the mediator mass (ie near Λ^2 naively). Terms in the theory $\sim s/\Lambda^2$ can no longer be neglected. Contributions from the particles that were integrated out become relevant. This does not mean the EFT approach is useless, only that it has a limited range of viability. The EFT approach is well justified at the LHC for large mediator masses, but while the validity of the EFT relies on a large mediator mass, the experimental sensitivity depends on the scale Λ. Since these quantities are related, there is only a small region of parameter space in which EFTs are both valid and useful at the LHC, which is a window for Λ around a TeV to a few TeV. Outside this region, the EFT cross sections will begin to become non-unitary [466, 467] and hence non-physical, which is a sign of the theory breaking down.

Because of these limits on EFT models, so-called simplified models were created, and have become an important part of the collider physics program for dark matter [468, 469, 222, 470, 471, 472, 473, 474, 475, 476]. Simplified models are models where the dark matter particle interacts with the SM through a mediator field. They are essentially simplified versions of hidden sector models, where the mediator is characterized by its spin and mass, taking only the phenomenologcially relevant parts of a more complete theory. Simplified models retain the simplicity of the EFT approach while being valid over the entire parameter space (they are careful to retain UV completeness) and capturing propagator dynamics that elude the EFTs. In fact, when one takes the infinite mass limit for the mediator of a simplified model, one obtains an EFT. The structural advantages of the simplified models come at the cost of slightly increased calculational complexity. Simplified models can be thought of as a simplified version of a more complete theory as well.

Simplified models are still simplifications, though, and are not complete theories (in most cases). Though

they will in general ameliorate the unitarity issue that plagues EFTs, they cannot solve it completely either [477, 478].

The most commonly explained simplified models are the vector-portal model, where the mediator is a massive vector boson, and the scalar (pseudoscalar)-portal models, where a scalar or pseudoscalar particle acts as the mediator. Both models have been well-studied [471, 472], and both are theoretically well-motivated.

The vector-portal model is characterized by a Lagrangian that includes terms of the form

$$\mathcal{L} \supset \frac{m_V^2}{2} V^\mu V_\mu + g_q V^\mu \gamma_\mu \bar{q} \left(1+\gamma^5\right) q + g_\chi V^\mu \gamma_\mu \bar{\chi} \left(1+\gamma^5\right) \chi \tag{5.45}$$

which is similar to those that appear in the prototypical Z' extensions of the SM. The dark matter particle χ is typically taken to be fermionic with a Dirac mass term, and there is an implicit sum over the active quark flavors. The Lagrangian (5.45) includes both vector interactions ($\sim \gamma^\mu$) and axial vector interactions ($\sim \gamma^\mu\gamma^5$) for full generality, but the simplified models are usually studied with only one of the interactions active. That is, the mediator is treated as if it interacts only through vector channels or only through axial vector channels when the bounds are computed. For a more detailed discussion of the differences between these two channels and the effects on the phenomenology, see Chapter 6 of this thesis.

The scalar-portal models use a Lagrangian which contains terms like

$$\mathcal{L} \supset g_q \phi \bar{q} q + g_\chi \phi \bar{\chi} \chi, \tag{5.46}$$

while the pseudoscalar-portal models have terms in the Lagrangian like

$$\mathcal{L} \supset g_q \tilde{\phi} \bar{q} q + g_\chi \tilde{\phi} \bar{\chi} \gamma^5 \chi. \tag{5.47}$$

As with the vector-portal case, the dark matter particles χ are typically taken to be Dirac fermions. Analysis of LHC data usually explores the region where the mediator is nearly on-shell (ie near the $m_{med} = 2m_{DM}$ resonance). Use of the narrow width approximation as discussed in Section 5.1.3 is common.

Simplified models are an important part of modern dark matter collider phenomenology, and that alone is enough of a reason to include them in this thesis. However, the two main models of particle dark matter that we discuss in this thesis are also nearly identical to simplified models. This allows the bounds reported for simplified models to be used with some adaptation. We frame our present discussion in a independent way. The example discussed at the end of this Chapter is Higgs-portal scalar dark matter, which is both a complete theory and a splendid example of a simplified model. As well, the Z'-portal dark matter discussed in Chapter 6 is an almost perfect example of the vector-portal simplified model. This comparison is addressed further in Chapter 6.

5.3.2 Missing energy

Pure dark matter production at particle colliders manifests as a phenomenon known as missing transverse energy or missing transverse momentum, depending on which is more convenient to describe the situation. This quantity is determined entirely by conservation of energy and momentum relations. The transverse momentum p_T is the momentum p projected onto the transverse plane (ie the components of p that are perpendicular to the axis of the collision). The transverse energy is then simply the fraction of energy associated with the transverse momentum component: $E_T = E \sin\theta$. Particle dark matter cannot be observed by the detectors, so any energy carried off by dark matter final states will be unobserved, and appear to be a violation of the kinematic conservation laws. One can then use those conservation laws to constrain the energy and the momentum of the dark matter final states without being able to observe them. Hence, 'missing energy.'

A missing energy signal is difficult to extract with any certainty due to the large number of possible things that can mimic it. If a jet or a lepton is missed or mis-tagged in the detector, than it can appear to be missing energy in the analysis, which can occur frequently with soft jets. As well, there is the irreducible neutrino background, which is identical to the missing energy signature produced by dark matter. When a Z boson is produced, it will decay into a pair of neutrinos 20% of the time [8], and the neutrinos will pass through the detector unnoticed. Production of W bosons also results in a significant number of neutrino final states.

Unfortunately, missing energy signatures are not very useful as a dark matter search tool, though they are necessarily common to all dark matter collider searches. This would be true even in the relatively clean environment of an electron collider, and it is especially apparent at a hadron collider like the LHC. Without SM particles in the final state, it is exceedingly difficult to extract any useful information out of a missing energy event, even if one is tagged correctly. A useful signature therefore requires SM particles in the final state, so that their momentum can be used to reconstruct the missing energy piece through conservation laws.

For SM final states to be observed, an event must have large p_T and admit the parton approximation, as discussed in Section 5.1. Because the visible SM component balances the invisible dark matter component, the dark matter final state will also have large transverse momentum (a pair of dark matter particles produced balanced against a SM signature will typically have collinear momentum).

5.3.3 Monojet searches

The monojet signal is what occurs with a final state of missing transverse energy and a single jet. A jet is a stream of hadrons with a closely aligned large transverse momentum p_T. The jet comes from a high energy colored particle (quark or gluon) that is usually emitted from the initial state of a production process, though emission from an intermediate state is possible for certain dark matter models. The colored particle then is subjected to confinement at high energies, a process known in collider physics as fragmentation, which results

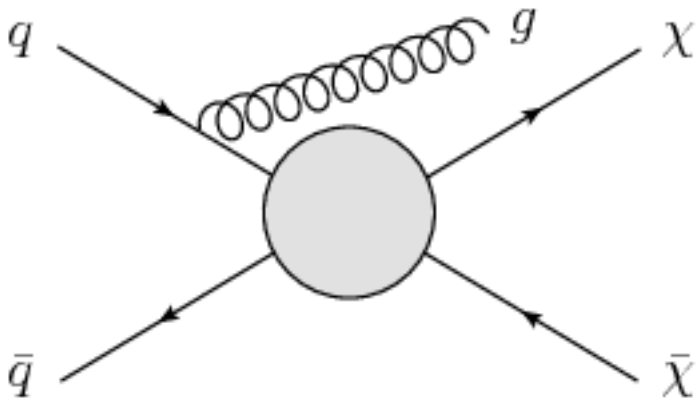

Figure 5.11: A diagrammatic representation of a monojet signature due to radiation of a gluon from the initial state. The internal structure of the dark matter production mechanism is denoted by the blob, in the EFT style. Diagram from reference [469].

in the jet of hadrons (and their decay products). For a monojet event to be considered a possible dark matter event, there must be no identified leptons, and mistagging of leptons causes significant error in analysis of the data. At the LHC, the monojet signal is the most prevalent of the mono-X signals because of the initial state radiation [479], and it is expected that the monojet signature will provide the strongest bounds on most dark matter models. This is a consequence of the LHC being a hadron collider. The monojet signature of dark matter is one of the most widely studied collider signatures of dark matter [480, 459, 461, 456, 458, 467, 481]. A diagram for the process in an EFT appears in Figure 5.11.

Events with only a single jet are actually rather rare [482], which makes the strict monojet signature as such of reduced practical value. The dijet and multijet with missing energy signatures have also been considered [462, 222].

5.3.4 Monophoton searches

The monophoton signature is characterized by a single high energy (large p_T) photon balanced by some amount of missing transverse energy. A basic EFT representation of a process that would generate the signature appears in Figure 5.12. Monophoton events are much less frequently occurring than monojet events at the LHC, because the LHC collides hadrons, but monophoton events are much cleaner when they do occur. There have been a number of experimental studies of the signature at the LHC [483, 484, 485, 486]. Backgrounds for the monophoton signature are usually very low, with mistagging of a lepton or jet far more likely to cause error than in the monojet signature. Dominant background processes include γZ production, where the Z decays to neutrinos, resulting in missing energy. This background is irreducible, as is usually the case when neutrinos are produced. Subdominant backgrounds include $W\gamma$ events where the W decays to a lepton and a neutrino and the lepton is mistagged, and Wj or Zj events where the jet is mistagged as a photon. Even smaller background processes include single top production, diboson production and diphoton

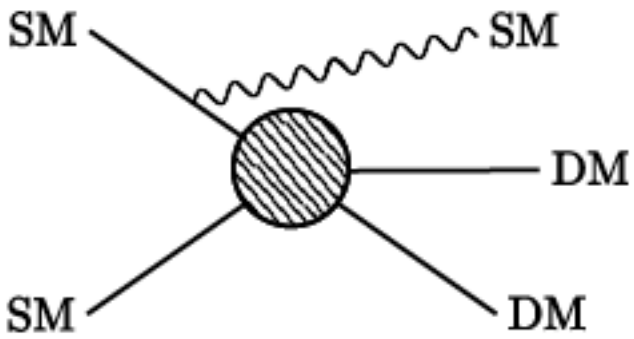

Figure 5.12: A diagrammatic representation of a monophoton signature from initial radiation of a SM particle. The internal structure of the dark matter production mechanism is denoted by the blob, in the EFT style. Diagram from reference [453].

events.

In general, the monophoton signature is not very constraining, though in reference [487] monophoton bounds on certain EFT dark matter operators have been converted to bounds on nuclear recoil cross sections. The monophoton signature has also been considered in references [458, 481].

5.3.5 Monohiggs searches

The monohiggs signature [488, 489] is one that has become possible now that the SM Higgs boson has been observed and its properties are known. In fact, such searches were proposed shortly after the observation of the Higgs was reported [490, 491, 492]. In particular, see reference [492] for estimates of LHC sensitivities and a very detailed study of the monohiggs signature. As indicated, the final state is missing transverse energy recoiling from a Higgs boson, which rapidly decays into its usual final states (predominantly $\bar{b}b$ pairs). The invariant mass of the final state Higgs is constrained to be near the Higgs mass pole of 125 GeV [490]. This makes identification of the signature from the observed Higgs decay products easier than might be expected. The monohiggs signature is especially promising for models in which the dark matter interacts directly with the Higgs (such as Higgs-portal dark matter), or is involved in electroweak symmetry breaking at all. It is also potentially useful for studying dark matter models that are coupled to the top sector, due to the strength of the top Yukawa coupling.

The monohiggs signature differs from the other mono-X signatures in that Higgs radiation from the initial states is highly suppressed. The Higgs couples very weakly to light quarks and gluons, meaning a monohiggs is more likely to be emitted from the dark matter side of the process. This allows the monohiggs technique to probe dark matter interactions with the SM in ways that the other signatures cannot.

The dominant irreducible background for the monohiggs signature is Zh production with the Z decaying into a pair of neutrinos, the SM contribution to missing energy. As mentioned above, the $\bar{b}b$ channel of Higgs decay is the largest, with a branching ratio of 0.577 [8]. Backgrounds for this signature are any dijet state

[493, 494, 495], of which there are many, though there has been work done looking into how to distinguish $\bar{b}b$ dijets from other dijets [496]. Also important is the $h \to \gamma\gamma$ signature [497, 498, 499, 500], which is much cleaner than the $\bar{b}b$ channel though it has a much lower branching ratio (around 2.28×10^{-3} [8]). This is simply due to the cleanliness of the $\gamma\gamma$ signal in comparison to any hadronic signal. Dominant backgrounds for this channel include $Z\gamma\gamma$ production and hZ and hW states with decays to neutrinos. Background estimates for both of these channels are available in reference [490], which treats the monohiggs signature from a simplified model and EFT perspective.

5.3.6 Other searches

There are some other mono-X signatures that have been considered in the literature, though not with the frequency and rigor of the three described above. This is for a variety of reasons, such as difficulty in extracting the signal or that the signature is produced very rarely in all but a handful of highly specialized models. While they are interesting to consider, these channels are unlikely to lead to the discovery of dark matter at the LHC. They are included here for completeness and to provide some examples of nonstandard dark matter signatures that are being considered.

Of these signatures, those that have received the most attention are the monogauge [501] and monobottom [502] signatures. The former involves the detection of a electroweak gauge boson, almost always taken to be a Z, balanced by missing transverse energy, while the latter is a single heavy quark, usually taken to be a bottom quark, balanced by missing transverse energy. The monobottom signature in particular is difficult to distinguish from a monojet [503, 504], though progress is being made [496]. The basic analysis of these signatures proceeds similarly to the previously discussed mono-X signatures, with some deviations that are explored in the above articles.

Mono-Z signatures have been studied in references [505, 506]. While the $Z \to l^+l^-$ channel final states are easier to observe than monojet or monophoton signatures, the branching ratio is much smaller. A Mono-W signature has been proposed, which in practice leads to a monolepton signature [507, 508]. This signature is almost useless because of high backgrounds. There are many neutrinos produced in association with these processes, and all SM W producing processes become background. The mono-W signature might be of value in the specialized case of isospin violating dark matter, however.

There have also been studies of the top pair signature [509, 510, 511] and the monotop signature [512, 513, 514, 502]. These signatures are expected to be very weak for most dark matter models, and are usually considered only for specialized models that interact primarily through the top sector.

5.4 Example: scalar Higgs-portal dark matter

As a simple demonstration of how some of the material discussed in this Chapter can be applied to a real model, we again return to the example of Higgs-portal scalar dark matter in this Section. Higgs-portal

scalars at particle colliders, and at the LHC in particular, have been considered extensively in the literature [515, 516, 517]. Part of this is because of the connection between the model and basic aspects of Higgs physics, which is a major focus of the LHC program. The scalar Higgs-portal model is thus valuable to examine as an example case of collider searches for dark matter. Collider signatures of dark matter are also considered for a different model in Chapter 6. Some signatures and techniques that apply to that model cannot be used for the Higgs-portal model, so the two models are complementary in that they allow different techniques to be demonstrated.

The primary constraint that collider data applies to the scalar Higgs-portal model comes from measurements of the invisible decay width of the SM Higgs boson. The bounds inferred from these measurements are discussed in Section 5.4.1. In Section 5.4.2 production rates for Higgs-portal scalars in hadron colliders are considered. The Section starts with a discussion of Higgs boson production, then moves on to consider Higgs-portal scalar production using the same mechanisms of gluon fusion and vector boson fusion. Section 5.4.3 contains a brief discussion of mono-X signatures of Higgs-portal scalar dark matter.

5.4.1 Bounds from the invisible Higgs decay width

One of the more stringent bounds on scalar Higgs-portal dark matter is obtained from bounds on the invisible Higgs boson decay width. This observable is of wide interest for the study of both SM physics and potential new physics. Bounds have been placed on the upper limits of the invisible Higgs branching ratio by ATLAS ($Br_{inv} < 0.28$) [518] and CMS ($Br_{inv} < 0.24$) [519].

For a Higgs-portal scalar of mass $m_S < m_h/2$, the Higgs will decay into invisible dark matter states at a rate governed by the strength of the Higgs-portal interaction η. The decay width is given by

$$\Gamma_{h\to SS} = \frac{\eta^2 v_h^2}{32\pi m_h^2}\sqrt{m_h^2 - 4m_S^2}. \tag{5.48}$$

One can relate the invisible decay width, the visible decay width (taken throughout to be $\Gamma_h = 0.00629044$ GeV [8]), and the invisible branching ratio through the definition of the branching ratio:

$$Br_{inv} = \frac{\Gamma_{inv}}{\Gamma_{inv} + \Gamma_{vis}}. \tag{5.49}$$

The invisible Higgs decay width to Higgs-portal scalars in Equation (6.18) is plotted for a selection of values of η_S in Figure 5.13. Also plotted are the bounds on the invisible Higgs decay width reported by the ATLAS and CMS experiments. The decay widths go to zero at $m_S = m_h/2$ because the decay is not kinematically allowed above that value. From Figure 5.13, it is clear that very small values of η_S are required to avoid the bounds on the invisible decay width.

Such small values present issues for reproducing observed abundances when trying to construct a dark matter model. It can also be seen that, even for larger values of η_S, the decay width drops rapidly enough near the half-mass resonance that the bounds could be avoided, at least in principle. In practical calculations,

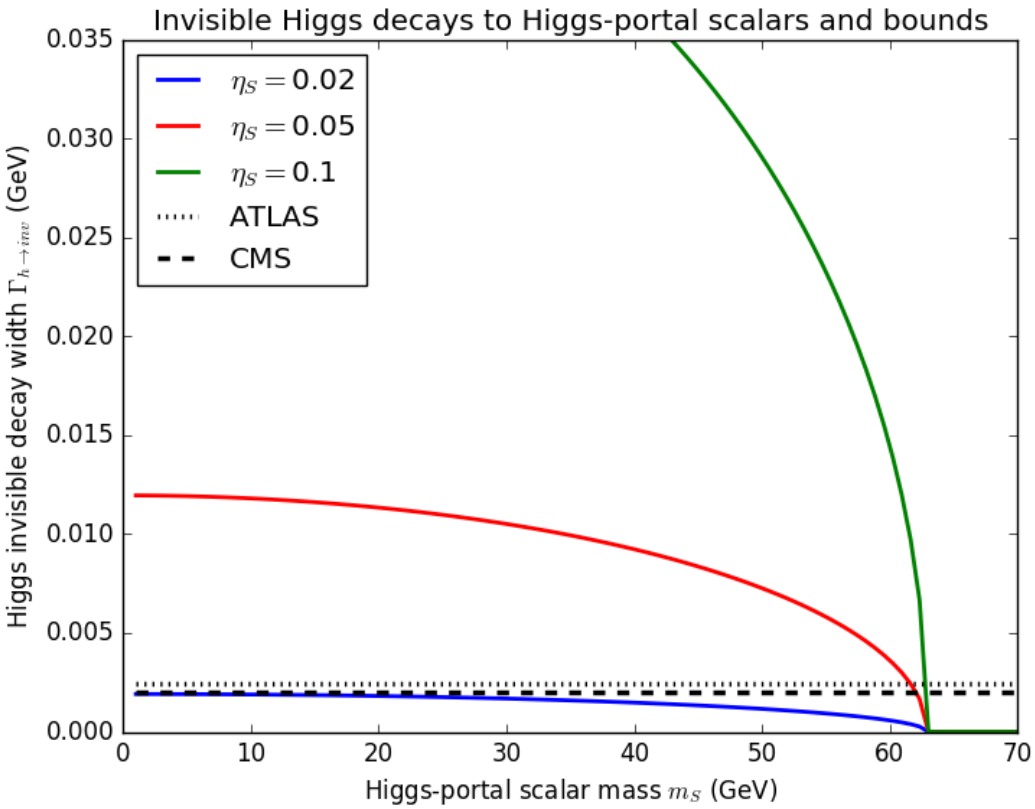

Figure 5.13: Invisible decay width of the SM Higgs boson to Higgs-portal scalars as a function of scalar mass plotted alongside bounds on the invisible decay width from ATLAS [518] and CMS [519]. Theoretical decay widths are plotted for a selection of values of the Higgs-portal coupling η_S.

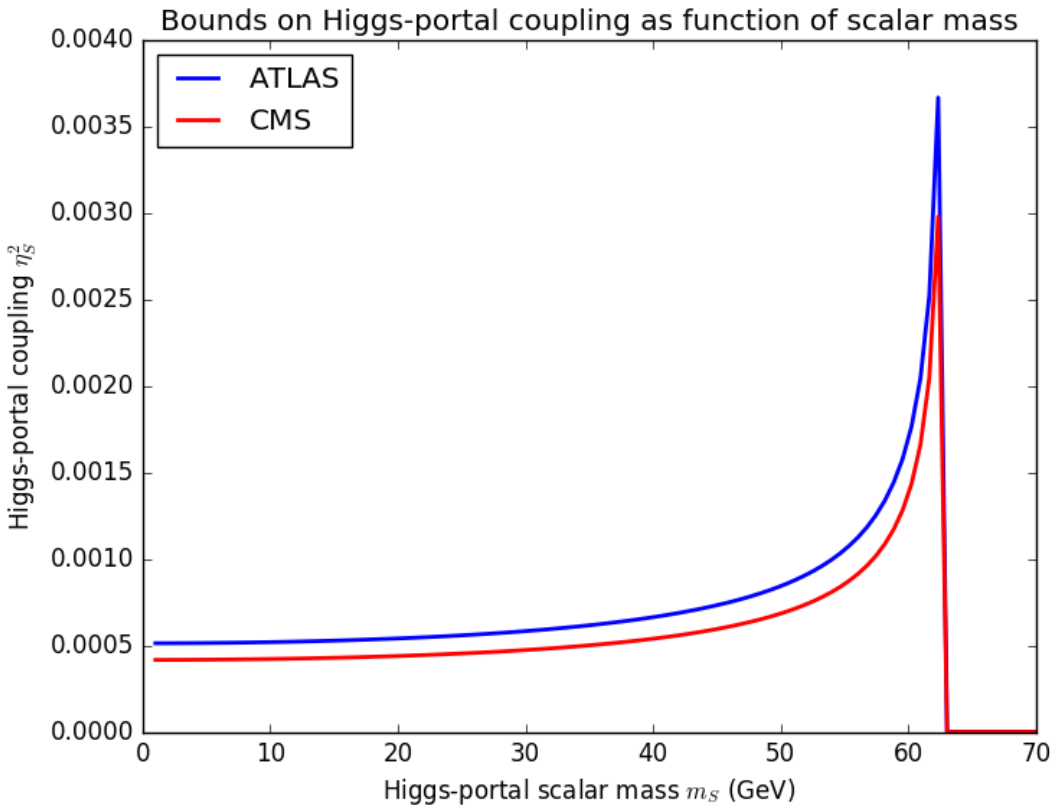

Figure 5.14: Bounds on the Higgs-portal coupling η_S as a function of Higgs-portal scalar mass computed from experimental bounds on the invisible Higgs decay width reported by ATLAS [518] and CMS [519]. See text for more details on the calculation.

however, this region near the resonance is best avoided, as was mentioned in Chapter 2. Most approximations made during dark matter phenomenology calculations tend to break down when Higgs-portal models are considered near the half-mass resonance.

The same bounds are presented in a different form in Figure 5.14. Here, the relation (5.49) is manipulated to the following:

$$\eta_S^2 = \frac{32\pi m_h^2}{v_h^2\sqrt{m_h^2 - 4m_S^2}} \frac{Br_{inv}\Gamma_{vis}}{1 - Br_{inv}}, \tag{5.50}$$

so that the ATLAS and CMS bounds on the invisible Higgs branching ratio are presented in terms of bounds on the Higgs-portal coupling η_S^2.

This presentation provides a complementary perspective on the bounds, and emphasizes how small the coupling needs to be to satisfy the experimental constraints. Again, the constraint seems to weaken near the half-mass resonance at 62.5 GeV, but the difficulties remain.

Because of these stringent bounds, and the difficulties of properly implementing the thermal production constraint in the region near the half-Higgs mass resonance, we do not consider Higgs-portal scalars with masses below $m_h/2$.

5.4.2 Production rates

To study collider signatures of Higgs-portal scalar dark matter, it is obviously important to understand the processes by which the dark matter particles are produced. While the basic production cross sections themselves are of limited phenomenological value, as the processes they are associated with lack an easily detectable signature, the cross sections for those processes that have signatures can be approximated as modifications to the basic production cross sections in many cases. This Section provides a detailed quantitative discussion of the production mechanisms of Higgs-portal scalars at the LHC.

Higgs production mechanisms

One advantage of Higgs-portal dark matter models over general hidden sector models, which is shared only by the now disfavoured Z-portal models, is a comparatively good understanding of the properties of the mediator particle. In particular, for collider searches, the parameter space is much reduced and the stringent bounds on mediator particles are not relevant. Additionally, if the production mechanisms of the mediator are well understood, the dark matter production mechanisms are also known. Processes for collider production of Higgs-portal dark matter are extensions of Higgs boson production mechanisms. To study the production of Higgs-portal scalars at colliders, we thus begin by reviewing Higgs boson production mechanisms.

This material has been known for some time; some of the original calculations are decades old. References are abundant. For a fairly complete reference, see reference [520], and for experimental results, see reference [421]. For a more pedagogical treatment, see either reference [423] or the final project of Part 3 of reference [3]. The are many other references in existence as well.

In contrast to an e^+e^- collider, Higgs production at a hadron collider is complicated by the effects of QCD. The SM Higgs boson interacts with fundamental SM fermions via a Yukawa coupling proportional to the mass of the fermion. In unitary gauge, this is for the physical Higgs h

$$\mathcal{L}_{Yuk} = \frac{m_f}{v_h} h \bar{\psi} \psi. \tag{5.51}$$

The Higgs vacuum expectation value is $v_h = 246$ GeV. Clearly, the larger the fermion mass, the stronger the interaction with the Higgs boson, which amounts to the top quark Yukawa coupling to the Higgs being the largest by a huge margin.

The Higgs also interacts at tree level with the massive weak gauge bosons. In the basis of physical states in unitary gauge, the interaction term is

$$\mathcal{L}_{hVV} = \frac{h}{v_h} \left(2 m_W^2 W_\mu^+ W^{-\mu} + m_Z^2 Z_\mu Z^\mu \right), \tag{5.52}$$

where the masses of the W and Z bosons are $m_W \simeq 80$ GeV and $m_Z \simeq 91$ GeV, respectively.

At the 1-loop level, the Higgs boson will interact with the photon and gluon fields, primarily through fermion loops, but also through a W boson loop in the case of the photon. The Feynman diagrams for these

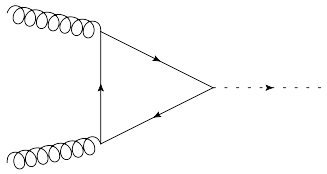

Figure 5.15: Feynman diagram for one contribution to the production of a Higgs boson through gluon fusion, the most common production mechanism at the LHC.

interactions are similar to those presented in Figure 5.15. It is common practice (though of dubious validity in many regimes) to integrate out the heavy loop particles and generate effective couplings between the Higgs and the massless gauge bosons of the form

$$\mathcal{L}_{hgg} = \frac{\alpha_s}{3\pi v_h} h G^{a\mu\nu} G^a_{\mu\nu}, \tag{5.53}$$

and

$$\mathcal{L}_{h\gamma\gamma} = g_{h\gamma\gamma} h F^{\mu\nu} F_{\mu\nu}, \tag{5.54}$$

where the strong coupling is as usual α_s, the Higgs field vacuum expectation value is v_h, and the coupling $g_{h\gamma\gamma}$ will be discussed below. These effective Lagrangians are valid in regions where the masses of the loop particles (the top quark and the W boson) can be taken to be infinite.

The expression for $g_{h\gamma\gamma}$ is more complicated than for the gluon coupling [521]. We present numerical values from a Madgraph [522] package (details here). The form of the coupling parameter is

$$g_{h\gamma\gamma} = -\frac{\alpha_{em}}{\pi v_h}\frac{47}{18}$$

$$\times \left(1 + \frac{66}{235}\tau_W + \frac{228}{1645}\tau_W^2 + \frac{696}{8225}\tau_W^3 + \frac{5248}{90475}\tau_W^4 + \frac{1280}{29939}\tau_W^5 + \frac{54528}{1646645}\tau_W^6 - \frac{56}{705}\tau_t - \frac{32}{987}\tau_t^2\right)$$

where $\tau_W = m_h^2/(4m_W^2)$ and $\tau_t = m_h/(4m_t^2)$.

It is clear from the mass scales involved that the top quark Yukawa coupling dominates, followed by the bottom quark and down the mass scale of fermions. For most purposes, anything below the bottom quark can be neglected. It would seem that the top and weak gauge bosons are the particles to consider when looking at how to produce a Higgs boson. However, one then needs to consider how these particles will appear in a proton-proton collision.

Light quarks and gluons are the most frequently encountered partons in the proton, with very heavy particles like the electroweak gauge bosons appearing far more rarely. Light quarks have a negligible Yukawa coupling to the Higgs, and gluons only couple to the Higgs at the 1-loop level, but the coupling is mediated by heavy quark loops. The weak vector boson coupling to the Higgs is strong, but the weak vector boson distributions in the proton are vanishingly small. All these factors become explicit when the cross sections are computed, and it turns out that the large top Yukawa coupling is enough to overcome the loop level suppression in the calculation.

For the SM Higgs, the dominant production mechanism at the LHC is gluon fusion. The Feynman diagram for this process is the one in Figure 5.15 at the parton level, taking the initial state gluons as partons of the colliding protons. In the way discussed earlier in this Chapter, one computes the cross section for the parton level process and then convolves with the gluon distribution functions to obtain the hadron level cross section. Numerical values for this cross section are found in reference [523], and the theoretical calculation itself can be found in the literature [524, 416]. The calculation is straightforward but long, refreshingly completely finite, with the result:

$$\sigma_{gg\to h} = \frac{m_h^2 G_F \alpha_s^2}{288\sqrt{2}\pi} \left| \frac{3}{2}\tau \left(1 + (1-\tau) f(\tau)\right) \right|^2 \tag{5.55}$$

where

$$f(\tau) = \begin{cases} \arcsin^2\left(\frac{1}{\sqrt{\tau}}\right) & \tau \geq 1 \\ \frac{1}{2}\left[\ln\left(\frac{1+\sqrt{1-\tau}}{1-\sqrt{1-\tau}}\right) - i\pi\right]^2 & \tau < 1 \end{cases} \tag{5.56}$$

and the variable τ is defined to be

$$\tau = \frac{4m_t^2}{m_h^2}. \tag{5.57}$$

Gluon fusion accounts for over 80% of Higgs production at the LHC.

The next dominant production mechanism is vector boson fusion (VBF), in which two W or Z bosons annihilate to a Higgs boson. VBF accounts for about 10% of Higgs production at the LHC. Much of the technical detail behind this production mechanism was discussed in Section 5.1.2, and will not be repeated here.

While a more complete treatment of the process of VBF requires evaluation of the five-point diagram illustrated in Figure 5.16, where the initial state quarks are partonic and the final state quarks fragment into jets, the effective vector boson approximation as discussed in Section 5.1.2 is frequently used. Explicit calculations have demonstrated that the approximation is accurate [525]. Given the inherit uncertainties in the parton model, this is usually accurate enough, though now that precision studies of the Higgs electroweak coupling are underway [526], more accuracy may be required.

The calculation of the cross section for VBF in the effective vector boson approximation is simple enough, being a tree level process. The vector boson distribution functions complicate things, but in a well behaved manner. The VBF cross section for Higgs production is about two orders of magnitude smaller than the GF cross section for Higgs production.

Aside from GF and VBF, there are several other subdominant Higgs production mechanisms that are considered at the LHC [421, 423], including, for example, heavy quark associated production, where the Higgs is produced along with a heavy quark. These production mechanisms are less important than even VBF, and so we do not consider their contributions to Higgs-portal scalar production. They are expected to contribute in roughly the same proportion as they do to SM Higgs production; that is, at the percent level [421].

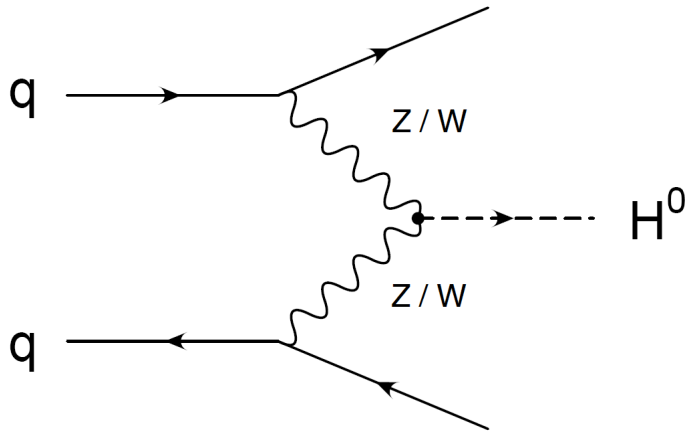

Figure 5.16: Feynman diagrams representing the production of the Higgs boson through the vector boson fusion mechanism in the partonic quark model. Diagram from reference [421].

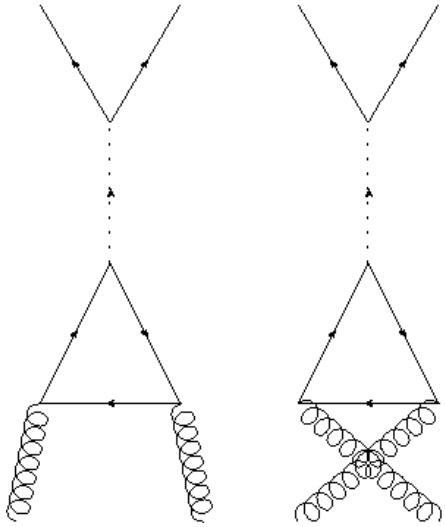

Figure 5.17: Feynman diagrams representing the production of Higgs-portal scalars through the gluon fusion mechanism. This process is an extension of the associated Higgs production mechanism.

Singlet production

As mentioned previously, the Higgs production cross mechanisms discussed in the last Section are also Higgs-portal scalar production mechanisms. In this Section, we present the full expressions for the production cross sections of Higgs-portal scalars at hadron colliders though the GF and VBF mechanisms.

One might be tempted to apply the narrow resonance approximation to calculate these cross sections, but as discussed in reference [527], the narrow resonance approximation is not always applicable to Higgs processes at LHC energy scales. This is due to off-shell electroweak vector boson interference effects in the region near the Higgs mass pole, and particularly affects the GF production mechanism. Because of these limitations, we avoid using the narrow resonance approximation.

Similarly, it is common in the literature to reduce the number of loops in collider physics process diagrams

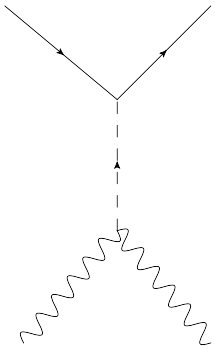

Figure 5.18: Feynman diagram representing the production of Higgs-portal scalars through the weak vector boson fusion mechanism. This diagram treats the weak bosons as partons in the proton, as discussed in Section 5.1.2.

by treating the top quark as infinitely heavy, and thus shrinking the effects of the top quark loop down to some static effective operator. The approach is tempting, as it allows higher order calculations to be done with much more ease. Unfortunately, for a scalar mediator with a mass of less than a TeV or so, this approximation is not valid for scalar mediated cross sections [472]. In fact, the loop effects become substantial for a scalar mass of ~ 100 GeV when the top quark mass is taken to be finite.

Much of the material in this Section was originally published by the author in reference [515]. Higgs-portal scalars at colliders, and at the LHC in particular, are also treated in references [516, 517, 528, 529, 530, 531, 532, 533, 525].

We proceed by discussing the two cross sections in parallel, as there is overlap between the two calculations. The primary variables that both results are presented in terms of are: x_1 and x_2, the parton momentum fractions for the gluons or weak gauge bosons, k_p, the initial proton energy, m_S, the mass of the Higgs-portal scalar, and $p_{S\parallel}$, the transverse momentum component of the final state scalar in the center of mass frame of the proton collision.

These results were computed in the following polarization basis for massive vector bosons:

$$\epsilon_1(k) = \frac{1}{\sqrt{2}}(0,1,0,0)\,, \tag{5.58}$$

$$\epsilon_2(k) = \frac{1}{\sqrt{2}}(0,0,1,0)\,, \tag{5.59}$$

$$\epsilon_3(k) = \left(\frac{|\mathbf{k}|}{m_V}, 0, 0, \frac{\omega_k}{m_V}\right). \tag{5.60}$$

The cross sections contain a number of factors, including the wavefunction normalization factor and the phase space integral factor. These terms can be simplified using kinematic relations to obtain simpler versions in terms of the above variables. In particular, conservation of energy can be used to rewrite the wavefunction normalization and relative velocity factors. The final expression for these terms is, for gluon fusion:

$$\frac{K_N}{v_{rel}} = \frac{(x_1+x_2)^2}{2\left(2x_1x_2k_p + (x_1-x_2)\,p_{S\|}\right)\left|(x_1^2+x_2^2)\,k_p - (x_1-x_2)\,p_{S\|}\right|} \tag{5.61}$$

and

$$\frac{K_N}{v_{rel}} = \frac{(x_1+x_2)^2}{\left(2x_1x_2k_p + (x_1-x_2)\,p_{S\|}\right)\left|(x_1^2+x_2^2)\,k_p - (x_1-x_2)\,p_{S\|}\right|\sqrt{x_1^2x_2^2k_p^4 - m_V^4}} \tag{5.62}$$

for vector boson fusion. For gluon fusion $v_{rel} = 2$, and $v_{rel} = \sqrt{\left(k_1^\mu k_{2\mu}\right)^2 - m_V^4}/k_1^0k_2^0$ for massive vector bosons with 4-momentum k^μ. Symmetry factors differ for each of the three initial states (W, Z, g). Integration over the phase space results in a term that is identical for both processes:

$$K_{Ph} = \frac{2\pi}{k_p^2}\mathrm{Re}\sqrt{\frac{4x_1x_2\left(x_1k_p - p_{S\|}\right)\left(x_2k_p + p_{S\|}\right)}{(x_1+x_2)^2} - m_S^2}. \tag{5.63}$$

The real part has been taken to enforce kinematic constraints.

The matrix elements can be calculated using the usual techniques. More details on the calculation of the gluon fusion matrix element are found in reference [534].

The production cross sections for scalar Higgs-portal singlets are then

$$\sigma_{PP/VV\to SS} = \int_{2m_S/k_p}^1 dx_1 \int_{L(x_1)}^1 dx_2 \int_{\frac{x_1-x_2}{2}k_p - \frac{x_1+x_2}{2}\sqrt{k_p^2 - \frac{m_S^2}{x_1x_2}}}^{\frac{x_1-x_2}{2}k_p + \frac{x_1+x_2}{2}\sqrt{k_p^2 - \frac{m_S^2}{x_1x_2}}} dp_{S\|}$$

$$\times K_{Ph}\left\{\frac{K_{NW}}{v_{rel}}\left[f_{W_T/p}(x_1)\,f_{W_T/p}(x_2)\left|\mathcal{M}_{TW}\right|^2 + f_{W_L/p}(x_1)\,f_{W_L/p}(x_2)\left|\mathcal{M}_{LW}\right|^2\right]\right.$$

$$\left. + \frac{1}{2}\frac{K_{NZ}}{v_{rel}}\left[f_{Z_T/p}(x_1)\,f_{Z_T/p}(x_2)\left|\mathcal{M}_{TZ}\right|^2 + f_{Z_L/p}(x_1)\,f_{Z_L/p}(x_2)\left|\mathcal{M}_{LZ}\right|^2\right]\right\} \tag{5.64}$$

for vector boson fusion and

$$\sigma_{PP/gg\to SS} = \frac{\alpha_s^2\eta^2m_t^4}{3^2 2^7\pi^2k_p^2}\int_{m_S^2/k_p^2}^1 dx_1 \int_{m_S^2/x_1k_p^2}^1 dx_2 \int_{\frac{x_1-x_2}{2}k_p - \frac{x_1+x_2}{2}\sqrt{k_p^2 - \frac{m_S^2}{x_1x_2}}}^{\frac{x_1-x_2}{2}k_p + \frac{x_1+x_2}{2}\sqrt{k_p^2 - \frac{m_S^2}{x_1x_2}}} dp_{S\|}\,\frac{f_{g/p}(x_1)\,f_{g/p}(x_2)}{x_1x_2}$$

$$\times\frac{K_N}{v_{rel}}\frac{K_{Ph}}{\left(m_h^2 - 4x_1x_2k_p^2\right)^2 + m_h^2\Gamma_h^2}\left[\Theta\left(m_t^2 - x_1x_2k_p^2\right)\left(1 - 2\frac{m_t^2 - x_1x_2k_p^2}{x_1x_2k_p^2}\arcsin^2\left(\sqrt{x_1x_2}k_p/m_t\right)\right)^2\right.$$

$$\left. + \Theta\left(x_1x_2k_p^2 - m_t^2\right)\left\{\left(1 + \frac{m_t^2 - x_1x_2k_p^2}{2x_1x_2k_p^2}\left[\ln^2\left(\frac{\sqrt{x_1x_2}k_p + \sqrt{x_1x_2k_p^2 - m_t^2}}{\sqrt{x_1x_2}k_p - \sqrt{x_1x_2k_p^2 - m_t^2}}\right) - \pi^2\right]\right)^2\right.\right.$$

$$+\pi^2\left(\frac{m_t^2-x_1x_2k_p^2}{x_1x_2k_p^2}\right)^2\ln^2\left(\frac{\sqrt{x_1x_2}k_p+\sqrt{x_1x_2k_p^2-m_t^2}}{\sqrt{x_1x_2}k_p-\sqrt{x_1x_2k_p^2-m_t^2}}\right)\Bigg\}\Bigg] \tag{5.65}$$

for gluon fusion.

The squared matrix elements for the VBF process are

$$|\mathcal{M}_T|^2=\frac{g_V^2\eta^2v^2}{\left(16\pi^2\right)^2}\frac{m_V}{\left(4x_1x_2k_p^2-m_h^2\right)^2+m_h^2\Gamma_h^2}, \tag{5.66}$$

for the transversely polarized vector boson and

$$|\mathcal{M}_L|^2=\frac{g_V^2\eta^2v^2}{m_V\left(16\pi^2\right)^2}\frac{\left(\sqrt{k_p^4x_1x_2+k_p\left(x_1^2+x_2^2\right)m_V^2}+m_V^4\right)^2}{\left(4x_1x_2k_p^2-m_h^2\right)^2+m_h^2\Gamma_h^2} \tag{5.67}$$

for the longitudinally polarized vector boson. This separated computation is required because the vector boson distribution functions are reported in longitudinal and transverse parts. We note that the longitudinal component dominates the transverse component by up to three orders of magnitude, which is in agreement with similar calculations [525]. The lower bound of the VBF x_2 cross section is

$$L(x_1)=\begin{cases}\frac{2m_S}{k_p}-x_1 & \text{if } x_1\leq\frac{2m_S}{k_p}\\ 0 & \text{if } x_1>\frac{2m_S}{k_p}\end{cases} \tag{5.68}$$

and is discussed further slightly below.

Convolution with the parton distribution functions $f_{X/p}(x)$ over the scaling variables $x_{1,2}$ and integration over the transverse momentum component $p_{S\parallel}$ gives the total proton level cross sections above.

The partonic nature of the VBF cross section makes it somewhat unreliable. There is an ambiguous kinetic constraint that could be imposed, requiring that there be enough energy available to produce on-shell electroweak vector bosons, which can be written using conservation of energy $k_p(x_1+x_2)>2m_V$ (assuming $m_V\ll k_p$, which is addressed below). The validity of this constraint is debatable, since it is inserted by hand and does not arise from any explicit Dirac deltas. This is a consequence of the parton model with very heavy partons, when the initial states are not truly asymptotically free, but we treat them as though they were. Without this constraint, the result becomes complex, as kinematically disallowed contributions are included.

This constraint may be supplanted by the usually stronger and certainly more solid constraint that there be enough energy available to produce the Higgs-portal scalar on-shell final states. That is, we require $k_p(x_1+x_2)>2m_S$. For $m_S>m_V$, this constraint is stronger than the one above, and we have restricted ourselves to that region of the parameter space. This kinematic constraint is used to obtain the integration bounds in Equation (5.68). This is integration over a box in the x_1-x_2 plane with a triangle near 0 omitted. Our parameterization of the integration region is one of many, chosen for no particular reason.

Moreover, as discussed in Section 5.1.2, the effective distribution functions for the electroweak gauge bosons are not valid to arbitrarily small x. The parameterizations break down, leading to unpredictable

errors. To avoid this, we cut off our integrations at $x = 0.1$ at the lowest, and assume that our calculated cross sections are underestimating the true values. Since $0.1k_p > m_V$ for LHC energies, this also justifies our neglect of m_V in the use of the conservation of energy relation to derive the kinematic bounds above.

Evaluation of the above cross sections is a somewhat numerically intensive affair, simply due to the number of integrations that needs to be done to obtain the cross section at a single mass point. Due to the unpleasant form of the parton distribution functions and the bounds on the $p_{S\parallel}$ integral, we have chosen to do the integrals numerically, and since all domains of integration are finite and all integrands are more or less well behaved, we have further chosen to use Gauss-Legendre quadrature.

Gauss-Legendre quadrature approximates an integral as a weighted sum according to the expression

$$\int_a^b dx f(x) \approx \frac{b-a}{2} \sum_i w_i f\left(\frac{b-a}{2} x_i + \frac{a+b}{2}\right). \tag{5.69}$$

The w_i are the weights and the x_i are the abscissa of the region of integration. A change of variables can change the interval of integration. We use the grids of weights and abscissas provided in an open source library (http://www.holoborodko.com/pavel/numerical-methods/numerical-integration/). All of our quadratures are done using a 32-point grid.

Evaluation of the GF cross section requires quadrature over only three variables, and so is relatively straightforward on a modern computer, despite the more complicated integrand. Evaluation of the VBF cross section is more numerically expensive, as the effective vector boson distribution functions themselves each require the evaluation of an integral. This can increase the evaluation time significantly. However, the calculations still proceeded rapidly enough that little effort was put into optimization of the numerical methods. There are certainly improvements that could have been made.

These production cross sections are plotted as a function of Higgs-portal scalar mass in Figures Figures 5.19, 5.20 and 5.21. As a consistency check, we note that the VBF production cross section is several orders of magnitude less than the GF production cross section, which is the naive expectation from considering the associated Higgs production cross sections. We include cross sections for production at the LHC with 8 TeV and 13 TeV, as well as production at a hypothetical 100 TeV proton collider.

The cross sections in Figures 5.19, 5.20 and 5.21 do not present any surprising features. The cross sections become much smaller as the scalar mass m_S increases, as the kinematic limit for production at the given collider energy is approached. Practically, masses above $0.25k_p$ or so are undetectable, even for more visible signatures than pure missing energy. The luminosity at the LHC is simply too small, and hadronic physics is simply too messy. Of course, larger masses are in principle detectable at the 100 TeV collider.

The rising behaviour of the VBF cross section in the low mass region is due to the interplay between the kinematic lower bound of integration and the lower bounds of integration required by the region of validity of the distribution function parameterization (ie 0.1). The peak occurs at $\sim 0.1 \times \sqrt{2} \times k_p$, and the cross section is not to be trusted below that threshold.

Figure 5.19: The cross sections for the production of Higgs-portal scalar dark matter plotted against mass for the GF and VBF processes at a 8 TeV proton collider. Cross section is in units of GeV^{-2}.

Figure 5.20: The cross sections for the production of Higgs-portal scalar dark matter plotted against mass for the GF and VBF processes at a 13 TeV proton collider. Cross section is in units of GeV^{-2}.

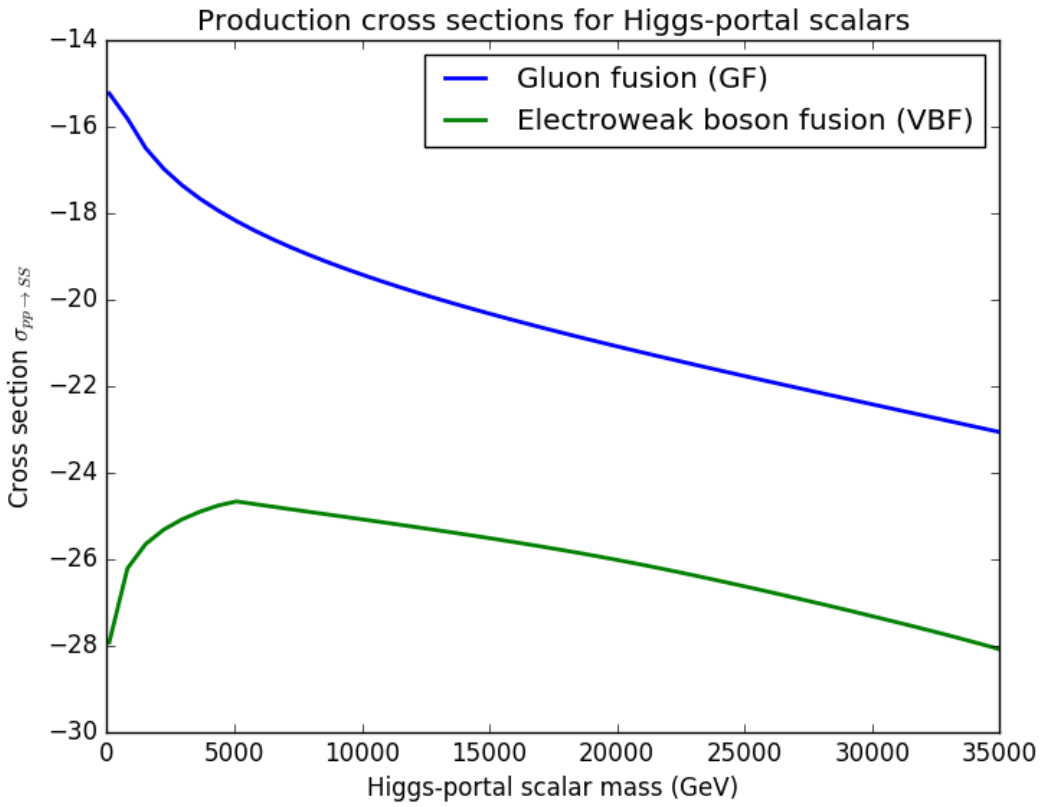

Figure 5.21: The cross sections for the production of Higgs-portal scalar dark matter plotted against mass for the GF and VBF processes at a 100 TeV proton collider. Cross section is in units of GeV^{-2}.

5.4.3 Mono-X searches

As was outlined in Section 5.3, pair production of particle dark matter with no associated large p_T SM matter makes a poor signature to seek. This statement holds in the case of Higgs-portal scalars, which means that the cross sections presented in the previous Section are of limited phenomenological value. Because of this, we consider in this Section mono-X signatures of Higgs-portal scalar dark matter at the LHC.

Rather, we consider monojet signatures of Higgs-portal scalar dark matter at the LHC. Of the possible mono-X signatures, we have chosen to work with only the monojet signature for a handful of reasons. First, for Higgs-portal scalars, the monojet signature is expected to be dominant [472]. It should be noted that associated top production is actually nearly as constraining as the monojet signatures [472]. We refrain from performing the analysis for the top signature because it is at best competitive with the monojet signature and it is reported [502] in a form unsuitable for comparison with the results we have, which is another point in favor of the monojet signature. The effective field theory results that are reported for the monojet signature [472] are easily transformed into something useful.

The Higgs-portal scalars are predominantly produced back-to-back (so there would be no observable missing energy in the pure production scenario), but monojets are possible from the radiation of gluons from the initial state (and the top quark loop).

Higgs-portal scalar mono-X signatures have occasionally been studied in the literature. There are only a handful of references due to the awkward timing of the experimental results. By the time mono-X studies had become more practical than speculative the parameter space of Higgs-portal scalars had already been severely restricted by direct detection experiments. Nonetheless, the fairly comprehensive reference [535] exists, as do some others [536, 537, 538, 492]. Reference [535] contains a detailed study of background processes to these mono-X signatures as well. For the monojet case, those primarily consist of $Z + j$ and $W + j$ events, where the weak gauge boson decays into neutrinos or miss-tagged leptons.

LHC monojet signature results are presented in terms of bounds on effective field theory scales Λ_*, as described in Section 5.3, for various effective field theory operators. To apply these results to our scalar Higgs-portal model requires a conversion of the bounds from an effective model to a complete model. The relevant effective operator is referred to as the R3 operator in reference [461], and describes gluon interactions with scalar dark matter, taking the form

$$\mathcal{O}_{R3} = \frac{\alpha_s}{8\Lambda_*^2}\chi^2 G^a_{\mu\nu}G^{\mu\nu a} \tag{5.70}$$

Bounds from monojet searches on the effective mass scale are presented in Figure 10f of reference [539]. These bounds are reported for the complex operator $\mathcal{O}_{C5}$, which is

$$\mathcal{O}_{C5} = \frac{\alpha_s}{4\Lambda_*^2}\chi^\dagger\chi G^a_{\mu\nu}G^{\mu\nu a} \tag{5.71}$$

The difference between these operators is a factor of two, and the reported bounds apply to both operators

up to this factor.

To translate these results, we would like an equivalent to the effective mass scale Λ_* for the Higgs-portal equivalent to the effective operator in Equation (5.70). Some analysis of equivalencies between effective field theories and simplified models is done in reference [468], and in the heavy mediator and heavy top mass limit, we find following their results, that the effective operator (5.70) can be written in terms of the parameters of the Higgs portal model as

$$\mathcal{O}_{EHP} = \frac{\eta_S}{m_h^2}\frac{\alpha_s}{4\pi}\chi^2 G^a_{\mu\nu}G^{\mu\nu a}. \tag{5.72}$$

This approximation is accurate to corrections of order $(1/m_h^4)$ and $(1/m_t^2)$, and of course corrections from QCD effects, which are likely much stronger. Note that though one might expect dependence on the top quark mass, this dependence cancels at leading order between the factor from the top propagator and the factor that appears in the Higgs-top Yukawa coupling. This equivalent mass scale in Equation (5.72) can be used to compare against the bounds reported in reference [539]. This is done in Figure 5.22. For an alternative analytic approximation to obtain the monojet cross section, see reference [535] (and also references [472] and [473]).

From Figure 5.22, it is clear that the Higgs-portal scalar model as implemented here is unconstrained by the 8 TeV LHC monojet bounds. This is not unexpected, as mono-X searches are typically not constraining for any but the most specialized models at this point. This very basic analysis has been included only as a demonstration. We note that the monojet bounds for the 13 TeV LHC have recently been reported [479] in terms of vector-portal simplified models, but the data itself has not yet been made public, and so we have not attempted to analyze it. Further monojet studies with the LHC should with more data reach the point of being able to constrain the Higgs-portal scalar model in this mass range, and higher energy colliders will be able to probe higher mass ranges.

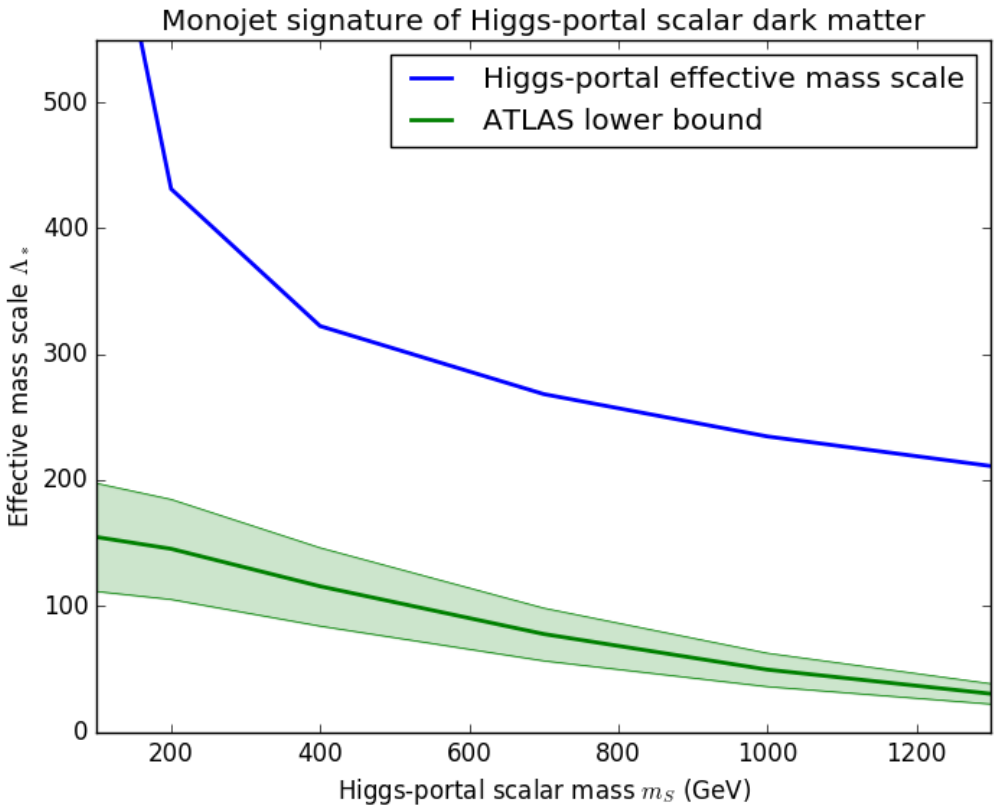

Figure 5.22: Lower bounds on the effective mass scale Λ_* with 95% confidence from the monojet signature extracted from 8 TeV ATLAS data, plotted alongside the effective Higgs-portal mass scale as described in the text. The Higgs-portal mass scale was computed using the thermal constraints on the Higgs-portal coupling that were discussed in Chapter 2. The shaded region is the 2σ error. Bounds reported in reference [539].

Chapter 6

Asymptotically safe vector-portal dark matter

This Chapter contains work from a project that applies the techniques of radiative symmetry breaking to a simple beyond SM theory. The key theoretical ideas behind this project involve exploration of a conformal symmetry that can act as a custodial symmetry of the SM, solving certain aspects of the hierarchy problem. If an extended SM is conformal at high energies, the parameters of that theory can be evolved down to phenomenological scales to provide predictions. This idea has been explored in the past [540, 541], but the technical details are difficult, which makes connections to reasonable phenomenology sensitive to theoretical inputs. This project, as detailed in this Chapter, is exploratory, with a preliminary model that lacks some theoretical rigor. The author's role in this project is primarily on the phenomenological side, and so the focus lies on that aspect. Further details of the technical theoretical parts of the project are outside of the expertise of the author, and the interested reader is referred to the literature [542, 543, 256, 544], though a brief overview is provided in Appendix C.

The model we work with in this Chapter is the SM extended by a complex scalar and a $U(1)'$ gauge symmetry, as well as a dark matter sector. The scalar is charged under the $U(1)'$ group, and by breaking the $U(1)'$ gauge symmetry radiatively, the scalar acquires a nonzero vacuum expectation value. If the scalar additionally couples to the SM Higgs field, this vacuum expectation value can cause electroweak symmetry breaking as well. Requiring the theory to be asymptotically safe generates UV boundary conditions that can be used as inputs to the renormalization group equations, which can in turn be used to connect the UV scales with the symmetry breaking scales. The UV boundary conditions can be translated into parameters at the electroweak scale that can be compared against experimental results, making the model highly predictive from purely theoretical principles. This model is an example of a complicated beyond SM theory that uses scalar field theory to address the fundamental scale problems with the SM as well as, with a slight extension, addressing the dark matter problem.

This Chapter consists of a discussion of the phenomenology of this model. First, the model is constructed in detail in Section 6.1, with an emphasis on observable results and constraints. Constraints from collider experiments are addressed in Section 6.2, and the detection prospects of the dark matter sector are discussed in Section 6.3. As the contributions of the author to this project were primarily on the phenomenological side, the theoretical construction is not emphasized, though it is probably the most compelling aspect of the model.

As mentioned previously, this model is a simple one constructed to demonstrate the validity and usefulness of this framework. In particular, these kinds of theoretical approaches are important in standard dark matter phenomenology, where additional constraints are very important. It is for this reason that the dark matter sector, which is not crucial to this model, is emphasized in this thesis. This project demonstrates that valid UV theoretical concerns can be used to obtain meaning ful phenomenological constraints. The usefulness of this approach is illustrated here with a simple model, but it can certainly be extended to more complicated models.

6.1 Model

6.1.1 Theoretical construction

The beyond SM parts of this model can be divided into two hidden sectors: the gauge-scalar sector consisting of a second scalar, the $U(1)'$ gauge boson and the additional fermions required for anomaly cancellation; and the dark matter sector, which includes the dark matter particle. We construct the model systematically, beginning from the inclusion of an additional $U(1)'$ gauge symmetry and a complex massless scalar field. The scalar will acquire a vacuum expectation value through quantum corrections and radiatively break the $U(1)'$ symmetry. This follows the standard Coleman-Weinberg mechanism [545] for radiative symmetry breaking in massless scalar QED. The Lagrangian of the beyond SM gauge-scalar sector, including interactions with the SM Higgs, is

$$\mathcal{L}_{BSM} \subset D_\mu H^\dagger D^\mu H + D_\mu S^\dagger D^\mu S - \lambda_2 |S|^2 H^\dagger H - \lambda_3 |S|^4 - \lambda_1 \left(H^\dagger H\right)^2 - \frac{1}{4} B'^{\mu\nu} B'_{\mu\nu} \tag{6.1}$$

The $U(1)'$ extended gauge covariant derivative is

$$D'_\mu = \partial_\mu - i g_3 \frac{\lambda_a}{2} G^a_\mu - i g_2 \frac{\tau_i}{2} W^i_\mu - iY \left(g_Y B_\mu + g_m B'_\mu\right) - i g' Q'_B B'_\mu. \tag{6.2}$$

The field strength tensor of the B' gauge field is as usual $B'_{\mu\nu} = \partial_\mu B'_\nu - \partial_\nu B'_\mu$.

It is well known that the Coleman-Weinberg mechanism cannot be used to generate electroweak symmetry breaking [545], because of the large top quark Yukawa coupling which spoils the stability of the Higgs potential. However, by introducing an interaction between the new scalar and the SM Higgs field, referred to as a 'Higgs-portal' interaction, the radiative symmetry breaking in the $U(1)'$ sector can be communicated to the Higgs sector of the SM and can trigger electroweak symmetry breaking. The reasoning is that an interaction of the form $\lambda_2 |S|^2 H^\dagger H$ becomes after radiative symmetry breaking of $U(1)'$ something containing a term $\sim v_s \lambda_2 H^\dagger H$, where v_s is the vacuum expectation value of the singlet field. This is the equivalent of the negative mass term that needs to be inserted by hand into the SM description of spontaneous electroweak symmetry breaking (see Chapter 1). Thus radiative symmetry breaking leads to electroweak symmetry

Table 6.1: Scalar charge assignments

Gauge group	S	H
$SU(3)_c$	1	1
$SU(2)_L$	1	2
$U(1)_Y$	0	1/2
$U(1)'$	2	0

breaking, which follows in the usual fashion. The charges of the scalars in the theory under all gauge groups are included in Table 6.1.

We now consider the requirements of the gauge sector. The $U(1)'$ gauge field will in general mix with the SM $U(1)^Y$ hypercharge gauge field [448, 546]. Terms of the form

$$\mathcal{L}_{mix} = \frac{\epsilon_{mix}}{2} B^{\mu\nu} B'_{\mu\nu} \tag{6.3}$$

can be included in the Lagrangian at tree level, and even if tree level terms are neglected, loop order effects induce similar effective couplings without careful fine-tuning [547]. Justification needs to be provided for ignoring mixing effects in the phenomenology. To avoid complications later on, we explicitly include a tree level mixing term whose effects are taken into account in the covariant derivative (6.2), in the factor g_{mix}. We note that transforming the mixing terms into something that is phenomenologically useful is somewhat delicate. Discussion of the required transformations is deferred to Appendix E. As is discussed there, one can perform transformations into a basis of eigenstates that includes the usual electroweak gauge bosons of the SM and an additional Z' boson that acts as the mediator of the $U(1)'$ gauge force. The Z' will be the focus of much of our phenomenological effort.

6.1.2 Fermion fields

Interactions with fermion fields are very important, as they are essentially the phenomenological interactions of the model.

Constraints on new neutral resonances that couple to the first two generations of charged leptons are very strong [548, 448], and models with couplings near the electroweak scale are ruled out for Z' masses up to ~ 3.5 TeV. To avoid these stringent constraints, we make our model leptophobic; that is, we set the $U(1)'$ charges of all charged leptons to zero. The only SM fermions charged under $U(1)'$ will be quarks. We note that setting lepton charges to zero only removes direct tree level interactions with leptons. There will still be interactions induced by the gauge boson mixing discussed above and by radiative corrections as can be seen in the covariant derivative (6.2), though they will be much suppressed in comparison to the case where the leptons have $U(1)'$ charge. Thus it is still necessary to check that the model is consistent with the LHC dilepton constraints, which is discussed in Section 6.2.1.

Table 6.2: Standard Model fermion charge assignments

Gauge group	$q_L^{u,d}$	u_R	d_R	$q_L^{c,s}$	c_R	s_R	$q_L^{t,b}$	t_R	b_R	l_L (all gens)	e_R (all gens)
$SU(3)_c$	3	3	3	3	3	3	3	3	3	1	1
$SU(2)_L$	2	1	1	2	1	1	2	1	1	2	1
$U(1)_Y$	1/3	4/3	-2/3	1/3	4/3	-2/3	1/3	4/3	-2/3	-1	-2
$U(1)'$	0	0	0	0	0	0	1/3	1/3	1/3	0	0

As written, the model is not consistent, because the introduction of a new gauge group generates new perturbative anomalies. These anomalies can be cancelled if the fermion charges under $U(1)'$ take on certain values. We refrain from a full discussion of the constraint equations that are used to generate anomaly-free charge assignments, instead referring the interested reader to the discussions in [548, 448, 446, 549]. The $U(1)_{B-L}$ model is a popular and well motivated anomaly-free theory, but we do not work with it here.

Leptophobic models have attractive phenomenological properties, as the lack of lepton $U(1)'$ charges greatly reduces the constraints from LEP data and electroweak precision experiments, not to mention the ever-strengthening LHC dilepton bounds on neutral resonances. Leptophobic $U(1)'$ models have been discussed frequently in the literature, as sectors of E_6 GUTs [550, 551, 552, 553, 554] and in their own right [555, 556]. Models in which only the third generation has $U(1)'$ charge are also theoretically well motivated [557, 558, 559], which will be important later.

These charge assignments require the introduction of additional fermions to satisfy the anomaly-free conditions. These 'spectator' fermions, which are denoted $\psi^d_{L,R}$, $\psi^l_{L,R}$ and $\psi^e_{L,R}$ in Table 6.3, are present solely to cancel anomalies, and (in our model) they have no effect on the phenomenology. The various ψ have SM charges equal to the SM fermion indicated in the superscript. They are vectorlike (ψ_L and ψ_R have the same charges) under the SM gauge group, so explicit mass terms do not violate $SU(2)_L$ gauge invariance and can be included to provide masses without appeal to any symmetry breaking mechanism. For brevity, we do not include the spectator fermions in any expressions of the Lagrangian of the theory from this point on.

Also required is a right handed neutrino charged under $U(1)'$. This neutrino couples to the singlet field through a term [548, 560, 561]

$$\mathcal{L}_M = -Y_M^{ij}\nu_{Ri}^{\bar{c}}\nu_{Rj}S + (\text{h.c.}) \tag{6.4}$$

where the i, j are flavor indices. One such neutrino is required for each generation of SM particle charged under the $U(1)'$. From the interaction with the singlet field, the neutrino will acquire a Majorana mass of $m_\nu = \sqrt{2}v_s Y_M$ after $U(1)'$ symmetry breaking, where as before v_s is the vacuum expectation value of the singlet field. Unlike the spectator fermions above, the fixed mass scale of the neutrinos mean that they may influence the phenomenology significantly.

Table 6.3: Exotic fermion charge assignments

Gauge group	ν_R	ψ^l_L	ψ^l_R	ψ^e_L	ψ^e_R
$SU(3)_c$	1	1	1	1	1
$SU(2)_L$	1	2	2	1	1
$U(1)_Y$	0	-1	-1	-2	-2
$U(1)'$	-1	-1	0	-1	0

The vector and axial charges of the fermions can be written in terms of the $U(1)'$ charges $Q'_{iL,R}$ of the left and right handed components and the $U(1)'$ gauge coupling g' (this holds for any Abelian $U(1)$ gauge group):

$$V_f = g\left(\frac{Q_{fL}+Q_{fR}}{2}\right),$$

$$A_f = -g\left(\frac{Q_{fL}-Q_{fR}}{2}\right). \tag{6.5}$$

These are the vector and axial charges in the case where mixing is neglected. The left and right handed projection operators are $P_L = (1/2)(1-\gamma^5)$ and $P_R = (1/2)(1+\gamma^5)$ as usual. Mixing is discussed in Appendix E.

Inclusion of the mixed currents in Equation (6.5) leads to

$$\begin{aligned} J^\mu_Z &= g_Y\left(Q^Y_L \bar{f}\gamma^\mu P_L f + Q^Y_R \bar{f}\gamma^\mu P_R f\right) \\ &= \bar{f}\gamma^\mu\left(V^Z_f + A^Z_f\gamma^5\right) f, \end{aligned} \tag{6.6}$$

$$\begin{aligned} J^\mu_{Z'} &= \left(g'Q'_L + g_{mix}Q^Y_L\right)\bar{f}\gamma^\mu P_L f + \left(g'Q'_R + g_{mix}Q^Y_R\right)\bar{f}\gamma^\mu P_R f \\ &= \bar{f}\gamma^\mu\left(V'_f + A'_f\gamma^5\right) f. \end{aligned} \tag{6.7}$$

In the second lines of Equations (E.12) and (E.13), we have introduced the mixed vector and axial generalized charges V'_f and A'_f, which are extended versions of 6.5 that include a term proportional to g_{mix}. These are the quantities that are most useful for phenomenological calculations, and we express our cross section results in terms of these charges. It should be emphasized that V_f and A_f are simply convenient notation. They are not formal renormalized couplings that run through the renormalization group nor conserved quantum numbers, though they contain both of those objects. The couplings g' and g_{mix} are governed by the behaviour of the renormalization group, however. Their running is outlined in Appendix C.

Finally, we must apply some phenomenological constraints that are discussed in subsequent Sections to make the model concrete. The solutions of the renormalization group equations presented in Appendix C constrain the number of generations of SM fermions that can be charged under $U(1)'$ to be no more than 2,

otherwise the potential becomes unstable. This constraint necessarily introduces non-universal couplings, and hence the possibility of flavor changing neutral currents (FCNCs) as detailed in Appendix F. Phenomenological constraints from the absence of any observed FCNCs involving the first two generations of SM fermions are very strong, requiring that only the third generation of SM fermions be charged under $U(1)'$. Thus the model as made concrete here is both leptophobic and tritophilic, with only the t and b quarks carrying fundamental charge under $U(1)'$. This introduces a number of interesting issues.

6.1.3 Hidden sector fields

This Section discusses the fields that are a part of this model not immediately accessible to the SM. This includes the right handed neutrino fields introduced for the purposes of anomaly cancellation, as well as additional dark matter candidates added as extensions to the basic model to address the dark matter problem.

As we have determined the model must be tritophilic, there need only be a single right handed neutrino to cancel the perturbative anomalies. The neutrino is sterile in the sense that it is charged only under $U(1)'$ and that it thus belongs to the hidden sector. Phenomenologically, it may contribute to the decay of the Z' boson, depending on the mass hierarchy.

A few remarks about interactions with the SM neutrino sector are in order. As the model is presented, with only a Majorana mass term for the right handed neutrino, it cannot generate light neutrino masses, as there is no mixing between the left (SM) and right handed neutrino sectors. However, by adding a Higgs-neutrino Yukawa term [560, 561]

$$\mathcal{L}_D = -Y_D^{ij} \bar{\nu}_{Ri} H^\dagger l_{Lj} S + (\text{h.c.}) \tag{6.8}$$

a Dirac neutrino mass term can be generated. In combination with the heavy Majorana mass term above, the seesaw mechanism [448] can be enabled, explaining the light neutrino mass hierarchy. We do not explicitly include a Dirac term here, which would need to be included in the renormalization group equations, and would affect their solutions. Such an extension is perhaps a natural next step in this work. The origin of these Dirac mass terms is left unstated, though in our model it would be through the process of radiative symmetry breaking. The mass terms also need not all be nonzero, but some must be, as a nonzero neutrino mass has been experimentally confirmed.

It is also possible to include additional particles charged under $U(1)'$ that could act as hidden sector dark matter, with the dominant channel being the vector portal, as realized by Z' mediation. Such particles are given mass through a mechanism deliberately left ambiguous, usually taken to be some relic of higher order physics that will only softly break any required symmetries.

The relevant part of the Lagrangian for Dirac fermionic dark matter χ takes the form

$$\mathcal{L}_\chi = \bar{\chi} \left(i \not{D}'_\mu - m_\chi \right) \chi \tag{6.9}$$

where D'_μ is the $U(1)'$ covariant derivative introduced earlier. As noted above, the mass m_χ is inserted by hand and is for now a free parameter of the theory. This sector of the theory is essentially QED with a massive mediator, and is decoupled from the rest of the model aside from the vector portal opened by the Z' boson. As the fermion χ couples only to the Z', there are no constraints on the charge, and so we arbitrarily take said charge to be unity. This leads to a generalized vector charge of $V'_\chi = g'$ and a generalized axial charge of $A'_\chi = 0$. We consider the restriction to vector-charged dark matter to be an appropriate choice for these exploratory studies. Axial dark matter differs slightly, and these differences have been explored in the literature [562, 446].

6.1.4 UV concerns

The model described above is, before radiative symmetry breaking, invariant under scaling transformations $x^\mu \to x^{\mu\prime} = \lambda x^\mu$ up to the explicit fermion mass terms for χ and ψ, which we will discuss shortly. A Poincaré invariant theory with scaling symmetry in four dimensions is usually taken to have full conformal symmetry, so we will use the term 'conformal' from now on.

Earlier, we suggested that the conformal symmetry be used as a custodial symmetry to guard the Higgs mass terms against quadratic divergences. We elaborate slightly on that point. The quadratic divergences are not explicitly cancelled as in supersymmetry, but instead one argues that they vanish because the theory runs to a fixed point. Once the theory has reached a UV fixed point, there must necessarily be no quadratic divergences. In this way the Higgs mass is protected.

While the explicit fermion mass terms for the χ and the ψ particles do violate the scaling invariance of theory, they only do so 'softly.' That is, these terms do not destroy the ability of the scaling symmetry to protect the Higgs mass. In Appendix C, we will provide some details of the renormalization group analysis and the symmetry breaking pattern. The fermion mass terms break the custodial conformal symmetry only softly, similar to gaugino mass terms in supersymmetric theories. Of course, higher order contributions can still affect the UV fixed points. For the χ, the mass scale is assumed to be small enough that these contributions are negligible. For the ψ, which has been given a high mass to decouple it from the phenomenology, there would be problems if not for the fact that the ψ couples to the scalar sector only at two loops, which sufficiently suppresses its contributions.

The χ and ψ mass terms then are necessarily effective terms generated by some UV scale process. This argument makes an appeal to physics in the UV which is decoupled from the phenomenological scale, and so prevents the theory from being UV complete as presented.

In theories that introduce new massive vector bosons, care must be taken to ensure that longitudinal degrees of freedom do not cause violations of the unitarity of the S matrix [563]. Unitarity violations manifest themselves as cross sections for processes involving the vector boson growing without bound as the center of mass energy $\sqrt{s} \to \infty$. Unitarity violations are usually taken to be a sign of an incomplete theory. We will briefly discuss potential unitarity violating effects in our models. There is a detailed discussion of

unitarity bounds in simplified vector-portal models in [477].

For self-scattering processes of fermions axially charged under $U(1)'$ to preserve unitarity, the fermion mass is bounded from above by [477]

$$m_f \lesssim \sqrt{\frac{\pi}{2}} \frac{m_{Z'}}{A'_f}. \tag{6.10}$$

For $m_{Z'} > 1$ TeV and $g' \sim 0.1$ as is the case in this model, this bound is satisfied for all SM fermions. It will be seen in Section 6.3.4 that the dark matter candidate χ satisfies this bound when constrained by thermal abundances as well. This bound can be used to provide an upper bound of $\sim \mathcal{O}(100\,\text{TeV})$ on the masses of the spectator fermions ψ. Spectator fermions carrying SM charge (even color) near this bound are beyond the reach of any current experiment, including the LHC, and so are not subject to any constraint.

Processes involving external Z' bosons also lead to unitarity violations when there are nonzero axial fermion couplings [564, 565, 566]. These violations occur at a scale

$$\sqrt{s} \sim \frac{\pi m_{Z'}^2}{A_f'^2 m_f} \tag{6.11}$$

where f is any fermion charged under $U(1)'$. For SM fermions and the dark matter candidate χ, this scale is near or above the UV scales that form the boundary conditions of the model. In the case of the spectator fermions unitarity is violated at a scale $\sqrt{s} \sim m_\psi$, when the process $\psi\bar{\psi} \to Z'Z'$ becomes kinematically available, which is high enough that the phenomenology is unaffected. These unitarity violations are a further indication that our theory as presented is not UV complete, and are an unfortunate consequence of our inclusion of explicit mass fermion mass terms. These issues could be rectified with a more comprehensive analysis of mass generation mechanisms for the χ and ψ fermions in the UV. We refrain from doing so here, leaving such extensions to a future work.

6.1.5 Model parameters

The renormalization group equations for the model as discussed in Appendix C can be solved with the boundary conditions that generate an asymptotically safe scenario as well as some additional constraints on the system detailed in the Appendix, leading to constraints on the parameters of the theory [544]. The renormalization group equations have been solved for three different values of the Z' mass, listed in Table 6.4, and the other phenomenological parameters of the theory that can be extracted from the solutions to the renormalization group equations are presented as well.

The λ_2 and λ_3 couplings are very small in all three scenarios. The $U(1)'$ gauge coupling parameter g' and the gauge mixing parameter, which characterizes the kinetic mixing angle between the two $U(1)$ gauge groups, decrease as $m_{Z'}$ increases. The Yukawa couplings of the top quark t to the SM Higgs field and the right handed neutrino ν_R to the scalar singlet are, respectively, Y_t and Y_ν. The vacuum expectation value of

Table 6.4: Model parameters

$M_{Z'}$ (TeV)	$10^6\lambda_2$	$10^6\lambda_3$	g'	g_m	Y_ν	Y_t	m_{ν_R} (TeV)	v_s (TeV)	m_S (GeV)
1.9	-6	-4.05	0.18	0.042	0.28	0.77	2.02	5.1	20
3.4	-0.59	-0.13	0.1	0.023	0.16	0.74	3.72	16.9	11.5
6.8	-0.036	-0.002	0.05	0.011	0.08	0.70	7.59	68.8	6

the singlet field is v_s and can be combined with the neutrino Yukawa coupling to give a mass for the right handed neutrino m_{ν_R}. Finally, the singlet itself has a mass of m_S.

6.2 Collider phenomenology and constraints

There are several constraints that can be applied to the gauge sector of the model, before even considering the dark matter extension. In fact, searches for mediators are generally much more constraining than searches for dark matter such a monojet searches [567]. With this in mind, we forgo the latter and concentrate on the former in this Chapter.

Extensions of the SM by heavy neutral gauge bosons have existed in the literature for decades, and have been the subject of experimental searches for nearly as long. None of these searches has detected the presence of such a boson, so results are reported in the form of constraints on the properties of hypothetical new gauge bosons. A variety of constraints apply, depending on the SM fermionic charge assignments and the mass scale of the new boson. Both kinetic and mass mixing angles are also constrained, though kinetic mixing angles less so.

A quantity required for most collider analysis of the Z' is its decay width. The total decay width of the Z' to Dirac fermions (SM or otherwise) is

$$\Gamma_{Z'\to\bar{f}f} = \sum_f \Theta\left(m_{Z'} - 2m_f\right) \frac{N_c m_{Z'}}{12\pi} \sqrt{1 - \frac{4m_f^2}{m_{Z'}^2}} \left[V_f'^2 \left(1 + \frac{2m_f^2}{m_{Z'}^2}\right) + A_f'^2 \left(1 - \frac{4m_f^2}{m_{Z'}^2}\right)\right] \tag{6.12}$$

where N_c is the number of colors of fermion f, and V_f' and A_f' are the generalized vector and axial charges of the fermion as defined in Equation (E.13). Note that even those SM fermions that do not couple directly to the $U(1)'$ gauge field (the first two generations of quarks and the charged leptons) contribute to the decay width at tree level due to the mixing induced coupling. The Heaviside step function $\Theta(x-a)$ is taken to enforce kinematic constraints.

The decay width to right handed Majorana neutrinos is

$$\Gamma_{Z'\to\nu_R\nu_R} = \sum_{generations} \Theta\left(m_{Z'} - 2m_{\nu_R}\right) \frac{g'^2 m_{Z'}}{24\pi} \sqrt{1 - \frac{4m_{\nu_R}^2}{m_{Z'}^2}} \left(1 - \frac{m_{\nu_R}^2}{m_{Z'}^2}\right) \tag{6.13}$$

In the tritophilic model under consideration, the number of generations is one.

Table 6.5: Total Z' SM decay widths

$M_{Z'}(TeV)$	1.9	3.4	6.8
$\Gamma_{Z'}(GeV)$	3.24	1.76	0.84

There are other subdominant contributions to the Z' decay width (the diboson contribution in particular will be discussed in Section 6.2.6), but the above expressions include the dominant components. Others will be neglected. We include for reference in Table 6.5 numerical values for the total Z' decay width for the scenarios discussed in Section 6.1.5.

Any discussion of Z' physics will typically consider bounds on the properties of the Z' boson obtained from electroweak precision experiments [568, 448]. However, in our model, these bound provide little value. The constraints on new neutral spin-1 bosons come from precision studies of electroweak processes and are typically capable of constraining a Z' boson with a mass of up to a few hundred GeV. This is simply because of the energy scales at which these experiments can be performed. Unfortunately, these bounds do not apply for a Z' of several TeV, such as appears in the scenarios of the model under discussion here.

As a quick example, take the Z' contribution to the muon $g-2$ (the anomalous magnetic moment), which decreases with increasing $m_{Z'}$ like $\sim 1/m_{Z'}^2$ [569], with current bounds restricting masses of $\mathcal{O}(100\text{ GeV})$. This is even before recalling that our model is tritophilic and leptophobic, and so has highly suppressed couplings to the second generation of SM leptons. Clearly, this bound does not extend high enough in the mass parameter space to constrain the model.

There are actually very few articles discussing experimental constraints on model independent kinetic mixing. The only one that is relevant is reference [570], which uses electroweak precision data, and only provides constraints for an Z' mass of up to 1 TeV. Anything higher is essentially unconstrained. The relevant figure illustrating this is in the reference.

The standard technique to obtain estimates for the production and decay of a Z' boson in a hadron collider is the narrow resonance approximation [7]. Given that a ratio Γ/m of 0.05 is usually accepted as a narrow enough width for the narrow resonance approximation to apply, the SM contributions to the Z' decay width in Table 6.5 clearly present no issues. Hidden sector contributions need to be considered, however. They will be discussed further in Section 6.3, and we will simply assume for now that they will not when included spoil the narrow width approximation (it will be seen that they do not).

The differential cross section for the production of a Z' boson of rapidity y from the collision of two protons is [448, 571, 572]

$$\frac{d}{dy}\sigma_{pp\to Z'} = \frac{4\pi^2 x_1 x_2}{3m_{Z'}^3}\sum_i \left[f_{q_i}^A(x_1)f_{\bar{q}_i}^B(x_2) + f_{\bar{q}_i}^A(x_1)f_{q_i}^B(x_2)\right] \times \Gamma_{Z'\to\bar{q}_i q_i}. \tag{6.14}$$

The Bjorken scaling variables x_1 and x_2 are related to the rapidity through

Table 6.6: Z' production cross section numerical coefficients C_s (units of $1/\text{GeV}^3$)

$M_{Z'}$	$\sqrt{s} = 8$ TeV	$\sqrt{s} = 13$ TeV	$\sqrt{s} = 14$ TeV
1.9 TeV	2.14×10^{-10}	9.32×10^{-10}	1.11×10^{-9}
3.4 TeV	1.52×10^{-12}	2.69×10^{-11}	3.64×10^{-11}
6.8 TeV	2.80×10^{-20}	1.83×10^{-14}	4.55×10^{-14}

$$x_{1,2} = \frac{m'_Z}{\sqrt{s}} e^{\pm y} \tag{6.15}$$

where the center of mass energy of the proton collision is $2E = \sqrt{s}$. The functions $f(x)$ are the proton parton distribution functions, as discussed in Chapter 5. In our calculations we have used the NLO MSTW grids [418], which have a convenient Mathematica implementation. The cross section is obtained after integration with respect to rapidity over the region $-\ln(\sqrt{s}/m_{Z'}) \leq y \leq \ln(\sqrt{s}/m_{Z'})$. Our results are presented with a QCD K factor of 1, but even with a conservative K factor of 1.5, our conclusions do not change.

The cross section for production of a Z' in proton-proton collisions can then be written

$$\sigma_{pp\to Z'} \simeq C_s \left(\frac{2\Gamma\left(Z' \to u\bar{u}\right) + \Gamma\left(Z' \to d\bar{d}\right)}{\text{GeV}} \right) \tag{6.16}$$

The computed values for C_s at the LHC energies and Z' mass values of interest are presented in Table 6.6.

6.2.1 Dilepton constraints

The dilepton bound provides the most stringent signal on the parameters of a new Z' for most $U(1)'$ extensions of the SM. The dilepton bounds are stronger than the dijet bounds because lepton signals are relatively clean, even at the LHC. It is to avoid these bounds that leptophobic variants of $U(1)'$ have gained popularity in the past few years.

Our model is leptophobic, but the Z' nonetheless interacts with leptons through the mixing parameter g_{mix}. While the interaction is highly suppressed, it is still important to check if the bounds are satisfied. It is only meaningful to compare the 8 TeV results against the bounds reported in [573], as that is the energy the bounds apply to. The 6.8 TeV Z' is beyond the reach of the 8 TeV LHC, and so is unconstrained, and the 3.4 TeV Z' is below the bounds and so likewise unconstrained. However, the 1.9 TeV Z' is ruled out by the dilepton constraints.

6.2.2 Dijet constraints

Generally, the dijet signature is, after the dilepton, the next most important for a Z' produced at a hadron collider. As mentioned above, this is because the dijet channel is very messy compared to the dilepton channel. For a standard leptophobic model, the dijet constraints would be the strongest, but for our model, the Z' couplings to the light quarks and leptons are the same, mediated by the mixing with SM hypercharge.

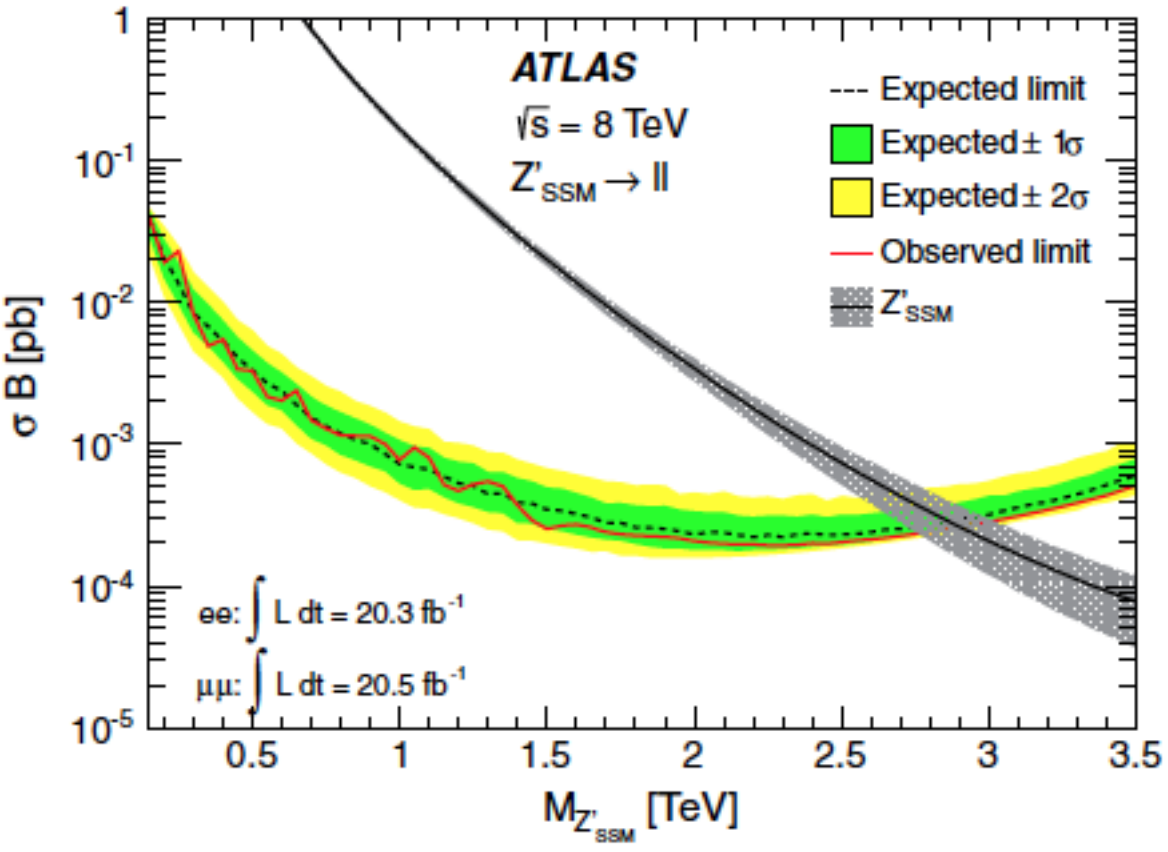

Figure 6.1: Bounds on vector resonances from cross section × branching ratio to the dilepton (dielectron and dimuon) channels. Values above the line are excluded with 95% confidence. Figure originally published in reference [573].

Table 6.7: Dilepton decay widths and cross sections (units of fb)

$M_{Z'}$	$\Gamma_{Z'\to\bar{l}l}$	$\sigma_{pp\to Z'\to\bar{l}l}$ $\sqrt{s}=8$ TeV	$\sqrt{s}=13$ TeV	$\sqrt{s}=14$ TeV
1.9 TeV	0.67 GeV	4.27	18.59	22.14
3.4 TeV	0.36 GeV	0.029	0.518	0.701
6.8 TeV	0.16 GeV	2.40×10^{-10}	1.57×10^{-4}	3.90×10^{-4}

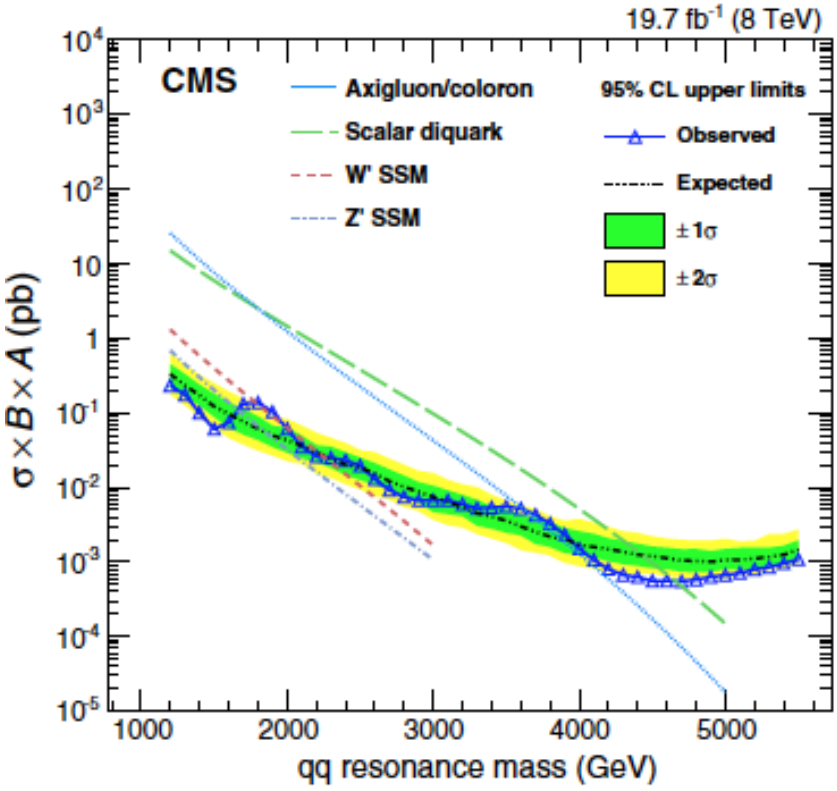

Figure 6.2: Bounds on vector resonances from cross section × branching ratio to the dijet channels for a variety of models. Values above the line are excluded with 95% confidence. Figure originally published in reference [574].

Because of this, the dilepton constraints are actually stronger than the dijet constraints, despite the model being leptophobic.

We check if our model satisfies the dijet bounds for each of the scenarios discussed in Section 6.1.5. The bounds used are those published in reference [574]. The dijet signature is in general much larger than the dilepton signature (by a factor of 4 or 5, depending on the center of mass energy), which is due to the contribution of the bottom quark, which has fundamental $U(1)'$ charge. However, due to the cleanliness of the dilepton signal, the bounds end up being about an order of magnitude stronger. The dijet bounds do not end up constraining the model at all.

Table 6.8: Dijet decay widths and cross sections (units of fb)

$M_{Z'}$	$\Gamma_{Z'\to\bar{q}q}$	$\sigma_{pp\to Z'\to\bar{q}q}$ $\sqrt{s}=8$ TeV	$\sqrt{s}=13$ TeV	$\sqrt{s}=14$ TeV
1.9 TeV	1.14 GeV	19.47	85.79	100.98
3.4 TeV	0.62 GeV	0.11	1.95	2.64
6.8 TeV	0.30 GeV	9.41×10^{-10}	6.14×10^{-4}	1.53×10^{-3}

Table 6.9: Ditop decay widths and cross sections (units of fb)

$M_{Z'}$	$\Gamma_{Z'\to\bar{t}t}$	$\sigma_{pp\to Z'\to\bar{t}t}$ $\sqrt{s}=8$ TeV	$\sqrt{s}=13$ TeV	$\sqrt{s}=14$ TeV
1.9 TeV	1.43 GeV	5.67	24.71	29.42
3.4 TeV	0.78 GeV	0.028	0.491	0.665
6.8 TeV	0.38 GeV	2.48×10^{-10}	1.62×10^{-4}	4.03×10^{-4}

6.2.3 Ditop constraints

Another potential channel by which the Z' may make itself known is the ditop channel, consisting of a pair of top quarks. As the top quark is much heavier than other potential final state particles, the ditop channel has less data available, and due to the extra complication introduced by the electroweak decay of the top quark before hadronization, the final channels are complicated. Nonetheless, analysis on this channel has been done [575].

In beyond SM searches, the ditop channel is usually not very important. However, in the model being considered in this Chapter, the top couples preferentially to the Z' boson, meaning it becomes important to consider the ditop bounds and compare them against the theory. Ditop production rates for our leptophobic tritophilic $U(1)'$ model in the standard approximation are presented in Table 6.9, for the usual range of 8 TeV, 13 TeV and 14 TeV.

The bounds reported in reference [575] are reproduced in Figure 6.3. From examining the data, it is clear that the ditop bounds do not constrain the model. In fact, the ditop constraints remain less constraining than the dijet constraints, not only due to the contribution of the unsuppressed bottom quark to the dijet channel, but also because of the mixing induced coupling to SM hyperchanrge. The mixing induced couplings are strong enough that when combined with the strong bounds reported in the dijet channel, the model can be constrained much more than is currently possible for the ditop channel.

6.2.4 Invisible Higgs decay width constraints

The radiative symmetry breaking scenario was enabled by the introduction of a scalar electroweak singlet, which broke the $U(1)'$ symmetry upon obtaining a vacuum expectation value. The singlet remains in the model as a light scalar, with mass values as listed in Table 6.4 for the various scenarios. The singlet has some phenomenological relevance, in that it opens a new potential decay channel for the SM Higgs boson. The singlet is invisible, so this decay channel must be compared against the bounds on the invisible Higgs decay width.

The decay proceeds through the three-point term in the scalar sector, which is made explicit in unitary gauge

$$\mathcal{L}_{hss} = \frac{\lambda_2 v_h}{2} S^2 h. \tag{6.17}$$

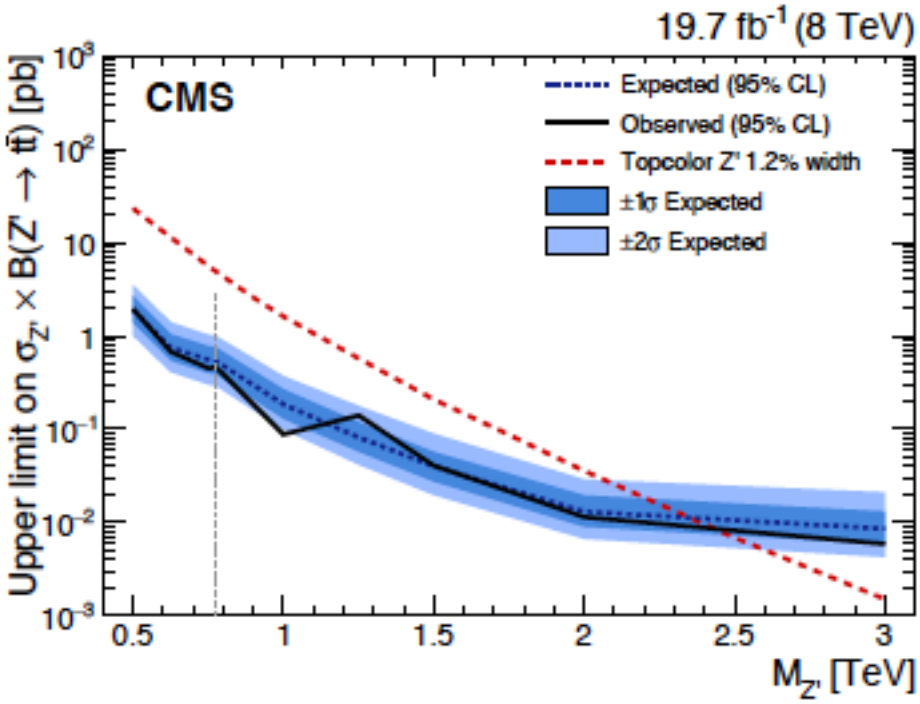

Figure 6.3: Bounds on vector resonances from cross section × branching ratio to the ditop channels. Values above the line are excluded with 95% confidence. Figure originally published in reference [575].

A simple calculation using this interaction yields the singlet contribution to the Higgs decay width

$$\Gamma_{h\to ss} = \frac{\lambda_2^2 v_h^2}{32\pi m_h^2}\sqrt{m_h^2 - 4m_s^2}. \tag{6.18}$$

Comparing with the bounds plotted in Figures 13 and 14 of Chapter 5, it can be seen that the highly suppressed interaction is orders of magnitude smaller than that required by the bounds near the singlet mass determined by the model. We can conclude that the measured invisible Higgs decay width does not constrain the singlet sector of the model in the slightest.

6.2.5 FCNC constraints

While meson mixing experiments have placed strong constraints [576, 577, 578, 579] on FCNCs that act between the first two generations, the mass scale of the top has so far prevented even the LHC from placing any bounds on the third generation [580, 581]. In our models, this is exacerbated by the high mass of the Z' and the small kinetic mixing angle. Bounds will likely be placed as more Run-II data is analyzed.

We provide a brief example of a comparison of our model to the constraints. Mixing of kaons ($K^0 - \bar{K}^0$ mixing) involves kaon oscillations, which are governed by quark flavor mixing. Observation of kaon mixing provides bounds limiting FCNCs between the first and third generations. More specifically [582], the difference in charges Q'_3 and Q'_1 is approximately, in terms of the new gauge boson parameters,

Table 6.10: Diboson cross section $\sigma_{pp\to Z'\to W^+W^-}$ (units of fb)

$M_{Z'}$	$\sqrt{s} = 8$ TeV	$\sqrt{s} = 13$ TeV	$\sqrt{s} = 14$ TeV
1.9 TeV	0.013	0.058	0.069
3.4 TeV	9.15×10^{-5}	1.62×10^{-3}	2.19×10^{-3}
6.8 TeV	7.50×10^{-13}	4.90×10^{-7}	1.22×10^{-6}

$$g' \left|Q'_3 - Q'_1\right| < \frac{10^{-5} m_{Z'}}{1\text{GeV}} \tag{6.19}$$

which is satisfied for our model by an order of magnitude or so. Observations of the mixing of $B^0 - \bar{B}^0$ impose weaker constraints [582].

6.2.6 Diboson prediction

One of the more interesting phenomenological signatures of Z' models that mix with the SM Z boson is the diboson signature. A diboson event is one with the decay signature of two weak gauge bosons, either W^+W^- or ZZ.

The diboson channel in our case is enabled by the mixing parameter. To calculate the cross section, we employ the narrow resonance approximation, using the decay with of the Z' to W^+W^- of [583]

$$\Gamma_{Z'\to W^+W^-} = \frac{g_{mix}^2}{48\pi} Y_H^2 m_{Z'}. \tag{6.20}$$

The cross section for Z' mediated diboson production is then

$$\sigma_{pp\to W^+W^-} \simeq \sigma_{pp\to Z'} \times \Gamma_{Z'\to W^+W^-} \tag{6.21}$$

using the approximation in Equation (6.16). The cross section values for the scenarios discussed are presented in Table 6.10. Diboson bounds from LHC data are nowhere near these values yet, so these numbers cannot provide any useful constraints. However, they are a prediction that the model is making, and since the diboson signature is a commonly studied one, it is important to keep note of what might be observed. See references [447, 584] for examples of the analysis of a potential diboson signal.

6.3 Dark matter phenomenology

Vector-portal models of dark matter have been explored in great depth [562, 585, 586, 587, 588, 589, 446, 590, 567, 591, 592, 586, 593, 562, 549, 594, 595, 471, 589, 569, 596, 597, 598, 599, 600, 601, 602], both in simplified versions and as embeddings in larger theories. In particular, collider production signals of vector-portal dark matter have been discussed in great detail in the literature [603, 604, 605, 567, 606, 607, 469, 473, 451, 608, 609]. The traditional vector-portal model of dark matter involves the extension of the SM gauge group by

an Abelian gauge group $U(1)'$ and a dark matter particle charged under $U(1)'$. The $U(1)'$ gauge boson is given a mass, by hand or through some symmetry breaking mechanism, and acts as a mediator between the visible and dark sectors, exemplifying hidden sector dark matter [432].

As one of the dimension four portals, the vector portal has been studied in a wide variety of situations. In fact, many realizations of the SUSY WIMP involved Z boson mediated interactions. The generic model of vector-portal dark matter is a simplified model [610, 476, 473, 611, 470, 468] that attempts to describe interactions with minimal number of new parameters required for a consistent quantum field theory. In this Section we will describe our basic extension of the simplified vector-portal model.

Even outside of the context of dark matter, extensions of the SM involving $U(1)'$ gauge groups are prevalent in the literature (for reviews, see [568, 448]). Extra $U(1)'$ gauge groups appear in a variety of GUTs (E_6, $SO(10)$, $SU(5)$ and others) [444, 445], in little Higgs models [612, 613, 614, 61], in theories with extra dimensions [615, 616], and in string and brane inspired models [617]. They also appear in various dynamical symmetry breaking scenarios [618]. One of the most popular minimal extensions of the SM is the $U(1)_{B-L}$ model, where the quantity $B - L$ is gauged. It should be noted that many $U(1)'$ models are embedded in a theory that contains some kind of W' boson [447, 584, 619]. We do not consider models with W' bosons here.

In this Section, we consider constraints from thermal production, from direct detection bounds and from indirect detection each in turn. There are three potential dark matter candidates in the model. We do not consider collider constraints on the dark matter sector, because collider constraints on the mediator (the $U(1)'$ sector) are much stronger in general. Some of the results appearing here were discussed briefly in reference [620].

6.3.1 Nuclear recoil cross sections for tritophilic vector-portal dark matter

As discussed in detail in Chapter 3, one of the primary search techniques for dark matter is direct detection, where the recoil signatures of ambient dark matter scattering from detector nuclei are sought. To study these processes and make meaningful predictions, the nuclear recoil cross sections must be known. For a model of vector-portal dark matter with universal gauge couplings to all SM generations, such as is usually studied in the literature, this is straightforward, and expressions for the cross sections are widely available [121].

The model that is discussed in this Chapter is not one with family universal couplings, however, and this complicates things. Couplings to the first generation of quarks, which comprise the valence charge of the nucleon, are highly suppressed with respect to the couplings to the third generation of quarks, which appear in small amounts in the nucleon distribution. Moreover, couplings to the third generation of quarks facilitate an effective coupling to gluons, which make up the majority of the nucleon binding energy. It is thus important to weigh carefully each of these contributions to the effective interaction between the Z' boson and a nucleon before making any claims about nuclear recoil cross section exclusion limits.

We use the results that first appeared in reference [547]. It is shown in the reference that the dominant

contribution to a Z'-nucleon interaction comes from the mixing-induced interaction with the light quarks, at least for the hierarchy of couplings we are dealing with in this model. There are more wide-ranging implications discussed in the reference, and in Appendix G, which provides a summary of the calculation in reference [547].

Other approaches used by those few who have taken the effort to address this problem include the construction of effective couplings using renormalization group improved couplings [596, 621, 622], and the construction of a loop-order effective coupling between the gluon and the Z' [623]. The first of these alternatives is a well-constructed complementary approach that it would be interesting to compare to, especially when considering the implications of the results presented in reference [547].

6.3.2 Scalar singlet dark matter

The first potential dark matter candidate to be considered in this model is the scalar singlet responsible for breaking the $U(1)'$ symmetry. The singlet is a variant of Higgs-portal dark matter as discussed in Appendix B and as used as an example model in previous Chapters. The properties of the scalar, including mass and coupling to the Higgs, are determined by the boundary conditions of the renormalization group evolution and appear in Table 6.4 for the three scenarios discussed. These values allow a preliminary analysis to be made.

At a first glance, the case looks promising. The values of the Higgs-portal coupling are small enough that the scalar is compatible with low mass bounds on nuclear recoil cross sections from CDMS [191]. The scalar is charged under the $U(1)'$ gauge group and is therefore a complex singlet, not an absolutely stable real singlet, as is the model discussed in Appendix B. However, the symmetry breaking pattern induces a mixing with the SM Higgs boson, as discussed in Section 6.1.1. This mixing will open an invisible Higgs decay channel, which has been discussed in Section 6.2.4, but it will also open a decay channel for the singlet. The singlet will have a nonzero decay width, dominated by decays to charm quarks and tau leptons, given by

$$\Gamma_S = \sum_f \frac{N_c \lambda_2^2 v_s^2 m_f^2}{m_h^4} \sqrt{1 - \frac{4m_f^2}{m_S^2}} \tag{6.22}$$

where the sum is over all fermions that couple to the SM Higgs boson that satisfy the kinematic constraint of $m_f < 2m_S$. The Higgs-portal coupling is λ_2, and the scalar singlet vacuum expectation value is v_s. There will also be a subdominant contribution from the decay to a bottom quark and an off-shell W boson, similar to the Higgs. However, unlike the Higgs, the W mass is larger than the singlet mass to such a degree that the process is highly suppressed.

For the scenarios reported in Table 6.4, with masses $m_S = (20, 11.5, 6)$ GeV, the decay widths are $\Gamma_S = (7.39 \times 10^{-10}, 5.21 \times 10^{-11}, 3.88 \times 10^{-13})$ GeV. Transforming to seconds, the singlet lifetimes are, respectively, $\tau_S = (8.90 \times 10^{-16}, 1.26 \times 10^{-14}, 1.70 \times 10^{-12})$ s. These values are far less than the generally accepted lifetime for unstable dark matter, which is on the scale of hundreds of millions of years. This short

lifetime rules the singlet out as a dark matter candidate.

6.3.3 Neutrino dark matter

The second candidate in the model is the right handed neutrino ν_R, originally introduced to cancel new perturbative gauge anomalies. It is charged under $U(1)'$ and, in the basic case presented in Section 6.1.2, has a Majorana mass term generated by the breaking of the $U(1)'$ gauge symmetry. Like the scalar discussed above, its mass and couplings are completely determined by the solutions to the renormalization group equations. In the case where there is no Dirac mass term, and the seesaw mechanism has not been activated, the neutrino is stable, and can in principle act as cold dark matter. For a detailed review of the phenomenology of right handed neutrinos, see reference [91].

A general review of the many considerations required when dealing with vector-portal Majorana dark matter appears in reference [624]. In our case, the neutrino behaves as more or less a standard hidden sector Majorana fermion, coupling to the $U(1)'$ field through the covariant derivative in the usual way. It also interacts with the scalar singlet which generates its mass.

Technically, the right handed neutrino is a dual-portal model of dark matter, as the scalar singlet can act as a mediator to the SM sector as well. This interaction proceeds through scalar exchange, where the scalar singlet mixes with the SM Higgs and so allows interactions with all SM particles that couple to the Higgs field. The singlet-Higgs mixing angle is so small, however, that this contribution is suppressed by several orders of magnitude when compared to the vector-portal interactions, even those induced by $Z - Z'$ mixing. Because of this suppression, we ignore the singlet as a mediator in our discussions of the phenomenology, taking the model to be vector-portal only. Note also that a Majorana particle will have zero vector coupling with a spin-1 boson, meaning $V'_\nu = 0$, considerably simplifying some of the calculations in comparison to the general Dirac fermion case. See also reference [625] for a very similar model to the one discussed here, with a focus on the phenomenology of the neutrino dark matter.

Thermal constraints

In this section we review the thermal production process for our model and obtain constraints on the parameter space. For a more detailed discussion of the subtleties involved in production mechanisms of vector-portal dark matter, see [585]. Because we have constrained the coupling parameters of the theory by UV boundary conditions and constraints in Appendix C, we are able instead to constrain the mass. This leads to a fully constrained parameter space where only specific mass and coupling values satisfy the WIMP thermal production scenario.

The current abundance of cold dark matter can be used to constrain the thermally averaged annihilation cross sections of the dark matter particle. In principle, finding this relationship requires a full solution of the Boltzmann equation describing the number density evolution of the thermal relic up to freeze–out, but in practice a number of assumptions and approximations are made. This relationship can be used to constrain

the unknown parameters of the model that enter the annihilation cross sections for a given abundance, usually a coupling strength or mass for single–species dark matter. In our case, the various UV scenarios constrain the coupling mediating the annihilation cross section, and so the abundance provides a constraint on the mass of the dark matter particle. In fact, due to the behaviour of the cross sections, this becomes more of a strong prediction.

We first compute the cross sections for an arbitrary center of mass energy s and then apply the thermal averaging approximation from Chapter 2. Following Cline [588], we use the approximation $T = m_\chi/20$ for the freeze–out temperature. We compare these thermally averaged annihilation cross sections to the value of $\langle \sigma v \rangle = 2.2 \times 0.7 \times 10^{-26}$ cm^3/s obtained from Steigman [118]. The reference fully details the estimations used when obtaining this number. The model they use is a simple toy case with minimal beyond SM content, and the factor of 0.7 reflects the estimated effect of a further increase of the number of relativistic degrees of freedom that our model requires beyond what they used. A more complete treatment of this issue requires solving the Boltzmann equation for our model, and is left for future work, but we find this approximate treatment adequate.

The key constraint is whether or not the Majorana neutrino dark matter is compatible with the abundance constraints. We consider in this Section only the case where the Majorana neutrino dark matter is thermally produced. Alternative production mechanisms [91] could change the results of this Section. It should be noted that a threshold approximation for the annihilation cross section will not suffice here [588], as is occasionally done in the literature, as off-threshold contributions contribute significantly.

The annihilation cross sections to fermions are [121]

$$\sigma(s) = \frac{N_c}{48\pi s}\sqrt{\frac{1-4m_f^2/s}{1-4m_\nu^2/s}}\frac{A_\nu'^2}{\left(s-m_{Z'}^2\right)^2+m_{Z'}^2\Gamma_{Z'}^2}$$

$$\times\left\{A_f'^2 4m_\nu^2\left[m_f^2\left(7-\frac{6s}{m_{Z'}^2}+\frac{3s^2}{m_{Z'}^4}\right)-s\right]+A_f'^2 s\left(s-4m_f^2\right)+V_f'^2\left(2m_f^2+s\right)\left(s-4m_\nu^2\right)\right\} \tag{6.23}$$

where s is the center of mass energy squared of the interaction, A' and V' are the generalized couplings, and m_i are masses. Fermions have N_c colors, and the Z' boson has a decay width of $\Gamma_{Z'}$.

The velocity-weighted annihilation cross section to the $Z'Z'$ final state is [588]

$$\sigma v = \frac{g'^4}{128\pi m_\nu^2}\left(\frac{Q_0 Q_1 - Q_2 Q_3 Q_l}{Q_d y^{3/2}\sqrt{y-1}}\right) \tag{6.24}$$

where $y = s/4m_\nu^2$, $R = m_{Z'}/m_\nu$, $R_S = m_S/m_\nu$ and the Q_i are

$$Q_0 = 16\sqrt{y-1}\sqrt{y-R^2}(2y-R^2),$$

$$Q_1 = 16(1-y)(-4R^2+R^4+4y)(3R^4-4yR^2+4y^2)$$

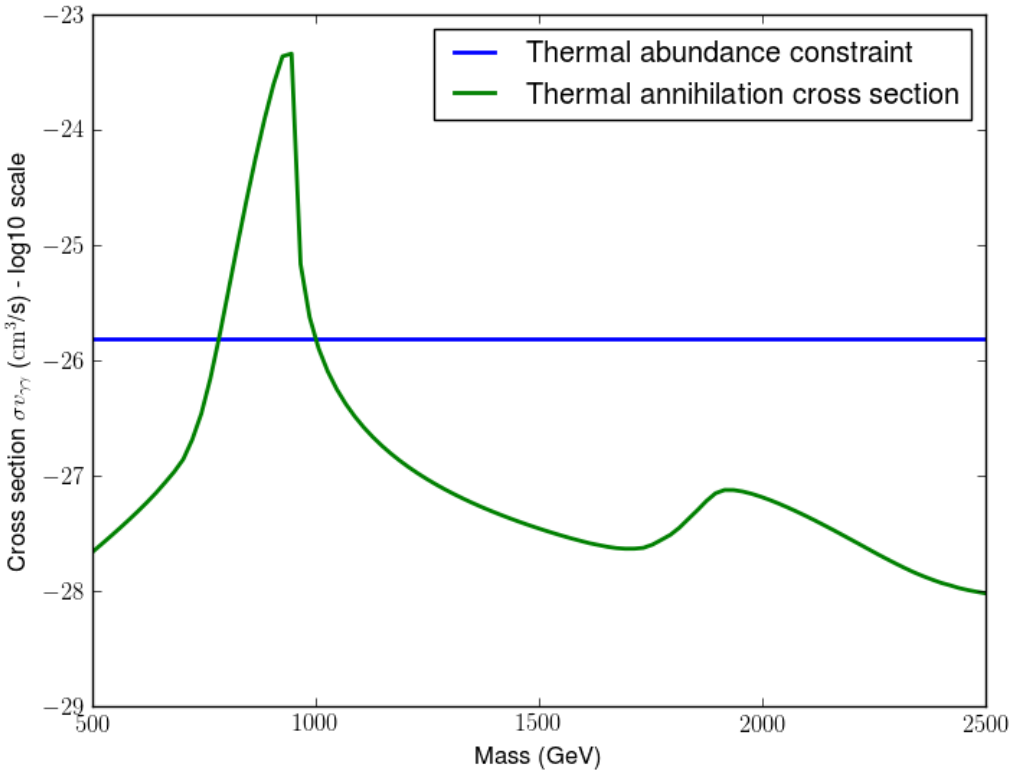

Figure 6.4: The thermal annihilation cross section for Majorana dark matter interacting with a Z' boson of mass 1.9 TeV as a function of dark matter mass, plotted alongside the cross section required to reproduce the observed thermal abundance as computed in reference [118].

$$-8(R_S^2-4y)(-4R^2+R^4+4y)(R^4-2yR^2+4y^2)$$

$$-(R_S^2-4y)^2\left[-R^8+2R^4(R^2+y)8(R^4-4yR^2+2y^2)\right],$$

$$Q_2 = 2(4y-R_S^2)(-4R^2+R^4+4y),$$

$$Q_3 = 8(R^2-2y)(-4R^4+R^6+8yR^2-8y^2)$$

$$+(R_S^2-4y)\left[16y(y-R^2)+4R^2(R^2-y)(R^2+4y)-R^4(R^4+4y^2)\right],$$

$$Q_l = \ln\left[\frac{\left(R^2-2(y+\sqrt{y-1}\sqrt{y-R^2})\right)^4}{(-4R^2+R^4+4y)^2}\right],$$

$$Q_d = R^4(R^2-2y)(R_S^2-4y)^2(-4R^2+R^4+4y). \tag{6.25}$$

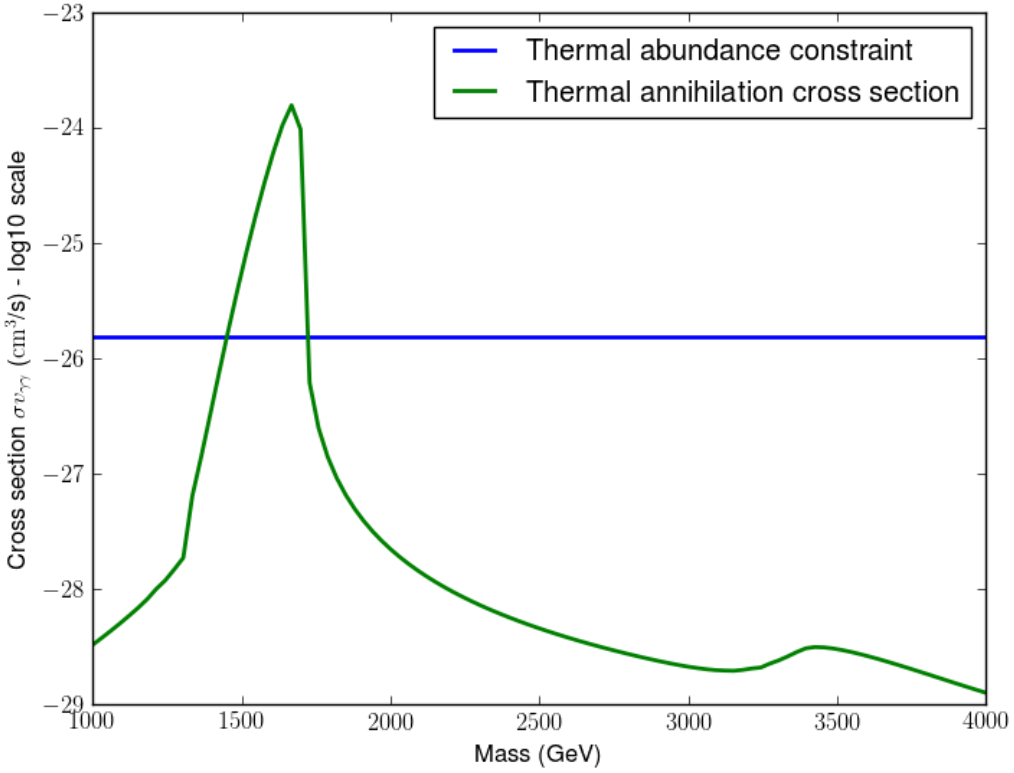

Figure 6.5: The thermal annihilation cross section for Majorana dark matter interacting with a Z' boson of mass 3.4 TeV as a function of dark matter mass, plotted alongside the cross section required to reproduce the observed thermal abundance as computed in reference [118].

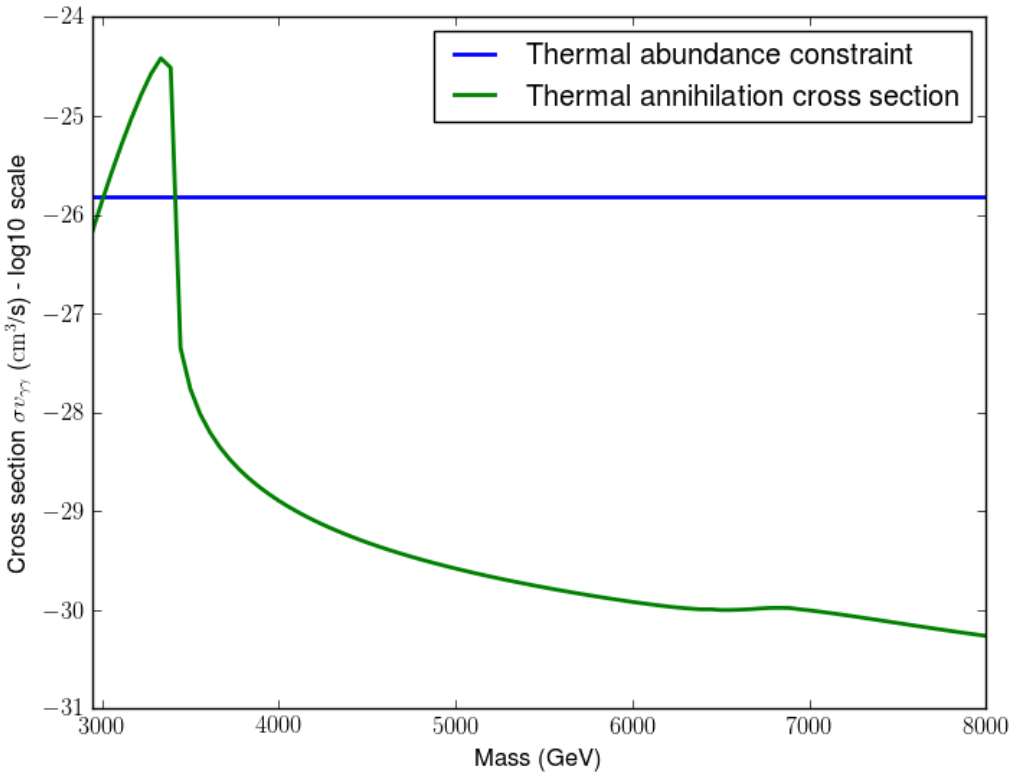

Figure 6.6: The thermal annihilation cross section for Majorana dark matter interacting with a Z' boson of mass 6.8 TeV as a function of dark matter mass, plotted alongside the cross section required to reproduce the observed thermal abundance as computed in reference [118].

In Figures 6.4, 6.5 and 6.6, the thermal averages of these cross sections have been summed and plotted as a function of neutrino mass m_ν. Included is the abundance required annihilation cross section from reference [118]. The thermally allowed values occur where the lines cross.

From these figures it can be seen that the required masses for the neutrinos to make up thermal dark matter are far below the masses required by the symmetry breaking scenario, which appear in Table 6.4. The abundance of the neutrinos can be manipulated by allowing a Yukawa coupling to the Higgs, which generates a Dirac mass term and enables annihilation through the Higgs portal as well as mixing with SM neutrinos. The neutrino mixing allows non-resonant thermal production of the neutrino dark matter. However, this mechanism will generally make the neutrino abundance too large without fine some fine tuning, as well as allowing dark matter decay, which introducing a whole new set of concerns. There are also several other production mechanisms for neutrino dark matter that have been considered that rely on exotic effects, such as couplings to gravitational scalars.

As the neutrino dark matter allowed by this model does not match the basic thermal production scenario, we refrain from considering it any further.

6.3.4 Dirac dark matter

As discussed in Section 6.1, the model admits a dark sector charged under the $U(1)'$ gauge group. The dark sector could in principle be very large and contain any number of new particle species, we consider only the simple case of a Dirac fermion, primarily to test whether the phenomenology is at all interesting.

The dark matter particle χ is charged under $U(1)'$ with a charge of unity and has no SM charge. In this preliminary case, we set the Yukawa coupling to the scalar S to zero, though this is in general unnatural. We also insert the Dirac mass term by hand, appealing to UV physics for a mass generation mechanism. As the χ is vectorlike under all gauge groups, including the $U(1)'$ group, such a mass term violates no gauge symmetries and so is allowed.

The model as presented is an example of generic vector-portal dark matter. These models are very well studied, but usually the $U(1)'$ gauge parameter is an unconstrained degree of freedom. In our case, $U(1)'$ gauge parameter and the mixing parameter are fixed by the renormalization group analysis, leading to a very interesting and powerful reduction of the parameter space. The dark matter sector of this project was in part an attempt to determine how useful RNG techniques with theoretically motivated boundary conditions could be as an additional constraint on simple dark matter models.

That this model is somewhat of a toy becomes apparent when considering the mass term of the Dirac dark matter and its origin. Technically, the mass term is assumed small enough that any breaking of the conformal symmetry is considered to be 'soft', in the context discussed in Appendix C. A proper treatment would require specification of the mass generation mechanism, at least through some effective means, and inclusion of a contribution to the renormalization group equations.

Thermal Constraints

As the Dirac dark matter does not have a mass constrained by the model as the neutrino dark matter does, we expect that the thermal abundance condition can be used to derive meaningful constraints on the model. This is done in the usual way, by calculating the thermal annihilation cross sections and comparing them against the expected cross section as calculated from the observed abundance.

The dark matter fermion can annihilate through a number of channels, most enabled through mixing between the Higgs and singlet or between the Z and Z' gauge bosons. We argue that most of these contributions are subdominant and only very few cross sections need to be considered. The tree level annihilation channels are (all s-channel, except for the annihilations directly to $U(1)$ gauge bosons, which proceed through the u and t-channels).

$$\chi\bar{\chi} \to Z, Z' \to f\bar{f}$$

$$\chi\bar{\chi} \to Z, Z' \to \nu_R\nu_R$$

$$\chi\bar{\chi} \to ZZ, ZZ', Z'Z'$$

$$\chi\bar{\chi} \to Z, Z' \to WW$$

$$\chi\bar{\chi} \to Z, Z' \to Zh, Z'h, ZS, Z'S \tag{6.26}$$

At this time, we ignore any possible loop-order channels, though they might in fact be larger than some of the mixing induced channels listed here.

Anything involving a Z in an intermediate or final state is suppressed by the $Z - Z'$ mixing, which is very small with our mass hierarchy, and so we neglect the Z-channel contributions. Most of the processes with final state scalars are suppressed by the Higgs–portal mixing, which is constrained to be very small by the Z' mass scale, so contributions with scalar final states are also neglected. It should be noted that since the Higgs has nonzero hypercharge, the $\chi\bar{\chi} \to Z' \to Z'h$ channel may be nonnegligible for larger values of g_{mix} (approaching unity), but our values are much smaller. The only potential scalar final state contribution is from $\chi\bar{\chi} \to Z' \to Z'S$, but it is highly suppressed near threshold due to kinematic effects and further suppressed by powers of the singlet vacuum expectation value in the denominator.

Annihilation to leptons is naturally suppressed due to the 'leptophobic' nature of the model. The neutrino channel is a bit of a special case. The branching ratio for the decay $Z' \to \nu_R\nu_R$ is small but nonnegligible, which leads us to suspect that this annihilation channel may be important. In fact, we have taken the right-handed neutrino sector to be Majorana, meaning the neutrinos are required to have a purely axial

coupling with the Z'. However, despite the relative size of the cross section, annihilation to neutrinos does not contribute to the thermal relic abundance calculations. Since we have arbitrarily chosen the dark fermion χ to have a purely vector coupling, the annihilation channel to neutrinos has an amplitude of zero at leading order.

The mass of the dark fermion is not generated by any symmetry breaking mechanism, so it does not require Yukawa couplings to any scalar fields. This means there are no scalar-mediated annihilation channels in this basic case.

There are thus two annihilation channels to consider:

$$\chi\bar{\chi} \to q\bar{q}, \tag{6.27}$$

$$\chi\bar{\chi} \to Z'Z'. \tag{6.28}$$

The relativistic annihilation cross section for the process $\chi\bar{\chi} \to Z' \to f\bar{f}$ is given by [121] (note that in our case $A'_\chi = 0$, simplifying the cross section considerably)

$$\sigma(s) = \frac{N_c}{12\pi s}\sqrt{\frac{1-4m_f^2/s}{1-4m_\chi^2/s}}\frac{1}{\left(s-m_{Z'}^2\right)^2+m_{Z'}^2\Gamma_{Z'}^2}$$

$$\times\Bigg\{A_f'^2A_\chi'^2 4m_\chi^2\left[m_f^2\left(7-\frac{6s}{m_{Z'}^2}+\frac{3s^2}{m_{Z'}^4}\right)-s\right]+A_f'^2A_\chi'^2 s\left(s-4m_f^2\right)+A_f'^2v_\chi'^2\left(s-4m_f^2\right)\left(2m_\chi^2+s\right)$$

$$+V_f'^2\left(2m_f^2+s\right)\left[A_\chi'^2\left(s-4m_\chi^2\right)+V_\chi'^2\left(2m_\chi^2+s\right)\right]\Bigg\} \tag{6.29}$$

The annihilation cross sections to the Z' are [588]

$$\sigma v = \frac{g'^4}{128\pi m_\chi^2}\left(\frac{Q_0Q_1-Q_2Q_3Q_l}{Q_d y^{3/2}\sqrt{y-1}}\right) \tag{6.30}$$

where $y = s/4m_\chi^2$, $R = m_{Z'}/m_\chi$, and the Q_i are

$$Q_0 = 16\sqrt{y-1}\sqrt{y-R^2}(2y-R^2),$$

$$Q_1 = 2+R^4+2y,$$

$$Q_2 = -4R^2+R^4+4y,$$

$$Q_3 = 2\left(-2-2R^2+R^4+4y+4y^2\right),$$

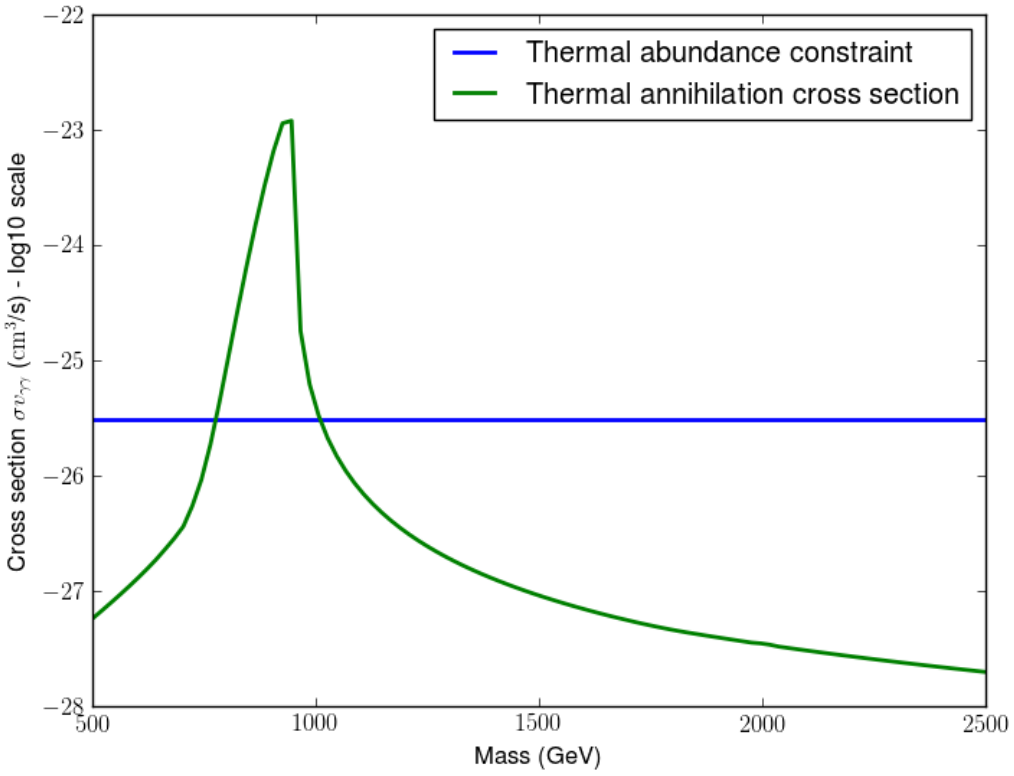

Figure 6.7: The thermal annihilation cross section for Dirac dark matter interacting with a Z' boson of mass 1.9 TeV as a function of dark matter mass, plotted alongside the cross section required to reproduce the observed thermal abundance as computed in reference [118].

$$Q_l = \ln\left[\frac{\left(R^2 - 2(y + \sqrt{y-1}\sqrt{y-R^2})\right)^4}{(-4R^2 + R^4 + 4y)^2}\right],$$

$$Q_d = (R^2 - 2y)(-4R^2 + R^4 + 4y). \tag{6.31}$$

The basic procedure for the comparison with the required thermal abundance is as described in the discussion of Majorana dark matter in the previous Section. The results of our comparisons are illustrated in Figures 6.7, 6.8 and 6.9.

From Figures 6.7, 6.8 and 6.9, it is obvious that the Z' mass resonance in the annihilation cross section to fermions plays a crucial role in allowing the cross sections of the model to reach the required values. Thermally allowed masses for the model as described are thus limited to two values for each scenario, near $m_\chi = m_{Z'}/2$. There would be a similar resonance near half the Z mass, near 45 GeV, but it would be much too weak to match the thermal abundance [447]. It should be noted that these results assume that 100% of the observed abundance is accounted for by this vector-portal Dirac dark matter, which is not strictly necessary [588]. We nonetheless in the interests of simplicity assume that the χ makes up all of the observed

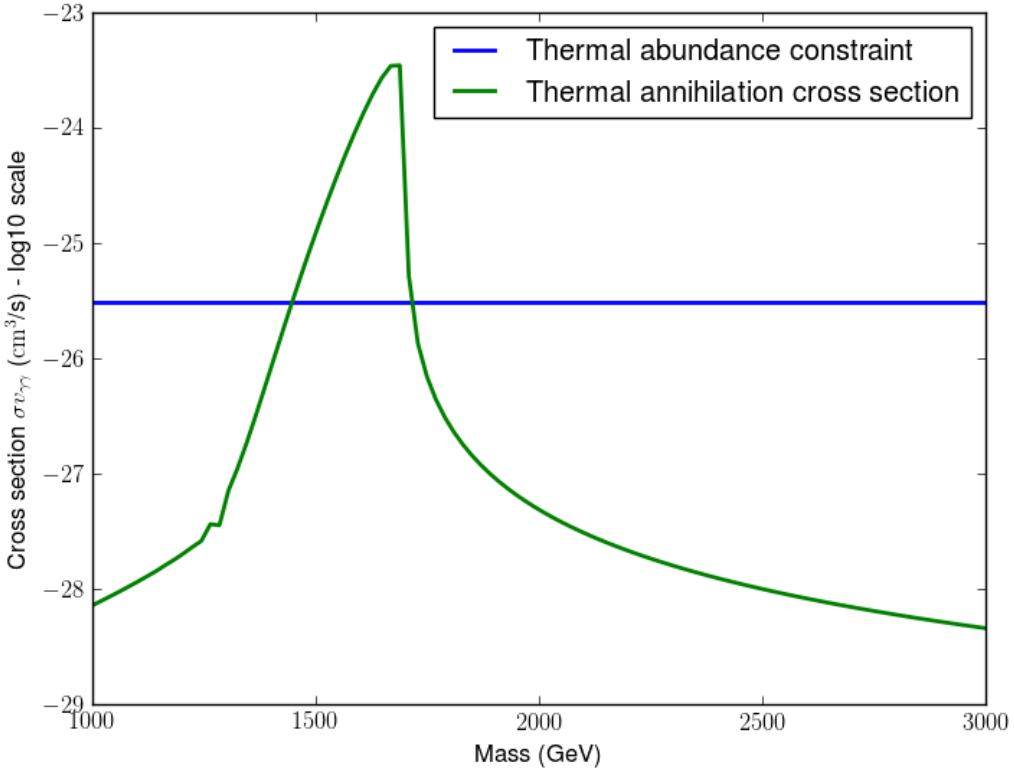

Figure 6.8: The thermal annihilation cross section for Dirac dark matter interacting with a Z' boson of mass 3.4 TeV as a function of dark matter mass, plotted alongside the cross section required to reproduce the observed thermal abundance as computed in reference [118].

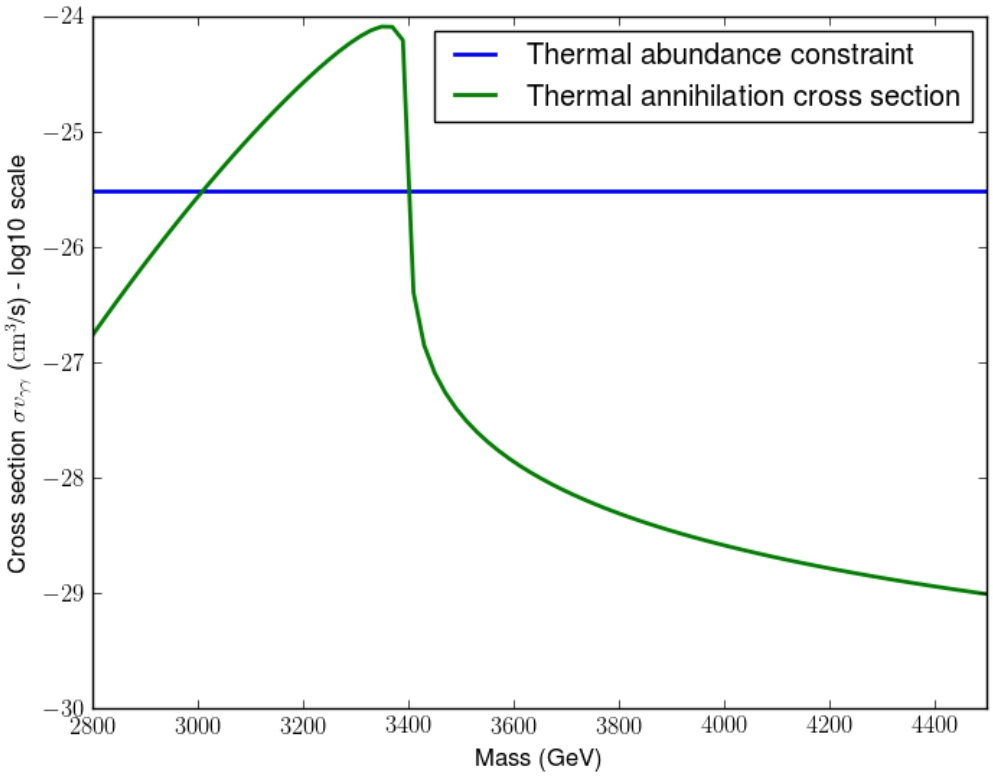

Figure 6.9: The thermal annihilation cross section for Dirac dark matter interacting with a Z' boson of mass 6.8 TeV as a function of dark matter mass, plotted alongside the cross section required to reproduce the observed thermal abundance as computed in reference [118].

Table 6.11: Thermally constrained dark matter masses

$M_{Z'}(TeV)$	$m_{\chi 1}$ (TeV)	$m_{\chi 2}$ (TeV)
1.9 TeV	0.772	1.015
3.4 TeV	1.454	1.717
6.8 TeV	3.015	3.398

Table 6.12: Z' decay widths for thermally constrained dark matter masses

$M_{Z'}(TeV)$	$\Gamma_{Z' \to \chi\chi(1)}$ (GeV)	$\Gamma_{Z' \to \chi\chi(2)}$ (GeV)
1.9 TeV	1.27	0
3.4 TeV	0.64	0
6.8 TeV	0.29	0.023

dark matter. It would be an interesting extension of the work to match thermal masses to fractions of the observed abundance.

The thermally allowed masses for Dirac fermionic dark matter are presented in Table 6.11 in units of TeV, with an accuracy in the tens of GeV (due primarily to the resolution of the mass grid the cross section calculation was done over).

Now, using Equation (6.12), we can compute the contribution to the Z' decay width from the dark matter fermions with these masses, presented in Table 6.12. These values are important phenomenologically, as they can have significant effects on the annihilation cross sections.

These decay widths are large compared to the SM decay widths of the Z' boson, but are small enough in comparison to $m_{Z'}$ that the narrow resonance approximation remains valid, leaving our collider phenomenology analysis accurate. Note as well that while the first two scenarios do not kinematically allow decay of an on-shell Z' to the larger of the two thermally allowable dark matter masses, the last scenario does, albeit highly suppressed. This fact has implications for the discussion of photon annihilation signals that will appear in Section 6.3.4.

Direct detection constraints

The strongest constraints on conventional WIMP dark matter models come from the bounds provided by nuclear recoil direct detection experiments as discussed in Chapter 3. For vector-portal dark matter models such as the one considered in this Chapter, the spin-1 mediator instigates contributions to the total nuclear recoil cross section from a number of different spin operators. A general overview of these operators appears in reference [586], and though many of them contribute, we are able to argue that most of them can be neglected.

For a general vector mediated interaction between two fermions, where both fermions have both vector

Table 6.13: Nuclear recoil cross sections for thermally constrained dark matter masses

$M_{Z'}(TeV)$	$\Gamma_{Z'\to\chi\chi(1)}$ (cm^2)	$\Gamma_{Z'\to\chi\chi(2)}$ (cm^2)
1.9 TeV	3.832×10^{-45}	3.834×10^{-45}
3.4 TeV	3.463×10^{-47}	3.464×10^{-47}
6.8 TeV	1.238×10^{-49}	1.238×10^{-49}

and axial couplings to the mediator, the four spin operators are:

$$(\bar{q}\gamma^\mu q)\,(\bar{\chi}\gamma_\mu\chi)\,, \tag{6.32}$$

$$(\bar{q}\gamma^\mu q)\,(\bar{\chi}\gamma_\mu\gamma_5\chi)\,, \tag{6.33}$$

$$(\bar{q}\gamma^\mu\gamma_5 q)\,(\bar{\chi}\gamma_\mu\chi)\,, \tag{6.34}$$

and

$$(\bar{q}\gamma^\mu\gamma_5 q)\,(\bar{\chi}\gamma_\mu\gamma_5\chi)\,. \tag{6.35}$$

Of these, we can immediately discount the second and fourth, as we have chosen the dark fermion χ to have only vector couplings to the Z'. This leaves the first and the third, which respectively generate a spin-independent contribution and a spin-dependent contribution to the cross section. In a comparison of the generic operators, the vector-vector interaction (6.32) dominates, with the axial-axial interaction (6.35) suppressed by spin factors and the axial-vector (6.34) and vector-axial (6.33) interactions suppressed by both spin factors and relative velocity. Given this relative cross section hierarchy, as well as the fact that spin independent bounds are much more constraining than spin dependent bounds, we consider only the spin independent vector-vector contribution, proportional to the operator in Equation (6.32).

The nonrelativistic nuclear recoil scattering cross section for vector-portal dark matter can thus be approximated as the spin-independent contribution, which is [588]:

$$\sigma = \frac{m_N^2 m_\chi^2 V_N'^2}{\left[m_{Z'}^4 + m_{Z'}^2\Gamma_{Z'}^2\right]\left[m_N + m_\chi\right]^2}.$$

It can be seen that the cross section is more or less independent of dark matter mass. This is because the factor of $m_{Z'}^4$ in the denominator dominates the cross section, leaving it roughly constant in m_χ.

Values of this cross section for the thermally allowed masses are presented in Table 6.13. From comparisons against the bounds presented and referenced in Chapter 3, we can see that the case of dark matter mediated by a 1.9 TeV Z' is ruled out by XENON1T and other experiments. This case is already inconsistent with dilepton bounds on massive mediators, so no new information is gained. The case of dark matter mediated by a 3.4 TeV Z' is not yet constrained by XENON1T [626], though it may be ruled out by the future experiments

discussed in Chapter 3. This case is, for now, still viable. The case of dark matter mediated by a 6.8 TeV Z' produces direct detection cross sections that are well below the neutrino floor [233], which means that until new techniques are developed to penetrate that background, direct detection experiments cannot say anything about that scenario.

Indirect detection constraints

In this section, we discuss the potential signals of our vector-portal model and the bounds that can be placed on the model from the nonobservation of a gamma ray signal

We consider first the potential for a monochromatic photon line from the annihilation of the Dirac dark matter particle, as such a signal provides the cleanest bounds. The annihilation proceeds through fermion loops and an intermediate Z'. Evaluation of this cross section is complicated by the intricate couplings of the fermions to the vector mediator. Nonetheless, the result is available in the literature. The annihilation cross section is [627]

$$\sigma v = \left| \sum_f \left(m_\chi^2 A_7^f(s) - \frac{1}{2} A_1^f(s) \right) \right|^2 \frac{\left(Q'_{\chi L} - Q'_{\chi R}\right)^2 g'^2 m_\chi^2}{4\pi m_{Z'}^2 \left(m_{Z'}^2 + \Gamma_{Z'}^2\right)}. \tag{6.36}$$

The internal functions are

$$A_1^f(s) = \frac{e^2 Q_f^2 g' A'_f N_c^f}{4\pi^2} \left[3 + \Lambda\left(s, m_f, m_f\right) + 2m_f^2 C_0\left(0, 0, s, m_f, m_f, m_f\right) \right] \tag{6.37}$$

and

$$A_7^f(s) = \frac{e^2 Q_f^2 g' A'_f N_c^f}{2\pi^2 s} \left[2 + \Lambda\left(s, m_f, m_f\right) \right], \tag{6.38}$$

where Q and Q' are the electromagnetic and $U(1)'$ charges of the indexed particle, A' is the generalized axial charge, e is the unit electric charge, N_c is the number of colors of a fermion, g' is the $U(1)'$ gauge coupling, and m is a mass. The loop functions are

$$\Lambda(s, m, m) = \sqrt{1 - \frac{4m^2}{s}} \ln \left[\frac{2m^2}{2m^2 - s\left(1 + \sqrt{1 - \frac{4m^2}{s}}\right)} \right] \tag{6.39}$$

and

$$C_0\left(0, 0, s, m, m, m\right) = \frac{1}{2s} \ln^2 \left[\frac{\sqrt{1 - \frac{4m^2}{s}} - 1}{\sqrt{1 - \frac{4m^2}{s}} + 1} \right]. \tag{6.40}$$

The Landau-Yang Theorem [628, 629] is a statement of conservation of angular momentum in the interactions of spin-1 particles. It essentially states that, in the vacuum, a spin-1 particle cannot annihilate into two spin-1 particles. This has obvious implications for the annihilation to $\gamma\gamma$, as the Theorem will apply

near the resonance of $m_\chi = m_{Z'}/2$, strongly suppressing the annihilation cross section to a pair of photons. This is also the region where the thermal constraints allow the mass of the dark matter particle to reside, meaning that a photon pair line signal of annihilating dark matter is almost useless for our model of fermionic vector-portal dark matter. Of the monochromatic lines, the γZ channel becomes dominant (in fact there is an enhancement near the pole [630]). Moreover, the factor $\left(Q'_{\chi L} - Q'_{\chi R}\right)$ makes the cross section zero in any case for our arbitrarily chosen case of vector charged dark matter.

As monochromatic line searches are suboptimal for this model of dark matter, and the mass scales involved are far too high for any explanation of the galactic core excess to be reasonable (though it has been considered in the context of similar models [446]), we consider flux comparisons to the Fermi dSph galaxy observations as discussed in Chapter 4. The dwarf galaxies are chosen from the selection suggested in reference [325], which probe the conventional WIMP cross section value for a variety of masses, and are the three considered in the Higgs-portal scalar example in Chapter 4 as well.

The basic visual analysis we do here is essentially the same as what was done in Chapter 4, comparing the predicted flux against the flux reported by Fermi in [316]. In the absence of any potential signal, we simply consider whether or not the observed flux is smaller than the predicted flux for a given scenario. If it is, we consider the scenario in question to be in conflict with the observations. This analysis is not particularly rigorous, but does generate some useful conclusions. The Figures in question are Figures 6.10 -6.18.

It should be noted that the discrepancies between the mass values, which are quite significant in the third scenario, are due to differences in the Z' decay width to dark matter, recorded in Table 6.12. These results are conservative because they include only contributions from the fermionic SM final states. There are also subdominant contributions from the annihilations to Z' final states for some of these mass values. The Z' would then decay into SM and dark particles, resulting in a cascade of photonic contributions to the final state flux. Final states involving scalars would also contribute to this cascade.

From our basic visual analysis, the scenario with annihilating dark matter mediated by a 1.9 TeV Z' boson is ruled out by the observations of all three dwarfs. However, we have found that this scenario is inconsistent with both dilepton and direct detection bounds. The second scenario, with a 3.4 TeV Z', is also inconsistent with these observations, though the smaller mass value of the thermally allowed pair produces a photon flux only slightly over what is observed. The third scenario, with a Z' mass of 6.8 TeV is more ambiguous. The larger mass value is certainly not consistent with the observations, mostly due to the reduced decay width of the Z' to dark matter, but the smaller mass value of 3015 GeV is only inconsistent with the low energy region of the flux. There is tension, but this case is worth further consideration in the future.

For the model in general, the 1.9 TeV Z' scenario is strongly disfavored by multiple observations, while there are some conflicts with Fermi dwarf observations for the other two scenarios, though the one with a 6.8 TeV Z' has much less tension. Regardless, the gamma ray sector provides the greatest hurdle to the model, mostly because the tritophilia of the model provides no suppression of a photon annihilation signal, unlike in collider experiments and direct detection. In fact, one might expect that for a model like this, the gamma

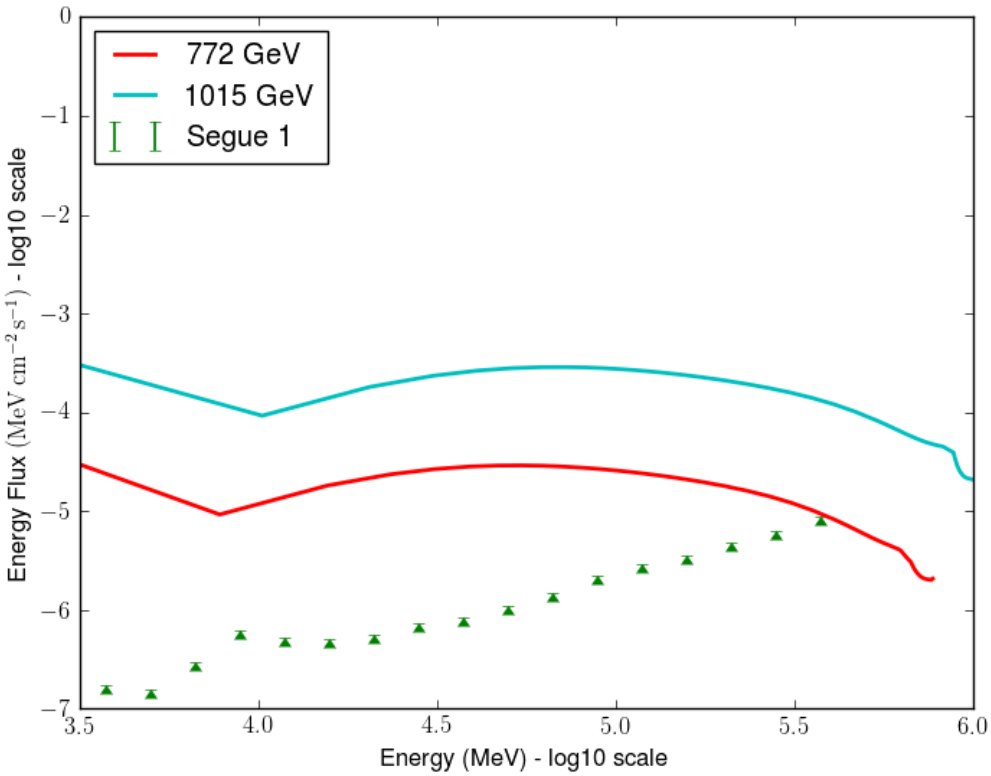

Figure 6.10: The predicted energy scaled photon flux for the annihilation of thermally constrained Dirac dark matter of two different masses interacting with a Z' boson of mass 1.9 TeV as a function of photon energy in MeV, plotted on a double logarithmic scale alongside the energy scaled flux observed from the dwarf galaxy Segue 1 as reported in reference [316].

ray signal would be the first sign of dark matter.

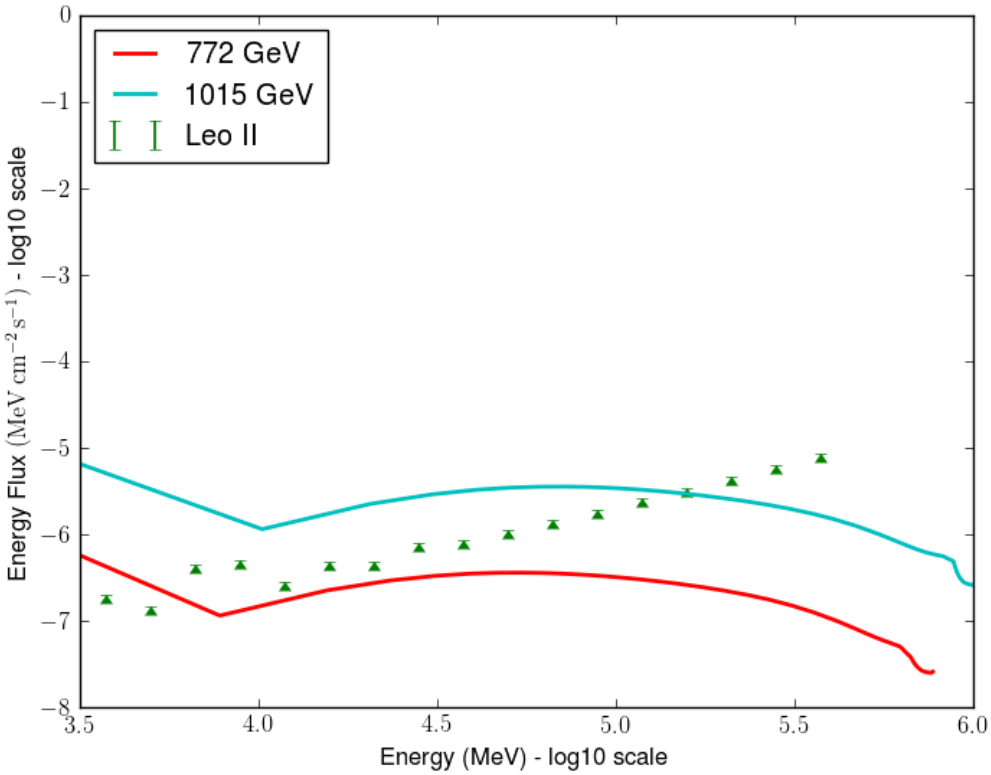

Figure 6.11: The predicted energy scaled photon flux for the annihilation of thermally constrained Dirac dark matter of two different masses interacting with a Z' boson of mass 1.9 TeV as a function of photon energy in MeV, plotted on a double logarithmic scale alongside the energy scaled flux observed from the dwarf galaxy Leo II as reported in reference [316].

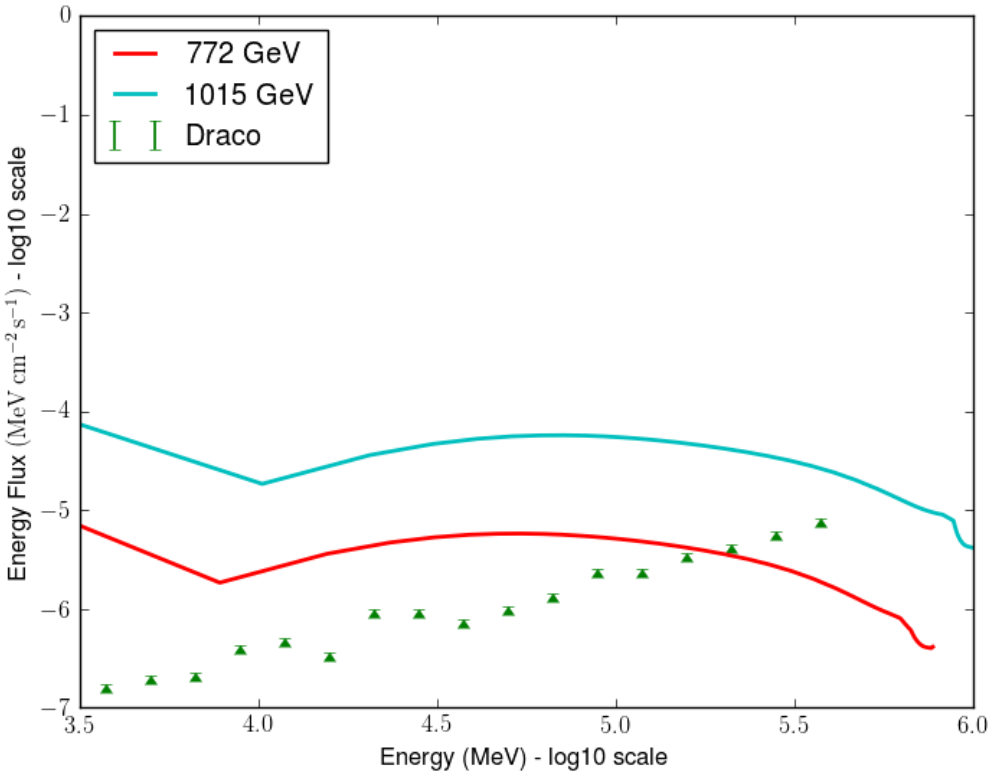

Figure 6.12: The predicted energy scaled photon flux for the annihilation of thermally constrained Dirac dark matter of two different masses interacting with a Z' boson of mass 1.9 TeV as a function of photon energy in MeV, plotted on a double logarithmic scale alongside the energy scaled flux observed from the dwarf galaxy Draco as reported in reference [316].

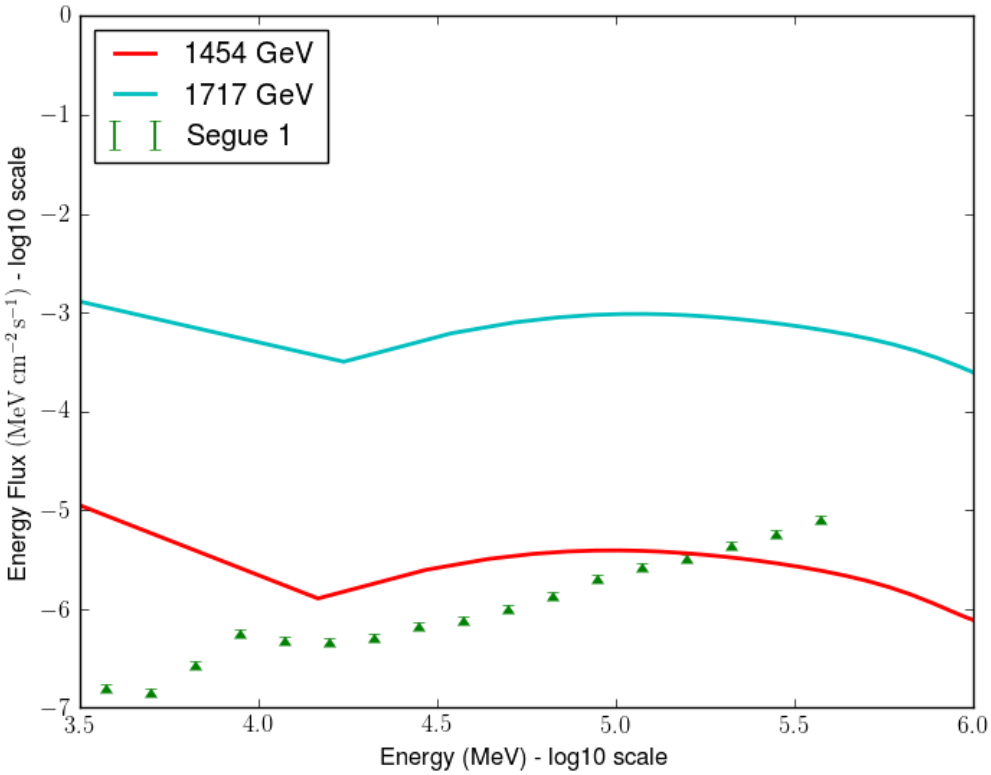

Figure 6.13: The predicted energy scaled photon flux for the annihilation of thermally constrained Dirac dark matter of two different masses interacting with a Z' boson of mass 3.4 TeV as a function of photon energy in MeV, plotted on a double logarithmic scale alongside the energy scaled flux observed from the dwarf galaxy Segue 1 as reported in reference [316].

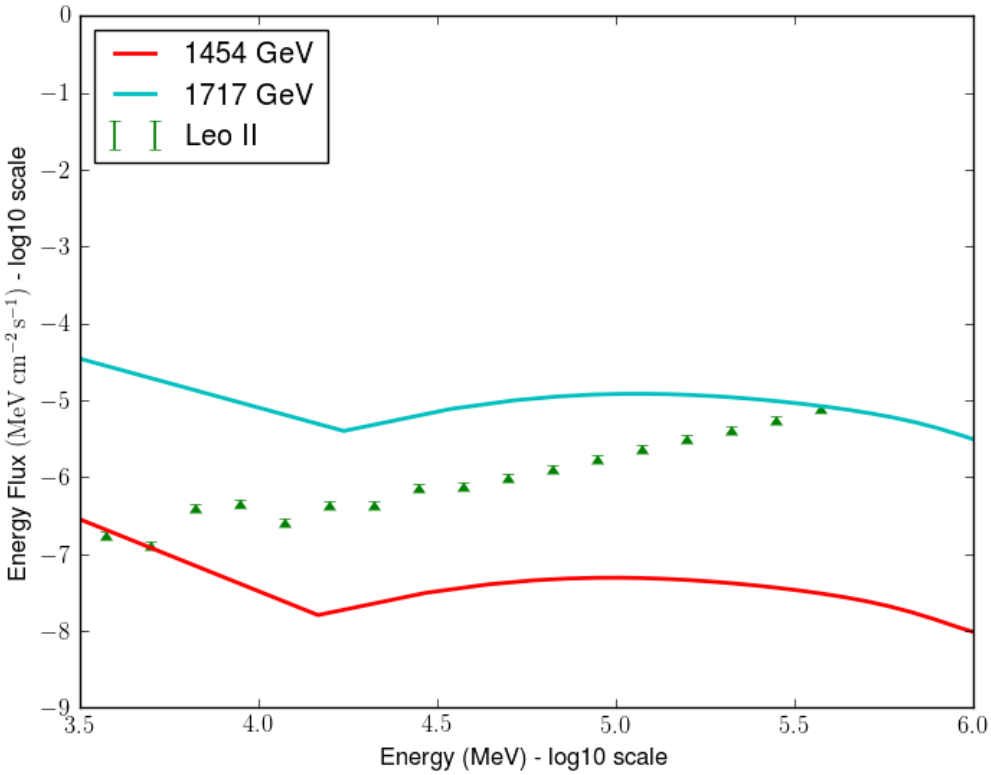

Figure 6.14: The predicted energy scaled photon flux for the annihilation of thermally constrained Dirac dark matter of two different masses interacting with a Z' boson of mass 3.4 TeV as a function of photon energy in MeV, plotted on a double logarithmic scale alongside the energy scaled flux observed from the dwarf galaxy Leo II as reported in reference [316].

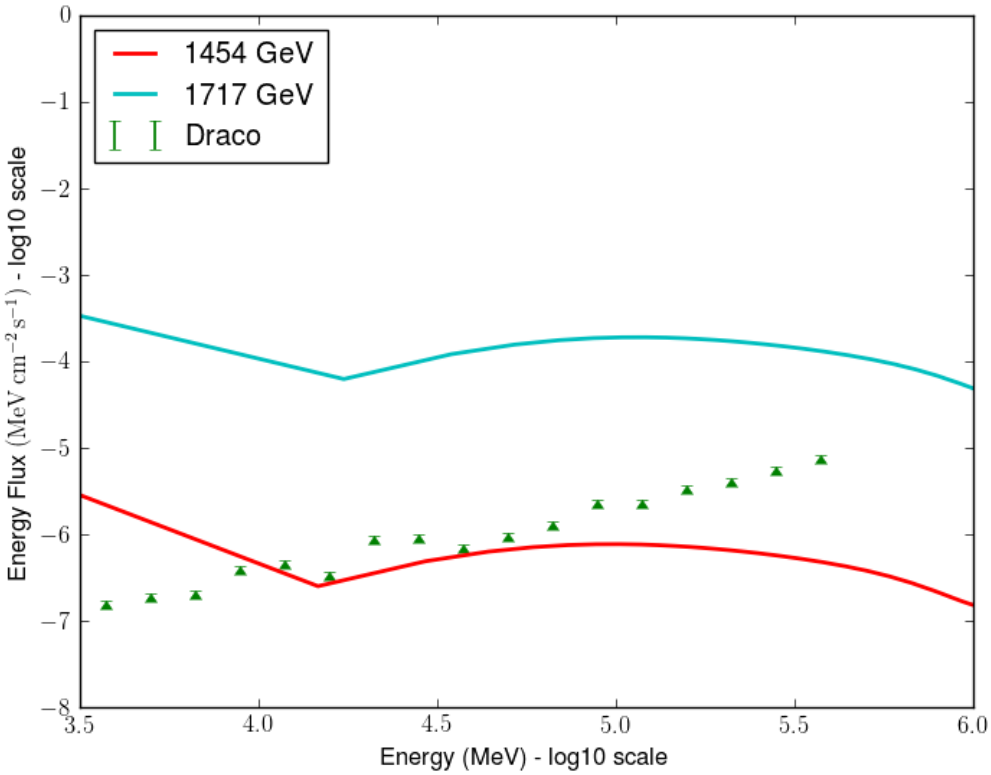

Figure 6.15: The predicted energy scaled photon flux for the annihilation of thermally constrained Dirac dark matter of two different masses interacting with a Z' boson of mass 3.4 TeV as a function of photon energy in MeV, plotted on a double logarithmic scale alongside the energy scaled flux observed from the dwarf galaxy Draco as reported in reference [316].

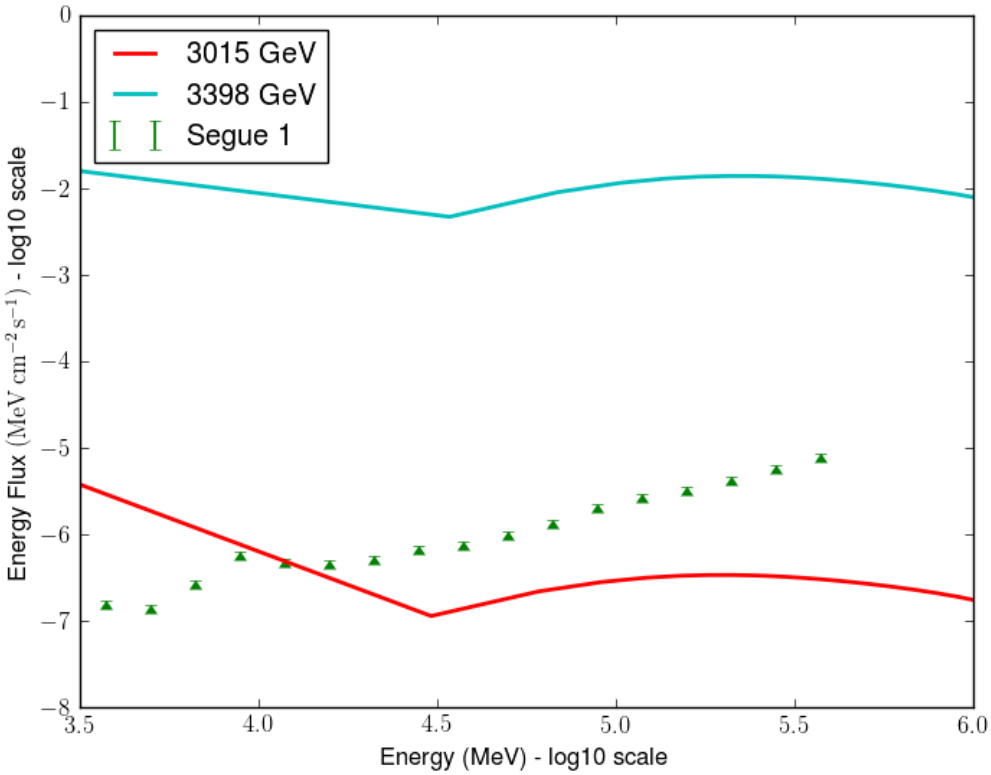

Figure 6.16: The predicted energy scaled photon flux for the annihilation of thermally constrained Dirac dark matter of two different masses interacting with a Z' boson of mass 6.8 TeV as a function of photon energy in MeV, plotted on a double logarithmic scale alongside the energy scaled flux observed from the dwarf galaxy Segue 1 as reported in reference [316].

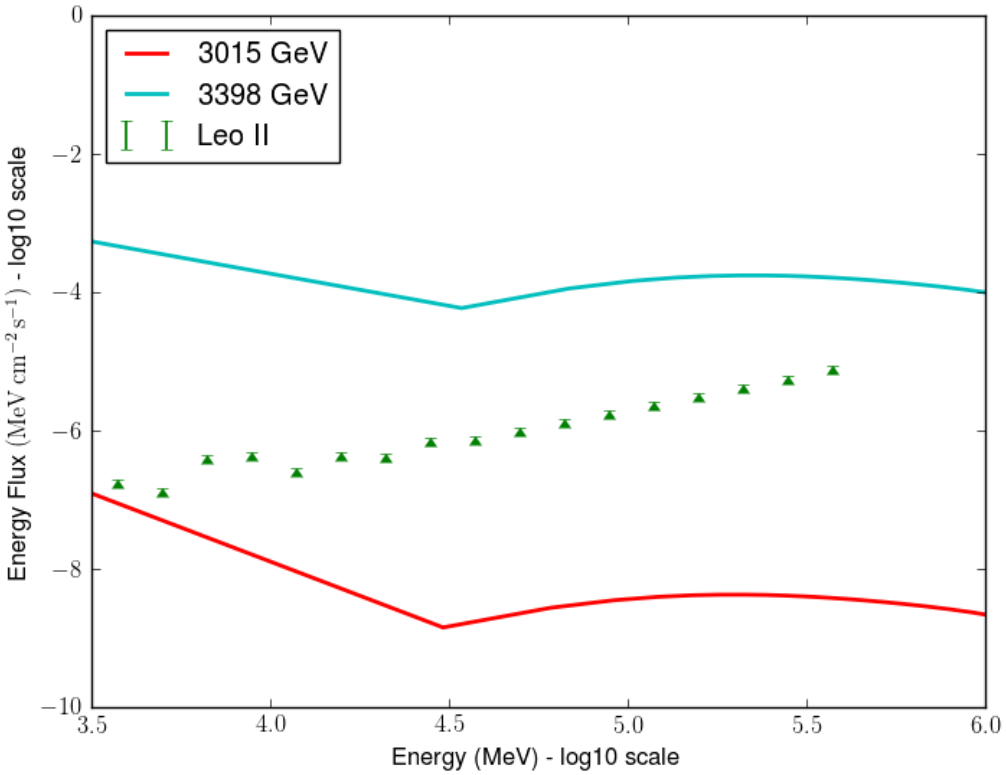

Figure 6.17: The predicted energy scaled photon flux for the annihilation of thermally constrained Dirac dark matter of two different masses interacting with a Z' boson of mass 6.8 TeV as a function of photon energy in MeV, plotted on a double logarithmic scale alongside the energy scaled flux observed from the dwarf galaxy Leo II as reported in reference [316].

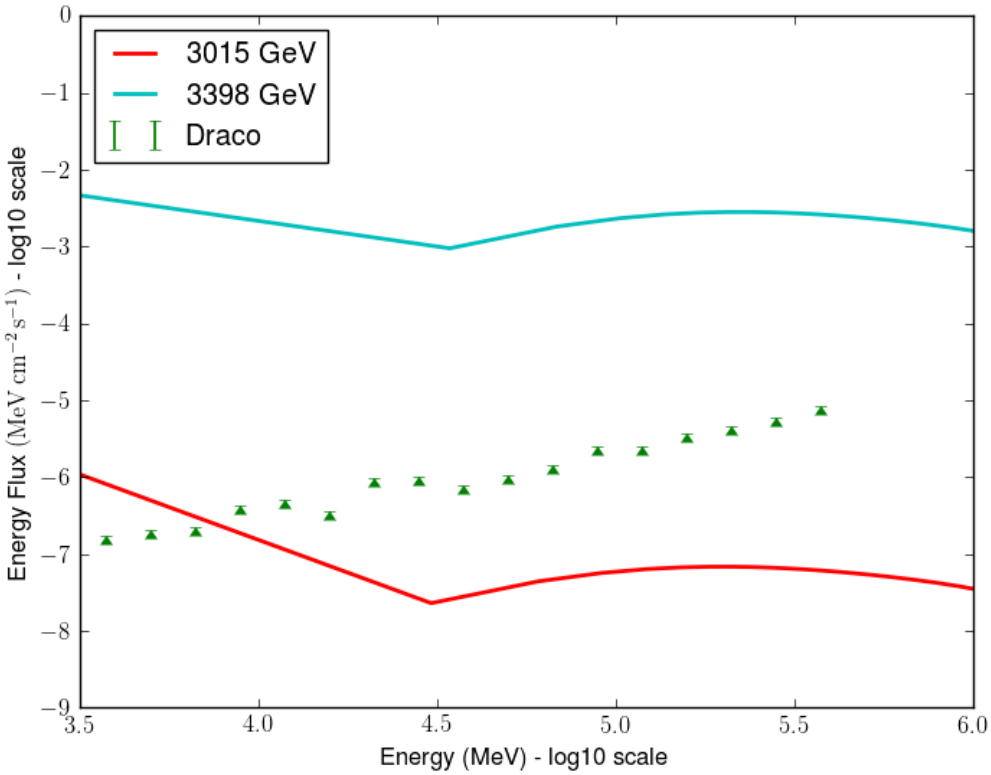

Figure 6.18: The predicted energy scaled photon flux for the annihilation of thermally constrained Dirac dark matter of two different masses interacting with a Z' boson of mass 6.8 TeV as a function of photon energy in MeV, plotted on a double logarithmic scale alongside the energy scaled flux observed from the dwarf galaxy Draco as reported in reference [316].

Chapter 7

Closing remarks

These concluding remarks bring to an end the main body of this thesis. They summarize the work that has been presented here, as well as providing some points to consider for future work in this area.

Chapters 2-5 provided an exposition of a variety of standard techniques in particle dark matter phenomenology, including the calculation of thermal abundances (Chapter 2), direct detection (Chapter 3), indirect detection through gamma rays (Chapter 4), and detection in particle colliders (Chapter 5). Within each Chapter, the techniques were applied to the simple example of scalar Higgs-portal dark matter. These Higgs-portal studies were drawn from references [631, 240, 239, 515] as well as being work that appeared for the first time in this thesis.

While the basic Higgs-portal model of particle dark matter is compelling due to its simplicity, it is necessary to admit that the model as presented is losing explanitory power regarding the dark matter problem. While high mass regions are still viable and will remain safe from direct detection experiments for some time, the mass hierarchy of superheavy dark matter warrants some theroretical explanation. There are many extensions of the basic model, even simple ones, that may yet be viable, including embeddings of the model into highe theories, similar to Chapter 6, as well as extensions in the scalar sector, with additional Higgs-type bosons.

Chapter 6 was the exploration of a specifiic model of beyond SM particle physics that admitted several different models of particle dark matter. The model itself was a variant of the $U(1)'$ extended SM constructed from theoretical considerations, as outlined in Appendix C, and those theoretical considerations allowed the solution of the renormalization group equations which provided values for couplings and masses that could be used to make phenomenological calculations. Two of the possible particle dark matter models proved to be inconsistent with observed constraints on dark matter when the values obtained form the renormalization group equations were applied, but the third case remains viable. The final model is a Dirac fermion charged under the new gauge group that acts as vector-portal dark matter, communicating with the SM through the exchange of the mediator of the new gauge group. Collider constraints place limits on the properties of the mediator, and thermal abundance constraints for dark matter, combined with the theroretical constraints from the renormalization group equations restrict the parameter space down to a handful of points. This is one of the more interesting aspects of the model, that theoretical boundary conditions at extremely high energies can be used to constrain phenomenological models to such an extent. These possible parameter

sets are compared against dark matter direct and indirect detection exclusion limits, with the result that the lower mediator mass scenarios are inconsistent with observations, and that tensions exist between the observations and the predictions of the higher mediator mass scenarios. There is a signifiacant amount of work that could be done with this model in the future, both on the phenomenological side and on the theoretical side. For instance, the neutrino sector of the model could be examined in more detail, with alternate production mechanisms explored to avoid the constraint imposed by basic thermal production. Introduction of a Dirac mass term and activation of the seesaw effect would open more phenomenological doors, and allow an approach parallel to the one taken in Chapter 6. As well, the collider phenomenology of the model could be explored in greater depth, including the phenomenology at lepton colliders (important for Z' models in particular), and the expected signatures of the various possible dark matter sectors. Certain aspects of the theoretical side are already being explored [632, 633, 634], and there are many other interesting ideas waiting.

Also discussed briefly in Chapter 6 and in more depth in Appendix G is the low energy form of the interaction between the nucleon and a tritophilic (interacting with only the third SM generation) Z' boson. Appendix G is a summary of the work presented in reference [547], and the results of that reference are applied to the model of Chapter 6. The conclusions of reference [547] have implications that warrant further consideration. In particular, these results are important because they demonstrate that many of the standard beyond SM models that appear in the literature, those relying on 'phobias', couplings that are indentically, but arbitrarily, zero, are not consistent. Quantum mixing effects will generate a small but phenomenologically relevant interaction which is enough to impose bounds on many of these models, as is illustrated by the dilepton constraints on the model discussed in Chapter 6. There is work to be done in probing exactly where these models begin to fail, and what symmetries can be imposed to preserve these 'phobias'.

References

[1] CMS, S. Chatrchyan *et al.*, Phys. Lett. **B716**, 30 (2012), 1207.7235.

[2] ATLAS, G. Aad *et al.*, Phys. Lett. **B716**, 1 (2012), 1207.7214.

[3] M. E. Peskin and D. V. Schroeder, *An Introduction to quantum field theory* (Addison-Wesley, 1995).

[4] M. D. Schwartz, *Quantum Field Theory and the Standard Model* (Cambridge University Press, 2014).

[5] T. P. Cheng and L. F. Li, *Gauge theory of elementary particle physics* (Oxford Science Publications, 1984).

[6] L. H. Ryder, *Quantum field theory* (Cambridge University Press, 1996).

[7] B. De Wit and J. Smith, *Field Theory in Particle Physics Volume 1* (North-Holland, Amsterdam, Netherlands, 1986).

[8] Particle Data Group, C. Patrignani *et al.*, Chin. Phys. **C40**, 100001 (2016).

[9] I. Gel'fand, *Representations of the rotation and Lorentz groups and their applications* (Pergamon Press, 1963).

[10] R. Dick, *Advanced Quantum Mechanics* (Springer, 2012).

[11] J. C. Collins, *Renormalization*, Cambridge Monographs on Mathematical Physics Vol. 26 (Cambridge University Press, Cambridge, 1986).

[12] C. G. Callan, Jr., Phys. Rev. **D2**, 1541 (1970).

[13] K. Symanzik, Commun. Math. Phys. **18**, 227 (1970).

[14] K. Symanzik, Commun. Math. Phys. **23**, 49 (1971).

[15] S. Weinberg, *The quantum theory of fields. Vol. 2: Modern applications* (Cambridge University Press, 2013).

[16] J. Goldstone, Nuovo Cim. **19**, 154 (1961).

[17] J. Goldstone, A. Salam, and S. Weinberg, Phys. Rev. **127**, 965 (1962).

[18] M. Roos, (2010), 1001.0316.

[19] Y. Sofue, M. Honma, and T. Omodaka, Publ. Astron. Soc. Jap. **61**, 227 (2009), 0811.0859.

[20] V. C. Rubin and W. K. Ford, Jr., Astrophys. J. **159**, 379 (1970).

[21] V. Rubin, N. Thonnard, and W. Ford Jr, L107 **225** (1978).

[22] V. C. Rubin, N. Thonnard, and W. K. Ford, Jr., Astrophys. J. **238**, 471 (1980).

[23] H. Babcock, Lick Observatory Bull. **19**, 41 (1939).

[24] M. Persic and P. Salucci, Astrophys. J. Suppl. **99**, 501 (1995), astro-ph/9502091.

[25] R. Massey, T. Kitching, and J. Richard, Rept. Prog. Phys. **73**, 086901 (2010), 1001.1739.

[26] T. Treu, Ann. Rev. Astron. Astrophys. **48**, 87 (2010), 1003.5567.

[27] MACHO, C. Alcock *et al.*, Astrophys. J. **542**, 281 (2000), astro-ph/0001272.

[28] S. Weinberg, *Cosmology* (Oxford, UK: Oxford University Press, 2008).

[29] D. Clowe *et al.*, Astrophys. J. **648**, L109 (2006), astro-ph/0608407.

[30] R. Thompson, R. Davé, and K. Nagamine, Mon. Not. Roy. Astron. Soc. **452**, 3030 (2015), 1410.7438.

[31] D. Paraficz *et al.*, Astron. Astrophys. **594**, A121 (2016), 1209.0384.

[32] A. Robertson, R. Massey, and V. Eke, Mon. Not. Roy. Astron. Soc. **465**, 569 (2017), 1605.04307.

[33] C. Lage and G. R. Farrar, JCAP **1502**, 038 (2015), 1406.6703.

[34] F. Zwicky, Helv. Phys. Acta **6**, 110 (1933), [Gen. Rel. Grav.41,207(2009)].

[35] A. Kashlinsky, Phys. Rept. **307**, 67 (1998), astro-ph/9806236.

[36] N. A. Bahcall and X.-h. Fan, Astrophys. J. **504**, 1 (1998), astro-ph/9803277.

[37] D. Merritt, Astrophys. J. **313**, 121 (1987).

[38] R. G. Carlberg *et al.*, Astrophys. J. **516**, 552 (1999).

[39] M. G. Walker *et al.*, Astrophys. J. **704**, 1274 (2009), 0906.0341.

[40] J. Wolf *et al.*, Mon. Not. Roy. Astron. Soc. **406**, 1220 (2010), 0908.2995.

[41] Planck, P. A. R. Ade *et al.*, Astron. Astrophys. **594**, A13 (2016), 1502.01589.

[42] A. Mazumdar and J. Rocher, Phys. Rept. **497**, 85 (2011), 1001.0993.

[43] WMAP, G. Hinshaw *et al.*, Astrophys. J. Suppl. **170**, 288 (2007), astro-ph/0603451.

[44] N. W. Boggess *et al.*, Astrophys. J. **397**, 420 (1992).

[45] WMAP, G. Hinshaw *et al.*, Astrophys. J. Suppl. **208**, 19 (2013), 1212.5226.

[46] G. Efstathiou, J. R. Bond, and S. D. M. White, Mon. Not. Roy. Astron. Soc. **258**, 1 (1992).

[47] S. Contreras, I. Zehavi, C. M. Baugh, N. Padilla, and P. Norberg, Mon. Not. Roy. Astron. Soc. **465**, 2833 (2017), 1607.06154.

[48] A. D. Ludlow *et al.*, Mon. Not. Roy. Astron. Soc. **432**, 1103 (2013), 1302.0288.

[49] J. R. Ellis, J. S. Hagelin, D. V. Nanopoulos, K. A. Olive, and M. Srednicki, Nucl. Phys. **B238**, 453 (1984).

[50] S. Profumo and C. E. Yaguna, Phys. Rev. **D70**, 095004 (2004), hep-ph/0407036.

[51] J. R. Ellis, K. A. Olive, Y. Santoso, and V. C. Spanos, Phys. Rev. **D71**, 095007 (2005), hep-ph/0502001.

[52] J. R. Ellis, K. A. Olive, and C. Savage, Phys. Rev. **D77**, 065026 (2008), 0801.3656.

[53] U. Chattopadhyay, A. Corsetti, and P. Nath, Phys. Rev. **D68**, 035005 (2003), hep-ph/0303201.

[54] G. Jungman, M. Kamionkowski, and K. Griest, Phys. Rept. **267**, 195 (1996), hep-ph/9506380.

[55] J. Silk *et al.*, *Particle Dark Matter: Observations, Models and Searches* (Cambridge Univ. Press, Cambridge, 2010).

[56] CMS, A. M. Sirunyan *et al.*, (2017), 1710.09154.

[57] ATLAS, M. Aaboud *et al.*, (2017), 1711.01901.

[58] ATLAS, CMS, A. Ventura, Searches for supersymmetry, in *21st International Conference on Particles and Nuclei (PANIC 17) Beijing, China, September 1-5, 2017*, 2017, 1711.00152.

[59] H.-C. Cheng, J. L. Feng, and K. T. Matchev, Phys. Rev. Lett. **89**, 211301 (2002), hep-ph/0207125.

[60] A. Birkedal, A. Noble, M. Perelstein, and A. Spray, Phys. Rev. **D74**, 035002 (2006), hep-ph/0603077.

[61] M. Perelstein, Prog. Part. Nucl. Phys. **58**, 247 (2007), hep-ph/0512128.

[62] M. Schmaltz and D. Tucker-Smith, Ann. Rev. Nucl. Part. Sci. **55**, 229 (2005), hep-ph/0502182.

[63] N. Arkani-Hamed, A. G. Cohen, E. Katz, and A. E. Nelson, JHEP **07**, 034 (2002), hep-ph/0206021.

[64] Z. Chacko, H.-S. Goh, and R. Harnik, Phys. Rev. Lett. **96**, 231802 (2006), hep-ph/0506256.

[65] M. Farina, JCAP **1511**, 017 (2015), 1506.03520.

[66] L. Wang, J. M. Yang, and J. Zhu, Phys. Rev. **D88**, 075018 (2013), 1307.7780.

[67] J. E. Kim, Phys. Rept. **150**, 1 (1987).

[68] J. E. Kim and G. Carosi, Rev. Mod. Phys. **82**, 557 (2010), 0807.3125.

[69] L. D. Duffy and K. van Bibber, New J. Phys. **11**, 105008 (2009), 0904.3346.

[70] R. D. Peccei and H. R. Quinn, Phys. Rev. Lett. **38**, 1440 (1977).

[71] R. D. Peccei and H. R. Quinn, Phys. Rev. **D16**, 1791 (1977).

[72] M. S. Turner, Phys. Rev. Lett. **59**, 2489 (1987), [Erratum: Phys. Rev. Lett.60,1101(1988)].

[73] S. Chang and K. Choi, Phys. Lett. **B316**, 51 (1993), hep-ph/9306216.

[74] K. S. Jeong, M. Kawasaki, and F. Takahashi, JCAP **1402**, 046 (2014), 1310.1774.

[75] L. F. Abbott and P. Sikivie, Phys. Lett. **120B**, 133 (1983).

[76] J. Preskill, M. B. Wise, and F. Wilczek, Phys. Lett. **120B**, 127 (1983).

[77] M. Dine and W. Fischler, Phys. Lett. **120B**, 137 (1983).

[78] Super-Kamiokande, S. Fukuda *et al.*, Phys. Lett. **B539**, 179 (2002), hep-ex/0205075.

[79] S. Dodelson and L. M. Widrow, Phys. Rev. Lett. **72**, 17 (1994), hep-ph/9303287.

[80] K. Abazajian, G. M. Fuller, and M. Patel, Phys. Rev. **D64**, 023501 (2001), astro-ph/0101524.

[81] H. Ishida, K. S. Jeong, and F. Takahashi, Phys. Lett. **B731**, 242 (2014), 1309.3069.

[82] A. Boyarsky, D. Iakubovskyi, and O. Ruchayskiy, Phys. Dark Univ. **1**, 136 (2012), 1306.4954.

[83] H. Yuksel, J. F. Beacom, and C. R. Watson, Phys. Rev. Lett. **101**, 121301 (2008), 0706.4084.

[84] A. Kusenko, Phys. Rept. **481**, 1 (2009), 0906.2968.

[85] K. Abazajian and S. M. Koushiappas, Phys. Rev. **D74**, 023527 (2006), astro-ph/0605271.

[86] G. Belanger, A. Pukhov, and G. Servant, JCAP **0801**, 009 (2008), 0706.0526.

[87] A. Boyarsky, O. Ruchayskiy, and M. Shaposhnikov, Ann. Rev. Nucl. Part. Sci. **59**, 191 (2009), 0901.0011.

[88] E. Ma, Phys. Rev. **D73**, 077301 (2006), hep-ph/0601225.

[89] A. Kusenko, F. Takahashi, and T. T. Yanagida, Phys. Lett. **B693**, 144 (2010), 1006.1731.

[90] M. Drewes *et al.*, JCAP **1701**, 025 (2017), 1602.04816.

[91] M. Drewes, Int. J. Mod. Phys. **E22**, 1330019 (2013), 1303.6912.

[92] M. E. Anderson, E. Churazov, and J. N. Bregman, Mon. Not. Roy. Astron. Soc. **452**, 3905 (2015), 1408.4115.

[93] NEXT, J. Martín-Albo *et al.*, JHEP **05**, 159 (2016), 1511.09246.

[94] S. Dell'Oro, S. Marcocci, M. Viel, and F. Vissani, Adv. High Energy Phys. **2016**, 2162659 (2016), 1601.07512.

[95] O. Lantwin, PoS **EPS-HEP2017**, 304 (2017), 1710.03277.

[96] M. Milgrom, Astrophys. J. **270**, 365 (1983).

[97] M. Milgrom, Astrophys. J. **270**, 371 (1983).

[98] M. Milgrom, Astrophys. J. **270**, 384 (1983).

[99] K. G. Begeman, A. H. Broeils, and R. H. Sanders, Mon. Not. Roy. Astron. Soc. **249**, 523 (1991).

[100] R. B. Tully and J. R. Fisher, Astronom. Astrophys. **54**, 661 (1977).

[101] R. H. Sanders and S. S. McGaugh, Ann. Rev. Astron. Astrophys. **40**, 263 (2002), astro-ph/0204521.

[102] M. Milgrom, (2008), 0801.3133.

[103] J. D. Bekenstein, Phys. Rev. **D70**, 083509 (2004), astro-ph/0403694, [Erratum: Phys. Rev.D71,069901(2005)].

[104] J. D. Bekenstein, PoS **JHW2004**, 012 (2005), astro-ph/0412652.

[105] Y. Fujii and K. Maeda, *The scalar-tensor theory of gravitation* (Cambridge University Press, 2007).

[106] M.-C. Chiu, C.-M. Ko, and Y. Tian, Astrophys. J. **636**, 565 (2006), astro-ph/0507332.

[107] R. Takahashi and T. Chiba, Astrophys. J. **671**, 45 (2007), astro-ph/0701365.

[108] C. Skordis, Phys. Rev. **D74**, 103513 (2006), astro-ph/0511591.

[109] C. Skordis, D. F. Mota, P. G. Ferreira, and C. Boehm, Phys. Rev. Lett. **96**, 011301 (2006), astro-ph/0505519.

[110] E. W. Kolb and M. S. Turner, Front. Phys. **69**, 1 (1990).

[111] A. Maleknejad, M. M. Sheikh-Jabbari, and J. Soda, Phys. Rept. **528**, 161 (2013), 1212.2921.

[112] F. L. Bezrukov, A. Magnin, and M. Shaposhnikov, Phys. Lett. **B675**, 88 (2009), 0812.4950.

[113] A. H. Guth and S.-Y. Pi, Phys. Rev. **D32**, 1899 (1985).

[114] A. D. Linde, Phys. Lett. **116B**, 335 (1982).

[115] J. Bernstein, *KINETIC THEORY IN THE EXPANDING UNIVERSE* (Cambridge University Press, Cambridge, U.K., 1988).

[116] B. W. Lee and S. Weinberg, Phys. Rev. Lett. **39**, 165 (1977).

[117] M. Archidiacono, S. Hannestad, A. Mirizzi, G. Raffelt, and Y. Y. Y. Wong, JCAP **1310**, 020 (2013), 1307.0615.

[118] G. Steigman, B. Dasgupta, and J. F. Beacom, Phys. Rev. **D86**, 023506 (2012), 1204.3622.

[119] P. Gondolo and G. Gelmini, Nucl. Phys. **B360**, 145 (1991).

[120] P. Gondolo and J. Edsjo, Phys. Atom. Nucl. **61**, 1081 (1998), [Yad. Fiz.61,1181(1998)].

[121] A. Berlin, D. Hooper, and S. D. McDermott, Phys. Rev. **D89**, 115022 (2014), 1404.0022.

[122] H. Baer, K.-Y. Choi, J. E. Kim, and L. Roszkowski, Phys. Rept. **555**, 1 (2015), 1407.0017.

[123] L. J. Hall, K. Jedamzik, J. March-Russell, and S. M. West, JHEP **03**, 080 (2010), 0911.1120.

[124] C. E. Yaguna, JHEP **08**, 060 (2011), 1105.1654.

[125] A. K. Das, *Finite Temperature Field Theory* (World Scientific, New York, 1997).

[126] J. I. Kapusta and C. Gale, *Finite-temperature field theory: Principles and applications* (Cambridge University Press, 2011).

[127] T. Wizansky, Phys. Rev. **D74**, 065007 (2006), hep-ph/0605179.

[128] N. Baro, F. Boudjema, and A. Semenov, Phys. Lett. **B660**, 550 (2008), 0710.1821.

[129] M. Beneke, F. Dighera, and A. Hryczuk, JHEP **10**, 45 (2014), 1409.3049, [Erratum: JHEP07,106(2016)].

[130] J. D. Lewin and P. F. Smith, Astropart. Phys. **6**, 87 (1996).

[131] C. E. Yaguna, Phys. Rev. **D95**, 055015 (2017), 1610.08683.

[132] R. Bernabei *et al.*, Eur. Phys. J. **C23**, 61 (2002).

[133] M. Blennow, S. Clementz, and J. Herrero-Garcia, JCAP **1604**, 004 (2016), 1512.03317.

[134] G. Barello, S. Chang, and C. A. Newby, Phys. Rev. **D90**, 094027 (2014), 1409.0536.

[135] PandaX-II, X. Chen *et al.*, (2017), 1708.05825.

[136] XENON, E. Aprile *et al.*, (2017), 1704.05804.

[137] S. Scopel and K.-H. Yoon, JCAP **1602**, 050 (2016), 1512.00593.

[138] CDMS, S. Arrenberg, PoS **IDM2010**, 021 (2011).

[139] J. Kumar and D. Marfatia, Phys. Rev. **D88**, 014035 (2013), 1305.1611.

[140] V. Barger, W.-Y. Keung, and G. Shaughnessy, Phys. Rev. **D78**, 056007 (2008), 0806.1962.

[141] R. H. Helm, Phys. Rev. **104**, 1466 (1956).

[142] R. Bernabei *et al.*, Int. J. Mod. Phys. **A21**, 1445 (2006), astro-ph/0511262.

[143] R. Bernabei *et al.*, Phys. Rev. **D77**, 023506 (2008), 0712.0562.

[144] V. A. Dzuba, V. V. Flambaum, and M. Pospelov, Phys. Rev. **D81**, 103520 (2010), 1002.2979.

[145] B. M. Roberts, V. A. Dzuba, V. V. Flambaum, M. Pospelov, and Y. V. Stadnik, Phys. Rev. **D93**, 115037 (2016), 1604.04559.

[146] XENON, E. Aprile *et al.*, Phys. Rev. Lett. **118**, 101101 (2017), 1701.00769.

[147] A. M. Green, Mod. Phys. Lett. **A27**, 1230004 (2012), 1112.0524.

[148] J. I. Read, J. Phys. **G41**, 063101 (2014), 1404.1938.

[149] F. J. Kerr and D. Lynden-Bell, Mon. Not. Roy. Astron. Soc. **221**, 1023 (1986).

[150] M. C. Smith *et al.*, Mon. Not. Roy. Astron. Soc. **379**, 755 (2007), astro-ph/0611671.

[151] N. W. Evans, C. M. Carollo, and P. T. de Zeeuw, Mon. Not. Roy. Astron. Soc. **318**, 1131 (2000), astro-ph/0008156.

[152] M. Vogelsberger *et al.*, Mon. Not. Roy. Astron. Soc. **395**, 797 (2009), 0812.0362.

[153] D. N. Spergel, Phys. Rev. **D37**, 1353 (1988).

[154] P. Gondolo, Phys. Rev. **D66**, 103513 (2002), hep-ph/0209110.

[155] D. P. Snowden-Ifft, C. J. Martoff, and J. M. Burwell, Phys. Rev. **D61**, 101301 (2000), astro-ph/9904064.

[156] R. J. Gaitskell, Ann. Rev. Nucl. Part. Sci. **54**, 315 (2004).

[157] J. Liu, X. Chen, and X. Ji, Nature Phys. **13**, 212 (2017).

[158] T. Marrodán Undagoitia and L. Rauch, J. Phys. **G43**, 013001 (2016), 1509.08767.

[159] XENON, J. Angle *et al.*, Phys. Rev. Lett. **100**, 021303 (2008), 0706.0039.

[160] XENON100, E. Aprile *et al.*, Astropart. Phys. **35**, 573 (2012), 1107.2155.

[161] XENON, E. Aprile *et al.*, JCAP **1604**, 027 (2016), 1512.07501.

[162] LUX, D. S. Akerib *et al.*, Nucl. Instrum. Meth. **A704**, 111 (2013), 1211.3788.

[163] S. P. Ahlen *et al.*, Phys. Lett. **B195**, 603 (1987).

[164] MiniCLEAN, W. H. Lippincott *et al.*, Phys. Rev. **C86**, 015807 (2012), 1111.3260.

[165] A. Bolozdynya, Nucl. Instrum. Meth. A **422**, 314 (1999).

[166] P. Sorensen, JCAP **1009**, 033 (2010), 1007.3549.

[167] COUPP, E. Behnke *et al.*, Phys. Rev. **D86**, 052001 (2012), 1204.3094, [Erratum: Phys. Rev.D90,no.7,079902(2014)].

[168] PICO, C. Amole *et al.*, Phys. Rev. Lett. **118**, 251301 (2017), 1702.07666.

[169] S. Ahlen *et al.*, Int. J. Mod. Phys. **A25**, 1 (2010), 0911.0323.

[170] F. Mayet *et al.*, Phys. Rept. **627**, 1 (2016), 1602.03781.

[171] J. B. R. Battat *et al.*, Phys. Rept. **662**, 1 (2016), 1610.02396.

[172] E. Daw *et al.*, Astropart. Phys. **35**, 397 (2012), 1010.3027.

[173] J. Yoo *et al.*, JINST **10**, P04009 (2015), 1508.05897.

[174] DAMIC, J. Barreto *et al.*, Phys. Lett. **B711**, 264 (2012), 1105.5191.

[175] G. Gerbier *et al.*, (2014), 1401.7902.

[176] J. A. Formaggio and C. J. Martoff, Ann. Rev. Nucl. Part. Sci. **54**, 361 (2004).

[177] P. J. Fox, J. Liu, and N. Weiner, Phys. Rev. **D83**, 103514 (2011), 1011.1915.

[178] P. J. Fox, G. D. Kribs, and T. M. P. Tait, Phys. Rev. **D83**, 034007 (2011), 1011.1910.

[179] D. Mei and A. Hime, Phys. Rev. **D73**, 053004 (2006), astro-ph/0512125.

[180] SuperCDMS Soudan, R. Agnese *et al.*, Appl. Phys. Lett. **103**, 164105 (2013), 1305.2405.

[181] EDELWEISS Collaboration *et al.*, Phys. Lett. **B681**, 305 (2009), 0905.0753.

[182] CRESST, R. Strauss *et al.*, Eur. Phys. J. **C75**, 352 (2015), 1410.1753.

[183] J. J. Back and Y. A. Ramachers, Nucl. Instrum. Meth. **A586**, 286 (2008), 0709.3472.

[184] J. Amaré *et al.*, JCAP **1502**, 046 (2015), 1411.0106.

[185] DarkSide, P. Agnes *et al.*, Phys. Rev. **D93**, 081101 (2016), 1510.00702, [Addendum: Phys. Rev.D95,no.6,069901(2017)].

[186] PandaX, X. Cao *et al.*, Sci. China Phys. Mech. Astron. **57**, 1476 (2014), 1405.2882.

[187] DEAP-3600, P. A. Amaudruz *et al.*, (2017), 1707.08042.

[188] DARWIN, J. Aalbers *et al.*, JCAP **1611**, 017 (2016), 1606.07001.

[189] CRESST, G. Angloher *et al.*, Eur. Phys. J. **C76**, 25 (2016), 1509.01515.

[190] EURECA, G. Angloher *et al.*, Phys. Dark Univ. **3**, 41 (2014).

[191] SuperCDMS, R. Agnese *et al.*, Phys. Rev. Lett. **116**, 071301 (2016), 1509.02448.

[192] COUPP, E. Behnke *et al.*, Nucl. Phys. Proc. Suppl. **221**, 379 (2011).

[193] E. Behnke *et al.*, Astropart. Phys. **90**, 85 (2017), 1611.01499.

[194] DAMA, R. Bernabei *et al.*, Nucl. Instrum. Meth. **A592**, 297 (2008), 0804.2738.

[195] CoGeNT, C. E. Aalseth *et al.*, Phys. Rev. Lett. **106**, 131301 (2011), 1002.4703.

[196] UK Dark Matter, G. J. Alner *et al.*, Phys. Lett. **B616**, 17 (2005), hep-ex/0504031.

[197] CDEX, K.-J. Kang *et al.*, Front. Phys.(Beijing) **8**, 412 (2013), 1303.0601.

[198] SuperCDMS, R. Agnese *et al.*, Phys. Rev. Lett. **112**, 241302 (2014), 1402.7137.

[199] EDELWEISS, E. Armengaud *et al.*, JINST **12**, P08010 (2017), 1706.01070.

[200] CRESST, M. Bravin *et al.*, Astropart. Phys. **12**, 107 (1999), hep-ex/9904005.

[201] S. Cebrian *et al.*, Astropart. Phys. **15**, 79 (2001), astro-ph/0004292.

[202] Kims, H. S. Lee *et al.*, Phys. Lett. **B633**, 201 (2006), astro-ph/0509080.

[203] K. Abe *et al.*, Nucl. Instrum. Meth. **A716**, 78 (2013), 1301.2815.

[204] DarkSide, T. Alexander *et al.*, Astropart. Phys. **49**, 44 (2013), 1204.6218.

[205] MINICLEAN, K. Rielage *et al.*, Phys. Procedia **61**, 144 (2015), 1403.4842.

[206] ZEPLIN, T. J. Sumner, New Astron. Rev. **49**, 277 (2005).

[207] B. J. Mount *et al.*, (2017), 1703.09144.

[208] A. Zani, Adv. High Energy Phys. **2014**, 205107 (2014).

[209] A. Badertscher *et al.*, JINST **8**, C09005 (2013), 1309.3992.

[210] J. I. Collar *et al.*, New J. Phys. **2**, 14 (2000), astro-ph/0005059.

[211] PICO, C. Amole *et al.*, Phys. Rev. Lett. **114**, 231302 (2015), 1503.00008.

[212] Q. Riffard *et al.*, Dark Matter directional detection with MIMAC, in *Proceedings, 48th Rencontres de Moriond on Very High Energy Phenomena in the Universe: La Thuile, Italy, March 9-16, 2013*, pp. 227–230, 2013, 1306.4173.

[213] K. Nakamura *et al.*, J. Phys. Conf. Ser. **375**, 012013 (2012), 1109.3099.

[214] S. Ahlen *et al.*, Phys. Lett. **B695**, 124 (2011), 1006.2928.

[215] S. E. Vahsen *et al.*, EAS Publ. Ser. **53**, 43 (2012), 1110.3401.

[216] J. Conrad, Astropart. Phys. **62**, 165 (2015), 1407.6617.

[217] G. J. Feldman and R. D. Cousins, Phys. Rev. **D57**, 3873 (1998), physics/9711021.

[218] XENON100, E. Aprile *et al.*, Phys. Rev. **D94**, 122001 (2016), 1609.06154.

[219] LUX, D. S. Akerib *et al.*, Phys. Rev. Lett. **116**, 161302 (2016), 1602.03489.

[220] PandaX-II, C. Fu *et al.*, Phys. Rev. Lett. **118**, 071301 (2017), 1611.06553.

[221] CMS, A. M. Sirunyan *et al.*, JHEP **07**, 014 (2017), 1703.01651.

[222] ATLAS, M. Aaboud *et al.*, Phys. Rev. **D94**, 032005 (2016), 1604.07773.

[223] IceCube, M. G. Aartsen *et al.*, Phys. Rev. Lett. **110**, 131302 (2013), 1212.4097.

[224] DRIFT, J. B. R. Battat *et al.*, Astropart. Phys. **91**, 65 (2017), 1701.00171.

[225] PandaX-II, A. Tan *et al.*, Phys. Rev. Lett. **117**, 121303 (2016), 1607.07400.

[226] A. K. Drukier, K. Freese, and D. N. Spergel, Phys. Rev. **D33**, 3495 (1986).

[227] R. Bernabei *et al.*, Eur. Phys. J. **C73**, 2648 (2013), 1308.5109.

[228] M. Fairbairn and T. Schwetz, JCAP **0901**, 037 (2009), 0808.0704.

[229] J. H. Davis, Int. J. Mod. Phys. **A30**, 1530038 (2015), 1506.03924.

[230] R. W. Schnee, Introduction to dark matter experiments, in *In Physics of the Large and Small: Proceedings of the 2009 Theoretical Advanced Study Institute in Elementary Particle Physics, 629-681 (World Scientific, Singapore) Ed. Csaba Csaki and Scott Dodelson (2010)*, 2011, 1101.5205.

[231] J. Monroe and P. Fisher, Phys. Rev. **D76**, 033007 (2007), 0706.3019.

[232] L. E. Strigari, New J. Phys. **11**, 105011 (2009), 0903.3630.

[233] J. Billard, L. Strigari, and E. Figueroa-Feliciano, Phys. Rev. **D89**, 023524 (2014), 1307.5458.

[234] D. G. Cerdeño *et al.*, JHEP **05**, 118 (2016), 1604.01025, [Erratum: JHEP09,048(2016)].

[235] P. Grothaus, M. Fairbairn, and J. Monroe, Phys. Rev. **D90**, 055018 (2014), 1406.5047.

[236] J. H. Davis, JCAP **1503**, 012 (2015), 1412.1475.

[237] C. A. J. O'Hare, A. M. Green, J. Billard, E. Figueroa-Feliciano, and L. E. Strigari, Phys. Rev. **D92**, 063518 (2015), 1505.08061.

[238] J. B. Dent, B. Dutta, J. L. Newstead, and L. E. Strigari, Phys. Rev. **D93**, 075018 (2016), 1602.05300.

[239] R. Dick and F. S. Sage, Eur. Phys. J. **C72**, 2090 (2012).

[240] F. S. Sage and R. Dick, Astropart. Phys. **71**, 31 (2015).

[241] J. M. Cline, K. Kainulainen, P. Scott, and C. Weniger, Phys. Rev. **D88**, 055025 (2013), 1306.4710, [Erratum: Phys. Rev.D92,no.3,039906(2015)].

[242] M. A. Shifman, A. I. Vainshtein, and V. I. Zakharov, Phys. Lett. **B78**, 443 (1978).

[243] T. P. Cheng, Phys. Rev. **D38**, 2869 (1988).

[244] J. M. Alarcon, L. S. Geng, J. Martin Camalich, and J. A. Oller, Phys. Lett. **B730**, 342 (2014), 1209.2870.

[245] N. F. Nasrallah and K. Schilcher, Phys. Rev. **C89**, 045202 (2014), 1310.6114, [Addendum: Phys. Rev.C89,no.5,059904(2014)].

[246] C. Alexandrou *et al.*, Phys. Rev. **D91**, 094503 (2015), 1309.7768.

[247] XQCD, M. Gong *et al.*, Phys. Rev. **D88**, 014503 (2013), 1304.1194.

[248] P. Junnarkar and A. Walker-Loud, Phys. Rev. **D87**, 114510 (2013), 1301.1114.

[249] R. Babich *et al.*, Phys. Rev. **D85**, 054510 (2012), 1012.0562.

[250] QCDSF, G. S. Bali *et al.*, Phys. Rev. **D85**, 054502 (2012), 1111.1600.

[251] J. Stahov, H. Clement, and G. J. Wagner, Phys. Lett. **B726**, 685 (2013), 1211.1148.

[252] L. Alvarez-Ruso, T. Ledwig, J. Martin Camalich, and M. J. Vicente-Vacas, Phys. Rev. **D88**, 054507 (2013), 1304.0483.

[253] H.-Y. Cheng and C.-W. Chiang, JHEP **07**, 009 (2012), 1202.1292.

[254] ETM, A. Abdel-Rehim *et al.*, Phys. Rev. Lett. **116**, 252001 (2016), 1601.01624.

[255] DEAP, P. A. Amaudruz *et al.*, Nucl. Part. Phys. Proc. **273-275**, 340 (2016), 1410.7673.

[256] T. G. Steele, Z.-W. Wang, D. Contreras, and R. B. Mann, Phys. Rev. Lett. **112**, 171602 (2014), 1310.1960.

[257] L. Bian, T. Li, J. Shu, and X.-C. Wang, JHEP **03**, 126 (2015), 1412.5443.

[258] L. Bergström, P. Ullio, and J. H. Buckley, Astropart. Phys. **9**, 137 (1998).

[259] M. Cirelli *et al.*, JCAP **1103**, 051 (2011), 1012.4515, [Erratum: JCAP1210,E01(2012)].

[260] R. Dick, R. B. Mann, and K. E. Wunderle, Nucl. Phys. **B805**, 207 (2008), 0803.1444.

[261] T. Sjöstrand *et al.*, Comput. Phys. Commun. **191**, 159 (2015), 1410.3012.

[262] P. Ciafaloni *et al.*, JCAP **1103**, 019 (2011), 1009.0224.

[263] S. Profumo and P. Ullio, (2010), 1001.4086.

[264] M. Fornasa *et al.*, Mon. Not. Roy. Astron. Soc. **429**, 1529 (2013), 1207.0502.

[265] G. Bertone, M. Cirelli, A. Strumia, and M. Taoso, JCAP **0903**, 009 (2009), 0811.3744.

[266] J. Buch, M. Cirelli, G. Giesen, and M. Taoso, JCAP **1509**, 037 (2015), 1505.01049.

[267] A. E. Vladimirov *et al.*, Comput. Phys. Commun. **182**, 1156 (2011), 1008.3642.

[268] I. V. Moskalenko, Nuovo Cim. **C034N3**, 149 (2011), 1105.4921.

[269] Fermi-LAT, W. B. Atwood *et al.*, Astrophys. J. **697**, 1071 (2009), 0902.1089.

[270] T. C. Weekes *et al.*, Astropart. Phys. **17**, 221 (2002), astro-ph/0108478.

[271] MAGIC, E. Lorenz, New Astron. Rev. **48**, 339 (2004).

[272] H.E.S.S., J. A. Hinton, New Astron. Rev. **48**, 331 (2004), astro-ph/0403052.

[273] C. E. Fichtel, G. A. Simpson, and D. J. Thompson, Astrophys. J. **222**, 833 (1978).

[274] EGRET, P. Sreekumar *et al.*, Astrophys. J. **494**, 523 (1998), astro-ph/9709257.

[275] F. W. Stecker and M. H. Salamon, Astrophys. J. **464**, 600 (1996), astro-ph/9601120.

[276] R. Mukherjee and J. Chiang, Astropart. Phys. **11**, 213 (1999), astro-ph/9902003.

[277] C. D. Dermer, Astrophys. J. **659**, 958 (2007), astro-ph/0605402.

[278] Fermi-LAT, Astrophys. J. **743**, 171 (2011), 1108.1420.

[279] V. Pavlidou and B. D. Fields, Astrophys. J. **575**, L5 (2002), astro-ph/0207253.

[280] R. Makiya, T. Totani, and M. A. R. Kobayashi, Astrophys. J. **728**, 158 (2011), 1005.1390.

[281] U. Keshet, E. Waxman, A. Loeb, V. Springel, and L. Hernquist, Astrophys. J. **585**, 128 (2003), astro-ph/0202318.

[282] C. A. Faucher-Giguere and A. Loeb, JCAP **1001**, 005 (2010), 0904.3102.

[283] D. Malyshev, I. Cholis, and J. D. Gelfand, Astrophys. J. **722**, 1939 (2010), 1002.0587.

[284] M. Ahlers and J. Salvado, Phys. Rev. **D84**, 085019 (2011), 1105.5113.

[285] G. B. Gelmini, O. Kalashev, and D. V. Semikoz, JCAP **1201**, 044 (2012), 1107.1672.

[286] J. M. Siegal-Gaskins, R. Reesman, V. Pavlidou, S. Profumo, and T. P. Walker, Mon. Not. Roy. Astron. Soc. **415**, 1074 (2011), 1011.5501.

[287] F. Calore, M. Di Mauro, F. Donato, and F. Donato, Astrophys. J. **796**, 1 (2014), 1406.2706.

[288] P. Ullio, L. Bergstrom, J. Edsjo, and C. G. Lacey, Phys. Rev. **D66**, 123502 (2002), astro-ph/0207125.

[289] H.E.S.S., A. Abramowski *et al.*, Phys. Rev. **D90**, 122007 (2014), 1411.7568.

[290] Fermi-LAT, M. Ackermann *et al.*, Astrophys. J. **799**, 86 (2015), 1410.3696.

[291] B. Zhou *et al.*, Phys. Rev. **D91**, 123010 (2015), 1406.6948.

[292] Fermi-LAT, M. Ackermann *et al.*, JCAP **1509**, 008 (2015), 1501.05464.

[293] S. Ando and E. Komatsu, Phys. Rev. **D87**, 123539 (2013), 1301.5901.

[294] Fermi-LAT, M. Ackermann *et al.*, Phys. Rev. **D85**, 083007 (2012), 1202.2856.

[295] V. Springel *et al.*, Mon. Not. Roy. Astron. Soc. **391**, 1685 (2008), 0809.0898.

[296] S. Ando, Phys. Rev. **D80**, 023520 (2009), 0903.4685.

[297] V. Springel *et al.*, (2008), 0809.0894.

[298] L. Goodenough and D. Hooper, (2009), 0910.2998.

[299] D. Hooper and L. Goodenough, Phys. Lett. **B697**, 412 (2011), 1010.2752.

[300] T. Daylan *et al.*, Phys. Dark Univ. **12**, 1 (2016), 1402.6703.

[301] F. Calore, I. Cholis, C. McCabe, and C. Weniger, Phys. Rev. **D91**, 063003 (2015), 1411.4647.

[302] P. Agrawal, B. Batell, P. J. Fox, and R. Harnik, JCAP **1505**, 011 (2015), 1411.2592.

[303] F. Calore, I. Cholis, and C. Weniger, JCAP **1503**, 038 (2015), 1409.0042.

[304] Fermi-LAT, M. Ajello *et al.*, Astrophys. J. **819**, 44 (2016), 1511.02938.

[305] K. N. Abazajian, JCAP **1103**, 010 (2011), 1011.4275.

[306] C. Gordon and O. Macias, Phys. Rev. **D88**, 083521 (2013), 1306.5725, [Erratum: Phys. Rev.D89,no.4,049901(2014)].

[307] R. Bartels, S. Krishnamurthy, and C. Weniger, Phys. Rev. Lett. **116**, 051102 (2016), 1506.05104.

[308] S. K. Lee, M. Lisanti, B. R. Safdi, T. R. Slatyer, and W. Xue, Phys. Rev. Lett. **116**, 051103 (2016), 1506.05124.

[309] E. Carlson and S. Profumo, Phys. Rev. **D90**, 023015 (2014), 1405.7685.

[310] J. Petrović, P. D. Serpico, and G. Zaharijaš, JCAP **1410**, 052 (2014), 1405.7928.

[311] E. Carlson, T. Linden, and S. Profumo, Phys. Rev. **D94**, 063504 (2016), 1603.06584.

[312] D. Hooper and T. Linden, Phys. Rev. **D84**, 123005 (2011), 1110.0006.

[313] K. N. Abazajian and M. Kaplinghat, Phys. Rev. **D86**, 083511 (2012), 1207.6047, [Erratum: Phys. Rev.D87,129902(2013)].

[314] A. Cuoco, B. Eiteneuer, J. Heisig, and M. Krämer, JCAP **1606**, 050 (2016), 1603.08228.

[315] M. H. Chan and C. H. Leung, Sci. Rep. **7**, 14895 (2017), 1710.08123.

[316] Fermi-LAT, M. Ackermann *et al.*, Phys. Rev. Lett. **115**, 231301 (2015), 1503.02641.

[317] K. N. Abazajian and R. E. Keeley, Phys. Rev. **D93**, 083514 (2016), 1510.06424.

[318] J. Choquette, J. M. Cline, and J. M. Cornell, Phys. Rev. **D94**, 015018 (2016), 1604.01039.

[319] K. N. Abazajian, N. Canac, S. Horiuchi, and M. Kaplinghat, Phys. Rev. **D90**, 023526 (2014), 1402.4090.

[320] F. Yusef-Zadeh *et al.*, Astrophys. J. **762**, 33 (2013), 1206.6882.

[321] S. Mashchenko, A. Sills, and H. M. P. Couchman, Astrophys. J. **640**, 252 (2006), astro-ph/0511567.

[322] M. Mateo, Ann. Rev. Astron. Astrophys. **36**, 435 (1998), astro-ph/9810070.

[323] J. Grcevich and M. E. Putman, Astrophys. J. **696**, 385 (2009), 0901.4975, [Erratum: Astrophys. J.721,922(2010)].

[324] L. E. Strigari *et al.*, Astrophys. J. **678**, 614 (2008), 0709.1510.

[325] Fermi-LAT, M. Ackermann *et al.*, Phys. Rev. **D89**, 042001 (2014), 1310.0828.

[326] A. Geringer-Sameth *et al.*, Phys. Rev. Lett. **115**, 081101 (2015), 1503.02320.

[327] DES, Fermi-LAT, A. Albert *et al.*, Astrophys. J. **834**, 110 (2017), 1611.03184.

[328] Y. Zhao, X.-J. Bi, P.-F. Yin, and X.-M. Zhang, Chin. Phys. **C42**, 025102 (2018), 1702.05266.

[329] H.E.S.S., A. Abramowski *et al.*, Phys. Rev. Lett. **110**, 041301 (2013), 1301.1173.

[330] M. Duerr, P. Fileviez Pérez, and J. Smirnov, JHEP **06**, 152 (2016), 1509.04282.

[331] Fermi-LAT, M. Ackermann *et al.*, Phys. Rev. **D91**, 122002 (2015), 1506.00013.

[332] C. Weniger, JCAP **1208**, 007 (2012), 1204.2797.

[333] E. Tempel, A. Hektor, and M. Raidal, JCAP **1209**, 032 (2012), 1205.1045, [Addendum: JCAP1211,A01(2012)].

[334] M. Su and D. P. Finkbeiner, (2012), 1206.1616.

[335] Fermi-LAT, M. Ackermann *et al.*, Phys. Rev. **D88**, 082002 (2013), 1305.5597.

[336] S. Profumo, F. S. Queiroz, and C. E. Yaguna, Mon. Not. Roy. Astron. Soc. **461**, 3976 (2016), 1602.08501.

[337] J. E. Gunn, B. W. Lee, I. Lerche, D. N. Schramm, and G. Steigman, Astrophys. J. **223**, 1015 (1978).

[338] J. Silk and M. Srednicki, Phys. Rev. Lett. **53**, 624 (1984).

[339] HEAT, S. W. Barwick *et al.*, Phys. Rev. Lett. **75**, 390 (1995), astro-ph/9505141.

[340] T. Delahaye, R. Lineros, F. Donato, N. Fornengo, and P. Salati, Phys. Rev. **D77**, 063527 (2008), 0712.2312.

[341] A. Goudelis, Y. Mambrini, and C. Yaguna, JCAP **0912**, 008 (2009), 0909.2799.

[342] L. Bergstrom, T. Bringmann, and J. Edsjo, Phys. Rev. **D78**, 103520 (2008), 0808.3725.

[343] P. Picozza *et al.*, Astropart. Phys. **27**, 296 (2007), astro-ph/0608697.

[344] AMS, M. Aguilar *et al.*, Phys. Rev. Lett. **110**, 141102 (2013).

[345] GAPS, R. A. Ong *et al.*, The GAPS Experiment to Search for Dark Matter using Low-energy Antimatter, in *Proceedings, 35th International Cosmic Ray Conference (ICRC 2017): Bexco, Busan, Korea, July 12-20, 2017*, 2017, 1710.00452.

[346] Y. Cui, J. D. Mason, and L. Randall, JHEP **11**, 017 (2010), 1006.0983.

[347] A. W. Strong, I. V. Moskalenko, and V. S. Ptuskin, Ann. Rev. Nucl. Part. Sci. **57**, 285 (2007), astro-ph/0701517.

[348] V. S. Berezinsky, S. V. Bulanov, V. A. Dogiel, and V. S. Ptuskin, *Astrophysics of cosmic rays* (Amsterdam, Netherlands: North-Holland 534 p, 1990).

[349] J. Lavalle, AIP Conf. Proc. **1241**, 398 (2010), 0911.5102.

[350] A. Cuoco, J. Heisig, M. Korsmeier, and M. Krämer, (2017), 1704.08258.

[351] M. Korsmeier, F. Donato, and N. Fornengo, Phys. Rev. **D97**, 103011 (2018), 1711.08465.

[352] A. Coogan and S. Profumo, Phys. Rev. **D96**, 083020 (2017), 1705.09664.

[353] M.-Y. Cui, X. Pan, Q. Yuan, Y.-Z. Fan, and H.-S. Zong, JCAP **1806**, 024 (2018), 1803.02163.

[354] L. Bergstrom, J. Edsjo, and P. Gondolo, Phys. Rev. **D58**, 103519 (1998), hep-ph/9806293.

[355] R. Kappl and M. W. Winkler, Nucl. Phys. **B850**, 505 (2011), 1104.0679.

[356] V. D. Barger, K. Whisnant, S. Pakvasa, and R. J. N. Phillips, Phys. Rev. **D22**, 2718 (1980).

[357] L. Wolfenstein, Phys. Rev. **D17**, 2369 (1978).

[358] AMANDA, J. Ahrens *et al.*, Phys. Rev. **D66**, 032006 (2002), astro-ph/0202370.

[359] IceCube, R. Abbasi *et al.*, Phys. Rev. **D84**, 022004 (2011), 1101.3349.

[360] H. Yuksel, S. Horiuchi, J. F. Beacom, and S. Ando, Phys. Rev. **D76**, 123506 (2007), 0707.0196.

[361] IceCube, R. Abbasi *et al.*, (2012), 1210.3557.

[362] IceCube, M. G. Aartsen *et al.*, Phys. Rev. **D88**, 122001 (2013), 1307.3473.

[363] M. Wurm *et al.*, (2010), 1004.0831, [Astron. Nachr.331,512(2010)].

[364] J. Edsjo, J. Elevant, R. Enberg, and C. Niblaeus, JCAP **1706**, 033 (2017), 1704.02892.

[365] P. Baratella *et al.*, JCAP **1403**, 053 (2014), 1312.6408.

[366] S. M. Bilenky, C. Giunti, and W. Grimus, Prog. Part. Nucl. Phys. **43**, 1 (1999), hep-ph/9812360.

[367] IceCube, A. Achterberg *et al.*, Astropart. Phys. **26**, 155 (2006), astro-ph/0604450.

[368] IceCube, M. Ackermann *et al.*, Astrophys. J. **675**, 1014 (2008), 0711.3022.

[369] Super-Kamiokande, J. Hosaka *et al.*, Phys. Rev. **D73**, 112001 (2006), hep-ex/0508053.

[370] Super-Kamiokande, Y. Fukuda *et al.*, Phys. Rev. Lett. **81**, 1158 (1998), hep-ex/9805021, [Erratum: Phys. Rev. Lett.81,4279(1998)].

[371] Super-Kamiokande, K. Choi *et al.*, Phys. Rev. Lett. **114**, 141301 (2015), 1503.04858.

[372] C. E. Yaguna, JCAP **0903**, 003 (2009), 0810.4267.

[373] W.-L. Guo and Y.-L. Wu, Nucl. Phys. **B867**, 149 (2013), 1103.5606.

[374] VERITAS, V. A. Acciari *et al.*, Astrophys. J. **720**, 1174 (2010), 1006.5955.

[375] VERITAS, B. Zitzer, PoS **ICRC2015**, 1225 (2016), 1509.01105.

[376] VERITAS, E. Aliu *et al.*, Phys. Rev. **D85**, 062001 (2012), 1202.2144, [Erratum: Phys. Rev.D91,no.12,129903(2015)].

[377] J. Aleksić *et al.*, JCAP **1402**, 008 (2014), 1312.1535.

[378] Fermi-LAT, MAGIC, M. L. Ahnen *et al.*, JCAP **1602**, 039 (2016), 1601.06590.

[379] G. D. Martinez, J. S. Bullock, M. Kaplinghat, L. E. Strigari, and R. Trotta, JCAP **0906**, 014 (2009), 0902.4715.

[380] J. D. Simon *et al.*, Astrophys. J. **733**, 46 (2011), 1007.4198.

[381] VERITAS, P. Cogan, **3**, 1385 (2007), 0709.4233.

[382] L. E. Strigari, Phys. Rept. **531**, 1 (2013), 1211.7090.

[383] G. D. Martinez, Mon. Not. Roy. Astron. Soc. **451**, 2524 (2015), 1309.2641.

[384] G. Battaglia, A. Helmi, and M. Breddels, New Astron. Rev. **57**, 52 (2013), 1305.5965.

[385] Fermi-LAT, M. Ackermann *et al.*, Phys. Rev. **D86**, 022002 (2012), 1205.2739.

[386] M. Duerr, P. Fileviez Perez, and J. Smirnov, Phys. Lett. **B751**, 119 (2015), 1508.04418.

[387] A. Birkedal, K. T. Matchev, M. Perelstein, and A. Spray, (2005), hep-ph/0507194.

[388] J. F. Beacom, N. F. Bell, and G. Bertone, Phys. Rev. Lett. **94**, 171301 (2005), astro-ph/0409403.

[389] F. Nesti and P. Salucci, JCAP **1307**, 016 (2013), 1304.5127.

[390] M. Duerr, P. Fileviez Pérez, and J. Smirnov, JHEP **06**, 008 (2016), 1510.07562.

[391] P. Ko, W.-I. Park, and Y. Tang, JCAP **1409**, 013 (2014), 1404.5257.

[392] D. G. Cerdeno, M. Fornasa, A. M. Green, and M. Peiro, Phys. Rev. **D94**, 043516 (2016), 1605.05185.

[393] LUX, D. S. Akerib *et al.*, Phys. Rev. Lett. **112**, 091303 (2014), 1310.8214.

[394] LUX, D. S. Akerib *et al.*, Phys. Rev. Lett. **118**, 021303 (2017), 1608.07648.

[395] V. D. Barger and R. J. N. Phillips, *Collider physics* (, 1987).

[396] R. K. Ellis, W. J. Stirling, and B. R. Webber, Camb. Monogr. Part. Phys. Nucl. Phys. Cosmol. **8**, 1 (1996).

[397] L. Linssen, A. Miyamoto, M. Stanitzki, and H. Weerts, (2012), 1202.5940.

[398] C.-S. S. Group, (2015).

[399] M. Mangano, (2017), 1710.06353.

[400] T. Behnke *et al.*, (2013), 1306.6327.

[401] H. Baer *et al.*, (2013), 1306.6352.

[402] D. Brandt, H. Burkhardt, M. Lamont, S. Myers, and J. Wenninger, Rept. Prog. Phys. **63**, 939 (2000).

[403] L. Evans and P. Bryant, JINST **3**, S08001 (2008).

[404] S. Holmes, R. S. Moore, and V. Shiltsev, JINST **6**, T08001 (2011), 1106.0909.

[405] H. Abramowicz and A. Caldwell, Rev. Mod. Phys. **71**, 1275 (1999), hep-ex/9903037.

[406] V. D. Barger, M. S. Berger, J. F. Gunion, and T. Han, Phys. Rev. Lett. **75**, 1462 (1995), hep-ph/9504330.

[407] C. M. Ankenbrandt *et al.*, Phys. Rev. ST Accel. Beams **2**, 081001 (1999), physics/9901022.

[408] I. F. Ginzburg, M. Krawczyk, and P. Osland, Nucl. Instrum. Meth. **A472**, 149 (2001), hep-ph/0101229.

[409] D. M. Asner, J. B. Gronberg, and J. F. Gunion, Phys. Rev. **D67**, 035009 (2003), hep-ph/0110320.

[410] J. F. Gunion and H. E. Haber, Phys. Rev. **D48**, 5109 (1993).

[411] R. P. Feynman, Phys. Rev. Lett. **23**, 1415 (1969).

[412] J. Collins, *Foundations of perturbative QCD* (Cambridge University Press, 2013).

[413] D. R. Green, Camb. Monogr. Part. Phys. Nucl. Phys. Cosmol. **22**, 1 (2005).

[414] J. D. Bjorken and E. A. Paschos, Phys. Rev. **185**, 1975 (1969).

[415] J. D. Bjorken, Phys. Rev. **179**, 1547 (1969).

[416] M. Spira, A. Djouadi, D. Graudenz, and P. M. Zerwas, Nucl. Phys. **B453**, 17 (1995), hep-ph/9504378.

[417] G. Altarelli, Phys. Rept. **81**, 1 (1982).

[418] A. D. Martin, W. J. Stirling, R. S. Thorne, and G. Watt, Eur. Phys. J. **C63**, 189 (2009), 0901.0002.

[419] S. Alekhin, J. Blumlein, and S. Moch, Phys. Rev. **D89**, 054028 (2014), 1310.3059.

[420] S. Dulat *et al.*, Phys. Rev. **D93**, 033006 (2016), 1506.07443.

[421] LHC Higgs Cross Section Working Group, S. Dittmaier *et al.*, (2011), 1101.0593.

[422] T. Han, G. Valencia, and S. Willenbrock, Phys. Rev. Lett. **69**, 3274 (1992), hep-ph/9206246.

[423] J. F. Gunion, H. E. Haber, G. L. Kane, and S. Dawson, Front. Phys. **80**, 1 (2000).

[424] G. L. Kane, W. W. Repko, and W. B. Rolnick, Phys. Lett. **148B**, 367 (1984).

[425] ZEUS, S. Chekanov *et al.*, Eur. Phys. J. **C21**, 443 (2001), hep-ex/0105090.

[426] E. L. Berger, M. M. Block, and C.-I. Tan, Phys. Rev. Lett. **98**, 242001 (2007), hep-ph/0703003.

[427] C. G. Callan, Jr. and D. J. Gross, Phys. Rev. Lett. **22**, 156 (1969).

[428] S. Forte and L. Magnea, Phys. Lett. **B448**, 295 (1999), hep-ph/9812479.

[429] D. Berdine, N. Kauer, and D. Rainwater, Phys. Rev. Lett. **99**, 111601 (2007), hep-ph/0703058.

[430] E. Fuchs, S. Thewes, and G. Weiglein, Eur. Phys. J. **C75**, 254 (2015), 1411.4652.

[431] C. F. Uhlemann and N. Kauer, Nucl. Phys. **B814**, 195 (2009), 0807.4112.

[432] M. Pospelov, A. Ritz, and M. B. Voloshin, Phys. Lett. **B662**, 53 (2008), 0711.4866.

[433] B. Patt and F. Wilczek, (2006), hep-ph/0605188.

[434] V. González-Macías, J. I. Illana, and J. Wudka, JHEP **05**, 171 (2016), 1601.05051.

[435] A. Falkowski, J. Juknevich, and J. Shelton, (2009), 0908.1790.

[436] P. Ko and Y. Tang, Phys. Lett. **B751**, 81 (2015), 1508.02500.

[437] N. F. Bell, G. Busoni, and I. W. Sanderson, JCAP **1703**, 015 (2017), 1612.03475.

[438] ATLAS, M. Aaboud *et al.*, Phys. Lett. **B775**, 105 (2017), 1707.04147.

[439] ATLAS, M. Aaboud *et al.*, JHEP **09**, 001 (2016), 1606.03833.

[440] CMS, V. Khachatryan *et al.*, Phys. Rev. Lett. **117**, 051802 (2016), 1606.04093.

[441] A. Strumia, Interpreting the 750 GeV digamma excess: a review, in *Proceedings, 51st Rencontres de Moriond on Electroweak Interactions and Unified Theories: La Thuile, Italy, March 12-19, 2016*, pp. 407–426, ARISF, ARISF, 2016, 1605.09401.

[442] CMS, CMS-PAS-EXO-16-027 (2016).

[443] ATLAS, ATLAS-CONF-2016-059 (2016).

[444] J. L. Hewett, T. G. Rizzo, and J. A. Robinson, Phys. Rev. **D34**, 2179 (1986), [Phys. Rev.D33,1476(1986)].

[445] D. London and J. L. Rosner, Phys. Rev. **D34**, 1530 (1986).

[446] D. Hooper, Phys. Rev. **D91**, 035025 (2015), 1411.4079.

[447] J. Brehmer, J. Hewett, J. Kopp, T. Rizzo, and J. Tattersall, JHEP **10**, 182 (2015), 1507.00013.

[448] P. Langacker, Rev. Mod. Phys. **81**, 1199 (2009), 0801.1345.

[449] ATLAS, M. Aaboud *et al.*, Phys. Rev. **D96**, 052004 (2017), 1703.09127.

[450] ATLAS, M. Aaboud *et al.*, JHEP **10**, 182 (2017), 1707.02424.

[451] M. Chala, F. Kahlhoefer, M. McCullough, G. Nardini, and K. Schmidt-Hoberg, JHEP **07**, 089 (2015), 1503.05916.

[452] O. Buchmueller, C. Doglioni, and L. T. Wang, Nature Phys. **13**, 217 (2017).

[453] F. Kahlhoefer, Int. J. Mod. Phys. **A32**, 1730006 (2017), 1702.02430.

[454] M. E. Peskin, Supersymmetry in Elementary Particle Physics, in *Proceedings of Theoretical Advanced Study Institute in Elementary Particle Physics : Exploring New Frontiers Using Colliders and Neutrinos (TASI 2006): Boulder, Colorado, June 4-30, 2006*, pp. 609–704, 2008, 0801.1928.

[455] P. J. Fox and C. Williams, Phys. Rev. **D87**, 054030 (2013), 1211.6390.

[456] A. Rajaraman, W. Shepherd, T. M. P. Tait, and A. M. Wijangco, Phys. Rev. **D84**, 095013 (2011), 1108.1196.

[457] P. J. Fox, R. Harnik, J. Kopp, and Y. Tsai, Phys. Rev. **D84**, 014028 (2011), 1103.0240.

[458] P. J. Fox, R. Harnik, J. Kopp, and Y. Tsai, Phys. Rev. **D85**, 056011 (2012), 1109.4398.

[459] J. Goodman *et al.*, Phys. Lett. **B695**, 185 (2011), 1005.1286.

[460] Y. Bai, P. J. Fox, and R. Harnik, JHEP **12**, 048 (2010), 1005.3797.

[461] J. Goodman *et al.*, Phys. Rev. **D82**, 116010 (2010), 1008.1783.

[462] P. J. Fox, R. Harnik, R. Primulando, and C.-T. Yu, Phys. Rev. **D86**, 015010 (2012), 1203.1662.

[463] G. Busoni, A. De Simone, E. Morgante, and A. Riotto, Phys. Lett. **B728**, 412 (2014), 1307.2253.

[464] G. Busoni, A. De Simone, J. Gramling, E. Morgante, and A. Riotto, JCAP **1406**, 060 (2014), 1402.1275.

[465] G. Busoni, A. De Simone, T. Jacques, E. Morgante, and A. Riotto, JCAP **1409**, 022 (2014), 1405.3101.

[466] M. Endo and Y. Yamamoto, JHEP **06**, 126 (2014), 1403.6610.

[467] I. M. Shoemaker and L. Vecchi, Phys. Rev. **D86**, 015023 (2012), 1112.5457.

[468] J. Abdallah *et al.*, (2014), 1409.2893.

[469] O. Buchmueller, M. J. Dolan, and C. McCabe, JHEP **01**, 025 (2014), 1308.6799.

[470] J. Abdallah *et al.*, Phys. Dark Univ. **9-10**, 8 (2015), 1506.03116.

[471] O. Buchmueller, M. J. Dolan, S. A. Malik, and C. McCabe, JHEP **01**, 037 (2015), 1407.8257.

[472] M. R. Buckley, D. Feld, and D. Goncalves, Phys. Rev. **D91**, 015017 (2015), 1410.6497.

[473] P. Harris, V. V. Khoze, M. Spannowsky, and C. Williams, Phys. Rev. **D91**, 055009 (2015), 1411.0535.

[474] P. Harris, V. V. Khoze, M. Spannowsky, and C. Williams, Phys. Rev. **D93**, 054030 (2016), 1509.02904.

[475] Q.-F. Xiang, X.-J. Bi, P.-F. Yin, and Z.-H. Yu, Phys. Rev. **D91**, 095020 (2015), 1503.02931.

[476] A. J. Brennan, M. F. McDonald, J. Gramling, and T. D. Jacques, JHEP **05**, 112 (2016), 1603.01366.

[477] F. Kahlhoefer, K. Schmidt-Hoberg, T. Schwetz, and S. Vogl, JHEP **02**, 016 (2016), 1510.02110.

[478] C. Englert, M. McCullough, and M. Spannowsky, Phys. Dark Univ. **14**, 48 (2016), 1604.07975.

[479] ATLAS, M. Aaboud *et al.*, (2017), 1711.03301.

[480] M. Beltran, D. Hooper, E. W. Kolb, Z. A. C. Krusberg, and T. M. P. Tait, JHEP **09**, 037 (2010), 1002.4137.

[481] J.-F. Fortin and T. M. P. Tait, Phys. Rev. **D85**, 063506 (2012), 1103.3289.

[482] U. Haisch, F. Kahlhoefer, and E. Re, JHEP **12**, 007 (2013), 1310.4491.

[483] ATLAS, G. Aad *et al.*, Phys. Rev. Lett. **110**, 011802 (2013), 1209.4625.

[484] CMS, S. Chatrchyan *et al.*, Phys. Rev. Lett. **108**, 261803 (2012), 1204.0821.

[485] ATLAS, M. Aaboud *et al.*, Eur. Phys. J. **C77**, 393 (2017), 1704.03848.

[486] CMS, A. M. Sirunyan *et al.*, JHEP **10**, 073 (2017), 1706.03794.

[487] A. Askew, S. Chauhan, B. Penning, W. Shepherd, and M. Tripathi, Int. J. Mod. Phys. **A29**, 1430041 (2014), 1406.5662.

[488] CMS, A. M. Sirunyan *et al.*, JHEP **10**, 180 (2017), 1703.05236.

[489] ATLAS, M. Aaboud *et al.*, Phys. Rev. Lett. **119**, 181804 (2017), 1707.01302.

[490] A. Berlin, T. Lin, and L.-T. Wang, JHEP **06**, 078 (2014), 1402.7074.

[491] A. A. Petrov and W. Shepherd, Phys. Lett. **B730**, 178 (2014), 1311.1511.

[492] L. Carpenter *et al.*, Phys. Rev. **D89**, 075017 (2014), 1312.2592.

[493] ATLAS, G. Aad *et al.*, Phys. Rev. **D93**, 072007 (2016), 1510.06218.

[494] ATLAS, M. Aaboud *et al.*, Phys. Lett. **B765**, 11 (2017), 1609.04572.

[495] CMS, CMS-PAS-EXO-16-012 (2016).

[496] CMS, S. Chatrchyan *et al.*, JINST **8**, P04013 (2013), 1211.4462.

[497] ATLAS, G. Aad *et al.*, Phys. Rev. Lett. **115**, 131801 (2015), 1506.01081.

[498] CMS, CMS-PAS-EXO-16-011 (2016).

[499] ATLAS-CONF-2016-011 (2016).

[500] ATLAS, M. Aaboud *et al.*, Phys. Rev. **D96**, 112004 (2017), 1706.03948.

[501] CMS, A. M. Sirunyan *et al.*, JHEP **03**, 061 (2017), 1701.02042, [Erratum: JHEP09,106(2017)].

[502] ATLAS, M. Aaboud *et al.*, (2017), 1710.11412.

[503] P. Agrawal, B. Batell, D. Hooper, and T. Lin, Phys. Rev. **D90**, 063512 (2014), 1404.1373.

[504] T. Lin, E. W. Kolb, and L.-T. Wang, Phys. Rev. **D88**, 063510 (2013), 1303.6638.

[505] N. F. Bell *et al.*, Phys. Rev. **D86**, 096011 (2012), 1209.0231.

[506] L. M. Carpenter, A. Nelson, C. Shimmin, T. M. P. Tait, and D. Whiteson, Phys. Rev. **D87**, 074005 (2013), 1212.3352.

[507] N. F. Bell, Y. Cai, and R. K. Leane, JCAP **1601**, 051 (2016), 1512.00476.

[508] Y. Bai and T. M. P. Tait, Phys. Lett. **B723**, 384 (2013), 1208.4361.

[509] C. Arina *et al.*, JHEP **11**, 111 (2016), 1605.09242.

[510] ATLAS, G. Aad *et al.*, Eur. Phys. J. **C75**, 92 (2015), 1410.4031.

[511] CMS, CMS-PAS-EXO-16-005 (2016).

[512] J. Andrea, B. Fuks, and F. Maltoni, Phys. Rev. **D84**, 074025 (2011), 1106.6199.

[513] CMS, V. Khachatryan *et al.*, Phys. Rev. Lett. **114**, 101801 (2015), 1410.1149.

[514] CMS, CMS-PAS-EXO-16-040 (2016).

[515] F. S. Sage and R. Dick, J. Phys. **G41**, 105007 (2014).

[516] X.-G. He, T. Li, X.-Q. Li, J. Tandean, and H.-C. Tsai, Phys. Lett. **B688**, 332 (2010), 0912.4722.

[517] V. Barger, P. Langacker, M. McCaskey, M. J. Ramsey-Musolf, and G. Shaughnessy, Phys. Rev. **D77**, 035005 (2008), 0706.4311.

[518] ATLAS, G. Aad *et al.*, JHEP **01**, 172 (2016), 1508.07869.

[519] CMS, V. Khachatryan *et al.*, JHEP **02**, 135 (2017), 1610.09218.

[520] A. Djouadi, Phys. Rept. **457**, 1 (2008), hep-ph/0503172.

[521] M. A. Shifman, A. I. Vainshtein, M. B. Voloshin, and V. I. Zakharov, Sov. J. Nucl. Phys. **30**, 711 (1979), [Yad. Fiz.30,1368(1979)].

[522] J. Alwall *et al.*, JHEP **07**, 079 (2014), 1405.0301.

[523] ATLAS, CMS, G. Aad *et al.*, JHEP **08**, 045 (2016), 1606.02266.

[524] H. M. Georgi, S. L. Glashow, M. E. Machacek, and D. V. Nanopoulos, Phys. Rev. Lett. **40**, 692 (1978).

[525] Y. Mambrini, Phys. Rev. **D84**, 115017 (2011), 1108.0671.

[526] CMS, V. Khachatryan *et al.*, Phys. Rev. **D92**, 012004 (2015), 1411.3441.

[527] N. Kauer and G. Passarino, JHEP **08**, 116 (2012), 1206.4803.

[528] V. Barger, P. Langacker, M. McCaskey, M. Ramsey-Musolf, and G. Shaughnessy, Phys. Rev. **D79**, 015018 (2009), 0811.0393.

[529] S. Kanemura, S. Matsumoto, T. Nabeshima, and H. Taniguchi, Phys. Lett. **B701**, 591 (2011), 1102.5147.

[530] A. Djouadi, O. Lebedev, Y. Mambrini, and J. Quevillon, Phys. Lett. **B709**, 65 (2012), 1112.3299.

[531] T. Nabeshima, Higgs portal dark matter at a linear collider, in *International Workshop on Future Linear Colliders (LCWS11) Granada, Spain, September 26-30, 2011*, 2012, 1202.2673.

[532] A. Djouadi, A. Falkowski, Y. Mambrini, and J. Quevillon, Eur. Phys. J. **C73**, 2455 (2013), 1205.3169.

[533] A. Greljo, J. Julio, J. F. Kamenik, C. Smith, and J. Zupan, JHEP **11**, 190 (2013), 1309.3561.

[534] F. S. Sage, Detection of Scalar Singlet Dark Matter, Master's thesis, 2012.

[535] N. Craig, H. K. Lou, M. McCullough, and A. Thalapillil, JHEP **02**, 127 (2016), 1412.0258.

[536] D. Curtin, P. Meade, and C.-T. Yu, JHEP **11**, 127 (2014), 1409.0005.

[537] Y.-H. Chen, Z.-H. Guo, and H.-Q. Zheng, Phys. Rev. **D90**, 034013 (2014), 1311.3366.

[538] M. Endo and Y. Takaesu, Phys. Lett. **B743**, 228 (2015), 1407.6882.

[539] ATLAS, G. Aad *et al.*, Eur. Phys. J. **C75**, 299 (2015), 1502.01518, [Erratum: Eur. Phys. J.C75,no.9,408(2015)].

[540] G. Marques Tavares, M. Schmaltz, and W. Skiba, Phys. Rev. **D89**, 015009 (2014), 1308.0025.

[541] S. Abel and A. Mariotti, Phys. Rev. **D89**, 125018 (2014), 1312.5335.

[542] Z.-W. Wang, F. S. Sage, T. G. Steele, R. B. Mann, and T. Hanif, PoS **ICHEP2016**, 799 (2016), 1611.03297.

[543] Z.-W. Wang, T. G. Steele, T. Hanif, and R. B. Mann, JHEP **08**, 065 (2016), 1510.04321.

[544] Z.-W. Wang, F. S. Sage, T. G. Steele, and R. B. Mann, J. Phys. **G45**, 095002 (2018), 1511.02531.

[545] S. R. Coleman and E. J. Weinberg, Phys. Rev. **D7**, 1888 (1973).

[546] P. H. Chankowski, S. Pokorski, and J. Wagner, Eur. Phys. J. **C47**, 187 (2006), hep-ph/0601097.

[547] F. S. Sage, J. N. E. Ho, T. G. Steele, and R. Dick, (2016), 1611.03367.

[548] M. Carena, A. Daleo, B. A. Dobrescu, and T. M. P. Tait, Phys. Rev. **D70**, 093009 (2004), hep-ph/0408098.

[549] T. Appelquist, B. A. Dobrescu, and A. R. Hopper, Phys. Rev. **D68**, 035012 (2003), hep-ph/0212073.

[550] J. L. Hewett and T. G. Rizzo, Phys. Rept. **183**, 193 (1989).

[551] C.-W. Chiang, T. Nomura, and K. Yagyu, JHEP **05**, 106 (2014), 1402.5579.

[552] P. Ko, Y. Omura, and C. Yu, JHEP **06**, 034 (2015), 1502.00262.

[553] T. G. Rizzo, Phys. Rev. **D59**, 015020 (1998), hep-ph/9806397.

[554] K. S. Babu, C. F. Kolda, and J. March-Russell, Phys. Rev. **D54**, 4635 (1996), hep-ph/9603212.

[555] P. Fileviez Perez and M. B. Wise, Phys. Rev. **D82**, 011901 (2010), 1002.1754, [Erratum: Phys. Rev.D82,079901(2010)].

[556] C. D. Carone and H. Murayama, Phys. Rev. Lett. **74**, 3122 (1995), hep-ph/9411256.

[557] A. A. Andrianov, P. Osland, A. A. Pankov, N. V. Romanenko, and J. Sirkka, Phys. Rev. **D58**, 075001 (1998), hep-ph/9804389.

[558] C. T. Hill, Phys. Lett. **B345**, 483 (1995), hep-ph/9411426.

[559] R. S. Chivukula and E. H. Simmons, Phys. Rev. **D66**, 015006 (2002), hep-ph/0205064.

[560] M. Hashimoto, S. Iso, and Y. Orikasa, Phys. Rev. **D89**, 016019 (2014), 1310.4304.

[561] M. Hashimoto, S. Iso, and Y. Orikasa, Phys. Rev. **D89**, 056010 (2014), 1401.5944.

[562] O. Lebedev and Y. Mambrini, Phys. Lett. **B734**, 350 (2014), 1403.4837.

[563] M. S. Chanowitz, M. A. Furman, and I. Hinchliffe, Nucl. Phys. **B153**, 402 (1979).

[564] K. S. Babu, J. Julio, and Y. Zhang, Nucl. Phys. **B858**, 468 (2012), 1111.5021.

[565] M. Hosch, K. Whisnant, and B.-L. Young, Phys. Rev. **D55**, 3137 (1997), hep-ph/9607413.

[566] J. Shu, Phys. Rev. **D78**, 096004 (2008), 0711.2516.

[567] H. An, X. Ji, and L.-T. Wang, JHEP **07**, 182 (2012), 1202.2894.

[568] A. Leike, Phys. Rept. **317**, 143 (1999), hep-ph/9805494.

[569] A. Alves, A. Berlin, S. Profumo, and F. S. Queiroz, JHEP **10**, 076 (2015), 1506.06767.

[570] A. Hook, E. Izaguirre, and J. G. Wacker, Adv. High Energy Phys. **2011**, 859762 (2011), 1006.0973.

[571] T. Gherghetta, T. A. Kaeding, and G. L. Kane, Phys. Rev. **D57**, 3178 (1998), hep-ph/9701343.

[572] J. Kang and P. Langacker, Phys. Rev. **D71**, 035014 (2005), hep-ph/0412190.

[573] ATLAS, G. Aad *et al.*, Phys. Rev. **D90**, 052005 (2014), 1405.4123.

[574] CMS, V. Khachatryan *et al.*, Phys. Rev. **D91**, 052009 (2015), 1501.04198.

[575] CMS, V. Khachatryan *et al.*, Phys. Rev. **D93**, 012001 (2016), 1506.03062.

[576] S. Baek, J. H. Jeon, and C. S. Kim, Phys. Lett. **B641**, 183 (2006), hep-ph/0607113.

[577] C.-W. Chiang, N. G. Deshpande, and J. Jiang, JHEP **08**, 075 (2006), hep-ph/0606122.

[578] X.-G. He and G. Valencia, Phys. Rev. **D74**, 013011 (2006), hep-ph/0605202.

[579] C.-H. Chen and H. Hatanaka, Phys. Rev. **D73**, 075003 (2006), hep-ph/0602140.

[580] S. K. Gupta and G. Valencia, Phys. Rev. **D82**, 035017 (2010), 1005.4578.

[581] M. I. Gresham, I.-W. Kim, and K. M. Zurek, Phys. Rev. **D84**, 034025 (2011), 1102.0018.

[582] B. A. Dobrescu and C. Frugiuele, Phys. Rev. Lett. **113**, 061801 (2014), 1404.3947.

[583] J. Hisano, N. Nagata, and Y. Omura, Phys. Rev. **D92**, 055001 (2015), 1506.03931.

[584] A. Berlin, Phys. Rev. **D93**, 055015 (2016), 1601.01381.

[585] X. Chu, Y. Mambrini, J. Quevillon, and B. Zaldivar, JCAP **1401**, 034 (2014), 1306.4677.

[586] A. Alves, S. Profumo, and F. S. Queiroz, JHEP **04**, 063 (2014), 1312.5281.

[587] Y. Mambrini, JCAP **1107**, 009 (2011), 1104.4799.

[588] J. M. Cline, G. Dupuis, Z. Liu, and W. Xue, JHEP **08**, 131 (2014), 1405.7691.

[589] A. Alves, A. Berlin, S. Profumo, and F. S. Queiroz, Phys. Rev. **D92**, 083004 (2015), 1501.03490.

[590] T. Jacques *et al.*, JHEP **10**, 071 (2016), 1605.06513.

[591] E. Dudas, Y. Mambrini, S. Pokorski, and A. Romagnoni, JHEP **08**, 014 (2009), 0904.1745.

[592] E. Dudas, Y. Mambrini, S. Pokorski, and A. Romagnoni, JHEP **10**, 123 (2012), 1205.1520.

[593] G. Arcadi, Y. Mambrini, M. H. G. Tytgat, and B. Zaldivar, JHEP **03**, 134 (2014), 1401.0221.

[594] M. Abdullah *et al.*, Phys. Rev. **D90**, 035004 (2014), 1404.6528.

[595] N. F. Bell, Y. Cai, R. K. Leane, and A. D. Medina, Phys. Rev. **D90**, 035027 (2014), 1407.3001.

[596] F. D'Eramo, B. J. Kavanagh, and P. Panci, JHEP **08**, 111 (2016), 1605.04917.

[597] A. DiFranzo, P. J. Fox, and T. M. P. Tait, JHEP **04**, 135 (2016), 1512.06853.

[598] Z.-L. Han and W. Wang, (2018), 1805.02025.

[599] A. Alves, G. Arcadi, Y. Mambrini, S. Profumo, and F. S. Queiroz, JHEP **04**, 164 (2017), 1612.07282.

[600] W. Chao and Q. Yuan, (2017), 1711.11182.

[601] J. Ellis, A. Fowlie, L. Marzola, and M. Raidal, Phys. Rev. **D97**, 115014 (2018), 1711.09912.

[602] G. Arcadi, P. Ghosh, Y. Mambrini, M. Pierre, and F. S. Queiroz, JCAP **1711**, 020 (2017), 1706.04198.

[603] M. Fairbairn, J. Heal, F. Kahlhoefer, and P. Tunney, JHEP **09**, 018 (2016), 1605.07940.

[604] D. Racco, A. Wulzer, and F. Zwirner, JHEP **05**, 009 (2015), 1502.04701.

[605] J. Goodman and W. Shepherd, (2011), 1111.2359.

[606] M. T. Frandsen, F. Kahlhoefer, A. Preston, S. Sarkar, and K. Schmidt-Hoberg, JHEP **07**, 123 (2012), 1204.3839.

[607] H. Dreiner, D. Schmeier, and J. Tattersall, EPL **102**, 51001 (2013), 1303.3348.

[608] T. Jacques and K. Nordström, JHEP **06**, 142 (2015), 1502.05721.

[609] N. Okada and S. Okada, Phys. Rev. **D93**, 075003 (2016), 1601.07526.

[610] D. Abercrombie *et al.*, (2015), 1507.00966.

[611] LHC New Physics Working Group, D. Alves, J. Phys. **G39**, 105005 (2012), 1105.2838.

[612] N. Arkani-Hamed, A. G. Cohen, and H. Georgi, Phys. Lett. **B516**, 395 (2001), hep-th/0103135.

[613] N. Arkani-Hamed *et al.*, JHEP **08**, 021 (2002), hep-ph/0206020.

[614] T. Han, H. E. Logan, B. McElrath, and L.-T. Wang, Phys. Rev. **D67**, 095004 (2003), hep-ph/0301040.

[615] K. Agashe *et al.*, Phys. Rev. **D76**, 115015 (2007), 0709.0007.

[616] M. Carena, A. Delgado, E. Ponton, T. M. P. Tait, and C. E. M. Wagner, Phys. Rev. **D68**, 035010 (2003), hep-ph/0305188.

[617] M. Cvetic and P. Langacker, Phys. Rev. **D54**, 3570 (1996), hep-ph/9511378.

[618] C. T. Hill and E. H. Simmons, Phys. Rept. **381**, 235 (2003), hep-ph/0203079, [Erratum: Phys. Rept.390,553(2004)].

[619] A. Berlin, P. J. Fox, D. Hooper, and G. Mohlabeng, JCAP **1606**, 016 (2016), 1604.06100.

[620] F. S. Sage, Z.-W. Wang, R. Dick, T. G. Steele, and R. B. Mann, PoS **ICHEP2016**, 877 (2016), 1610.07574.

[621] F. D'Eramo and M. Procura, JHEP **04**, 054 (2015), 1411.3342.

[622] A. Crivellin, F. D'Eramo, and M. Procura, Phys. Rev. Lett. **112**, 191304 (2014), 1402.1173.

[623] P. Cox, A. D. Medina, T. S. Ray, and A. Spray, JHEP **06**, 110 (2016), 1512.00471.

[624] N. Okada and Y. Orikasa, Phys. Rev. **D85**, 115006 (2012), 1202.1405.

[625] P. Cox, C. Han, and T. T. Yanagida, JCAP **1801**, 029 (2018), 1710.01585.

[626] XENON, E. Aprile *et al.*, Phys. Rev. Lett. **121**, 111302 (2018), 1805.12562.

[627] M. Duerr, P. Fileviez Perez, and J. Smirnov, Phys. Rev. **D92**, 083521 (2015), 1506.05107.

[628] C.-N. Yang, Phys. Rev. **77**, 242 (1950).

[629] W.-Y. Keung, I. Low, and J. Shu, Phys. Rev. Lett. **101**, 091802 (2008), 0806.2864.

[630] E. Dudas, L. Heurtier, Y. Mambrini, and B. Zaldivar, JHEP **11**, 083 (2013), 1307.0005.

[631] F. S. Sage and R. Dick, (2016), 1604.04589.

[632] F. F. Hansen *et al.*, Phys. Rev. **D97**, 065014 (2018), 1706.06402.

[633] R. Mann *et al.*, Phys. Rev. Lett. **119**, 261802 (2017), 1707.02942.

[634] O. Antipin, N. A. Dondi, F. Sannino, A. E. Thomsen, and Z.-W. Wang, Phys. Rev. **D98**, 016003 (2018), 1803.09770.

[635] V. Silveira and A. Zee, Phys. Lett. **B161**, 136 (1985).

[636] J. McDonald, Phys. Rev. **D50**, 3637 (1994), hep-ph/0702143.

[637] J. McDonald, Phys. Lett. **B323**, 339 (1994).

[638] C. P. Burgess, M. Pospelov, and T. ter Veldhuis, Nucl. Phys. **B619**, 709 (2001), hep-ph/0011335.

[639] M. C. Bento, O. Bertolami, R. Rosenfeld, and L. Teodoro, Phys. Rev. **D62**, 041302 (2000), astro-ph/0003350.

[640] D. E. Holz and A. Zee, Phys. Lett. **B517**, 239 (2001), hep-ph/0105284.

[641] J. McDonald, Phys. Rev. Lett. **88**, 091304 (2002), hep-ph/0106249.

[642] G. Cynolter, E. Lendvai, and G. Pocsik, Acta Phys. Polon. **B36**, 827 (2005), hep-ph/0410102.

[643] M. Gonderinger, Y. Li, H. Patel, and M. J. Ramsey-Musolf, JHEP **01**, 053 (2010), 0910.3167.

[644] M. H. G. Tytgat, PoS **IDM2010**, 126 (2011), 1012.0576.

[645] X.-G. He and G. Valencia, Phys. Lett. **B707**, 381 (2012), 1108.0222.

[646] X.-G. He, S.-Y. Ho, J. Tandean, and H.-C. Tsai, Phys. Rev. **D82**, 035016 (2010), 1004.3464.

[647] X.-G. He, T. Li, X.-Q. Li, J. Tandean, and H.-C. Tsai, Phys. Rev. **D79**, 023521 (2009), 0811.0658.

[648] Y. Cai, X.-G. He, and B. Ren, Phys. Rev. **D83**, 083524 (2011), 1102.1522.

[649] S. Andreas, C. Arina, T. Hambye, F.-S. Ling, and M. H. G. Tytgat, Phys. Rev. **D82**, 043522 (2010), 1003.2595.

[650] S. Baek, P. Ko, W.-I. Park, and E. Senaha, JHEP **05**, 036 (2013), 1212.2131.

[651] K.-Y. Choi, H. M. Lee, and O. Seto, Phys. Rev. **D87**, 123541 (2013), 1304.0966.

[652] S. Baek, P. Ko, and W.-I. Park, Phys. Rev. **D90**, 055014 (2014), 1405.3530.

[653] H. Han and S. Zheng, JHEP **12**, 044 (2015), 1509.01765.

[654] J. A. Arroyo and S. Ramos-Sanchez, J. Phys. Conf. Ser. **761**, 012014 (2016), 1608.00791.

[655] K. Cheung, P. Ko, J. S. Lee, and P.-Y. Tseng, JHEP **10**, 057 (2015), 1507.06158.

[656] M. Escudero, A. Berlin, D. Hooper, and M.-X. Lin, JCAP **1612**, 029 (2016), 1609.09079.

[657] H. Han, J. M. Yang, Y. Zhang, and S. Zheng, Phys. Lett. **B756**, 109 (2016), 1601.06232.

[658] W. Chao, (2016), 1601.06714.

[659] P. Ko and H. Yokoya, JHEP **08**, 109 (2016), 1603.04737.

[660] G. Dupuis, JHEP **07**, 008 (2016), 1604.04552.

[661] T. Kamon, P. Ko, and J. Li, (2017), 1705.02149.

[662] Y. Hamada, H. Kawai, and K.-y. Oda, JHEP **07**, 026 (2014), 1404.6141.

[663] T. Mondal and T. Basak, Phys. Lett. **B744**, 208 (2015), 1405.4877.

[664] A. Aravind, M. Xiao, and J.-H. Yu, Phys. Rev. **D93**, 123513 (2016), 1512.09126.

[665] A. Urbano and W. Xue, JHEP **03**, 133 (2015), 1412.3798.

[666] C. Kouvaris, I. M. Shoemaker, and K. Tuominen, Phys. Rev. **D91**, 043519 (2015), 1411.3730.

[667] H. Han and S. Zheng, Nucl. Phys. **B914**, 248 (2017), 1510.06165.

[668] X.-G. He and J. Tandean, JHEP **12**, 074 (2016), 1609.03551.

[669] S. Dawson and H. E. Haber, A PRIMER ON HIGGS BOSON LOW-ENERGY THEOREMS, in *Workshop on High-energy Physics Phenomenology (WHEPP) Bombay, India, January 2-15, 1989*, pp. 0324–345, 1989.

[670] R. Barbieri and G. Curci, Phys. Lett. **B219**, 503 (1989).

[671] H.-Y. Cheng, Phys. Lett. **B219**, 347 (1989).

[672] Z. W. Wang, *Aspects of Radiative Symmetry Breaking in the Standard Model and Beyond*, PhD thesis, Saskatchewan U., 2016.

[673] W. A. Bardeen, On naturalness in the standard model, in *Ontake Summer Institute on Particle Physics Ontake Mountain, Japan, August 27-September 2, 1995*, 1995.

[674] S. R. Coleman and J. Mandula, Phys. Rev. **159**, 1251 (1967).

[675] S. Weinberg, Phys. Lett. **82B**, 387 (1979).

[676] R. Percacci, (2007), 0709.3851.

[677] J. Braun, H. Gies, and D. D. Scherer, Phys. Rev. **D83**, 085012 (2011), 1011.1456.

[678] P. H. Ginsparg, APPLIED CONFORMAL FIELD THEORY, in *Les Houches Summer School in Theoretical Physics: Fields, Strings, Critical Phenomena Les Houches, France, June 28-August 5, 1988*, pp. 1–168, 1988, hep-th/9108028.

[679] Y. Nakayama, Phys. Rept. **569**, 1 (2015), 1302.0884.

[680] G. Parisi, Phys. Lett. **39B**, 643 (1972).

[681] M. B. Einhorn and D. R. T. Jones, JHEP **03**, 047 (2015), 1410.8513.

[682] M. B. Einhorn and D. R. T. Jones, JHEP **01**, 019 (2016), 1511.01481.

[683] A. Salvio and A. Strumia, JHEP **06**, 080 (2014), 1403.4226.

[684] M. Shaposhnikov and C. Wetterich, Phys. Lett. **B683**, 196 (2010), 0912.0208.

[685] H. E. Camblong, L. N. Epele, H. Fanchiotti, and C. A. Garcia Canal, Annals Phys. **287**, 14 (2001), hep-th/0003255.

[686] S. D. M. White and M. J. Rees, Mon. Not. Roy. Astron. Soc. **183**, 341 (1978).

[687] W. Dehnen and J. Read, Eur. Phys. J. Plus **126**, 55 (2011), 1105.1082.

[688] M. Kuhlen, M. Vogelsberger, and R. Angulo, Phys. Dark Univ. **1**, 50 (2012), 1209.5745.

[689] J. F. Navarro, C. S. Frenk, and S. D. M. White, Astrophys. J. **462**, 563 (1996), astro-ph/9508025.

[690] A. Burkert, IAU Symp. **171**, 175 (1996), astro-ph/9504041, [Astrophys. J.447,L25(1995)].

[691] A. W. Graham, D. Merritt, B. Moore, J. Diemand, and B. Terzic, Astron. J. **132**, 2685 (2006), astro-ph/0509417.

[692] J. F. Navarro *et al.*, Mon. Not. Roy. Astron. Soc. **402**, 21 (2010), 0810.1522.

[693] P. B. Tissera, S. D. M. White, S. Pedrosa, and C. Scannapieco, Mon. Not. Roy. Astron. Soc. **406**, 922 (2010), 0911.2316.

[694] R. Ibata, M. Irwin, G. F. Lewis, and A. Stolte, Astrophys. J. **547**, L133 (2001), astro-ph/0004255.

[695] E. Starkenburg *et al.*, Astrophys. J. **698**, 567 (2009), 0903.3043.

[696] B. Holdom, Phys. Lett. **B166**, 196 (1986).

[697] K. S. Babu, C. F. Kolda, and J. March-Russell, Phys. Rev. **D57**, 6788 (1998), hep-ph/9710441.

[698] F. del Aguila, M. Masip, and M. Perez-Victoria, Nucl. Phys. **B456**, 531 (1995), hep-ph/9507455.

[699] R. Foot and X.-G. He, Phys. Lett. **B267**, 509 (1991).

[700] E. A. Paschos, Phys. Rev. **D15**, 1966 (1977).

[701] S. L. Glashow and S. Weinberg, Phys. Rev. **D15**, 1958 (1977).

[702] B. Holdom, Phys. Lett. **B339**, 114 (1994), hep-ph/9407311.

[703] V. Barger, C.-W. Chiang, P. Langacker, and H.-S. Lee, Phys. Lett. **B580**, 186 (2004), hep-ph/0310073.

[704] P. Langacker and M. Plumacher, Phys. Rev. **D62**, 013006 (2000), hep-ph/0001204.

[705] M. Franz, M. V. Polyakov, and K. Goeke, Phys. Rev. **D62**, 074024 (2000), hep-ph/0002240.

[706] Y. Zhang, Phys. Lett. **B720**, 137 (2013), 1212.2730.

[707] X.-D. Ji and W. Melnitchouk, Phys. Rev. **D56**, R1 (1997), hep-ph/9703363.

[708] C. Cronstrom, Phys. Lett. **B90**, 267 (1980).

Appendix A

Physical Constants and Units

This Appendix provides for convenience a description and tabulation of the units used throughout the majority of the thesis (natural units) and some of the physical constants that have been used in calculations.

Many of the results of the thesis are presented in natural units, with $\hbar = c = 1$. In this system, all quantities of relevance can be written in terms of some power of energy, which is typically in units of eV (electron volts) in particle physics. As the eV is a very small quantity compared to many physical scales of interest, keV (10^3 eV), MeV (10^6 eV), GeV (10^9 eV), and TeV (10^{12} eV) are all frequently used. For reference, the mass of the electron is 0.511 MeV and the mass of the proton is 938 MeV. Particle masses are exclusively written in units of energy (MeV/c^2 or GeV/c^2 or TeV/c^2), and because we work in natural units where $c^2 = 1$, the denominator is omitted for brevity. So, for example, the mass of the electron is stated to be 0.511 MeV.

In Table A.1 is a list of various quantities in natural units, including both the canonical mass dimension and their dimension in units of eV. Table A.2 includes a list of some useful quantities in the SI system and in natural units. These conversion factors have been used implicitly throughout the thesis, within the calculations and in the generation of the figures.

As particle astrophysics is a field that also requires the study of astronomical phenomena, the use of standard astronomical constants is required. Certain of such constants are presented here in Table A.3. These astronomical constants are presented in SI units, and that is generally how they are used throughout the thesis.

Table A.1: Quantities in natural units

Quantity	Scaling	Natural unit	Canonical dimension
time t	$t/\hbar$	eV^{-1}	-1
length l	$l/(\hbar c)$	eV^{-1}	-1
energy E	E	eV	1
momentum p	pc	eV	1
angular momentum L	$L/\hbar$	dimensionless	0
mass m	mc^2	eV	1
area A	$A/(\hbar c)^2$	eV^{-2}	-2
electric charge e^2	$\alpha = e^2/4\pi\epsilon_0\hbar c$	dimensionless	0
velocity v	v/c	dimensionless	0

Table A.2: Useful conversion factors

Quantity (SI units)	Value (Natural units)
$\hbar = 1.054 \times 10^{-34}$ J s	6.582×10^{-22} MeV s
$\hbar c$	0.197 326 GeV fm
$\hbar^2 c^2$	0.389 379 GeV^2 mb = 0.389 379 $\times 10^{-27}$ GeV^2 cm^2
$(1.16733/\ \hbar^2 c) \times 10^{-17}$ cm^3/s	GeV^{-2}
$k = 1.380 \times 10^{-23}$ J/K	$8.617\ 342 \times 10^{-5}$ eV/K
0.1975 fm	1 GeV^{-1}
6.59×10^{-25} s	1 GeV^{-1}

Table A.3: Astronomical constants

M_{sun}	1.989×10^{30} kg
parsec pc	3.0857×10^{16} m
light year ly	9.4607×10^{15} m

Appendix B

Higgs-portal Dark Matter

B.1 Introduction and literature review

The primary demonstrative model that is used in this thesis is minimal Higgs-portal scalar dark matter. The Higgs portal is the prototypical example of a scalar portal to a hidden sector. The model is useful for demonstrating the basic techniques of dark matter phenomenology because it is a complete QFT that contains minimal beyond SM particle content. The most minimal version of the model introduces three new degrees of freedom: a mass and two coupling parameters. At the classical level, it is a scalar-Yukawa theory, which allows for relatively simple calculations, and yet it is sophisticated enough to allow discussion of all the main channels of dark matter detection, as well as detailed calculations of thermal relic abundance constraints. This model is used as an example to illustrate the material in Chapters 2, 3, 4, and 5. This approach was chosen because the model is complete enough to illustrate each of the techniques discussed while still being simple enough to allow the presentation to avoid being bogged down in model-specific technical issues.

We briefly review the history of the model and trace its appearances in the literature. We have attempted to be exhaustive in this discussion, but we will no doubt have failed. Higgs-portal dark matter has exploded in popularity in the last decade as a minimal test case, and there are now hundreds of articles that mention it. It would be very difficult to reference them all. Nonetheless, the important papers are included here.

The model was originally proposed by Silveira and Zee in 1985 [635], when the dark matter problem had only recently caught the attention of particle physicists. Their basic construction has lasted more or less unchanged to the present as the minimal example of Higgs-portal dark matter. The next appearance in the literature was in an article by McDonald in the early nineties [636], which explored in detail the thermal abundance requirements of the model. It was here that the complex singlet variant was introduced. Another article using the same model but focusing more on baryogenesis was also published [637].

After these discussions, there was little activity until around the turn of the millenium, when the first generation of direct detection experiments began to come online. There were then several articles discussing the direct detection prospects of the model, as well as some more theoretical concerns [638, 639, 640, 641]. These basic treatments continued into the early 2000s [642], with an important discussion of the effect of the model on the stability of the Higgs potential in [643]. It was around this time that the term 'Higgs-portal' was coined [433].

Into the second generation of direct detection experiments, and when the community began to seriously study the potential signatures of annihilating dark matter, the model began to gain more interest. This is likely a consequence of the basic supersymmetric WIMP not having been observed in direct detection experiments. The first serious discussion of possible production of Higgs-portal dark matter at a particle collider was by Barger and collaborators [517, 528]. Detailed treatments of the indirect detection prospects also appeared in the last few years of the decade [260, 341, 372].

Leading up to and immediately after the discovery of the Higgs boson at the LHC in 2012 [1, 2], there were a number of articles dealing with all aspects of the model [644, 239, 241]. Several extensions of the basic model to include other features were considered [645, 646], as well as direct detection and collider detection possibilities [529, 530, 531, 532, 533, 239, 647, 648, 516, 649, 256]. Vector variants of the model have also been considered [650, 651].

As Run I of the LHC began to wind down and the intensive data analysis began, the collider community began to explore the so-called 'simplified models,' as discussed in Chapter 5. The Higgs-portal model is an almost archetypal example of a scalar-portal simplified model, and recieved a great deal of attention from the collider physics community in that context [470], as well as periodic updates as more data was analyzed [652, 653, 330, 654, 515, 535, 655, 656, 657, 658, 659, 660, 661]. Also explored were ties to cosmology [662], and attempted explanations of a variety of new cosmic ray phenomena [663, 314, 631]. Renormalization group improvements of the model have also been considered [543, 664, 665], as have strongly self-interacting variants [666, 667].

Currently, the model hovers on the edge of viability [240, 656]. In the low mass range, it is ruled out by direct detection experiments for thermally constrained values of the coupling parameter [668, 656].

B.2 Particle Physics Model

In minimal Higgs-portal dark matter models, the dark matter particle can be a scalar (S), a fermion (χ), or a vector (V). We will discuss only the scalar case as it is generally all that is required to illustrate a technique.

The Lagrangian for this theory prior to electroweak symmetry breaking is

$$\mathcal{L}_S = \mathcal{L}_{SM} - \frac{1}{2}\partial^\mu S \partial_\mu S - \frac{1}{2}m_S^2 S^2 - \frac{\lambda_S}{4}S^4 - \frac{\eta_S}{2}S^2 H^\dagger H. \tag{B.1}$$

The SM Lagrangian is $\mathcal{L}_{SM}$, and the SM Higgs doublet is H. The dark field S is a SM singlet, uncharged under all SM gauge groups and having tree level interactions with only the SM Higgs field. The singlet self-interaction couplings are denoted λ_S, and the Higgs-singlet couplings are η_S.

We note the presence of explicit mass terms for the singlet fields. There is no symmetry that would be violated by the inclusion of these terms, so they must be included. The reader is welcome to consider the models presented here effective theories, with the singlet mass terms generated by new physics at some higher energy scale.

Following electroweak symmetry breaking, and after a transformation to unitary gauge, the Lagrangians can be written in terms of the physical Higgs scalar h and the vacuum expectation value of the Higgs field v_h. These can be further simplified by including the Higgs contributions to the singlet masses through a relabelling

$$m_S^2 = m_{S0}^2 + \eta_S v_h^2/2 \tag{B.2}$$

This yields a Lagrangian suited for phenomenological calculations:

$$\mathcal{L}_S = \mathcal{L}_{SM} - \frac{1}{2}\partial^\mu S \partial_\mu S - \frac{1}{2}m_S^2 S^2 - \frac{\lambda_S}{4}S^4 - \frac{\eta_S v_h}{2}S^2 h - \frac{\eta_S}{4}S^2 h^2. \tag{B.3}$$

B.3 Cross Sections

This Section includes the annihilation cross sections for scalar Higgs-portal dark matter for convenience, though they also appear in the literature [631, 260]. The cross sections are

$$\sigma_{SS\to hh} = \frac{\eta_S^2}{32\pi}\frac{\sqrt{k^2+m_S^2-m_h^2}}{k\left(k^2+m_S^2\right)}\frac{\left(2k^2+m_S^2+m_h^2\right)^2}{\left(4k^2+4m_S^2-m_h^2\right)^2+m_h^2\Gamma_h^2}, \tag{B.4}$$

$$\sigma_{SS\to f\bar{f}} = \frac{\eta_S^2 N_C}{8\pi}\frac{\left(k^2+m_S^2-m_f^2\right)^{3/2}}{k\left(k^2+m_S^2\right)}\frac{m_f^2}{\left(4k^2+4m_S^2-m_h^2\right)^2+m_h^2\Gamma_h^2}, \tag{B.5}$$

$$\sigma_{SS\to ZZ,WW} = \frac{\eta_S^2}{16\pi(1+\delta_Z)}\frac{\sqrt{k^2+m_S^2-m_{Z,W}^2}}{k\left(k^2+m_S^2\right)}\frac{\left[2m_{Z,W}^4+\left(m_{Z,W}^2-2k^2-2m_S^2\right)^2\right]}{\left(4k^2+4m_S^2-m_h^2\right)^2+m_h^2\Gamma_h^2}, \tag{B.6}$$

The nonrelativistic velocity-averaged annihilation cross sections are obtained by multiplying the above cross sections with $2k/\sqrt{k^2+m_S^2}$ and taking the limit $k\to 0$. The resulting expressions, which are used for calculation of the photon spectra in Chapter 4, are

$$v\sigma_{SS\to hh} = \frac{\eta_S^2}{16\pi}\frac{\sqrt{m_S^2-m_h^2}}{m_S^3}\frac{\left(m_S^2+m_h^2\right)^2}{\left(4m_S^2-m_h^2\right)^2+m_h^2\Gamma_h^2}, \tag{B.7}$$

$$v\sigma_{SS\to f\bar{f}} = \frac{\eta_S^2 N_C}{4\pi}\frac{\left(m_S^2-m_f^2\right)^{3/2}}{m_S^3}\frac{m_f^2}{\left(4m_S^2-m_h^2\right)^2+m_h^2\Gamma_h^2}, \tag{B.8}$$

$$v\sigma_{SS\to ZZ,WW} = \frac{\eta_S^2}{8\pi(1+\delta_Z)}\frac{\sqrt{m_S^2 - m_{Z,W}^2}}{m_S^3}\frac{\left[2m_{Z,W}^4 + \left(m_{Z,W}^2 - 2m_S^2\right)^2\right]}{\left(4m_S^2 - m_h^2\right)^2 + m_h^2\Gamma_h^2}, \tag{B.9}$$

Also included here is the calculation for annihilation directly to photons in the velocity averaged non-relativistic limit. This is a loop–order effect, but we compute it using a tree–level approximation with an effective Higgs–photon vertex obtained by integrating out the high mass loop particles (t and W) [521]. This approximation is valid at low energies compared to the masses of the intermediate particles. Actual numerical values come from a Madgraph [522] package (details here). The form of the coupling parameter is

$$g_{h\gamma\gamma} = -\frac{\alpha}{\pi v_h}\frac{47}{18}$$

$$\times\left(1 + \frac{66}{235}\tau_W + \frac{228}{1645}\tau_W^2 + \frac{696}{8225}\tau_W^3 + \frac{5248}{90475}\tau_W^4 + \frac{1280}{29939}\tau_W^5 + \frac{54528}{1646645}\tau_W^6 - \frac{56}{705}\tau_t - \frac{32}{987}\tau_t^2\right) \tag{B.10}$$

where $\tau_W = m_h^2/(4m_W^2)$ and $\tau_t = m_h/(4m_t^2)$.

The matrix element for the annihilation of scalar singlets through the Higgs–mediated s–channel to photons using the above effective tree–level coupling is

$$i\mathcal{M} = \frac{i^3 g_{h\gamma\gamma} v_h \eta_S}{2}\frac{\left[g_{\mu\nu}p_1\cdot p_2 - p_{1\mu}p_{2\nu}\right]}{q^2 - m_h^2 + i\epsilon}\epsilon^{*\mu}(p_1)\epsilon^{*\nu}(p_2). \tag{B.11}$$

The intermediate 4–momentum is $q = p_1 + p_2 = k_1 + k_2$, where p_i are the outgoing photon 4–momenta and k_i are the incoming singlet 4–momenta. The tensor structure in the numerator comes from the generic form of a scalar–vector coupling. Squaring and summing over external polarizations while applying the Breit–Wigner prescription for the propagator of an unstable particle gives

$$\frac{1}{4}\sum_{pols}|\mathcal{M}|^2 = \frac{g_{h\gamma\gamma}^2 v_h^2 \eta_S^2 \left(p_1\cdot p_2\right)^2}{16\left[\left(q^2 - m_h^2\right)^2 + m_h^2\Gamma_h^2\right]}. \tag{B.12}$$

The cross section in the center of mass frame is

$$\left(\frac{d\sigma}{d\Omega}\right)_{CM} = \frac{1}{64\pi^2 E_{CM}^2}\frac{|\mathbf{p_f}|}{|\mathbf{p_i}|}\frac{1}{4}\sum_{pols}|\mathcal{M}|^2. \tag{B.13}$$

Writing our 4–vectors $p_{1,2} = (E_\gamma, 0, 0, \pm E_\gamma)$ and $k_{1,2} = (E_S, 0, 0, \pm\sqrt{E_S^2 - m_S^2} = \pm k)$, we get $(p_1\cdot p_2) = 2E_\gamma^2$ and $q^2 = 4E_\gamma^2 = 4E_S^2$. Conservation of energy tells us that $E_\gamma = E_S = E = E_{CM}/2$.

Inserting these expressions into the matrix element and then inserting that into the cross section gives

$$\left(\frac{d\sigma}{d\Omega}\right)_{CM} = \frac{1}{64\pi^2 4E^2}\frac{|\mathbf{p_f}|}{|\mathbf{p_i}|}\frac{g_{h\gamma\gamma}^2 v_h^2 \eta_S^2 E^4}{16\left[\left(4E^2 - m_h^2\right)^2 + m_h^2\Gamma_h^2\right]}. \tag{B.14}$$

Integration over angles gives a factor of 4π, leading to

$$\sigma_{SS\to\gamma\gamma} = \frac{g_{h\gamma\gamma}^2 v_h^2 \eta_S^2 E^3}{1024\pi k\left[\left(4E^2 - m_h^2\right)^2 + m_h^2\Gamma_h^2\right]}. \tag{B.15}$$

In the above k is the magnitude of the 3–momentum of the incoming particles in the center of mass frame and the energy $E = \sqrt{k^2 + m_S^2}$ is the center of mass energy. Taking this relativistic cross section to the velocity–averaged nonrelativistic limit as above yields

$$v\sigma_{SS\to\gamma\gamma} = \frac{g_{h\gamma\gamma}^2 v_h^2 \eta_S^2 m_S^2}{512\pi\left[\left(4m_S^2 - m_h^2\right)^2 + m_h^2\Gamma_h^2\right]}. \tag{B.16}$$

These cross sections are included here, and are compared against those found in the literature [330] in Chapter 4, which we also reproduce here:

$$\sigma_{SS\to\gamma\gamma} = \frac{4\eta_S^2 v_h^2}{\sqrt{s-4m_S^2}} \frac{\Gamma_{\gamma\gamma}(s)}{\left(s-m_h^2\right)^2 + m_h^2\Gamma_h^2} \tag{B.17}$$

$$\Gamma_{\gamma\gamma}(s) = \frac{\alpha_{em} s^{3/2}}{256\pi^3 v_h^2} \left| \sum_f N_C^f Q_f^2 A_{1/2}^h(\tau_f) + A_1^h(\tau_W) \right|^2 \tag{B.18}$$

$$A_{1/2}^h(\tau) = \frac{2}{\tau^2}\left[\tau + (\tau-1) f(\tau)\right] \tag{B.19}$$

$$A_1^h(\tau) = -\frac{1}{\tau^2}\left[2\tau^2 + 3\tau + 3(2\tau-1) f(\tau)\right] \tag{B.20}$$

$$f(\tau) = \begin{cases} \arcsin^2\left(\sqrt{\tau}\right) & \tau \le 1 \\ -\frac{1}{4}\left[\ln\left(\frac{1+\sqrt{1-\tau^{-1}}}{1-\sqrt{1-\tau^{-1}}}\right) - i\pi\right]^2 & \tau > 1 \end{cases} \tag{B.21}$$

$\tau_f = s/4m_f^2$, $\tau_W = s/4m_W^2$ (which we note is a different convention for the loop parameter τ than was used in Chapter 5.)

B.4 Hadronic matrix elements

As is discussed in detail in Chapter 3, a crucial ingredient in the nuclear recoil cross section for a dark matter model is the hadronic matrix element. However, the hadronic matrix element for a Higgs mediated model like the one described in this Appendix presents some unique difficulties. The Higgs interacts with fundamental particles with a strength proportional to their mass. But how does the Higgs interact with a hadron such as the nucleon, which has a mass arising from the gluonic binding energy?

Naive estimates of what the coupling should be violate a certain common sense. However, stepping beyond the naive estimate in a rigorous way required a certain insight into how one could represent the mass of the nucleon in fundamental terms. This insight dives directly into the fundamental nature of mass and how much of it can be described as a purely quantum phenomenon. Because of these implications, the work described in this Section remains quite important to this day.

The basic (and only) treatment of the interactions between the Higgs boson and the nucleon is that of Shifman, Vainshtein and Zakharov [242], which we follow. It was been further developed in references [669, 670, 671, 243] and recently updated [253].

The interaction between the SM physical Higgs boson h and an elementary SM fermion f is described by a Yukawa coupling:

$$\mathcal{L}_{Yuk} = \frac{m_f}{v_h} h\bar{f}f. \tag{B.22}$$

These interactions are proportional to the mass of the fermion m_f over the Higgs vacuum expectation value $v_h = 246$ GeV. These values range from roughly 2/3 for the top quark ($m_t = 173$ GeV [8]) to essentially zero for the electron ($m_e = 0.511$ MeV [8]) and light quarks ($m_u \approx 4$ MeV and $m_d \approx 7$ MeV [8]).

The naive approach takes the Higgs as interacting only with the masses of the valence quarks and generating a Higgs-nucleon effective Yukawa coupling proportional to $(2\times m_u + m_d)/v_h \approx 0.00006$. This is minuscule, and vanishes completely in the commonly used chiral limit ($m_u, m_d \to 0$). This is unacceptable, as it ignores radiative contributions to the coupling and also neglects the vast majority of the rest mass of the nucleon, which is generated by chiral symmetry breaking in QCD. To assume the Higgs couples only to fermion rest mass is inconsistent.

We understand, through the fundamentals of electroweak symmetry breaking that lead to Equation (B.22), how the Higgs couples to quarks. We are also able to compute the 1-loop interaction between the Higgs and gluon fields. The question is, how to relate those microscopic interactions to the interaction of the Higgs with a bound state such as the nucleon?

The answer lies in the energy-momentum tensor of the hadron. The mass of a quantum state can be expressed in terms of its energy-momentum tensor (using the nucleon as an example)

$$m_N \bar{\Psi}_N \Psi_N = \langle N | \Theta^{\mu}_{\ \mu} | N \rangle \tag{B.23}$$

One can expand the energy-momentum tensor as

$$\Theta^{\mu}_{\ \mu} = \left[\frac{\beta(\alpha_s)}{4\alpha_s} \right] G_{\rho\nu} G^{\rho\nu} + m_u \bar{u}u + m_d \bar{d}d + m_s \bar{s}s + \sum_Q m_Q \bar{Q}Q \tag{B.24}$$

where $G_{\mu\nu}$ is the gluon field strength tensor and $\beta(\alpha_s) = -\left(9 - \frac{2n_Q}{3}\right)\frac{\alpha_s^2}{2\pi} + O(\alpha_s)$ is the QCD beta function for n_Q heavy quarks.

The inclusion of the light quarks in the matrix element is simply quantifying the matter component of the nucleon. The heavy quark term is the same, though their existence is due to quantum effects, rather than the presence of valence quarks. The first expression on the right hand side of Equation (B.24), the contribution to the nucleon energy-momentum tensor from the gluon binding force, requires some explanation. The inspiration for including the gluon binding force in this form comes from the Weyl or Trace anomaly, which states that the vacuum expectation value of the energy-momentum tensor is nonzero, or $\langle \Theta^{\mu}_{\mu} \rangle \neq 0$. The classical energy-momentum tensor has zero vacuum expectation value, but quantum corrections induce a nonzero vacuum expectation, generating an anomaly in the quantum theory. The above term is simply the vacuum expectation value of the energy-momentum tensor of QCD.

By inserting the explicit expression (B.24) for the nucleon energy-momentum tensor into the expectation value in Equation (B.23), we are able to relate the components of the nucleon to its observable mass. We can then compute the Higgs-nucleon coupling by summing contributions from the interactions of the Higgs with the components.

The heavy quark term can be enfolded into the anomaly term by using the heavy quark expansion. To first order

$$\sum_h m_Q \bar{Q}Q \longrightarrow -\frac{2}{3}\frac{\alpha_s}{8\pi} n_Q G_{\mu\nu} G^{\mu\nu} + \ldots \tag{B.25}$$

This term can be absorbed into the other gluon term, leaving

$$\langle N \left| \Theta'_{\mu\mu} \right| N \rangle = \left\langle N \left| \left[-\frac{9\alpha_s}{2\pi}\frac{1}{4\alpha_s} \right] G_{\mu\nu} G^{\mu\nu} + \sum_{q=uds} m_q \bar{q}q \right| N \right\rangle + \ldots \tag{B.26}$$

We can now understand that in the chiral limit, the effective current for heavy quarks looks like

$$\sum_Q m_Q \bar{Q}Q \longrightarrow -\frac{2}{3}\frac{\alpha_s}{8\pi} n_Q G_{\mu\nu} G^{\mu\nu} \tag{B.27}$$

Thus the heavy quark term can be written as a contribution to the gluon term.

One can obtain the gluon contribution itself by noting that in the chiral limit

$$m_N \simeq -\frac{9\alpha_s}{8\pi} \langle N | G_{\mu\nu} G^{\mu\nu} | N \rangle \tag{B.28}$$

where m_N is the phenomenological nucleon mass. By subtracting off light quark contributions from the right hand side to break the chiral limit, one can obtain the approximate gluonic contribution:

$$m_N - \langle N \left| m_u \bar{u}u + m_d \bar{d}d + m_s \bar{s}s \right| N \rangle \simeq -\frac{9\alpha_s}{8\pi} \langle N | G_{\mu\nu} G^{\mu\nu} | N \rangle. \tag{B.29}$$

The light quark contributions can be determined from the nucleon-pion sigma term

$$\sigma_{\pi N} = \frac{1}{2}(m_u + m_d) \langle N \left| \bar{u}u + \bar{d}d \right| N \rangle \tag{B.30}$$

which can be extracted from the experimental pion-nucleon scattering amplitude [243]. With zero strangeness in the nucleon, the Higgs-nucleon coupling can then be written as

$$\frac{h}{v_h} Y_{Nh} \bar{\Psi}_N \Psi_N = \frac{h}{v_h} \left\langle N \left| \Theta'_{\mu\mu} \right| N \right\rangle = \frac{h}{v_h} \left\langle N \left| \sum_Q m_Q \bar{Q} Q \right| N \right\rangle \tag{B.31}$$

$$= \frac{h}{v_h} \left(-\frac{2}{3} n_Q \right) \left\langle N \left| \frac{\alpha_s}{8\pi} G_{\mu\nu} G^{\mu\nu} \right| N \right\rangle \approx \frac{n_Q 2 m_N}{27 v_h} h \bar{\Psi}_N \Psi_N \tag{B.32}$$

$$= \frac{3}{v_h} (70\, MeV) h \bar{\Psi}_N \Psi_N \tag{B.33}$$

In the above, Y_{Nh} is the effective mass of the nucleon for the purposes of its coupling to the Higgs field, in analogy with the Yukawa couplings to fundamental fermions, while m_N is the phenomenological mass of the nucleon, appearing in an estimate of the matrix element. The number of heavy quarks has been set to three in the last step, and the vacuum expectation value of the Higgs field is taken to be $v_h = 246$ GeV. This method produces an effective Higgs-nucleon coupling constant of 0.853×10^{-3} with zero strangeness. This is actually larger than a basic coupling governed by $m_N / v_h \approx 0.4 \times 10^{-3}$.

Later treatments of this procedure note [243, 669, 670, 671] that the assumption of zero strangeness is not accurate. Inclusion of a nonzero strange quark term in Equation (B.29) leads to couplings larger by a factor of three. The strange quark content of the nucleon can be characterized by the parameter

$$y = \frac{\langle N \left| \bar{s} s \right| N \rangle}{\frac{1}{2} \langle N \left| \bar{u} u + \bar{d} d \right| N \rangle} \tag{B.34}$$

A strangeness of zero corresponds to $y = 0$.

Cheng [253] estimates the total light quark contributions to be 410 MeV, leading to a vacuum scaled Higgs-nucleon coupling of $v g_{hNN} = 530$ MeV, or $g_{hNN} \simeq 0.21 \times 10^{-3}$ as a dimensionless quantity. The numerical value of course varies with the strangeness, as discussed in Chapter 3. See references [240, 253] and the references contained therein for further details.

Appendix C

Asymptotically Safe Radiative Symmetry Breaking

This Appendix includes a discussion of the theoretical background that lies behind the phenomenological model discussed in Chapter 6. This work is more fully explored in reference [544] (see also reference [672]). The theoretical framework is provided in brief, with technical details mostly remaining in the references. The work presented in this Appendix represents the parts of the project that were the responsibility of the author's collaborators, and hence lie outside of his expertise. As this thesis is primarily focussed on phenomenology, the theoretical underpinnings have been relegated to this Appendix.

C.1 Asymptotic safety

The fundamental theoretical idea that lies behind this model is the notion of asymptotic safety, specifically as a means of realizing a conformal symmetry as the custodial symmetry for the Higgs mass. This provides a way to address the hierarchy problem and, as we will see later, electroweak symmetry breaking. For a summary of these ideas, see reference [542]. As mentioned in broad strokes in Chapter 1, the Higgs mass is highly sensitive to quantum corrections. A theory in which a symmetry is exploited to protect the Higgs mass against those corrections is said to have a custodial symmetry. Bardeen [673] pioneered the use of a conformal symmetry as a custodial symmetry for the Higgs mass. Combining AS with quantum conformal symmetry addresses naturalness as well. Only SUSY, global or gauge symmetries, and conformal symmetries can be custodial according to the Coleman-Mandula Theorem [674].

Conformal symmetry as a custodial symmetry for the SM is tied to the notion of asymptotic safety. Asymptotic safety can be thought of as a generalization of asymptotic freedom, as discussed in Chapter 1. In asymptotic freedom, the coupling parameter runs to zero at high energies, which entails a noninteracting UV theory. In an asymptotically safe theory, the coupling parameter runs to some finite nonzero value, called an interacting fixed point. The theory remains interacting to any energy, but the coupling approaches a constant, avoiding such issues as the Landau poles that plague generic $U(1)$ gauge theories. More formally, a theory is asymptotically safe if there exist a finite number of finite parameters that define the theory at arbitrarily high energies. Asymptotic safety is an attempt to generate a kind of nonperturbative renormalizability, and was originally proposed in the context of gravitational theories [675]. More details about asymptotic safety [676, 677] are available in the literature.

Next, we provide a few quick details about conformal symmetries. The conformal group in d dimensions is the group $SO(d+1,1)$. By definition, a conformal transformation is an invertible transformation $x^{\mu\prime} \to x^{\mu}$ that leaves the metric tensor $g_{\mu\nu}$ of a d-dimensional space invariant up to a scaling:

$$g'_{\mu\nu}\left(x^{\mu\prime}\right) = \Lambda\left(x^{\mu}\right) g_{\mu\nu}\left(x^{\mu}\right) \tag{C.1}$$

This has the consequence of preserving angles between vectors, but not necessarily distances.

A conformal field theory is one that is invariant under conformal transformations (see reference [678] for general details). In particle physics, the most important conformal transformation is scaling:

$$x^{\mu} \to x^{\mu\prime} = \lambda x^{\mu} \tag{C.2}$$

for the case which also preserves Lorentz covariance (time and space are scaled by the same factor). In fact, scaling is so important in particle physics that there is the tendency to refer to scale-invariant field theories as conformal field theories, and though it is often the case that a scale-invariant theory is also conformal, examples where that is not the case exist [679].

What is usually taken as the criterion for a field theory being a conformal theory is the beta function being zero. As was discussed in Chapter 1, the beta function describes the way the parameters of the theory change as the interaction scale changes due to quantum corrections. When the beta function is zero, there is no change with scale, and hence the theory is scale-invariant. This is not quite a rigorous theorem [680], but it is frequently taken to be one.

For the conformal symmetry to be realized in nature, it must obviously be broken at some scale, as observed reality is clearly not scale invariant. One might expect that this breaking would spoil the custodial nature of the symmetry, but that can be avoided if the breaking is sufficiently 'soft.' In the context of symmetry breaking and custodial symmetries, 'softness' is analogous to photons being described as 'hard' or 'soft:' that is, the photon is high energy or low energy with respect to some energy scale relevant to the process being considered. A 'softly' broken symmetry is one in which the breaking terms are small enough at high energies that the symmetry is essentially unbroken, while the soft terms are enough to break the symmetry at low energies.

For a custodial symmetry of the Higgs mass, this means that UV corrections to the Higgs mass are so small that no divergent contributions to the scalar mass are generated. There may be finite corrections, but there can be no quadratic corrections. There are no cancellations, because there is nothing that needs to be cancelled. That the theory is scale invariant at some point means that the divergences do not spoil the symmetry. One way of characterizing the soft breaking of conformal symmetry is by saying the breaking terms do not spoil the conformal fixed point at high energy. Inclusion of soft symmetry breaking terms is a symptom of an effective theory wanting a UV completion. Note that to be custodian of the Higgs mass, the conformal symmetry must be a quantum conformal symmetry. A conformal symmetry is a fragile custodial symmetry, as threshold contributions from new states at higher energy scales can easily break the conformal symmetry.

If one is considering asymptotic safety, it is important to consider gravitational contributions. This is done by treating gravity as a conformal theory that reduces to the standard Einstein-Hilbert gravity at low energies [681, 682, 683]. In the brief discussion that follows, gravity is treated as an external field, contributing to the particle physics system but unaffected by it.

The gravitational contribution to the beta function is [684]

$$\beta_j^{grav} = \frac{a_j}{8\pi} \frac{k^2}{M_p^2(k)} x_j. \tag{C.3}$$

Gravitational contributions to the SM β function in the gauge and Yukawa sectors are negative [684], which guarantees the associated couplings are asymptotically safe to any scale. However, the contribution to the SM Higgs quartic coupling is positive, so to retain asymptotic safety, the Higgs quartic coupling must run to a fixed point ($\lambda_1(m_{UV}) = 0$, $\beta_{\lambda_1}(m_{UV}) = 0$), which will stabilize the Higgs vacuum. A sector of the theory is noninteracting is the coupling $\lambda(\mu) = 0$ and is fixed if the beta function $\beta(\mu) = 0$.

For $\lambda \neq 0$ at the fixed point, the gravitational contribution β_{grav} is nonzero, and hence the point is not actually fixed, so the fixed point must be noninteracting. In this scenario, the system is UV complete and all SM couplings hit a Gaussian (noninteracting) fixed point at some high energy scale. The UV boundary conditions can then be exploited to provide a stable Higgs vacuum, leading to electroweak symmetry breaking.

C.2 Electroweak symmetry breaking

We now seek to tie the asymptotically safe theory to phenomenology, specifically to electroweak symmetry breaking. The SM is classically conformal up to the Higgs masslike term that generates electroweak symmetry breaking spontaneously in the SM. To generate electroweak symmetry breaking 'naturally', one would like to modify the SM at some high energy scale to include a symmetry that can act as a custodian for the Higgs mass. In our case, this is the conformal symmetry, which is softly broken at low energies, but is restored at high energies and can act thus act as a custodial symmetry. This model is, in the scalar sector, a variant of the complex singlet extension of the SM, complete with hidden $U(1)$ gauge symmetry and Higgs-portal interaction. Extending the SM is necessary to include asymptotic safety. In the minimal case, the SM can be extended by an additional $U(1)$ gauge symmetry.

Electroweak symmetry breaking can be realized through the Coleman-Weinberg (CW) mechanism of radiative symmetry breaking. Radiative symmetry breaking is essentially the breaking of a classical symmetry through quantum radiative corrections. The CW mechanism is an explicit realization of radiative symmetry breaking [545], which was applied with great success to massless scalar QED. It is well known that the CW technique does not work as a dynamical symmetry breaking mechanism in the SM because of the large top quark Yukawa coupling, which dominates the effective potential and has negative sign, making the potential

unbounded from below. The scalar sector of the model is derived almost directly form scalar QED, in which the CW mechanism can be actualized, with the inclusion of a Higgs-portal interaction to communicate the radiative symmetry breaking to the electroweak sector, where electroweak symmetry breaking can occur.

The electroweak scale can be generated dynamically through the symmetry breaking process by a relabelling of degrees of freedom known as dimensional transmutation [685]. Essentially, dimensionless parameters (e and λ in scalar QED) exist in the theory, and a scale μ is introduced by the renormalization process. By relating the dimensionless parameters and the scale of the vacuum expectation value through the renormalization scale μ, we can write the theory in terms of one of the dimensionless parameters and the vacuum of the theory v, thus introducing a scale through renormalization into what was previously a scale invariant theory. The introduction of a dimensionful parameter is obviously why the technique is known as dimensional transmutation.

The CW mechanism is difficult to realize in our model. The asymptotically safe boundary condition in the UV needs $\beta_{\lambda_3} < 0$ at some high energy, while the CW mechanism requires $\beta_{\lambda_3} > 0$ at a high energy, where it can run to the IR from. This problem can be resolved by implementing a hierarchy of scales, and allowing β_{λ_3} to change sign some time between the two UV scales. The CW mechanism can work, therefore, when $\beta_{\lambda_3} < 0$ at high energies and $\beta_{\lambda_3} > 0$ at lower, but still high, energies, allowing the singlet quartic coupling to reach a noninteracting fixed point in the UV and triggering radiative symmetry breaking in the IR through the CW mechanism. This is obviously a delicate situation to realize naturally. Some of the tricks used are discussed in reference [544]. Radiative symmetry breaking occurs at the scale v_s in the singlet sector through the CW mechanism in the standard fashion, and this then triggers electroweak symmetry breaking in the Higgs sector through the Higgs-portal interaction. A negative mass-like term is generated by the Higgs-portal interaction term, which allows spontaneous electroweak symmetry breaking to proceed in the usual way.

This has been a basic sketch of how radiative symmetry breaking can be used to generate electroweak symmetry breaking. But one needs to solve the renormalization group equations to actualize this scenario and relate the theory to phenomenology.

C.3 Renormalization group analysis

The renormalization group equations are a system of nine equations, where the following beta functions were used [560, 561]

$$\begin{aligned}
16\pi^2\beta_{\lambda_1} &= \lambda_2^2 - 3\lambda_1 g_{mix}^2 + \frac{3}{8}g_{mix}^4 + \beta_{\lambda_1}^{SM};\\
16\pi^2\beta_{\lambda_2} &= 12 g_{mix}^2 g'^2 + 6Y_t^2\lambda_2 - 24 g'^2\lambda_2 + 4Y_M^2\lambda_2 + 4\lambda_2^2 + 12\lambda_1\lambda_2 + 8\lambda_2\lambda_3 - \frac{3}{2}\lambda_2\left(g_{mix}^2 + 3g_2^2 + g_1^2\right);\\
6\pi^2\beta_{\lambda_3} &= 96 g'^4 - 16Y_M^4 + 2\lambda_2^2 - \lambda_3\left(48 g'^2 + 8Y_M^2 + 20\lambda_3\right);\\
16\pi^2\beta_{Y_t} &= -\frac{17}{12}Y_t g_{mix}^2 - \frac{2}{3}Y_t g'^2 - \frac{5}{3}Y_t g' g_{mix} + \beta_{Y_t}^{SM};\\
16\pi^2\beta_{g'} &= \frac{1}{18}g'\left(76 g'^2 + 64 g' g_{mix} + 123 g_{mix}^2\right);\\
16\pi^2\beta_{g_{mix}} &= g_{mix}\left(\frac{41}{6}\left(g_{mix}^2 + 2g_1^2\right) + \frac{38}{9}g'^2\right) + \frac{32}{3}g'\left(g_{mix}^2 + g_1^2\right);\\
16\pi^2\beta_{Y_M} &= -6Y_M g'^2 + 6Y_M^3;\quad 32\pi^2\gamma_\varphi = Y_M^2 - 24 g'^2.
\end{aligned} \tag{C.4}$$

The difficulty of solving this system can be reduced by providing further constraints. The asymptotically safe boundary conditions are one:

$$\beta_{\lambda_1}(M_{UV}) = \beta_{\lambda_3}(M_{UV}) = \lambda_1(M_{UV}) = \lambda_2(M_{UV}) = \lambda_3(M_{UV}) = 0 \tag{C.5}$$

where the UV scale M_{UV} is not necessarily the Planck scale M_{pl}.

Table C.1: Parameters derived from the solution to the renormalization group equations

$M_{Z'}$ (TeV)	$10^6\lambda_2$	$10^6\lambda_3$	g'	g_m	Y_M	Y_t	m_{ν_R} (TeV)	v_1 (TeV)	m_S (GeV)
1.9	-6	-4.05	0.18	0.042	0.28	0.77	2.02	5.1	20
3.4	-0.59	-0.13	0.1	0.023	0.16	0.74	3.72	16.9	11.5
6.8	-0.036	-0.002	0.05	0.011	0.08	0.70	7.59	68.8	6

Mass values for the Z' boson were chosen somewhat arbitrarily and then those values were used as additional constraints on the renormalization group equations, through the relation:

$$m_{Z'} = 2g'v_s \tag{C.6}$$

Finally, radiative symmetry breaking provides a further constraint, through the Higgs-portal coupling. The Higgs mass is determined by electroweak symmetry breaking, but it is also an experimentally determined parameter. As electroweak symmetry breaking has been triggered by radiative $U(1)'$ symmetry breaking, one has the relation

$$2v_s\lambda_1 = -v_s^2\lambda_2 = m_h^2 \tag{C.7}$$

which acts as a constraint. Too light a Higgs mass and $\beta(\lambda_H)$ governing the quartic Higgs coupling goes negative and the Higgs quartic coupling λ_H crosses zero at some high energy scale, causing the Higgs potential to become unstable.

The renormalization group equations are then solved [544] with the above constraints and boundary conditions (C.5), yielding the results presented in Table C.1.

The $U(1)'$ gauge field can only couple to at most two generations of SM fermion, as contributions from more than one generation will cause the $U(1)'$ coupling to run to a Landau pole before the UV scale (this is in agreement with references [560, 561]). This would make the scenario untenable theoretically. That the $U(1)'$ gauge field can only couple to two generations while retaining stability can be considered a feature of the theory. Phenomenological constraints can be used to further restrict this to the third generation of SM fermions alone (see the discussion in Chapter 6).

Appendix D

Dark Matter Density Profiles

This Appendix provides some details about the density profiles of dark matter in the galactic halo. These profiles are input for many of the calculations that appear in this thesis, though often in an obscured way. As was discussed in Chapter 1, the present day structure of cold dark matter grows from accretion of smaller substructures over time [686]. Following these models the dark matter mass distribution in the galaxy can be parameterized as a function of radius, with the parameters of the fit and the functional form being determined from simulations of gravitational collapse and being fit to observations.

Profiles are obtained by fitting the solutions of N-body simulations, where N is now in the billions. Advanced techniques are used to treat large sets of particles (1000 solar masses or so) as discrete objects, which is generally a valid approximation to the galactic scale [148]. Until recently, these simulations have only taken cold dark matter into account, but baryonic effects can now be included to some extent. These baryonic effects, including stellar formation events, supernovae, and other events in the stellar lifecycle that provide feedback to the halo evolution can be important. For reviews of the numerical techniques, see [687, 688].

The generic form of a dark matter density profile is [689] (called the generalized Navarro-Frenk-White or NFW profile, as opposed to the specific one which has their fit parameters included)

$$\rho(r) = \frac{\rho_c}{\left(\frac{r}{r_s}\right)^{\gamma}\left[1+\left(\frac{r}{r_s}\right)^{\alpha}\right]^{\frac{(\beta-\gamma)}{\alpha}}}. \tag{D.1}$$

The parameter ρ_c is a characteristic density and r_s is a dimensionful parameter related to the core radius of the profile. The dimensionless parameters α, β and γ are fit to various simulations. Practically, the profiles terminate at some distance $r_{max} = Cr_s$, with C usually taken to be $\mathcal{O}(10)$. The standard NFW profile has the characteristic r^{-1} behaviour near the center and r^{-3} behaviour near the edge of the halo. The standard NFW profile appears to fit more or less all halos observed [148]. We use the standard NFW profile where an explicit profile is required.

Also of interest in the past few years are the Einasto profile:

$$\rho(r) = \rho_c \exp\left\{-\left(\frac{2}{\alpha}\right)\left[\left(\frac{r}{r_s}\right)^{\alpha}-1\right]\right\}, \tag{D.2}$$

and the Burkert profile

$$\rho(r) = \frac{\rho_c}{\left(\frac{r}{r_s}+1\right)\left[1+\left(\frac{r}{r_s}\right)^{2}\right]}. \tag{D.3}$$

These variant profiles emphasize different inputs than the basic NFW profile. The Burkert profile [690] and the Isothermal profile [99] are more closely fit to observations of galactic rotation curves than to numerical simulations. The Einasto profile [691, 692] is a better fit too more recent simulations, behaving differently to NFW in the core regions. As well, Einasto profiles tend to become steeper when baryonic effects are included [693].

There is evidence that dark matter halos are not smooth at sub-galactic scales [694, 695], indicating the existence of potential substructure. While halo substructures have not been observed, assuming their existence is not absurd, and their presence could have a significant effect on the detection of dark matter. For instance, direct detection experiments assume standard halo properties for the dark matter flux, as discussed in Chapter 3. Indirect searches, as well, could use more dense halo substructures as targets for annihilation observations [264].

Appendix E

Gauge Sector Mixing

This Appendix details the various technical details involved in going between the bare theoretical Lagrangian and the phenomenological Lagrangian of the model discussed in Chapter 6, particularly the details of the gauge group transformations. Much of this material is adapted from [546].

The gauge sector of the Lagrangian of a theory with a $U(1)_1 \times U(1)_2$ gauge symmetry and with explicit tree level kinetic mixing between the gauge fields is

$$\mathcal{L} = -\frac{1}{4}B^1_{\mu\nu}B^{1\mu\nu} - \frac{1}{4}B^2_{\mu\nu}B^{2\mu\nu} - \frac{\epsilon_m}{2}B^1_{\mu\nu}B^{2\mu\nu}. \tag{E.1}$$

The $B^i_{\mu\nu} = \partial_\mu A^i_\nu - \partial_\nu A^i_\mu$ are gauge field strength tensors as usual, with A^i_μ the gauge field of gauge group $U(1)_i$. The parameter ϵ_m, which is constrained by $|\epsilon_m| < 1$, describes the tree level mixing between the gauge fields $U(1)_1$ and $U(1)_2$. Such a term can be included because it violates neither of the gauge symmetries [696], generating a phenomenon characteristic of $U(1)$ gauge groups.

Coupling to generic matter fields Ψ_k is achieved through the gauge covariant derivative of the product group, given by

$$D_\mu = \partial_\mu + iY^a_k g_{ab} A^b_\mu, \tag{E.2}$$

where the Einstein summation convention over $a, b = 1, 2$ is understood. The Y^a_k can be understood as the gauge charges of the matter field Ψ_k under the gauge group $U(1)_a$, where the g_{ab} are the gauge coupling parameters, which unfortunately share notation with the metric tensor of curved spacetime. It should be pointed out that the two off-diagonal mixed components g_{12} and g_{21} will generate interactions if the matter fields carry the appropriate charge. These off-diagonal terms can be avoided at tree level by setting ϵ_m to zero, but all four components will run under renormalization group evolution and will in general have nonzero contributions from radiative corrections. This fact is of phenomenological importance for some models [547].

It is convenient to transform the Lagrangian of Equation (E.1) so as to remove the explicit kinetic mixing term. This will make the gauge boson propagators much simpler to deal with. To proceed, we write the fields $A^{1,2}_\mu$ in terms of new fields:

$$A^1_\mu = \frac{1}{\sqrt{2\,(1+\epsilon_m)}}A^Y_\mu + \frac{1}{\sqrt{2\,(1-\epsilon_m)}}A^E_\mu, \tag{E.3}$$

$$A^2_\mu = \frac{1}{\sqrt{2\,(1+\epsilon_m)}}A^Y_\mu - \frac{1}{\sqrt{2\,(1-\epsilon_m)}}A^E_\mu. \tag{E.4}$$

It can be easily seen that the kinetic cross term in Equation (E.1) will vanish after this transformation, though a counterterm will be required for renormalization. The covariant derivative retains the same form, with the transformed couplings:

$$D_\mu = \partial_\mu + iY^\alpha_k g_{\alpha\beta} A^\beta_\mu, \tag{E.5}$$

where we have denoted the transformation by greek indices: $\alpha, \beta = Y, E$. The Y^α_k and the $g_{\alpha\beta}$ are of course different from their latin indexed equivalents.

Because the off-diagonal terms in $g_{\alpha\beta}$ are related by the constraint of gauge invariance on the original Lagrangian, there is a rotational symmetry that can be exploited, allowing one of the four couplings to be set to zero (or some other convenient value) [546]. This will also prove to be helpful when considering the phenomenology.

The above analysis was generic to any $U(1)_1 \times U(1)_2$ gauge group, and is generalizable to the product of any number of $U(1)$ gauge groups, though with increasing complexity. To continue, we need to specify our model, including the symmetry breaking pattern. For consistency with the rest of the Chapter, we now refer

to the gauge group as $U(1)_Y \times U(1)'$. After breaking of $U(1)'$, but before electroweak symmetry breaking, we can make an orthogonal field redefinition

$$E_\mu = \frac{g_{EE}A^E_\mu + g_{EY}A^Y_\mu}{\sqrt{g^2_{EE}+g^2_{EY}}},\ B_\mu = \frac{-g_{EY}A^E_\mu + g_{EE}A^Y_\mu}{\sqrt{g^2_{EE}+g^2_{EY}}}. \tag{E.6}$$

The E_μ will pick up a mass term through $U(1)'$ breaking, and the B_μ will play the role of the SM hypercharge gauge field.

The full $U(1)_Y \times U(1)'$ neutral current coupling to matter Ψ_k can then be written

$$J_\mu = g_y Y^Y_k B_\mu + \left(g_E Y^E_k + g'_{mix} Y^Y_k\right) E_\mu, \tag{E.7}$$

where the new coupling parameters g_y, g_E and g' are

$$g_y = \frac{g_{EE}g_{YY} - g_{EY}g_{YE}}{\sqrt{g^2_{EE}+g^2_{EY}}} \tag{E.8}$$

$$g_E = \sqrt{g^2_{EE}+g^2_{EY}} \tag{E.9}$$

$$g'_{mix} = \frac{g_{YE}g_{EE} + g_{EY}g_{YY}}{\sqrt{g^2_{EE}+g^2_{EY}}} \tag{E.10}$$

Note that in this basis, the mixing is cast on to the E field, which couple to both E charges and Y charges, and that the B field couples only to Y charged particles. This is a consequence of using the extra degree of freedom allowed by the rotational invariance.

Following through with the usual gauge rotations in the SM gauge boson sector, we obtain

$$\begin{pmatrix} B_\mu \\ W^3_\mu \\ E_\mu \end{pmatrix} = \mathcal{M} \begin{pmatrix} A_\mu \\ Z_\mu \\ Z'_\mu \end{pmatrix} \tag{E.11}$$

where the mixing matrix $\mathcal{M}$ depends on the mixing angles, and has an explicit form available in the literature [546]. Included in the rotation is a redefinition of the gauge couplings into the phenomenological g' and g_{mix}.

The neutral current interactions of fermions with the Z and Z' take the form, including mixing effects:

$$\begin{aligned} J^\mu_Z &= g_Y \left(Y_L \bar{f}\gamma^\mu P_L f + Y_R \bar{f}\gamma^\mu P_R f\right) \\ &= \bar{f}\gamma^\mu \left(V^Z_f + A^Z_f \gamma^5\right) f, \end{aligned} \tag{E.12}$$

$$\begin{aligned} J^\mu_{Z'} &= \left(g' Q'_L + g_{mix} Y_L\right) \bar{f}\gamma^\mu P_L f + \left(g' Q'_R + g_{mix} Y_R\right) \bar{f}\gamma^\mu P_R f \\ &= \bar{f}\gamma^\mu \left(V'_f + A'_f \gamma^5\right) f. \end{aligned} \tag{E.13}$$

where the generalized charges are as defined in Chapter 6:

$$V_f = g' \left(\frac{Q'_{fL} + Q'_{fR}}{2}\right) + g_{mix} \left(\frac{Y_{fL} + Y_{fR}}{2}\right) \tag{E.14}$$

$$A_f = -g' \left(\frac{Q'_{fL} - Q'_{fR}}{2}\right) - g_{mix} \left(\frac{Y_{fL} - Y_{fR}}{2}\right). \tag{E.15}$$

For more details on gauge mixing effects in beyond SM $U(1)$ gauge groups, see references [696, 697, 698, 699]. They discuss gauge mixing effects in some detail for a variety of scenarios. Experimental bounds on mixing are reported most recently in reference [570].

Appendix F

Flavor-changing neutral currents

It is well known that there are no flavor changing neutral currents (FCNCs) at tree level in the SM [700, 701]. This is a consequence of the universality of SM neutral current couplings over the generations of fermions. In the model under consideration in Chapter 6, this is not the case, as only the third generation of quarks carries $U(1)'$ charge. This Appendix is a brief technical explanation of why mixed fermion couplings cannot be ignored.

FCNCs may occur when neutral currents with non-universal family couplings are introduced into the theory. They follow from the same misalignment of gauge and mass eigenstates in the fermion sector which lead to fermion mixing in SM charged currents, as parameterized by the Cabibbo-Kobayashi-Maskawa (CKM) matrix. FCNCs do not occur in the SM, because the electroweak neutral current couples in the same way to every generation of fermions within a family. These effects have been well-studied in the literature [702, 703, 704].

However, when the same analysis is applied to the case of a non-universal coupling, such as for the Z' discussed in Chapter 6 that couples only to a single generation of quarks, we see off-diagonal elements appear in the fermion mixing matrix, indicating fermion mixing. The following analysis is adapted from [704].

Consider the $U(1)'$ neutral current

$$J'_\mu = \sum_{i,j} \bar{\psi}_i \gamma_\mu \left[\epsilon'_{\psi_{Lij}} P_L + \epsilon'_{\psi_{Rij}} P_R \right] \psi_j. \tag{F.1}$$

The sum is over all fermions i and j. The chiral projectors as usual are $P_L = (1/2)(1-\gamma^5)$ and $P_R = (1/2)(1+\gamma^5)$, and the $\epsilon'_{\psi_{L,Rij}}$ describe the chiral couplings of the new gauge boson. For the case with no kinetic mixing (the case with kinetic mixing will be discussed at the end of the Appendix), $\epsilon'_{\psi_{L,Rii}} = g' Q'_{\psi_{iL,R}}$, with g' the $U(1)'$ gauge parameter and $Q'_{L,R}$ the $U(1)'$ chiral charge of the fermion $\psi_{L,R}$. We assume for simplicity in this example that there are no explicit mixed charges in this basis (that $\epsilon'_{\psi_{L,Rij}} = 0$ for $i \neq j$).

The fermion Yukawa matrices $\tilde{h}_\psi$ in the weak eigenstate basis can be diagonalized by unitary matrices $V_{L,R}^{\psi,ew}$:

$$h_\psi = V_R^{\psi,ew} \tilde{h}_\psi V_L^{\psi,ew\dagger}, \tag{F.2}$$

where the product of the up- and down-type matrices gives the CKM matrix

$$V_{CKM} = V_L^{u,ew} V_L^{d,ew\dagger}. \tag{F.3}$$

This means the fermion fields ψ_i must be multiplied by these matrices:

$$\psi_{(L,R)i} = V^{\psi,ew}_{(L,R)ij} \tilde{\psi}_{(L,R)j}. \tag{F.4}$$

This procedure is what leads to flavor changing charged currents in the SM, as parameterized by the CKM matrix.

Applying this same process to the $U(1)'$ gauge sector amounts to altering the neutral current (F.1) to become

$$J'_\mu = \sum_i \bar{\psi}_i \gamma_\mu \left[B_{ij}^{\psi_L} P_L + B_{ij}^{\psi_R} P_R \right] \psi_j \tag{F.5}$$

where the transformed chiral couplings (that mix the fermions) are

$$B_{ij}^{\psi_L} = \left(V_L^\psi \epsilon'_{\psi_L} V_L^{\psi\dagger} \right)_{ij}, \; B_{ij}^{\psi_R} = \left(V_R^\psi \epsilon'_{\psi_R} V_R^{\psi\dagger} \right)_{ij}. \tag{F.6}$$

with matrices $V^{\psi}_{L,R}$ that relate the fermion mass eigenstate basis to the $U(1)'$ gauge basis, that are not necessarily related to the CKM matrices. They are distinguished by the omission of the ew superscript. This will be addressed again later.

Note that the generations of fermions cannot be decoupled, as they share the same eigenstate rotation matrices. Consider the case of family universal couplings, as in the case of the SM weak neutral current. The epsilon are proportional to the identity matrix:

$$\epsilon^{SM}_{\psi_{L,R}} = \begin{pmatrix} \mathcal{A} & 0 & 0 \\ 0 & \mathcal{A} & 0 \\ 0 & 0 & \mathcal{A} \end{pmatrix} \tag{F.7}$$

When this matrix is inserted into (F.6), we see that the factor scaling the identity matrix can be factored out and the unitarity of the $V^{\psi}_{L,R}$ leaves the $B^{\psi_{L,R}}$ diagonal.

$$V^{\psi}_{L}\epsilon'_{\psi_L}V^{\psi\dagger}_{L} = V^{\psi}_{L}\begin{pmatrix} \mathcal{A} & 0 & 0 \\ 0 & \mathcal{A} & 0 \\ 0 & 0 & \mathcal{A} \end{pmatrix}V^{\psi\dagger}_{L}$$

$$= \mathcal{A}V^{\psi}_{L}\begin{pmatrix} 1 & 0 & 0 \\ 0 & 1 & 0 \\ 0 & 0 & 1 \end{pmatrix}V^{\psi\dagger}_{L} = \mathcal{A}V^{\psi}_{L}V^{\psi\dagger}_{L} = \mathcal{A}I_{3\times 3}$$

This implies that there are no flavor changing neutral currents, and no fermion mixing, as we know to be true for the SM neutral current.

However, when the $\epsilon'_{\psi_{L,R}}$ is not proportional to the identity, the above reasoning does not apply. Consider the following $\epsilon'_{\psi_{L,R}}$:

$$\epsilon'_{\psi_{L,R}} = \begin{pmatrix} \mathcal{A} & 0 & 0 \\ 0 & \mathcal{B} & 0 \\ 0 & 0 & \mathcal{B} \end{pmatrix}. \tag{F.8}$$

Inserting these matrices explicitly into (F.5) gives as a matrix equation for a single family (in our case, without kinetic mixing, $\epsilon'_{\psi_L} = \epsilon'_{\psi_R}$)

$$J'^{\Psi}_{\mu} = \bar{\Psi}\gamma_{\mu}\left(\left[V^{\Psi}_{L}\begin{pmatrix} \mathcal{A} & 0 & 0 \\ 0 & \mathcal{B} & 0 \\ 0 & 0 & \mathcal{B} \end{pmatrix}V^{\Psi\dagger}_{L}\right]P_L + \left[V^{\Psi}_{R}\begin{pmatrix} \mathcal{A} & 0 & 0 \\ 0 & \mathcal{B} & 0 \\ 0 & 0 & \mathcal{B} \end{pmatrix}V^{\Psi\dagger}_{R}\right]P_R\right)\Psi \tag{F.9}$$

where the Ψ are generation-vectors of fermion fields (ie $\Psi_D = D = (d, s, b)$ for down-type quarks), and the $V^{\Psi}_{L,R}$ are matrices denoted by the first member of the generation for simplicity. Note that the couplings are different in our case for the different families of fermions, so we should be using the notation $\mathcal{A}_{\Psi}$, where $\Psi = U,\ D,\ E$.

The matrix products are such that, for example, the element $B^{L}_{12} = B^{L*}_{21} = B^{L}_{ds} = V^{D}_{L,11}V^{D*}_{L,21}\mathcal{A} + V^{D}_{L,12}V^{D*}_{L,22}\mathcal{B} + V^{D}_{L,13}V^{D*}_{L,23}\mathcal{B}$. Note that this term will be 0 ($V^{d}_{L,11}V^{d*}_{L,21} + V^{d}_{L,12}V^{d*}_{L,22} + V^{d}_{L,13}V^{d*}_{L,23} = 0$ for a unitary matrix) if $\mathcal{A} = \mathcal{B}$. If $\mathcal{A} \neq \mathcal{B}$, then for this term to be zero, we need to be arbitrarily setting some of the $V^{D}_{L,ij}$ matrix elements to zero.

The element B^{L}_{ds} is off-diagonal, and therefore induces mixing between fermions in the neutral current. Most experimental bounds are presented in terms of these elements B^{L}_{ij}, as will be discussed later.

We can see the effects of the difference in couplings by splitting the current into its flavor conserving and flavor changing components:

$$J'^{\Psi}_{\mu} = \bar{\Psi}\gamma_{\mu}\mathcal{A}\left(\left[V^{\Psi}_{L}V^{\Psi\dagger}_{L}\right]P_L + \left[V^{\Psi}_{R}V^{\Psi\dagger}_{R}\right]P_R\right)\Psi$$

$$+ \bar{\Psi}\gamma_{\mu}\left(\left[V^{\Psi}_{L}\begin{pmatrix} 0 & 0 & 0 \\ 0 & \mathcal{A}-\mathcal{B} & 0 \\ 0 & 0 & \mathcal{A}-\mathcal{B} \end{pmatrix}V^{\Psi\dagger}_{L}\right]P_L + \left[V^{\Psi}_{R}\begin{pmatrix} 0 & 0 & 0 \\ 0 & \mathcal{A}-\mathcal{B} & 0 \\ 0 & 0 & \mathcal{A}-\mathcal{B} \end{pmatrix}V^{\Psi\dagger}_{R}\right]P_R\right)\Psi. \tag{F.10}$$

The first term conserves flavor, while the second term changes it. Note that the flavor changing parts of $B^{L,R}$ are proportional to the differences is the coupling of the gauge boson to different generations. This amounts to a difference in charge for a universal gauge coupling parameter. The explicit flavor changing part of $B^L_{ds} = \left(V^D_{L,12}V^{D*}_{L,22} + V^D_{L,13}V^{D*}_{L,23}\right)(\mathcal{A} - \mathcal{B})$.

The above expression is slightly misleading, as it seems to imply that all fermions will now couple to the Z' with coupling $\mathcal{A}$ in the flavor conserving part. This is not true, as those contributions are cancelled by the diagonal parts of the flavor changing term. The expression makes explicit the contributions of the off-diagonal terms in the flavor changing part, which is why it has been kept.

Inclusion of kinetic mixing is simple. The chiral charges are modified to include the mixing factor, in line with the effective current being used in Chapter 6: $J^{Z'}_\mu = \bar{\psi}\gamma_\mu\left(g'Q' + g_{mix}Q^Y\right)\psi$. For this model, using SM hypercharge values and $U(1)'$ charge values $Q'_{uL} = Q'_{uR} = Q'_{dL} = Q'_{dR} = 1/3$ and the remainder of the quarks having zero $U(1)'$ charge, get the following chiral couplings:

$$\begin{aligned}
\mathcal{A}_{uL} &= \frac{1}{3}g' + \frac{1}{3}g_{mix}, \mathcal{A}_{uR} = \frac{1}{3}g' + \frac{4}{3}g_{mix},\\
\mathcal{A}_{dL} &= \frac{1}{3}g' + \frac{1}{3}g_{mix}, \mathcal{A}_{dR} = \frac{1}{3}g' - \frac{2}{3}g_{mix},\\
\mathcal{B}_{uL} &= 0 + \frac{1}{3}g_{mix}, \mathcal{B}_{uR} = 0 + \frac{4}{3}g_{mix},\\
\mathcal{B}_{dL} &= 0 + \frac{1}{3}g_{mix}, \mathcal{B}_{dR} = 0 - \frac{2}{3}g_{mix}.
\end{aligned}$$

Note that the L and R components are no longer equal, since they have different SM hypercharge values. The differences are then:

$$\begin{aligned}
\mathcal{A}_{uL} - \mathcal{B}_{uL} &= \frac{1}{3}g',\\
\mathcal{A}_{uR} - \mathcal{B}_{uR} &= \frac{1}{3}g',\\
\mathcal{A}_{dL} - \mathcal{B}_{dL} &= \frac{1}{3}g',\\
\mathcal{A}_{dR} - \mathcal{B}_{dR} &= \frac{1}{3}g'.
\end{aligned}$$

The mixing contributions cancel out, leaving the flavor changing part of the neutral current proportional to the charge difference between generations. Note that there will be no flavor changing currents in the leptonic sector, because leptophobia implies all charges are zero, so $\mathcal{A}_e = \mathcal{A}_\mu = \mathcal{A}_\tau$. This is fortunate, since bounds on flavor changing neutral currents are much stronger in the leptonic sector [548].

In this example, we would find a $Z'ds$ vertex (at tree level) of the form

$$\mathcal{V}_{Z'ds} = \frac{1}{3}g_{Z'}Z'^\mu\gamma_\mu\bar{d}\left(\left(V^D_{L,12}V^{D*}_{L,22} + V^D_{L,13}V^{D*}_{L,23}\right)P_L + \left(V^D_{R,12}V^{D*}_{R,22} + V^D_{R,13}V^{D*}_{R,23}\right)P_R\right)s + \text{h.c.} \tag{F.11}$$

There is still the issue of the $V^\Psi_{L,R}$ matrices. In principle, they are free parameters of the theory, like the CKM matrix in the SM, and must be determined from experiment. Experimental bounds are presented in terms of the $B^{L,R}$ matrices, and many papers are unclear about what assumptions they are making about $V^\Psi_{L,R}$ when they compare to these bounds.

The purpose of this Appendix was to demonstrate that FCNCs do appear in the model discussed in Chapter 6. Their appearance follows from the need for stability in the renormalization group equations as discussed in Appendix C, which requires that at most two generations of SM fermions have fundamental $U(1)'$ charge. Phenomenological constraints on FCNCs constrain harshly mixing involving the first and second generations. Hence, if there is a generation of fermions with fundamental $U(1)'$ charge, it must be the third generation, making the model tritophilic.

Appendix G

Details of the tritophilic Z'-nucleon interaction

This Appendix summarizes some of the work done by the author in reference [547], which is an exploration of the effective nonrelativistic coupling between the nucleon and a tritophilic (couples to third generation only) Z' boson. The purpose of this study was to extract the dominant contributions to the nuclear recoil cross section for vector-portal dark matter with a tritophilic mediator. This model is considered in Chapter 6, and these results are applied there, but the model has also been considered in the literature [623, 596, 621, 622].

The results of the calculation done in this Appendix apply to a specific class of models in which there is a gauge group under which only the third generation of quarks is charged. The techniques used in this calculation are common ones in hadronic physics, and can be applied in many other situations. The calculation is done with a Z' that interacts with the third generation through its coupling g' and with other generations through a mixed coupling g_{mix}, of whose origin we remain agnostic. It could be generated by quantum effects, as we argue in [547], or have come from an explicit mass or kinetic mixing term in the Lagrangian of the theory.

It should be noted (see also reference [547]) that while it is common in model building to make a $U(1)'$ model 'leptophobic' or 'leptophilic' or in our case 'tritophilic' as a way of escaping inconvenient phenomenological bounds, gauge boson mixing effects mean that no model can truly be any of these things. These philias and phobias may set the bare charge to zero, and decouple certain sets of particles from the new gauge field to leading order, but quantum corrections will always induce kinetic and mass mixing effects even if they are not explicitly present in the bare theory. In reference [547], some basic analysis is done to demonstrate that one obtains a suppression that is limited by the gauge couplings. Thus, no model can truly evade phenomenological bounds, and even so-called leptophobic models must consider the stringent dilepton bounds.

The calculation proceeds along the same lines as the classic estimation of the Higgs-nucleon coupling by Shifman, Vainstein and Zakharov [242]. We work using the generalized axial and vector charges as defined in Chapter 6:

$$J_{Z'} = \bar{f}\gamma^{\mu}\left(V'_f + A'_f\gamma^5\right) f \tag{G.1}$$

The interaction current between the Z' and a nucleon can be written in terms of the nucleon components:

$$\begin{aligned} J^{\mu}_{Z'NN} Z'_{\mu}\bar{\Psi}_N\Psi_N = &\sum_{q=u,d,s} Z'_{\mu}\langle N|\bar{q}\gamma^{\mu}\left(V'_q + A'_q\gamma^5\right) q|N\rangle + \sum_{Q} Z'_{\mu}\langle N|\bar{Q}\gamma^{\mu}\left(V'_Q + A'_Q\gamma^5\right) Q|N\rangle \\ &+ \langle N|\Gamma^{\mu\nu\rho}_{Z'gg}\left(p_1,p_2\right) Z'_{\mu}\left(k\right) B_{\nu}\left(p_1\right) B_{\rho}\left(p_2\right)|N\rangle. \end{aligned} \tag{G.2}$$

The first term on the right hand side represents interactions with light quarks, the second interactions with heavy quarks, and the third with the gluonic binding energy of the nucleon. The light quark term can be represented in terms of the nucleon form factors and axial form factors:

$$V'_q\langle N|\bar{q}_j\gamma^{\mu}q_j|N\rangle = V'_q\bar{u}\left[F_1^j(k^2)\gamma^{\mu} + i\frac{\sigma^{\mu\nu}q_{\nu}}{2m_N}F_2^j(k^2)\right]u, \tag{G.3}$$

and

$$A'_q\langle N|\bar{q}_j\gamma^{\mu}\gamma^5q_j|N\rangle = A'_q\bar{u}\left[G_A^j(k^2)\gamma^{\mu}\gamma^5\right]u, \tag{G.4}$$

though these form factors are not necessary to describe the low momentum transfer limit that is of interest in nuclear recoil cross sections.

The heavy quark term can be evaluated using the heavy quark expansion as detailed in reference [705], which allows us to reframe the heavy quark degrees of freedom in terms of the light quark and gluon degrees of freedom. This is the same basic approach that was taken in reference [242]. To leading order in $1/m_Q^2$, where m_Q is the heavy quark mass, the heavy quark expansion of the vector part of the current is zero:

$$\langle N|\bar{Q}\gamma^{\mu}Q|N\rangle = 0 + \mathcal{O}\left(\frac{1}{m_Q^4}\right). \tag{G.5}$$

The heavy quark expansion of the axial part of the current can be related to the heavy quark expansion of the pseudoscalar current [705]:

$$\langle N|\bar{Q}\gamma^{\mu}\gamma^5 Q|N\rangle = \frac{-ig_s^2}{96\pi^2 m_Q^2}\langle N|\left(\partial^{\mu}\mathrm{Tr}_c\left[t^a G^a_{\alpha\beta}t^b\tilde{G}^{b\alpha\beta}\right]\right.$$
$$\left.+4\mathrm{Tr}_c\left[\left[D_{\alpha},t^a G^{a\alpha\nu}\right]t^b\tilde{G}^{b\mu}_{\nu}\right]\right)|N\rangle + \mathcal{O}\left(\frac{1}{m_Q^4}\right). \tag{G.6}$$

where the gluon field strength tensor is $G^a_{\mu\nu} = \partial_{\mu}B^a_{\nu} - \partial_{\nu}B^a_{\mu} + g_s f^{abc}B^b_{\mu}B^c_{\nu}$ and the dual gluon field strength tensor is $\tilde{G}_{\mu\nu} = (1/2)\epsilon^{\alpha\beta\mu\nu}G_{\alpha\beta}$. The trace is taken over colors and the $SU(3)_c$ gauge covariant derivative is D_{α}. After a Fourier transformation and using translation invariance, one can write the first term as

$$\frac{-ig_s^2}{96\pi^2 m_Q^2}\langle N|\partial^{\mu}\mathrm{Tr}_c\left[t^a G^a_{\alpha\beta}t^b\tilde{G}^{b\alpha\beta}\right]|N\rangle = \frac{-i\alpha_s k^{\mu}}{48\pi m_Q^2}\langle N|G^a_{\alpha\beta}\tilde{G}^{a\alpha\beta}|N\rangle. \tag{G.7}$$

where numerical values for the nucleon matrix element are reported in the literature [253] (about 380 MeV for the proton and about 11 MeV for the neutron). This contribution to the total is clearly suppressed by the momentum transfer and a factor of $1m_Q^2$. The second term in Equation (G.6) can be rewritten using the QCD equation of motion as

$$\frac{ig_s^2}{24\pi^2 m_Q^2}\langle N|\mathrm{Tr}_c\left[\left[D_{\alpha},t^a G^{a\alpha\nu}\right]t^b\tilde{G}^{b\mu}_{\nu}\right]|N\rangle = \frac{i\alpha_s}{24\pi m_Q^2}\langle N|g_s\sum_{q=u,d,s}\bar{q}\gamma_{\nu}\tilde{G}^{\mu\nu}q|N\rangle. \tag{G.8}$$

Expanding in Lorentz structures and setting the scalar part equal to zero by parity, one obtains

$$\sum_{q=u,d,s}\langle N|g_s\bar{q}\gamma_{\nu}\tilde{G}^{\nu\mu}q|N\rangle = F_S S^{\mu}. \tag{G.9}$$

where terms are proportional to the momentum transfer k^{μ} and the nucleon spin S^{μ}. In the forward matrix element limit that corresponds to low momentum transfer [706, 707], the form factor can be written

$$F_S S^{\mu} = \sum_{q=u,d,s} 2f_{N2,q}m_N^2 S^{\mu}. \tag{G.10}$$

where the coefficients $f_{N2,q}$ are estimated [707] to sum to 0.1 over the light flavors.

The dominant part of the heavy quark contribution to the current is then

$$\sum_Q\langle N|\bar{Q}\gamma^{\mu}\left(V'_Q + A'_Q\gamma^5\right)Q|N\rangle \simeq \sum_Q A'_Q\frac{4im_N^2\alpha_s\sum_{q=u,d,s}f_{N2,q}}{9\pi m_Q^2}S^{\mu}. \tag{G.11}$$

To compute the gluon contribution, we rely on a 1-loop expression for the $Z'gg$ interaction vertex $\Gamma^{\mu\nu\rho}_{Z'gg}(p_1,p_2)$ adapted from reference [627]. The expression is not reproduced here.

The crossed diagram under the exchange of the two gluon momentum also contributes, leading to a factor of two. The vertex function is in fact independent of the quark vector coupling V, depending only on the axial coupling. If the axial charge were zero, the coupling would then vanish.

The gluon contribution to the current

$$J^{G,\mu}_{Z'NN}Z'_{\mu} = \langle N|\Gamma^{\mu\nu\rho}\left(p_1,p_2\right)Z'_{\mu}\left(k\right)B_{\nu}\left(p_1\right)B_{\rho}\left(p_2\right)|N\rangle \tag{G.12}$$

can be reduced to

$$B_{\nu}\left(y\right)B_{\rho}\left(z\right) \simeq \frac{y^{\delta}}{2}G_{\delta\nu}(0)\frac{z^{\lambda}}{2}G_{\lambda\rho}(0). \tag{G.13}$$

by Fourier transforming to position space, and expanding in fixed point gauge [708], which allows the expansion of the gluon field strength tensors in the nucleon near the origin. The current now takes the form, with the color factors suppressed

$$J^{G,\mu}_{Z'NN} Z'_\mu \simeq \int d^4x d^4y d^4z \langle N|\tilde{\Gamma}^{\mu\nu\rho}(y,z)\, Z'_\mu(x)\, \frac{y^\delta}{2} G_{\delta\nu}(0) \frac{z^\lambda}{2} G_{\lambda\rho}(0)|N\rangle e^{ik\cdot x} e^{ip_1\cdot y} e^{ip_2\cdot z}. \tag{G.14}$$

By Fourier transforming back into momentum space, the position coordinates become momentum derivatives and by exploiting symmetry properties and conservation of momentum, the current can be written

$$J^{G,\mu}_{Z'NN} Z'_\mu \simeq \frac{1}{4}\langle N|\tilde{\Gamma}^{\mu\nu\rho}(p_1,p_2)\left(\frac{\partial}{\partial k^\delta} - \frac{\partial}{\partial k^\lambda}\right) Z'_\mu(k)\, G^\delta_\nu(0) G^\lambda_\rho(0)|N\rangle. \tag{G.15}$$

Pulling the vertex function and the derivatives outside the expectation value allows for significant simplification, leading to

$$J^{G,\mu}_{Z'NN} Z'_\mu \simeq \sum_Q A_1^Q(k) \frac{\partial}{\partial k^\delta} Z'_\mu(k)\, \langle N|\tilde{G}^\mu_\rho G^{\delta\rho}|N\rangle. \tag{G.16}$$

where the sum is over the fermions contributing to the loop in the vertex function, and an epsilon tensor was absorbed from the vertex function into the dual field strength tensor. The coefficient function A_1^Q takes the form

$$A_1^Q(k) = \frac{A'_Q N_c}{4\pi^2}\left[3 + \Lambda(s,m_Q,m_Q) + 2m_Q^2 C_0(0,0,s;m_Q,m_Q,m_Q)\right], \tag{G.17}$$

where the loop functions $\Lambda(s,m_Q,m_Q)$ and $C_0(0,0,s;m_Q,m_Q,m_Q)$ are

$$\Lambda(s,m,m) = \sqrt{1-\frac{4m^2}{s}} \ln\left[\frac{2m^2}{2m^2 - s\left(1+\sqrt{1-\frac{4m^2}{s}}\right)}\right] \tag{G.18}$$

and

$$C_0(0,0,s,m,m,m) = \frac{1}{2s}\ln^2\left[\frac{\sqrt{1-\frac{4m^2}{s}}-1}{\sqrt{1-\frac{4m^2}{s}}+1}\right]. \tag{G.19}$$

The matrix element $\langle N|\tilde{G}^\mu_\rho G^{\delta\rho}|N\rangle$ is the nucleon expectation value of a spin-2 twist-2 gluonic pseudotensor operator, which is a difficult expectation value to find numerical values for. Luckily, we will not need numerical values for this quantity. The variable $s = (p_1+p_2)^2$ is the momentum transfer in a nuclear recoil process, and the low-momentum transfer limit corresponds to $s = k^2 \to 0$. The function A_1^Q goes to zero in this limit, but we expand in powers of momentum transfer to be able to compare against other contributions. Expanding about $k^2 = 0$ gives

$$A_1^Q(k) = \left(\frac{A'_Q N_c}{4\pi^2}\right)\left(\frac{k^2}{12m_Q^2}\right) + \mathcal{O}\left(k^4\right). \tag{G.20}$$

which leads to the contribution from gluon interactions to the current

$$J^{G,\mu}_{Z'NN} Z'_\mu \simeq \frac{\partial}{\partial k^\delta} Z'_\mu(k) \frac{A'_Q}{16\pi^2 m_Q^2} k^2 \langle N|\tilde{G}^\mu_\rho G^{\delta\rho}|N\rangle. \tag{G.21}$$

This expression is suppressed by the square of the heavy quark mass as well as two powers of momentum transfer. It clearly contributes less than the other components.

From this calculation, the basic conclusion can be drawn that, for a coupling hierarchy of $g' > g_{mix}$ by an order of magnitude or so as one might expect, the light quark term dominates the effective current. This means that standard expressions for the nuclear recoil cross section assuming interactions with valence

quarks can be used, if one takes the effective charge to use the mixed coupling. The heavy quark and gluon field contributions are less, suppressed as they are. They begin to become relevant when g' is several orders of magnitude larger than g_{mix}, as is discussed more explicitly in reference [547]. Thus this Appendix has justified the expression we have used for the nuclear recoil cross section in Chapter 6, including the tritophilic nature of the model.